

**Quantitative Studies of the Martian South
Polar Region Using Spacecraft Images**

Thesis by
Kenneth Edward Herkenhoff

In partial fulfillment of the requirements for the degree of
Doctor of Philosophy

**California Institute of Technology
Pasadena, California**

1989
(Submitted May 24, 1989)

Copyright ©1989
Kenneth Edward Herkenhoff
All rights reserved

To my son, Lee James,
a far more perfect creation than this dissertation.

Acknowledgements

I first acknowledge my parents, without whom I would not exist, let alone complete graduate school. They provided me with all I needed to achieve the goals I set for myself, including copious encouragement and motivation. My wife, Lottie, suffered more than anyone as I pursued my Ph.D. I cannot thank her enough for the help she has given me along the way, and I hope that I may return the favor someday.

The first professional acknowledgment must go to my thesis advisor, Bruce Murray. He provided the impetus to carry on when I floundered and the feedback I repeatedly needed. The purpose of graduate school is to learn, and I learned a lot about scientific reasoning and writing from him. He and Larry Soderblom suggested the Mars south polar layered deposits as a research topic, and the deposits keep my interest today. None of us realized how much was involved in the project, but I now feel that it was all worthwhile. Larry gave me the opportunity to become acquainted with the people and the facilities at the U. S. Geological Survey in Flagstaff, Arizona, for which I shall always be grateful. I hope to continue my association with the USGS and with Larry in particular.

There are so many people at Caltech that I would like to thank that I hesitate to begin, in fear of forgetting someone. I thank my academic advisor, Dave Stevenson, for many hours of discussion and patience. I'm no physicist, but I know enough to recognize a great one when I meet him. Jim Westphal allowed me to use his VAX 11-780 when it was the only computer in the department, and was

patient and courteous when I hogged his disk space. Ed Danielson got me started on the system and provided helpful suggestions along the way. I feel fortunate to have been able to collaborate with Dave Paige on some very interesting research. Hopefully we'll publish it soon! As with so many students before me, Kay Campbell and Lorna Griffith got me through some tough administrative hassles.

The repeated assistance I received from various people at the U. S. Geological Survey in Flagstaff, Kay Edwards, Eric Eliason and Tammy Becker in particular, is gratefully acknowledged. I thank Phil Davis, Randy Kirk, Alfred McEwen, Andy Ingersoll and David Crisp for helpful suggestions and assistance. Peter Kupferman, Paul Jepsen, Tom Thorpe, Nancy Evans and Martha Baxter were helpful in obtaining and analyzing the Mariner 9 preflight calibration data; Jim Bell provided valuable information regarding archival telescopic data, and David Paige supplied Viking IRTM data. I also thank Yuk Yung for allowing me to use his RADIATE program and Mark Allen for assistance in modifying and implementing it.

It has become traditional to acknowledge fellow graduate students in doctoral dissertations at Caltech, which presents me with a dilemma. Merely listing past and present officemates would fill a page. Hence, I will mention only one, Jim Friedson. He was the best officemate a boy could ask for, and remains a good friend. Maybe we can share an office at JPL, Jim. I hope the rest of you don't take offense, because it has been fun (at times), and I thank you all.

This work was supported by NASA grants NGT-50096 and NAGW-1226.

Abstract

Spacecraft observations must be calibrated absolutely in order to investigate the photometric properties of the Martian surface and atmosphere. The accuracy of the Mariner 9 and Viking Orbiter television system calibration was evaluated by comparing the two data sets with each other and with Earth-based spectrophotometry of Mars and Phobos. The Viking imaging data are consistent with published estimates of the geometric albedo of Phobos, which is uncertain by about 20%. Mariner 9 data are calibrated to within about $\pm 20\%$ by comparing Phobos images with Viking data. Better photometric observations of Phobos are necessary to improve the calibration of the Viking Orbiter and Mariner 9 television systems. Similarly, inflight Phobos observations should be used to calibrate imaging systems on future Mars missions.

Mariner 9 images were processed for comparison with nearly simultaneous infrared spectra of the south polar cap of Mars recorded in 1971-72. Combined analysis of these observations indicates that the southern residual cap was covered by carbon dioxide frost throughout the summer, in agreement with Viking Orbiter measurements made three Mars years later. Thermal modeling of the spectra shows that areas of intermediate albedo are cooled to the sublimation temperature of CO_2 , suggesting that frost is present but not visible. Topographic roughness may shade the CO_2 from the sun and produce the variegated appearance of the residual cap.

Five color/albedo units, including polar frost, have been recognized and

mapped in the southern layered deposits on Mars. Atmospheric dust scattering was measured in shadows and modeled in order to remove the component of brightness due to the atmosphere and quantify the albedo and color of the surface. The layered deposits appear to be mantled by red dust, except where eolian stripping has exposed the underlying bedrock. Frost and bare ground are mixed below the resolution of the images in many areas adjacent to the polar cap, some of which appear to be younger than the surrounding layered terrain. Dark material has been deposited in topographic depressions in much of the south polar region, including the layered deposits. The available observational data suggest that the layered deposits are composed of bright dust, ice, and a small amount of dark material. If the dark material is sand, a periodic change in polar winds seems required in order to transport the sand poleward into the layered terrain. In any case, the observations are not consistent with the layered deposits being composed only of bright dust and ice.

Maximum slopes of 10-20 degrees occur on an exposure of layered deposits within the south polar residual cap of Mars. A new photoclinometric technique is used to produce profiles of slope and albedo using high resolution Mariner 9 images. Stereophotogrammetry is also used to constrain the photoclinometric solutions, which resolve layer thicknesses of 100-300 meters. The results are limited by the ~ 200 meter resolution of the images, and thinner (unresolved) layers are likely. The $\sim 25\%$ maximum albedo variations are correlated with slope, indicating

that frost is present on level areas. There is evidence for temporal changes in frost distribution in the 7 days (4° of L_s) between the two images used in this study, demonstrating that future photoclinometric studies of the polar regions must be attempted carefully. The magnitude of the slopes derived here suggest that the layers are competent, perhaps due to the presence of a weathering rind.

Weathering of the layered deposits by sublimation of water ice can account for the data presented here and previous observations of the north polar deposits. The non-volatile component of the layered deposits appears to consist mainly of bright red dust, with small amounts of dark dust or sand. Deposition of sand in the layered deposits is problematical, so inclusion of dark dust is preferred. The dark dust may be similar to the magnetic material found at the Viking Lander sites, and may therefore preferentially form $\sim 100\mu$ filamentary residue particles upon weathering. Once eroded from the layered deposits, these particles may then saltate to form the dark sand dunes found in both polar regions. Eventual destruction of the particles could allow recycling of the dark dust into the layered deposits via atmospheric suspension.

Contents

Acknowledgements	iv
Abstract	vii
List of Figures	xiii
List of Tables	xv
1 Introduction	1
1.1 Scientific Context	2
1.1.1 Polar Layered Deposits	3
1.1.2 Polar Caps	10
1.1.3 Mars Climate Changes	12
1.2 Database	14
1.3 Summary of Thesis Results	15
2 Television System Calibration	19
2.1 Limitations of Earth-Based Photometric Observations	21
2.2 Viking Orbiter Photometric Accuracy	23
2.2.1 Phobos Observations	25
2.2.2 Mars Observations	30
2.3 Mariner 9 Photometric Accuracy	34
2.3.1 Preflight Calibration	36
2.3.2 Phobos Observations	38
2.3.3 Mars Observations	39
2.4 Absolute Calibration Summary	41
3 Applications and Discussion	43
3.1 Composition of the South Polar Residual Cap	43
3.1.1 IRIS Observations	50

3.1.2	Television Observations	55
3.1.3	Analysis	60
3.1.4	Discussion	68
3.2	Color and Albedo of the South Polar Layered Deposits	70
3.2.1	Processing and Mapping Methods	72
3.2.2	Results and Interpretations	83
3.2.3	Discussion	93
3.2.4	Summary of Color and Albedo Results	100
3.3	High Resolution Topography and Albedo of the South Polar Layered Deposits	102
3.3.1	Data Processing and Modeling	103
3.3.2	Results and Discussion	123
3.3.3	Summary of High Resolution Topography and Albedo Results	144
4	Conclusions and Recommendations	146
4.1	Genetic and Climatic Implications	146
4.1.1	South Polar Residual Cap	147
4.1.2	Color and Albedo	149
4.1.3	High Resolution Topography and Albedo	152
4.1.4	Evolution of the Polar Layered Deposits	154
4.2	Absolute Calibration Improvement Using Phobos Observations	157
A	Mariner 9 Television Relative Calibration	159
A.1	Inherent Uncertainties in Mariner 9 Television Data	160
A.1.1	Residual Image	160
A.1.2	Dark Current	162
A.1.3	Light Transfer Curve	162
A.1.4	Shutter Exposure	166
A.1.5	Shading	169
A.1.6	Noise	170
A.2	Calibration Methods and Remaining Uncertainties	171
A.2.1	Residual Image	172
A.2.2	Dark Current	174
A.2.3	Light Transfer Curve	175
A.2.4	Shutter Exposure	179
A.2.5	Shading	179
A.2.6	Noise	183
A.3	Conclusion	184
B	Atmospheric Scattering Model	186

C FORTRAN code	197
C.1 Mariner 9 image processing software	197
C.2 Photoclinometric software	238
References	266

List of Figures

2.1	Phobos average reflectance vs. phase angle.	27
2.2	Viking Orbiter 1 and Earth-based observations of Arabia.	32
2.3	Earth-based and Viking Orbiter observations vs. phase angle.	33
3.1	Mariner 9 wide angle image of the south polar cap, orbit 28.	45
3.2	Mariner 9 narrow angle image of part of south polar cap, orbit 28.	47
3.3	Mariner 9 wide angle image of the south polar cap, orbit 116.	48
3.4	Mariner 9 narrow angle image of the south polar cap, orbit 116.	49
3.5	Midpoints of Mariner 9 IRIS footprints.	52
3.6	Mariner 9 IRIS brightness temperature spectra.	53
3.7	IRIS spectrum of south polar cap obtained on orbit 28.	54
3.8	Histograms of Lambert albedo.	58
3.9	2-component model fits to orbit 28 IRIS spectrum.	63
3.10	Three-component model results.	65
3.11	Three-component model time evolution.	67
3.12	Viking Orbiter 2 color mosaic.	73
3.13	Rev 407 red/violet ratio image.	75
3.14	Corrected color mosaic.	77
3.15	Corrected red/violet mosaic.	78
3.16	South polar photomosaic MC-30A/B.	79
3.17	Map of color/albedo units in the south polar layered terrain.	80
3.18	Detail of the vicinity of the south pole.	86
3.19	Red/violet ratio vs. violet Lambert albedo.	88
3.20	Violet vs. red Lambert albedo.	92
3.21	Mariner 9 south polar residual cap frame 173B1.	105
3.22	Mariner 9 south polar residual cap frame 188B2.	106
3.23	Comparison of atmospheric model and Mariner 9 data.	110
3.24	Profile 1 data with averages of 2-pixel increments.	115
3.25	Geometric relationships in photoclinometric model.	118
3.26	Constant- w model topography for profile 1.	120

3.27	Comparison of reflectance predicted by model slopes with profile 1 data from "albedo" image.	121
3.28	Profile 1 topography and albedo from iterative model.	124
3.29	Contrast enhanced image detail.	127
3.30	Profile 2 data with averages of 2-pixel increments.	128
3.31	Constant- w model topography for profile 2.	129
3.32	Comparison of reflectance predicted by model slopes and profile 2 data from "albedo" image.	130
3.33	Profile 2 topography and albedo from iterative model.	131
3.34	Profile 3 data with averages of 2-pixel increments.	134
3.35	Constant- w model topography for profile 3.	135
3.36	Comparison of reflectance predicted by model slopes with profile 3 data from "albedo" image.	136
3.37	Profile 3 topography and albedo from iterative model.	137
A.1	A-camera dark current frame.	163
A.2	B-camera dark current frame.	164
A.3	Dark current profiles.	165
A.4	A-camera calibration data for various vidicon areas.	167
A.5	A-camera calibration data for various filters.	168
A.6	B-camera calibration data for various temperatures.	175
A.7	A-camera linearized inflight calibration data.	178
A.8	Rev 3 linearized data for central area of vidicon vs. cosine of incidence angle.	182
B.1	Viking Orbiter 2 orbit 407 violet ($\lambda_{eff} = 0.45\mu$) shadow data with model fits.	191
B.2	Viking Orbiter 2 orbit 407 green ($\lambda_{eff} = 0.54\mu$) shadow data with model fits.	193
B.3	Viking Orbiter 2 orbit 407 red ($\lambda_{eff} = 0.59\mu$) shadow data with model fits.	194

List of Tables

2.1	Viking Orbiter moderate-phase Phobos observations.	28
2.2	Viking Orbiter 1 and Mariner 9 low-phase Phobos observations.	29
2.3	Mariner 9 calibration constants.	38
3.1	Observational geometry data for IRIS spectra midpoints.	51
3.2	Lambert albedos and colors of surface units.	82
3.3	Latitudes and Longitudes of Profile Endpoints.	113
3.4	Incidence, Emission and Phase Angles at Profile Endpoints.	113
A.1	Mariner 9 vidicon shading.	170
A.2	Accuracy of Mariner 9 calibration.	184
B.1	Atmospheric dust scattering parameters.	192

Chapter 1

Introduction

Mars has long been intriguing to both scientists and the public. Television images of Mars can be appreciated by the layman and are valuable to scientists as well. The most common use of imaging data to date has been in photogeologic investigations, in which errors in calibration are less critical than in quantitative studies. Much has been learned in the past few years regarding vidicon calibration, enabling quantification of the photometry of the Martian surface and atmosphere. This type of analysis can constrain the optical properties of atmospheric particles and the texture, albedo, and color of the surface. Properly calibrated images can be used to model the topography of small features on Mars using photoclinometry. Hence, television data are widely applicable to the study of Mars.

The body of work presented in this dissertation was motivated by an interest in the geology of the Martian polar layered deposits. The layered deposits are widely believed to record climate variations on Mars, but the available observational evidence has not yet allowed interpretation of the climate history. As quantitative investigations of Mars utilizing television images require that the data be properly

calibrated, considerable effort was put into calibrating Mariner 9 data (Appendix A) and verifying the absolute accuracy of Viking Orbiter images (Chapter 2). The resulting uncertainties in the imaging data permit studies of the photometry of the Martian surface and atmosphere, and therefore allow application of photoclinometric models to assess topographic slopes (Chapter 3).

Previous results regarding Mars polar geology, the composition of the polar caps, and Martian climate changes are reviewed in the next section. Key scientific questions concerning these subjects are emphasized. The imaging database limitations that pertain to studies of the polar regions are then described, followed by a summary of the important results of this thesis.

1.1 Scientific Context

The published literature dealing with the polar regions of Mars is voluminous, reflecting widespread scientific interest in the subject. The north polar layered deposits have been more extensively studied than their southern counterparts, as reviewed in the next section. I have therefore chosen to analyze the best television images of the south polar region in order to enhance our knowledge of layered terrain geology.

The dynamic history of the theory and observations of the polar caps is presented after a review of geological and topographic studies. The astronomical theory of orbital and axial variations is then briefly reviewed, and the attempt

to relate the stratigraphy of the layered deposits to theoretical climate changes is examined.

1.1.1 Polar Layered Deposits

The polar layered deposits on Mars are believed to record global climate cycles, but the details of the processes involved and their relative roles in layer formation remain obscure (Thomas *et al.*, 1989). The “conventional wisdom” among Mars researchers is that the layered deposits were formed by periodic variations in the deposition of dust and ice caused by climate changes over at least the last 10^7 to 10^8 years (Murray *et al.*, 1972; Soderblom *et al.*, 1973; Cutts, 1973b; Cutts *et al.*, 1976; Cutts *et al.*, 1979; Squyres, 1979; Toon *et al.*, 1980; Howard *et al.*, 1982b; Carr, 1982; Pollack and Toon, 1982; Plaut *et al.*, 1988). However, a consensus regarding the detailed historical evolution of the layered deposits and the time interval involved has not been reached. Cutts and Lewis (1982) have made a first attempt at modeling the stratigraphy of the layered deposits with simplifying assumptions, but more work is needed in this area. In addition, the overall current erosional/depositional state of the layered deposits and the cause of the marked differences between the north and south are unknown.

Topography and Morphology

Layered deposits were first recognized in the south polar region and described by Murray *et al.* (1972), who found that they lie unconformably on cratered terrain and other units. They counted 20-40 layers and estimated the total thickness of the deposits to be ~ 1 km. The outline of the residual cap and the presence of numerous roughly spiral dark bands within it were attributed to the topography of the subjacent layered deposits: equatorward-facing slopes were defrosted due to increased insolation. Cutts (1973b) first recognized these dark bands as topographic troughs, and proposed that they were formed by eolian erosion and deposition. Mariner 9 images also revealed layered terrain in the north polar region (Soderblom *et al.*, 1973), but at lower resolution.

Dzurisin and Blasius (1975) combined stereophotogrammetric results with radio occultation measurements given by Kliore *et al.* (1973) to find that the southern layered deposits are higher in elevation than the northern deposits, although the northern deposits were inferred to be much thicker (4-6 km). Their thickness estimate of 1-2 km for the southern deposits has been used by many workers, but is based only on data in the vicinity of the residual cap. In addition, assumptions had to be made regarding the underlying topography, so that the southern deposits may in fact be considerably thicker. Despite a 2.5° tilt uncertainty in their results, they proposed that a regional slope of less than 1 degree may cause the offset of the south residual cap with respect to the geometric pole, and that the stability of the

cap is controlled by insolation. Finally, they concluded that both depositional and erosional processes are required to explain the complex topographic configuration of the layered deposits.

Cutts *et al.* (1976, 1979) first recognized unconformities in the layered deposits and low amplitude undulations in the level areas between troughs, with wavelengths similar to the widths of the troughs (5-10 km). They interpreted these undulations as fossil permanent cap margins, formed as dust was periodically deposited on the advancing or retreating permanent cap. Squyres (1979) pointed out that the model of Cutts *et al.* (1979) cannot explain the presence of the troughs, which he attributed to eolian erosion during periods when the permanent cap vanishes. His concept of trough lengthening parallel to wind directions is not consistent with present surface indicators of wind patterns, however. He also proposed that the low-amplitude undulations are left by the poleward migration of troughs, but the lack of cross-sectional exposures prevents testing of such hypotheses.

Howard *et al.* (1982a) found steep arcuate scarps eroded into the north polar layered deposits. These scarps slope 20 – 30° and are a few hundred meters high. They may be sites of enhanced erosion and appear to be the source of dark material that forms dunes nearby (Thomas and Weitz, 1989).

The erosional and depositional processes thought to be important in layered terrain formation and evolution are expected to leave topographic signatures. The topography of the layered deposits can yield profound geologic constraints, as

demonstrated by the results presented above. Better regional topographic information is therefore needed in both polar regions. Such information can be used to more precisely address such problems as the total thickness, density, and overall stratigraphy of the deposits. In particular, low-amplitude undulations have not been found in the south polar region, and should be a target of future exploration.

Previous efforts to derive slopes and heights of layered deposit exposures have been published (Dzurisin and Blasius, 1975; Blasius *et al.*, 1982; Howard *et al.*, 1982a). Blasius *et al.* (1982) found that layer contrasts were enhanced in the north polar deposits by retention of frost during the summer on relatively level slopes. By comparing such images with images of the same area taken during the spring (when the frost cover was essentially complete), they concluded that variations in layer composition also influence frost retention. However, the magnitude of albedo variations in the layered deposits has not been previously quantified due to limitations in photoclinometric techniques and the fundamental ambiguity between albedo and slope effects.

Murray *et al.* (1972) first recognized that most of the layering observed in the south polar region is due to the "staircase" topography of the deposits, but noted that albedo variations between layers are indicated in some cases. Photoclinometry has not been applied successfully to the south polar layered deposits, however. Dzurisin and Blasius (1975) used stereophotogrammetry across exposures of layered deposits within the southern residual cap and found overall slopes in

the range of 1-5 degrees. Stereogrammetry can establish the elevation difference between distinct surface points, but cannot resolve the topography of individual layers. Photoclinometric techniques can distinguish topographic features as small as the resolution of the image will permit, but are sensitive to errors in estimates of level surface reflectance and atmospheric scattering (Howard *et al.*, 1982a).

Stratigraphy and Geologic History

Study of high-resolution Viking Orbiter images of the north polar deposits confirms that erosion occurs on equatorward-facing slopes, while poleward-facing slopes are currently undergoing deposition aided by the presence of perennial frost (Squyres, 1979; Howard *et al.*, 1982b). These processes result in poleward migration of the topographic troughs in the layered deposits, as indicated by stratigraphic relationships exposed in trough junctions (Howard *et al.*, 1982b). The north polar areas studied by Howard *et al.* (1982b) show that deposition of 5-10 layers, each 14-46 m thick (Blasius *et al.*, 1982), is occasionally interrupted by periods of erosion; this scenario has apparently continued to the present. They find that either widespread erosion occurs during the time intervals represented by the unconformities, or deposition dominates erosion in the long term. If massive erosion does not occur episodically, then the youth of the deposits is paradoxical (Howard *et al.*, 1982b). A conjectured resolution of this paradox is that basal melting occurs when the thickness of the layered deposits becomes great enough, removing material as

groundwater or by glacial flow (Clifford, 1987). The appearance of a series of ridges parallel to the limit of the north polar layered deposits is possible evidence of glacial flow, as these features may be moraines (Howard *et al.*, 1982b). Further geologic study of the polar regions is needed to resolve this problem.

Cutts *et al.* (1976) found no craters larger than about 300 m in the north polar layered terrain, implying very rapid deposition or erosion: about 1 mm per year. A few craters found in the south polar layered terrain indicate that the surface of the southern deposits is about 120 million years old (Plaut *et al.*, 1988), but the possibility that these features have been exhumed by recent erosion was not taken into account, suggesting that this age is an upper limit. It should be emphasized that the cratering flux at Mars is sufficiently uncertain that the above surface ages and deposition rates should be considered only relative to other areas on Mars, and not in an absolute sense. For comparison, the present dust deposition rate is estimated by Pollack *et al.* (1979) to be about 0.3 mm/yr, sufficient to form a single layer in 100,000 years. In any case, the layered deposits have been subjected to recent modification, and probably record the last tens to hundreds of millions of years of Martian climate changes.

Schultz and Lutz (1988) have presented evidence for ancient polar deposits at low latitudes near 0° and 180°W longitude. They interpret these and other observations as indicating reorientation of the rotation axis of Mars. While rather controversial, their hypothesis would constrain the age of the present polar deposits

to well under 3 billion years.

Composition

The composition of the layered deposits is poorly constrained. Malin (1986) estimates the density of the northern deposits to be 1gcm^{-3} , indicating that they are mostly ice. However, the volume of the north polar layered deposits is poorly known, and even the optimistic uncertainty of 50% stated by Malin (1986) allows for up to 50% dust. High resolution Viking Orbiter images of the northern deposits show that dark, saltating material is being derived from erosion of the layered deposits (Thomas and Weitz, 1989). These observations suggest that dark material has somehow been incorporated into the layered deposits, perhaps as saltating sand during periods of poleward winds. However, the color and albedo of the north polar deposits suggest that bright red dust is the major non-volatile component of the layered deposits (Thomas and Weitz, 1989).

The lack of observed flow features indicates that glacial flow has not recently occurred in the layered deposits, and led Hofstadter and Murray (1989) to conclude that the layered deposits are less than 40% water ice by volume. However, their modeling suggests that nearly pure water ice would not flow either. In the ice-rich case, some type of protective surface layer is required to lower the sublimation rate of the deposits (Hofstadter and Murray, 1989).

North/South Differences

The south polar layered deposits have not been studied in the same detail as their northern counterparts due to the lack of imagery of the same resolution. However, the television data are sufficient to reveal the major differences between the layered deposits at the two poles. The extent of the layered terrain is greater in the south, while the residual polar cap is smaller (Tanaka and Scott, 1987), exposing a much larger area of layered deposits. Off-cap winds have stripped and dissected the layered deposits (Cutts, 1973a), but the topographic troughs seen also in the north are still evident (Howard *et al.*, 1982b). There is no counterpart in the south for the erg that surrounds the north polar cap, but dark dunes are found in topographic depressions near the southern layered terrain (Thomas, 1982). The reasons for these differences are not known, but may include: asymmetry in polar insolation due to the present orbital eccentricity, elevation differences between the poles, and the recent climate history. The steep scarps found in the north polar layered deposits that appear to be the source of dune material (Thomas and Weitz, 1989) have not been identified in the south.

1.1.2 Polar Caps

The discovery by Mariner 4 in 1965 that the Martian atmosphere consists of 5-6 millibars of nearly pure carbon dioxide led Leighton and Murray (1966) to propose that the polar caps are CO₂ frost in equilibrium with the atmosphere.

Infrared observations by Mariner 7 in 1969 confirmed their prediction by showing that the southern seasonal cap temperature was that expected for subliming CO₂ frost (Neugebauer *et al.*, 1971; Herr and Pimentel, 1969). Mariner 9 and Viking measurements also supported the CO₂ composition of the seasonal caps in detail (Hanel *et al.*, 1972a; Kieffer *et al.*, 1976b).

Leighton and Murray (1966) also predicted that the CO₂ partial pressure in the Martian atmosphere is determined by a permanent reservoir of solid CO₂ in equilibrium with the atmosphere. The mass of the atmosphere was therefore believed to be determined by the annual heat balance at the poles, and the permanent reservoir of CO₂ was expected at the north pole due to its lower elevation (Murray and Malin, 1973). Mariner 9 data led Ingersoll (1974) to argue against a permanent CO₂ reservoir in equilibrium with the atmosphere and to propose that there is no excess carbon dioxide on the surface. This proposal was supported by Viking Orbiter summertime observations of the north polar residual cap, which demonstrated that the northern residual cap is composed of water ice (Kieffer *et al.*, 1976a; Farmer *et al.*, 1976).

Surprisingly, Viking Orbiter observations also demonstrated that CO₂ frost was present on the south polar residual cap throughout the summer of 1977 (Kieffer, 1979). Two other observations suggest that the summer of 1977 may not have been typical, however. Global water vapor measurements in 1969 by Barker *et al.* (1970) have been interpreted by Jakosky and Barker (1984) as evidence that the seasonal

carbon dioxide frost completely sublimed that year, exposing the residual water ice cap. Secondly, James *et al.* (1979) noted that the south polar seasonal cap receded more slowly in 1977 than in 1971-72, as observed by Mariner 9. Pollack and Toon (1982) have suggested that the interannual variations in cap retreat are due to variations in the amount of dust incorporated into the cap. More observations of the south polar residual cap are clearly needed, but the available data suggest that there is just enough CO₂ to cover the southern cap throughout the summer.

This apparent coincidence is paradoxical in light of the substantial variations in climate expected for Mars (discussed in the next section). A resolution of this paradox may be provided by the presence of a reservoir of carbon dioxide with a response time longer than one Mars year. Fanale and Cannon (1974, 1979) proposed that the atmosphere plus cap system is in transient equilibrium with a much larger reservoir of adsorbed CO₂ in the regolith. Such a reservoir may keep the atmosphere/cap system in approximate balance on timescales comparable to the astronomical variations in Martian climate.

1.1.3 Mars Climate Changes

Oscillations of Mars' orbital parameters and obliquity are caused by gravitational perturbations by the sun and the other planets. Ward (1974, 1979) quantified these oscillations and predicted their effects on the climate of Mars (Ward *et al.*, 1974). The obliquity varies with a period of 1.2×10^5 and an amplitude that

varies up to 26° (from 12 to 38 degrees) on a timescale of 1.2 million years, changing the average annual polar insolation by a factor of 2. Changes in orbital eccentricity ($0.004 \leq e \leq 0.141$) produce seasonal north/south asymmetries in daily insolation with periods of 9.5×10^5 and 2 million years. The sign of these asymmetries is modulated by the precession of the equinoxes on a 51,000 year timescale. The current obliquity of 25° is near the mean value, while the present eccentricity (0.093) is somewhat above average.

As described above, these orbital/axial variations are believed to cause periodic changes in Martian climate that are recorded in the layered deposits. Toon *et al.* (1980) modeled the effects of the astronomical variations to predict that 40 meter thick layers of dust and ice are deposited at the poles during low obliquity, when permanent CO_2 caps form. Ten meters of dust are then concentrated at the surface during periods of high obliquity, when dusty water ice is unstable at the poles. They conclude that the extent of the layered deposits marks the maximum extent of the permanent H_2O ice caps that form during periods of low obliquity.

Toon *et al.* (1980) assumed that the Martian climate has been similar to the present climate since the formation of a large carbon dioxide reservoir in the regolith. They also assumed that the layered deposits are mostly water ice. Although these assumptions are reasonable, other scenarios are equally possible. Predicting past climate effects is complicated by the fact that the present dust and volatile cycles are poorly understood (Thomas *et al.*, 1989). For example,

the current rate of dust deposition in the polar regions is very uncertain (Pollack and Toon, 1982; Jakosky and Martin, 1987), and is critical to understanding the formation of the layered deposits.

Despite these uncertainties, Cutts and Lewis (1982) have attempted to model the stratigraphy of the layered deposits using simple models of the interaction of astronomical variations and geologic processes. They find that obliquity variations exert a dominant influence on variations in layer thickness, and that the sequential thickness variations are very sensitive to the model parameters that control the fraction of time that deposition occurs. While they are tempted to associate the groups of 5-10 layers separated by unconformities (Howard *et al.*, 1982b) with models having infrequent deposition, the major changes in model results for small variations of assumed parameters preclude any firm conclusions.

The central question of whether or not the polar layered deposits can be interpreted in terms of climate variations cannot yet be answered with certainty. More information regarding the stratigraphy and composition of the layered deposits is required, and may be provided by the upcoming Mars Observer mission.

1.2 Database

The Mariner 9 (1971-72) and Viking (1976-80) spacecraft returned tens of thousands of images of Mars, many of which were taken from observing geometries unattainable from Earth. The time span over which these data were acquired could

facilitate studies of variations in albedo over time scales up to four Mars years. The upcoming Mars Observer mission can dramatically extend that time base. Therefore, the Mariner 9 and Viking data are of continuing value to the study of Mars. In particular, the highest-resolution pictures of Mars' south polar region (~ 70 m/pixel) were taken by the narrow angle camera aboard Mariner 9. The best color observations of the south polar region were made by Viking Orbiter 2 at lower resolution (~ 500 m/pixel).

However, the usefulness of imaging data for photometric studies of Mars has been limited by the accuracy of absolute radiometric calibration of the vidicon cameras (Thorpe, 1973b, 1977a; Young, 1974a; James *et al.*, 1979; Lumme *et al.*, 1981; McCord *et al.*, 1982). Several authors have questioned the accuracy of television system calibration (*e.g.*, Veverka and Burns, 1980), prompting further analysis of the absolute accuracy of Mars imaging data. Recent efforts to improve the calibration of the Viking Orbiter cameras (at the U. S. Geological Survey in Flagstaff) and of the Mariner 9 cameras (Chapter 2) make possible better application of orbital imaging data to important Mars problems requiring absolute radiometry (*e.g.*, atmospheric scattering).

1.3 Summary of Thesis Results

The accuracy of the Mariner 9 and Viking Orbiter television systems were evaluated by comparing the two data sets with each other and with Earth-based

spectrophotometry of Mars and Phobos (chapter 2). The Viking imaging data are consistent with published estimates of the geometric albedo of Phobos, which is uncertain by about 20%. Mariner 9 data are calibrated to within about $\pm 20\%$ by comparing Phobos images with Viking data. Recommendations are made for improvement of the absolute calibration of television images of Mars using future observations of Phobos.

Three principal applications of quantitative imagery of the south polar region of Mars are carried out using the techniques and background in Appendices A and B:

- (1) Mariner 9 images recorded in 1971-72 were processed for comparison with nearly simultaneous infrared spectra of the south polar cap of Mars. Combined analysis of these two sets of observations indicates that the southern residual cap was covered by carbon dioxide frost throughout the summer, in agreement with Viking Orbiter measurements made three Mars years later. Thermal modeling of the spectra shows that areas of intermediate albedo are cooled to the sublimation temperature of CO_2 , suggesting that frost is present but not visible. Topographic roughness may shade the CO_2 from the sun and produce the variegated appearance of the residual cap (section 3.1).

- (2) Five color/albedo units, including polar frost, have been quantified and mapped in the southern layered deposits on Mars. Atmospheric dust scattering was measured in shadows and modeled in order to remove the component of brightness

in Mars images due to the atmosphere and quantify the albedo and color of the surface. The layered deposits appear to be mantled by red dust, except where eolian stripping has exposed the underlying bedrock. Frost and bare ground are mixed below the resolution of the images in many areas adjacent to the polar cap, some of which appear to be younger than the surrounding layered terrain. Dark material has been deposited in topographic depressions in much of the south polar region, including the layered deposits. These observational data suggest that the layered deposits are composed of bright dust, ice, and a small amount of dark material. If the dark material is sand, a periodic change in polar winds seems required in order to transport the sand poleward into the layered terrain. In any case, the observations are not consistent with the layered deposits being composed only of bright dust and ice (section 3.2).

(3) A new photoclinometric technique was used to produce profiles of slope and albedo using high resolution Mariner 9 images. Maximum slopes of 10-20 degrees were measured on an exposure of layered deposits within the south polar residual cap of Mars. These slopes are steeper than those previously estimated, suggesting that the layers are fairly competent, perhaps due to the presence of a weathering rind. Stereophotogrammetry is also used to constrain the photoclinometric solutions, which resolve layer thicknesses of 100-300 meters. The results are limited by the ~ 200 meter resolution of the images, and thinner (unresolved) layers are likely. The $\sim 25\%$ maximum albedo variations are correlated with slope, indi-

cating that frost is present on level areas. There is evidence for temporal changes in frost distribution in the 7 days (4° of L_s) between the two images used in this study, demonstrating that future photoclinometric studies of the polar regions must be attempted carefully. If the observed albedo variations are entirely due to incomplete frost coverage, an upper limit of 15% can be placed on intrinsic albedo variations in the non-volatile component of the resolved layers (section 3.3).

The results, when considered together, suggest the following general conclusions. The recent evolution of the south polar layered deposits is constrained by the local topography and albedo of layered deposit exposures. Weathering of the layered deposits by sublimation of water ice can account for the data presented here and previous observations of the north polar deposits. Hypotheses regarding the composition and origin of the south polar layered deposits are constrained by the color and albedo of the deposits. The non-volatile component of the layered deposits appears to consist mainly of bright red dust, with small amounts of dark dust or sand. Deposition of sand in the layered deposits is problematical, so inclusion of dark dust is preferred. The dark dust may be similar to the magnetic material found at the Viking Lander sites, and may therefore preferentially form $\sim 100\mu$ filamentary residue particles upon weathering. Once eroded from the layered deposits, these particles may then saltate to form the dark sand dunes found in both polar regions. Eventual destruction of the particles could allow recycling of the dark dust into the layered deposits via atmospheric suspension (chapter 4).

Chapter 2

Television System Calibration

Knowledge of the absolute spectral reflectivity of Mars can enable useful study of the planet's surface composition, particle size, and texture. The uncertainties in such data must be understood, however, before the reliability of scientific results can be determined. Absolute measurements are also required in the study of atmospheric scattering, which must be understood before photoclinometric techniques can be applied to Mars images. This chapter describes a reconciliation of ground-based photometric observations with Mars-orbiting spacecraft television data. The uncertainty in Martian spacecraft photometry is large, but careful observations of Phobos can provide the photometric standard necessary to materially improve the accuracy of existing spacecraft data and to properly calibrate future data.

The accuracy of the absolute radiometric calibration of the Mariner 9 and Viking Orbiter cameras is estimated in this chapter using the following methods:

1. Viking Orbiter 1 low phase angle television observations of Phobos were compared to Earth-based albedo measurements, confirming the absolute calibra-

tion of the Viking Orbiter cameras to within the estimated 20% accuracy of the telescopic data.

2. Viking images of Arabia were compared to Earth-based spectrophotometric observations at 5° phase angle.
3. Mariner 9 preflight calibration data were analyzed and used to predict the absolute response of both Mariner 9 cameras to solar radiation.
4. Mariner 9 narrow angle images were compared to Viking observations of Phobos at intermediate phase angles in order to determine the absolute response of the Mariner 9 narrow angle (B) camera during flight.
5. Mariner 9 images of dust storms were used to calibrate the wide angle (A) camera with respect to the narrow angle camera in four spectral bandpasses.

The absolute radiometric uncertainty of Viking Orbiter images is no greater than 20%, and Mariner 9 images are calibrated to about the same accuracy, as shown below. A procedure involving ground-based and new spacecraft observations of Phobos that could significantly reduce these uncertainties and assure accurate future measurements is then proposed.

2.1 Limitations of Earth-Based

Photometry of Mars

Although the spectral resolution obtainable from telescopic observations is good, spatial resolution is limited by atmospheric seeing and by the small angular size of the Martian disk. Furthermore, phase angle coverage is limited to about 45 degrees maximum, with surface resolution decreasing with increasing phase. Despite these limitations, telescopic observers have tried to quantify photometric properties of Mars. In particular, phase-dependent color variations have been reported in disk-integrated photometric data (O'Leary and Rea, 1968; O'Leary and Jackel, 1970; de Vaucouleurs, 1964) and in spectrophotometric observations of Arabia (McCord and Westphal, 1971).

McCord and Adams (1969) used de Vaucouleurs' (1964) calculations to find the disk-integrated spectral geometric albedo of Mars between 0.3 and 1.3 microns, but suggested that their results may be too low by about 5%. In fact, the wide-band albedo data given by de Vaucouleurs are based upon photometric observations made during the 1950's, and do not account for the "opposition effect" observed more recently. He shows data indicating a roughly $\pm 10\%$ longitudinal brightness variation, but claims a 3% mean error in his estimate of the visual geometric albedo. The data are more scattered at other wavelengths, and de Vaucouleurs (1964) admits that "much remains to be done to define [Mars']

photometric parameters better.” Spatial and temporal color and albedo variations must be quantified more precisely, and phase-dependent color variations should be investigated. McCord and Westphal (1971) obtained the spectral geometric albedo of certain regions of Mars by scaling telescopic relative reflectance data, but their spatial resolution was limited to about 200 km. They claim that their results are accurate to $\sim 5\%$ if the opposition effect is neglected. However, McCord (1989) has more recently acknowledged that their absolute calibration accuracy is not known. As Young (1974b) concludes, ground-based planetary albedo determinations “may be uncertain by at least ten percent, apart from the effects of errors in size.”

The existence of phase-dependent color variations has been questioned by Young (1974b), who found errors of up to 0.07 in the visual magnitudes given by O’Leary and Rea (1968). The ground-based data in Figure 2.3, taken from O’Leary and Rea (1968), have not been corrected and may therefore be too large by up to 0.01 at low phase angles. Observations made at the subsequent opposition by O’Leary and Jackel (1970), however, also show color variations with phase. Such color variations may be caused by temporally variable dust distribution or atmospheric scattering, or may be due to intrinsic surface and/or atmospheric photometric properties that do not change with time. However, Thorpe (1977b) used Viking Orbiter images to conclude that the atmospheric phase function varies with wavelength, the color becoming less red with increasing phase rather than more red as reported by O’Leary and Rea (1968). Therefore, atmospheric photometry cannot

be responsible for the telescopically observed phase-dependent color changes, since the atmospheric color changes in the opposite sense (Thorpe, 1978).

Given the uncertainty in the cause and magnitude of phase-dependent color variations, spacecraft observations can be accurately compared to ground-based spectrophotometry only if the measurements are acquired at similar phase angles. In addition, temporal variations in the color and albedo of Mars indicate that only simultaneous observations can be accurately compared.

2.2 Viking Orbiter Photometric Accuracy

The absolute accuracy at midscale of the Viking Orbiter television calibration given by Klaasen *et al.* (1977) is 9% (1σ) on average in the central 500×500 pixels (20%) of an image, 13% in the corners and for individual pixels. However, two nearly simultaneous Viking images of Phobos taken at low phase angle differ by 18%, as shown in Figure 2.1. These data, discussed in detail below, suggest that the calibration procedures currently in use may not be accurate to 13%.

McCord *et al.* (1982) estimate that the standard deviation of Viking albedo measurements in the region they studied is 15%. They find that the ratio of red to violet albedo measured by the Viking cameras was never as large as that calculated from telescopic spectral reflectivity observations of bright regions and dust clouds. Although this discrepancy may be due to interannual variations in surface distribution of dust as they suggest, calibration errors in either or both data sets cannot be

ruled out. Unfortunately, there are no published Earth-based spectrophotometric measurements taken during the Viking mission. It is shown below, however, that available telescopic observations of Arabia are indeed consistent with Viking data taken at a similar phase angle.

Viking IRTM solar band measurements of Martian bolometric albedo were also analyzed, but the uncertainty in the spectral bandpass of the solar channel is too large to allow an accurate comparison with imaging data. Such a comparison is sensitively dependent upon the (poorly known) spectral reflectivity of the observed area and is therefore not useful in evaluating the calibration of the television systems.

Each of the two Viking Orbiters carried two narrow-angle cameras: numbers 4 and 7 on Viking Orbiter 1; numbers 6 and 8 on Viking Orbiter 2. Technical details regarding the Viking television system may be found in Benesh and Thorpe (1976). I have used the Planetary Image Cartography System (PICS, distributed by the U. S. Geological Survey in Flagstaff, Arizona) to process Viking Orbiter images. The radiometric calibration parameters used in PICS have been improved over those presented by Klaasen *et al.* (1977), but have not been published. Images calibrated using PICS are therefore compared with ground-based photometry of Phobos and Mars. Observations of Deimos were also analyzed, but greater surface albedo variations and smearing of the low-phase Viking images make these data less suitable for calibration purposes.

2.2.1 Phobos Observations

Unlike Mars, Phobos is not believed to vary in brightness over time, does not have prominent albedo variations, and is spectrally neutral at visible wavelengths (Veverka and Burns, 1980). The geometric albedo of Phobos in the V (visible) band given by Pang *et al.* (1983) is 0.07 ± 0.01 , where the 14% uncertainty in albedo is presumably an indication of the scatter of the Viking and Mariner 9 star tracker data. The low phase observation of Phobos reported by Zellner and Capen (1974) is critical to the evaluation of Phobos' geometric albedo. The most recent triaxial model of Phobos' shape (T. Duxbury, personal communication, 1988) was used to estimate the illuminated areal cross-section of Phobos as seen in 1973 by Zellner and Capen. The derived value of $407 \pm 11 \text{ km}^2$, combined with the published V magnitude of 12.0 ± 0.2 , yields a reflectivity of 0.054 ± 0.011 at 1.6° phase angle. The 20% RMS uncertainty in this value is due to both "large and uncertain probable errors" in Zellner and Capen's photometry and the $\sim 3\%$ (1σ) dimensional uncertainty. Evidently, Zellner and Capen encountered difficulties in making photometric measurements of Phobos due to its proximity to Mars, compelling them to specify a rather large (0.2 magnitude) uncertainty in their brightness determination. The corresponding error in the derived geometric albedo is 20%, much larger than the error in cross-section.

The absolute calibration of the Viking Orbiter 1 cameras may be checked by comparing Phobos images with the geometric albedo given above. A similar

comparison of Deimos observations was not made due to smearing of the low-phase images and greater albedo variations on the surface of Deimos. Average reflectances from images taken through the clear filter at low phase angles are presented in Figure 2.1. The reflectances were derived by averaging the pixel values that were greater than the background level. Linear extrapolation of these data to zero phase angle yields a geometric albedo of 0.061 ± 0.010 , slightly less than that found by Pang *et al.* (1983) in nearly the same spectral region. The 16% RMS uncertainty in this extrapolation is due to the data scatter (6% RMS), sampling errors in the vidicon cameras (7% or less), and the absolute error in the Viking calibration given by Klaasen *et al.* (1977). Both the sampling errors and the linear extrapolation tend to underestimate the geometric albedo, so that a value of 0.065 is probably a close approximation to the correct albedo. Klaasen *et al.* (1979) found a geometric albedo of 0.066 ± 0.006 (1σ) through a different analysis of the same Viking data, assuming an 8% (1σ) uncertainty in the absolute calibration. In addition, the Viking data agree well with the Earth-based measurement at 1.6° phase reported by Zellner and Capen (1974), as shown in Figure 2.1.

The small difference between the spectral bandpasses of the Viking cameras (clear filter) and the telescopic (V band) measurements allows direct comparison of the two observations of spectrally neutral Phobos. The 1.5° phase Viking image has Phobos at the left edge of the central 500×500 pixels and average raw data numbers (DN) just below midscale, so that the absolute uncertainty in the

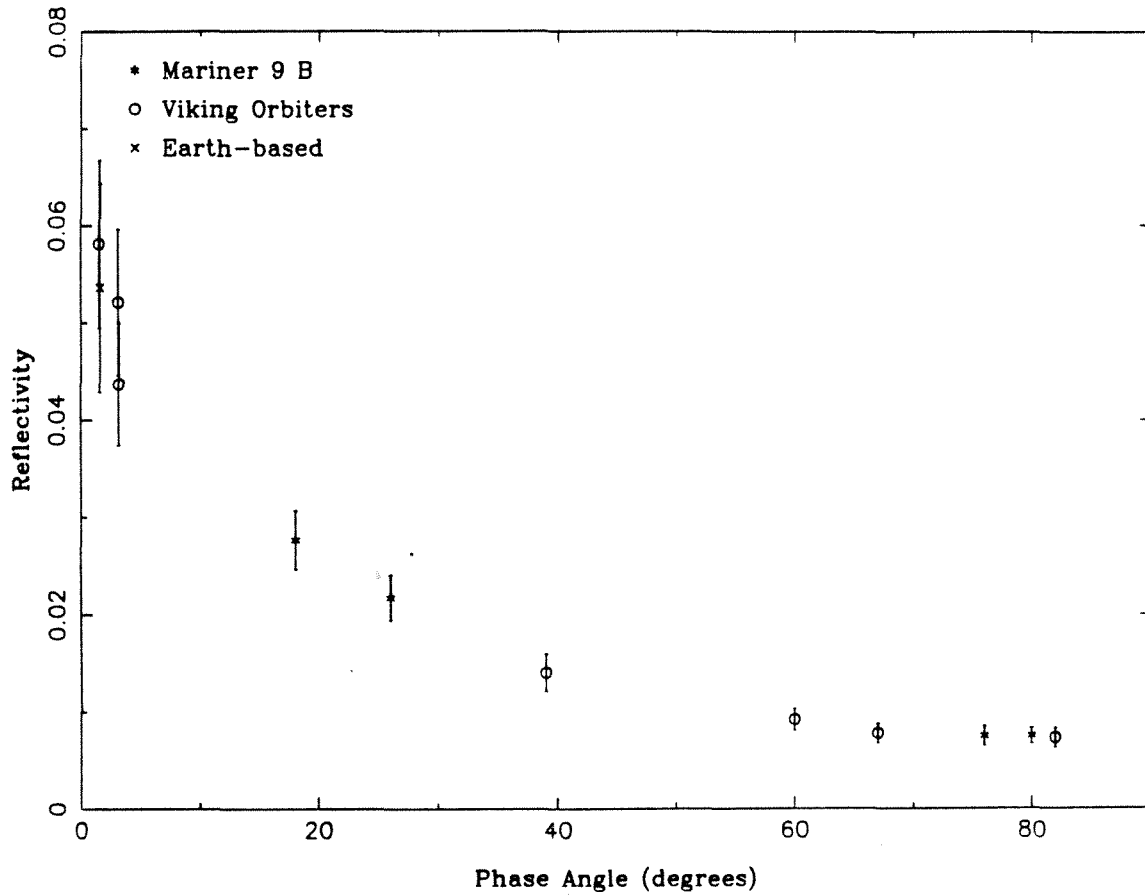


Figure 2.1: Phobos average reflectance vs. phase angle. Error bars represent the RMS combination of sampling errors, the 13% uncertainty in the absolute response of Viking cameras (Klaasen *et al.*, 1977), and the 9% uncertainty in the relative response of the Mariner 9 B camera. The 20% total uncertainty in the Earth-based measurements (Zellner and Capen, 1974) is also shown. The Mariner 9 data (minus-blue filter) have been scaled to agree with the Viking data (clear filter) at large phase angles.

Camera	Clear	Violet	Green	Red
4	-	0.0108	0.0120	0.0127
7	0.0117	0.0107	0.0118	0.0120
6	0.0077	0.0072	0.0080	0.0077
8	0.0081	0.0086	0.0083	0.0089

Table 2.1: Viking Orbiter moderate-phase Phobos observations, comparing responses of cameras 4 and 7. Spectrally neutral reflectance of Phobos is evident.

reflectivity according to Klaasen *et al.* (1977) is about 10%. The two data points at 3.2° phase (with overlapping error bars) are from nearly simultaneous Viking images through different cameras. The camera 4 brightness is 18% larger than the camera 7 brightness, probably due to differences in calibration between the two cameras. Examination of 9 other higher-phase image pairs indicates that the RMS difference between the responses of cameras 4 and 7 is only 7%. The fact that Phobos appears at opposite sides (far left for camera 4, far right for camera 7) of the low phase frames suggests that improper dark current shape correction may be the cause of the larger difference between the responses of the cameras in this case. Table 2.1, in which the data for cameras 4 and 7 were taken nearly simultaneously while the data for cameras 6 and 8 were not, shows that the deviation between cameras 4 and 7 depends upon the filter used. A similar comparison of the response of camera 6 with respect to camera 8 could not be made using Phobos data. In any case, these data show that Phobos' reflectivity does not vary greatly with wavelength, in agreement with Earth-based spectrophotometric data.

The low-phase data in Figure 2.1 are given in Table 2.2, along with the

Picture no.	Phase	Latitude	Longitude	Reflectivity
849A61	3.2	10.2°N	30.2°W	0.0437 ± 0.0063
849A62	3.1	10.2°N	30.2°W	0.0521 ± 0.0075
849A82	1.5	9.2°N	29.5°W	0.0581 ± 0.0086
Telescopic	1.6	18.5°S	108.8°W	0.0536 ± 0.0107
129B6	18.4	29.6°S	15.4°W	0.028 ± 0.003
53B16	26.1	32.1°S	22.9°W	0.022 ± 0.002

Table 2.2: Viking Orbiter 1 (top), telescopic, and Mariner 9 (bottom) low-phase Phobos observations.

subspacecraft and subearth locations. As in Figure 2.1, uncertainties in the absolute calibration of Viking Orbiter and ground-based data are shown, while uncertainties in the Mariner 9 data correspond to relative calibration errors. These data will be useful in the future for more precise absolute calibration of the Mariner 9 and Viking Orbiter cameras.

I conclude that the absolute calibration of the Viking cameras is consistent with the Earth-based Phobos data, and that the calibration of all the Viking Orbiter cameras is correct to within at least the 20% estimated uncertainty in the telescopic observations of Phobos. With the exception of one pair of Viking Orbiter 1 images, there is no evidence that the absolute uncertainty of 13% reported by Klaasen *et al.* (1977) is overly optimistic. Further work needs to be done, but for the purposes of the present studies, a 13% absolute uncertainty will be assumed for the Viking Orbiter cameras. Methods of improving the absolute calibration of the television systems will be discussed in chapter 4.

2.2.2 Mars Observations

During orbit 322, Viking Orbiter 2 recorded a sequence of images of Arabia during a dust storm ($L_s = 295^\circ$). Surface features were completely obscured, reducing the complications due to possible variations in surface photometry, color, and shadowing. Camera pointing information was used to find specific locations in overlapping images taken through red (camera 6) and violet (camera 8) filters. Data values in such image pairs yield red/violet ratios of 3.0 at a phase angle of 74.5 degrees. Earth-based relative spectral reflectance observations of dust storms in their early phases (McCord *et al.*, 1977; Figure 2.2) were weighted by the spectral response of the Viking Orbiter cameras (K. Klaasen, personal communication, 1987) to find a red/violet ratio of 3.6 at about 5° phase angle. A decrease in red/violet atmospheric reflectance with phase angle has also been deduced from Viking Orbiter data by Thorpe (1977b).

Similar spectra of Arabia taken in 1969 (McCord and Westphal, 1971) yield a red/violet ratio of 3.2 at 5° phase, 1° incidence, and 6° emission angle. Viking Orbiter 1 images of Arabia ($19.6^\circ N, 310.7^\circ W$) taken during orbit 793 ($L_s = 131^\circ$) at the same phase angle as the 1969 Earth-based observations have a red/violet ratio of 2.9, only 10% smaller than the 1969 Arabia data. Hence, the Viking color observations are consistent with the 1969 Arabia data within the uncertainty of the Viking calibration, as shown in Figure 2.2. In addition, Arabia's red/violet ratio at 5° phase is nearly identical to the red/violet ratio of dust storms at moderate

phase angles, as observed during orbit 322. This deduction will be used below in the calibration of the Mariner 9 A camera.

McCord and Westphal (1971) did not include an opposition surge in their calculations, so that their estimates of geometric albedo are probably too low. Mars appears limb-darkened at most visible wavelengths, so the normal reflectance is not equal to geometric albedo in general. Limb darkening is minimal in blue light (0.42μ), so McCord and Westphal (1971) used blue data to equate their reflectances with geometric albedo. The data in Figure 2.2 at other wavelengths are therefore interpreted as estimates of reflectance at 5° phase angle rather than as geometric albedos. Surface features were barely visible in the rev 793 images, indicating a dust optical thickness near unity.

The effect of variable dust opacity at moderate phase angles can be seen in Figure 2.3 by comparing data from images of Arabia taken between dust storms at 78° phase (red/violet = 2.9) with images of dust-shrouded Arabia at 74.5° phase (red/violet = 3.0). This comparison indicates that atmospheric dust only slightly increases overall albedo without significantly altering the color of Arabia at these phase angles. A reasonable interpretation of these results is that Arabia is covered by a layer of dust of the same composition as suspended dust.

Figure 2.3 also illustrates the spatial variability in the albedo of Arabia at 36 and 50 degrees phase. Red/violet ratios of 3.0 to 3.3 are observed in this phase angle range at various points on the surface (dust opacity was low). Overall,

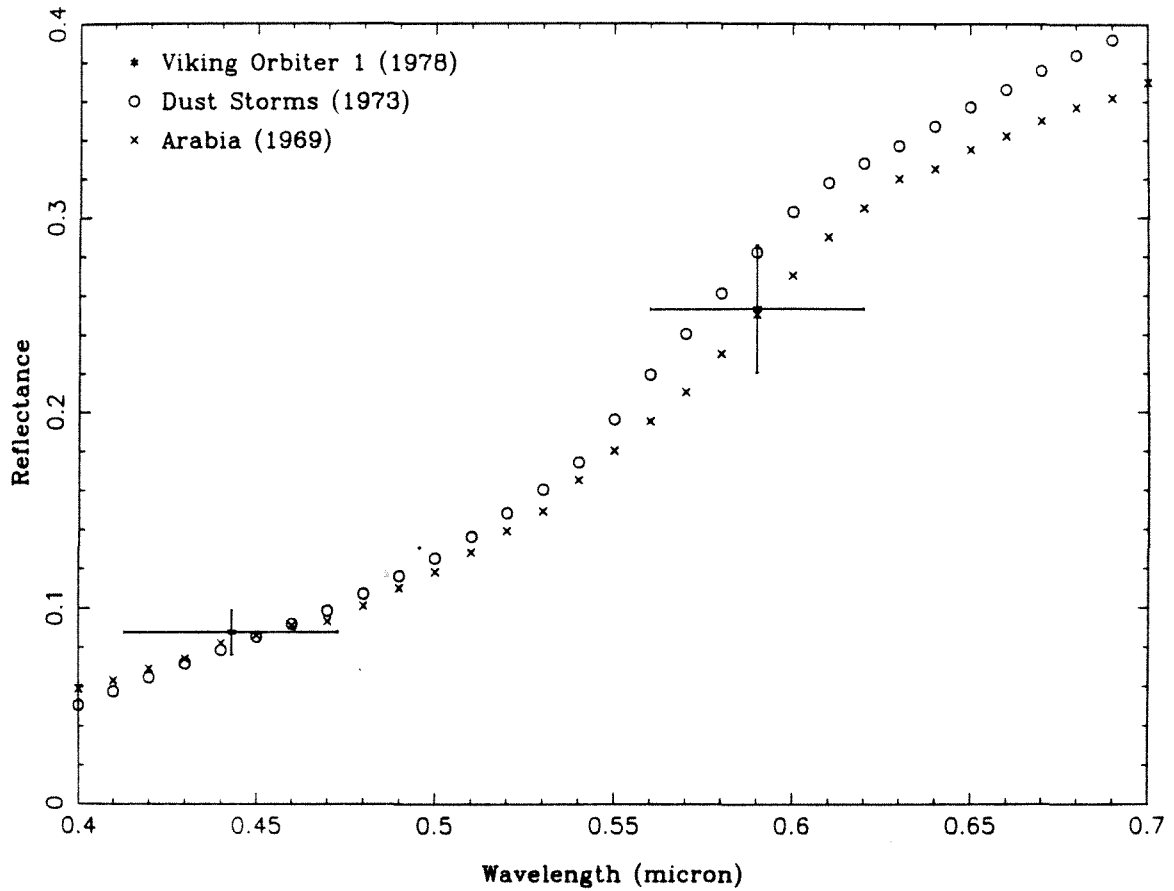


Figure 2.2: Comparison of Viking Orbiter 1 imaging data (13% error bars) of a dust storm over Arabia with Earth-based spectral albedo data, interpolated to 10 nm intervals. The telescopic dust storm data (McCord *et al.*, 1977) have been scaled to equal the 1969 Arabia data (McCord and Westphal, 1971) at 0.45 micron. The full width at half maximum of the spectral response of each of the Viking camera/filter combinations is 0.04 to 0.05 micron.

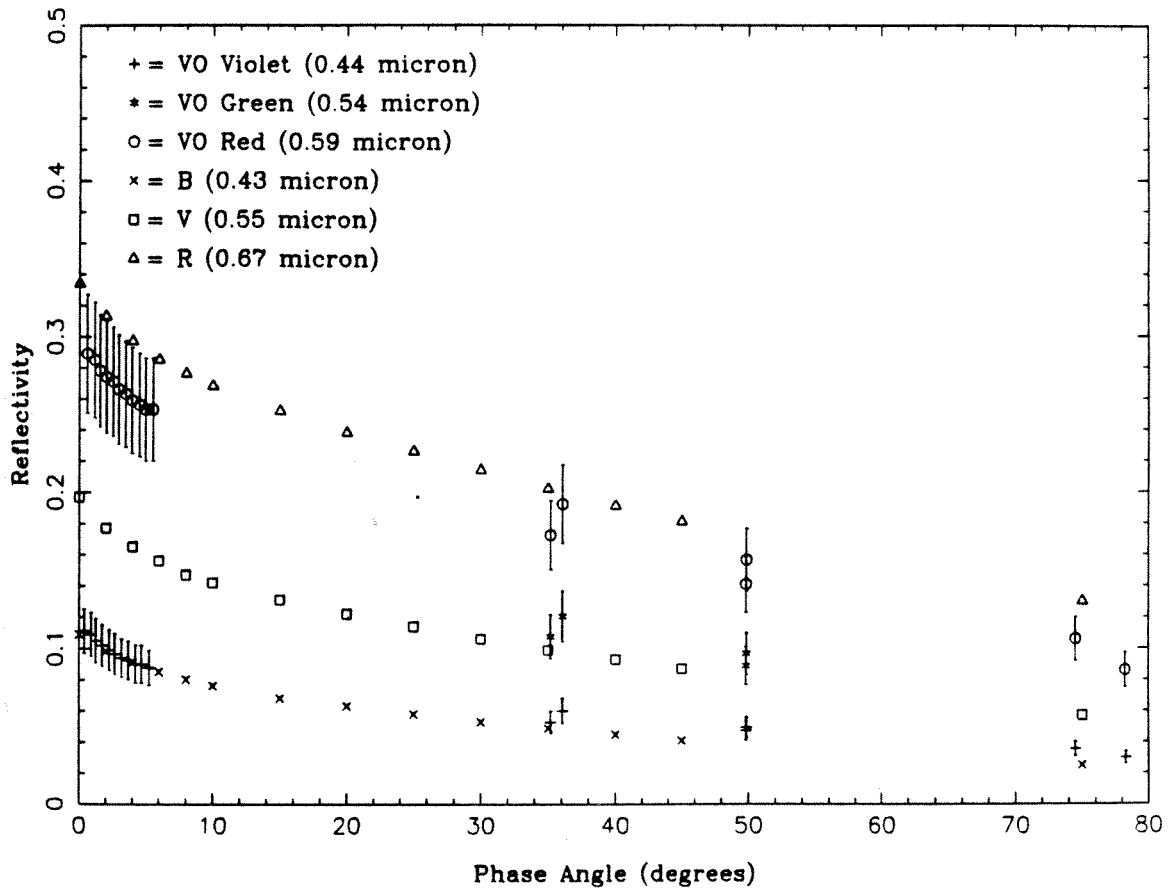


Figure 2.3: Comparison of Viking Orbiter observations of Arabia (13% error bars) and Earth-based integral disk photometry (O'Leary and Rea, 1968). Telescopic data have been extrapolated to 75° phase for comparison.

the Viking Orbiter observations presented in Figure 2.3 indicate that the color of Arabia does not vary significantly between 5 and 80 degrees phase (red/violet = 3.1 ± 0.2). Thus, the phase-dependent color changes first noted by O'Leary and Rea (1968) appear to be confined to the opposition surge (phase angle $\leq 5^\circ$). This inference will be used in section 3.1.2 below.

Evaluation of the surface photometry of Arabia is complicated by spatial and temporal variability of atmospheric dust opacity. McCord *et al.* (1977) argue that the differences in the measured color of Arabia from year to year may be due to variations in volatile condensation, but it should be emphasized that calibration errors cannot be ruled out. The data analyzed here indicate that spacecraft observations are in rough agreement with Earth-based measurements, but that the photometric characteristics of Mars are variable and complex, making evaluation of the Viking Orbiter television calibration using Mars as a "standard" difficult.

2.3 Mariner 9 Photometric Accuracy

The Mariner 9 television sub-systems were calibrated before flight sufficiently well to derive absolute radiometry with one exception: the spectral response of the vidicons was measured satisfactorily only between 500 and 700 nanometers (nm) wavelength (H. T. Enmark, personal communication, 1985). The relative spectral response below 500 nm given by Snyder (1971) is in error by an unknown amount, making absolute radiometric calibration using these data impossible for the

short-wavelength filters on the A (wide angle) camera. It is fortuitous that most A frames were taken through the orange and 60° polarizing filters, the latter of which cuts off just below 500 nm (Cutts, 1974). The B camera has only one filter ("minus blue" or yellow) and an effective wavelength of 0.57μ . Thorpe (1973a) concluded that Mariner 9 absolute calibration is accurate to 15% (1σ) at midscale (100 to 138 DN, 15% of the dynamic range) in the central 400×400 pixels (27%) of the 832×700 pixel frames.

Absolute radiometric calibration can also be achieved through analysis of inflight photography. Images of star fields and Saturn were recorded for this purpose (Thorpe, 1972; 1973a), but the read beam interactions with small charge distributions on the vidicon (and the uncertain contribution of Saturn's rings to the to the integrated response) make these data less suitable than Phobos or Mars images. Unfortunately, Earth-based photometric observations of Mars during the Mariner 9 mission (1971-72) have not been published, nor have conversion factors from Mariner 9 data number (DN) to reflectivity. The rather uncertain parameters derived from the preflight calibration data are therefore compared with inflight observations of Phobos and Mars in order to estimate the absolute response of the Mariner 9 cameras.

2.3.1 Preflight Calibration

Calibration data values for light-cannon luminance are given by Snyder (1971) in foot-Lamberts (ft-L), as measured with a photometer and a 100 ft-L reference source. For perfectly diffusing faceplates on the light cannons, the luminance is numerically equal to luminous emittance in lumens ft^{-2} (Sears, 1949). The exposure (in ft-L seconds) required to yield a mid-scale (128 DN) response for each camera/filter combination may be found using the polynomial fits of these data described in Appendix A. The luminous emittance of the light cannon that produces a linearized, shading-corrected DN value of D at a pixel in a given camera and filter is $L_c = DA_f/t$ lumens ft^{-2} , where A_f is the conversion factor in ft-L-s per DN for filter f and t is the exposure time in seconds. A_f is evaluated at inflight temperatures by interpolating between calibration temperatures. Since the relative spectral radiance of the light cannons used for calibration is known (Snyder, 1971), the light cannon radiance required to produce a given DN value may be calculated:

$$10.76L_c = 683 \int P_\lambda C_\lambda d\lambda \quad (10.76 \text{ ft}^2 = 1 \text{ m}^2),$$

where $C_\lambda = C\hat{C}_\lambda$ is the light cannon spectral radiance in $\text{Wm}^{-2}\text{nm}^{-1}\text{sr}^{-1}$ and P_λ is the photopic luminous efficiency of the eye (McCartney, 1976). \hat{C}_λ is the relative spectral radiance of the light cannon, normalized at 555 nm. C is constant with respect to wavelength, and may be evaluated as follows:

$$C = \frac{10.76L_c}{683 \int P_\lambda \hat{C}_\lambda d\lambda} \text{ Wm}^{-2}\text{sr}^{-1}.$$

The effective radiance producing the observed television signal with any given filter is the light cannon radiance weighted by the system response:

$$I = \frac{\int C_\lambda T_\lambda f_\lambda V_\lambda d\lambda}{\int T_\lambda f_\lambda V_\lambda d\lambda} \text{ Wm}^{-2} \text{ sr}^{-1},$$

where T_λ is the optical system spectral transmittance, f_λ is the filter spectral transmittance, and V_λ is the vidicon spectral response. The solar irradiance at Mars, as observed by the same system, is

$$\pi F = \frac{\int S_\lambda T_\lambda f_\lambda V_\lambda d\lambda}{\int T_\lambda f_\lambda V_\lambda d\lambda} \text{ Wm}^{-2},$$

where $S_\lambda = S \hat{S}_\lambda$ is the solar spectral flux at Mars in Wm^{-2} . \hat{S}_λ is the solar flux at 1 astronomical unit (AU) normalized at 555 nm (Neckel and Labs, 1984; Arvesen *et al.*, 1969) and $S = 18.6/R^2 \text{ Wm}^{-2}$, where R is the distance of Mars from the sun in AU . The ratio of observed brightness to that of a Lambert reflector at the same location is

$$\begin{aligned} \frac{I}{F} &= \frac{C \int \hat{C}_\lambda T_\lambda f_\lambda V_\lambda d\lambda}{S \int \hat{S}_\lambda T_\lambda f_\lambda V_\lambda d\lambda} \\ &= 8.51 \times 10^{-4} L_c R^2 \frac{\int \hat{C}_\lambda T_\lambda f_\lambda V_\lambda d\lambda}{\int \hat{S}_\lambda T_\lambda f_\lambda V_\lambda d\lambda \int P_\lambda \hat{C}_\lambda d\lambda}. \end{aligned}$$

The integral $\int P_\lambda \hat{C}_\lambda d\lambda$ has been evaluated numerically by evaluating P_λ and \hat{C}_λ in 10 nm bins and summing. The other integrals can be evaluated in a similar fashion for each filter and camera, so that

$$\frac{I}{F} = \frac{DB_f R^2}{t}, \quad B_f = 8.51 \times 10^{-4} A_f \frac{\int \hat{C}_\lambda T_\lambda f_\lambda V_\lambda d\lambda}{\int \hat{S}_\lambda T_\lambda f_\lambda V_\lambda d\lambda \int P_\lambda \hat{C}_\lambda d\lambda}.$$

Camera/Filter	A_f	B_f (preflight)	B_f (Phobos)	B_f (Mars)
A 2 (orange)	0.313	2.84×10^{-5}	-	4.31×10^{-5}
A 4 (green)	0.261	2.04×10^{-5}	-	3.56×10^{-5}
A 5 (60° pol.)	0.234	1.89×10^{-5}	-	2.63×10^{-5}
A 6 (blue)	0.149	1.08×10^{-5}	-	1.80×10^{-5}
B (minus blue)	0.050	4.00×10^{-6}	4.75×10^{-6}	-

Table 2.3: Mariner 9 calibration constants.

Values of A_f and B_f (in $\text{sec DN}^{-1}\text{AU}^{-2}$) are tabulated in Table 2.3. Analysis of the uncertainty in B_f is impossible due to the lack of error estimates for the vidicon spectral response V_λ in Snyder (1971). The uncertainty in A_f estimated from temporal variations in bench calibration data (Snyder, 1971) is about 6% (1σ), and the accuracy of B_f is no better than 10% (1σ).

2.3.2 Phobos Observations

Phobos was observed by Mariner 9 at lower resolution than most Viking Orbiter images, but at similar phase angles. Average reflectances were compared and used to calibrate the Mariner 9 B camera (Figure 2.1). Comparison of Deimos observations is complicated by albedo variations, but yields similar results. The resulting calibration parameter, given in Table 2.3, indicates a 19% decrease in B camera sensitivity between preflight calibration and Mars orbit. The corrected reflectivities derived from the Mariner 9 images are in error by 5 to 10% (at most) due to sampling errors, while the Viking images of approximately the same face of Phobos used for comparison have sampling errors of only 3%. Average reflectances

were calculated by averaging the pixel values greater than the background noise level. All of the images used for this comparison have Phobos within the central 400×400 pixels of the frame. The accuracy of the calibration of the Mariner 9 B camera by this method is also limited by the 13% absolute accuracy of the Viking Orbiter calibration (Klaasen *et al.*, 1977) and the phenomena listed in Table A.2 of Appendix A, and is therefore about 20% RMS. It was not possible to calibrate the A camera by this method, due to the small size of Phobos' disk in the wide-angle images: the fraction of pixels that were only partially filled by Phobos was too large to obtain accurate average reflectances. The A camera is therefore calibrated by comparing nearly simultaneous A and B camera images of dust-shrouded Mars.

2.3.3 Mars Observations

Mariner 9 observations of the 1971 global dust storm are used to calibrate the A camera with respect to the B camera, taking into account the differences in spectral bandpass between the B camera and the various filters on the A camera. Although the absolute brightness of Mars was not measured from Earth during the Mariner 9 mission, the *relative* spectral reflectivity of certain regions at certain times is reportedly known to about 1% precision in visible light (McCord *et al.*, 1977). McCord *et al.* (1977) observed several dust storms at low phase angles during the 1973 opposition, finding their relative spectral reflectivity to be similar to that of bright areas such as Arabia. As described in the previous section, the color of Arabia

is similar to that of dust storms observed by the Viking Orbiters at moderate phase angles. The Arabia spectrum shown in Figure 2.2 was therefore used to find the response of each of the filters on the Mariner 9 A camera relative to the B camera. The relative spectral response of the vidicons must be known for this analysis, so that errors in calibration are expected to be larger for the short wavelength filters.

An orbit 106 A camera image of a dust-shrouded Arabia taken through the orange filter was compared to a nearly simultaneous B frame in order to calibrate the A camera at orange wavelengths. The incidence (79°), emission (10°), and phase (72°) angles of the two images are essentially identical. Specific points were located in both images using Supplementary Experiment Data Record (SEDR) information, the error in location being about 0.1° (Blasius, 1973). Similar data comparisons for the same filter using orbit 10 images (at 58° phase) yield the same calibration parameters, indicating that the atmospheric opacity was large enough to obscure differences in surface albedo and photometric properties. Comparison of other images taken on orbit 10 through other filters gives the calibration parameters shown in Table 2.3. Images of Arabia taken through the 60° polarizing filter on orbits 145 and 147 (at about 71° phase) show some surface features, so smooth areas were chosen for data gathering in both A and B frames. In all cases averages of small areas within the central 200×200 pixels of the images were used to compare the responses of various camera/filter combinations. In Table 2.3 the results of this analysis are compared to the values derived above using preflight calibration data. A

40-75% decrease in the sensitivity of the A camera between preflight calibration and Mars orbit is indicated. It should be noted, however, that the preflight calibration is sufficiently uncertain (due mainly to the lack of proper vidicon spectral response measurements) that the actual decrease in sensitivity may not be so large.

Thus, the accuracy of the Mariner 9 absolute calibration is limited by the accuracy of Viking Orbiter calibration and by the uncertainty in the relative spectral response of the Mariner 9 vidicons. The phenomena listed in Table A.2 also contribute to the absolute uncertainty of the Mariner 9 calibration. It is reasonable to conclude that the absolute calibration of the Mariner 9 television system, after correction to match Viking Orbiter measurements of Phobos, is accurate to within about $\pm 20\%$ RMS. Although larger than the 15% uncertainty estimated by Thorpe (1973a) for certain conditions, the calibration accuracy may be improved using future observations of Phobos, as described in the previous section. In particular, future spacecraft images of Phobos should be taken in the observing geometries given in Table 2.2.

2.4 Absolute Calibration Summary

By analyzing images of Phobos, the absolute calibration of the Viking Orbiter cameras has been verified to within the accuracy of published measurements of Phobos' albedo (20%). Comparison of Mariner 9 and Viking Orbiter Phobos observations are used to calibrate the Mariner 9 cameras to $\sim 20\%$ accuracy. Thus,

Viking Orbiter and Mariner 9 images of Mars may be used (with 20% uncertainty) to investigate the albedo, color and photometric properties of the surface and atmosphere of the planet.

Chapter 3

Applications and Discussion

Three applications of quantitative television imaging analysis of the south polar region are described in this chapter. The first makes use of nearly simultaneous Mariner 9 images and infrared spectra to show that carbon dioxide frost was present on the southern residual cap throughout the summer of 1971-72. The second uses a Viking Orbiter 2 color mosaic to map 5 color and albedo units in the south polar layered terrain and constrain the composition of the layered deposits. Finally, a Mariner 9 high resolution stereo image pair is used to ascertain the slopes and albedo along profiles within an exposure of the layered deposits, using a new photoclinometric technique. The results of each of these applications are discussed below; implications of the results are discussed in the final chapter.

3.1 Composition of the South Polar Residual Cap

The existence of a permanent solid carbon dioxide reservoir on the surface of Mars is still debated, as detailed in the introduction. Such a reservoir would

control the mass of CO₂ in the atmosphere and significantly affect climatic responses to astronomical variations in Mars' orbit and obliquity. The objective of this first application of television images of Mars is to resolve the question of the south polar residual cap composition during the 1971-72 season. Previous studies of Mariner 9 infrared measurements were limited by their low spatial resolution (Hanel *et al.*, 1972a). In the work reported here, contemporaneous television imaging data is used to determine the relative contributions of unresolved thermal components (frost and bare ground) within the field of view of the Mariner 9 Infrared Interferometer Spectrometer (IRIS).

In a study by Paige, Herkenhoff and Murray (1989), Mariner 9 IRIS data were compared with nearly simultaneous television observations made during the southern summer, when the polar cap was nearing its minimum residual configuration. Contrary to previous conclusions based on television imaging analysis alone (Murray *et al.*, 1972), Paige *et al.* (1989) conclude that the south residual cap remained covered by sublimating CO₂ throughout the 1971-72 season. My unique responsibility in that work was the specialized processing and analysis of key Mariner 9 A frames to facilitate evaluation of the albedo variations within each IRIS field of view.

Early in that summer, the residual cap was uniformly covered by seasonal CO₂ frost, which gradually sublimed to expose the patchy residual cap. Figure 3.1 is a wide-angle view of the residual cap during orbit 28 ($L_s = 301$), showing an outlier

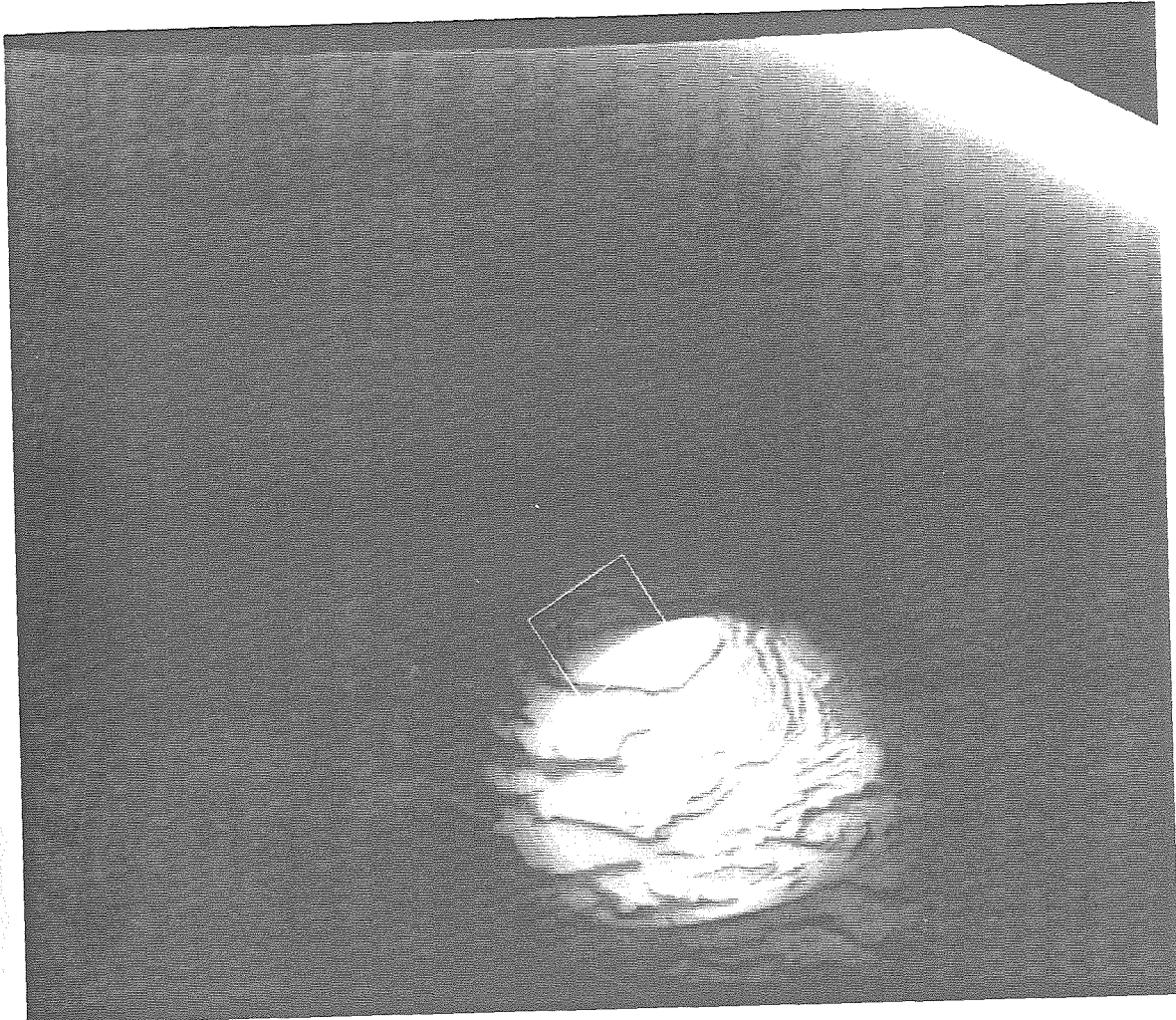


Figure 3.1: Mariner 9 wide angle image of the south polar cap, orbit 28. Footprint of IRIS spectrum 2834 highlighted, footprint of B frame from same orbit outlined.

of seasonal frost near the residual cap. The presence of the seasonal frost outlier indicates that sublimating CO₂ frost also was at least partially covering the residual cap. All of the images shown here have been geometrically corrected for camera distortions, but have not been projected onto the surface. A high resolution image taken during the same orbit (Figure 3.2; location outlined in Figure 3.1) shows that the seasonal frost was still fairly uniformly covering the residual cap. By orbit 116 ($L_s = 326$), the seasonal outlier had vanished (Figure 3.3) and the residual cap appeared much more variegated (Figure 3.4; location outlined in Figure 3.3). By this time the cap had already shrunk to a size smaller than ever observed by the Viking Orbiters 3 Mars years later. The patchy appearance of the 1971-72 cap led Murray *et al.* (1972) to conclude that all of the seasonal CO₂ frost had sublimed away, exposing a residual water ice cap.

The low spatial resolution of the IRIS instrument complicates the interpretation of the spectra, as various types of surface units are included within a single observation. By combining higher resolution information from the television system with the IRIS data, contributions to the observed infrared brightness from multiple sources can be distinguished. The intrinsic albedo contrast between CO₂ or H₂O frost and the unfrosted ground (exposed unambiguously in the surrounding terrain) allows modeling of the IRIS spectra based upon the distribution of reflectivities observed by the television cameras.

The IRIS and television data are described below, followed by an analysis

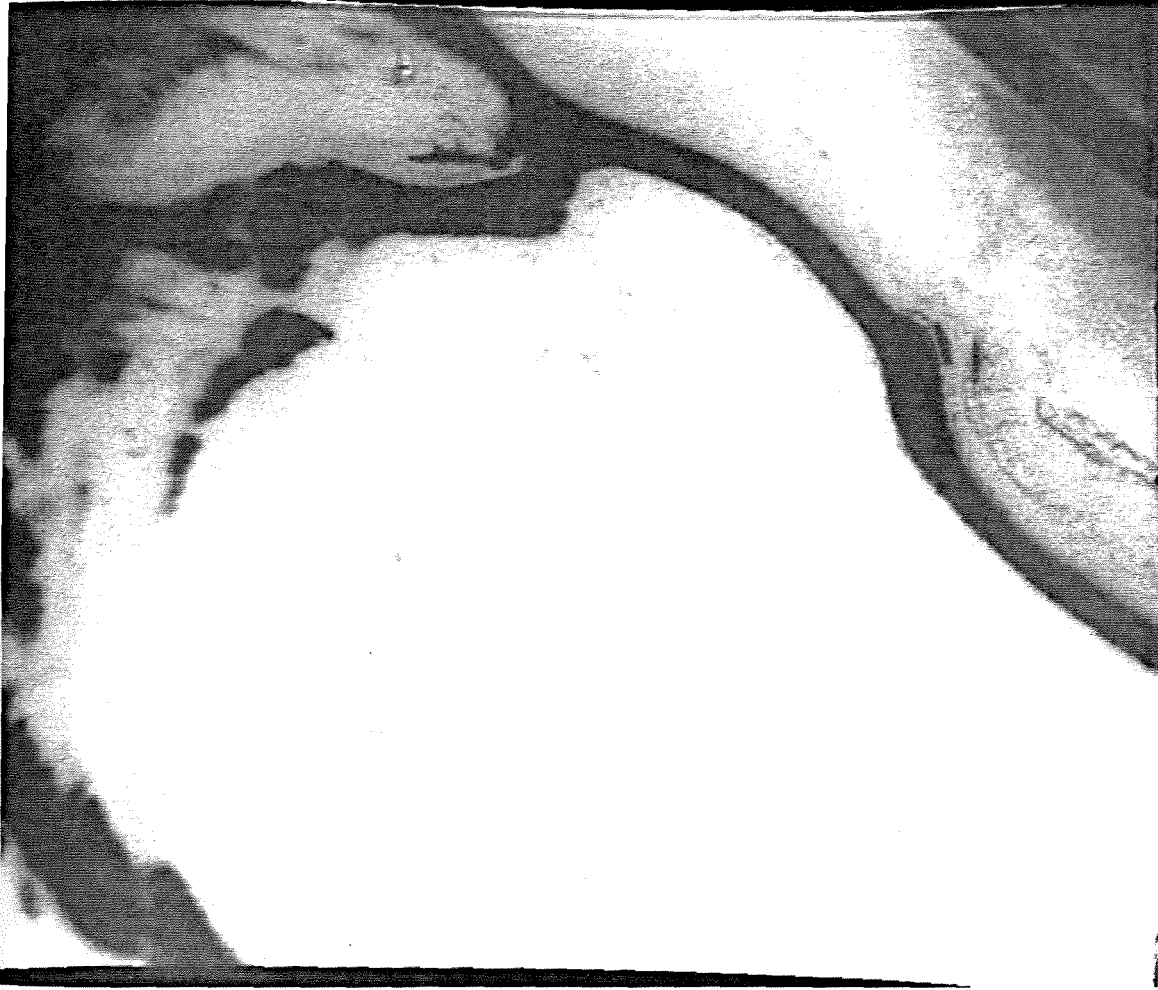


Figure 3.2: Mariner 9 narrow angle image of part of south polar cap, orbit 28.

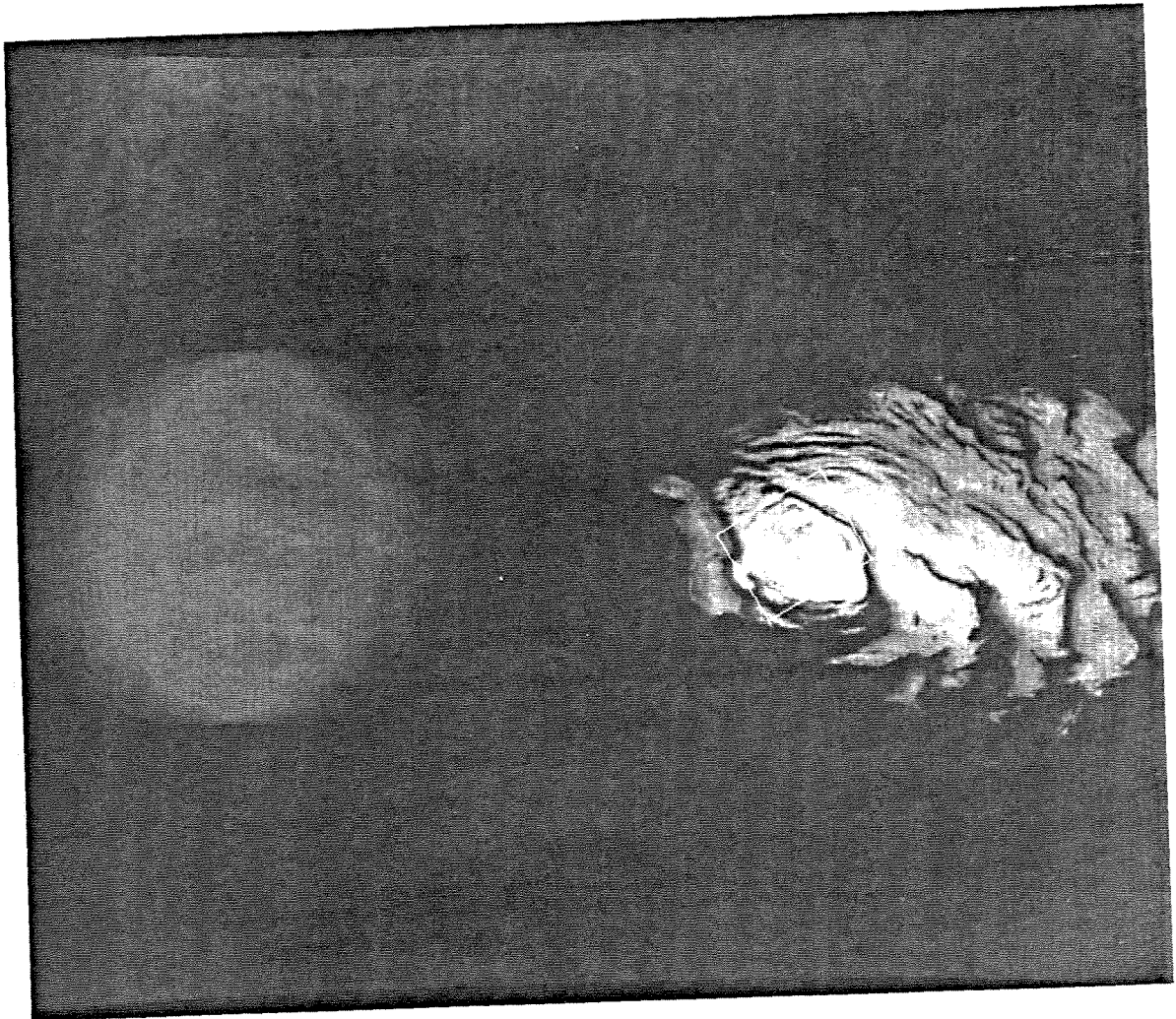


Figure 3.3: Mariner 9 wide angle image of the south polar cap, orbit 116. Footprint of IRIS spectrum 1120 highlighted, footprint of B frame from same orbit outlined.



Figure 3.4: Mariner 9 narrow angle image of the south polar cap, orbit 116.

of the results. The television data processing and analysis described in section 3.1.2 was performed entirely by the author. The IRIS data reduction and thermal modeling reported below were performed by David Paige (UCLA), who also collaborated on the creation of the histograms. The main conclusion of this work, that the south polar residual cap was cooled to solid CO₂ temperatures throughout the summer of 1971-72, is then discussed along with my view of the implications for the structure of the polar cap. Details of this work may be found in Paige *et al.* (1989).

3.1.1 IRIS Observations

The Mariner 9 IRIS had a spectral resolution of 2.4 cm^{-1} from 5 to 50 microns (μ) wavelength. Its instantaneous field of view was circular, 4.5 degrees of arc in diameter, with negligible response to radiation outside this field of view. The field swept about 1° across Mars during a 21 second integration period, so that some surface points were observed during only part of the integration period. The instrument was calibrated by viewing an on-board warm blackbody and deep space. A more detailed description of the IRIS is given by Hanel *et al.* (1972b).

Spectra that were well centered on the residual cap and that were acquired from favorable viewing geometries exist for orbits 28 ($L_s = 301$), 58 ($L_s = 310$), 116 ($L_s = 326$), and 188 ($L_s = 345$). The details of the observational geometry for all of these spectra are given in Table 3.1. Dave Paige and I found the locations of the IRIS footprint at 9 times during the integration period of each spectrum

Orbit	Spectrum	Incidence	Emission	Phase	Local Time
28	2817	70.2	51.7	21.3	2.65
28	2833	65.4	45.1	21.4	13.65
28	2834	66.1	46.7	21.4	13.30
58	2081	70.4	48.0	26.0	8.26
58	2084	67.5	43.9	26.0	11.50
116	1109	74.3	43.5	42.9	8.31
116	1116	72.7	44.0	38.8	11.40
116	1117	72.1	44.0	38.8	12.23
188	1002	82.5	46.3	61.3	8.95
188	1003	81.6	46.0	61.2	10.30

Table 3.1: Observational geometry data for IRIS spectra midpoints (in space and time). Angles in degrees, time in hours.

by interpolation of geometric information from adjacent spectra. The footprints of spectra (at the midpoints of their integration times) for which such interpolation was possible are shown in Figure 3.5. The corresponding spectra are shown in Figure 3.6, where noisy data at the spectral extremes have been removed.

As discussed in detail by Paige *et al.* (1989), the spectra show contributions from atmospheric CO₂ and dust, but relatively clear atmospheric windows occur at 7, 12, and 34 μ . Figure 3.7 illustrates the various features in a typical IRIS spectrum. The brightness temperatures measured at the window wavelengths are assumed to equal the surface emission. Because the atmosphere is generally warmer than the surface of the south polar cap, these measurements will tend to overestimate the surface emission, reinforcing the conclusion that the residual cap is cooled to solid CO₂ temperatures.

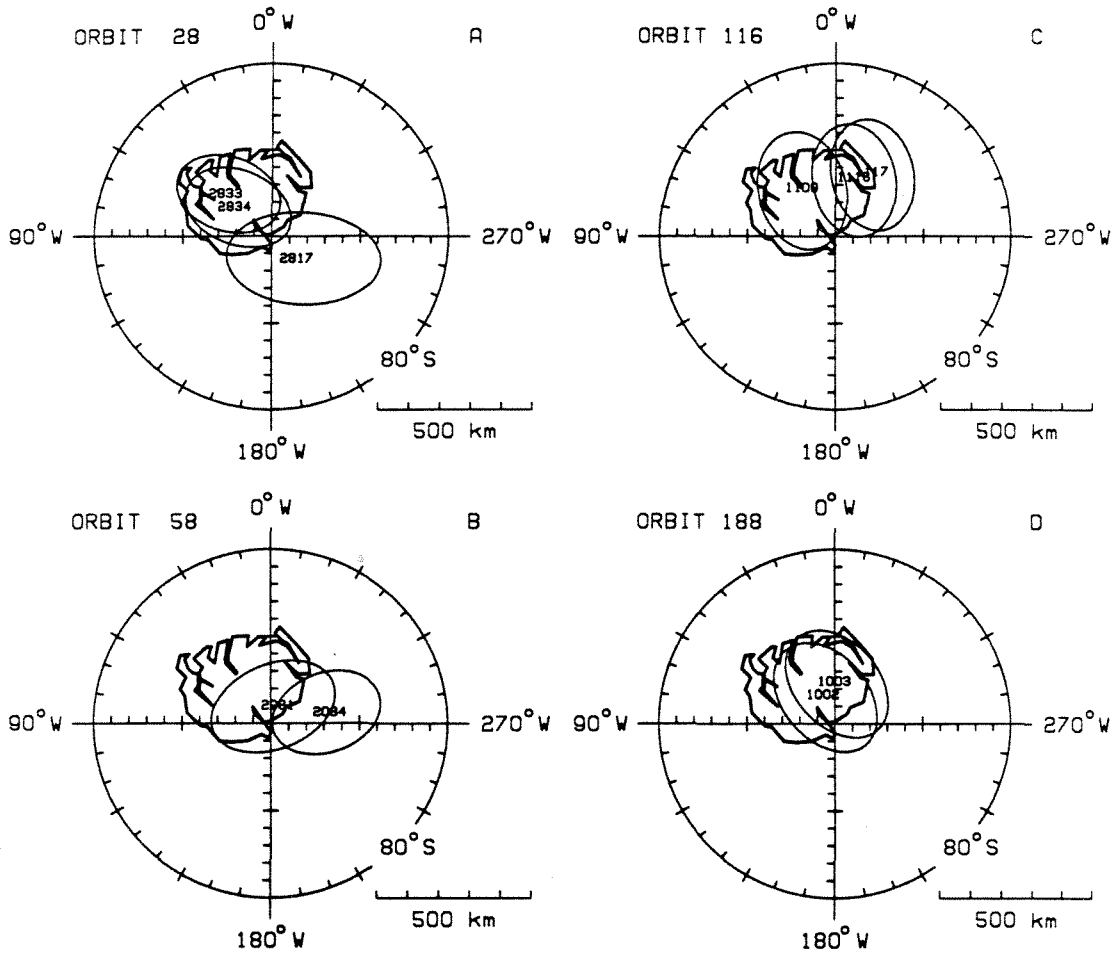


Figure 3.5: Midpoints of Mariner 9 IRIS footprints on map of south polar region. Outline of residual cap and IRIS spectrum numbers are shown.

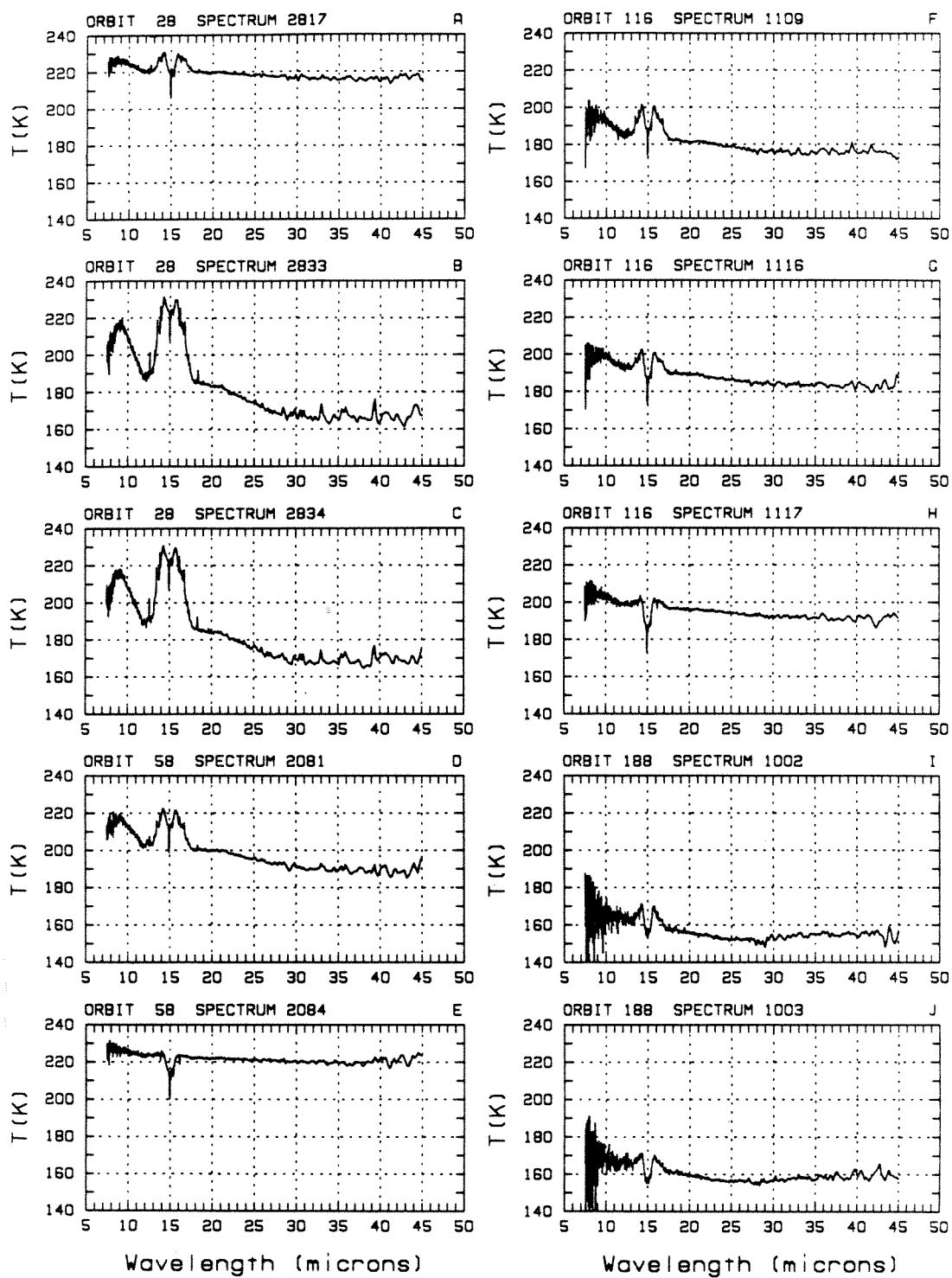


Figure 3.6: Mariner 9 IRIS brightness temperature spectra.

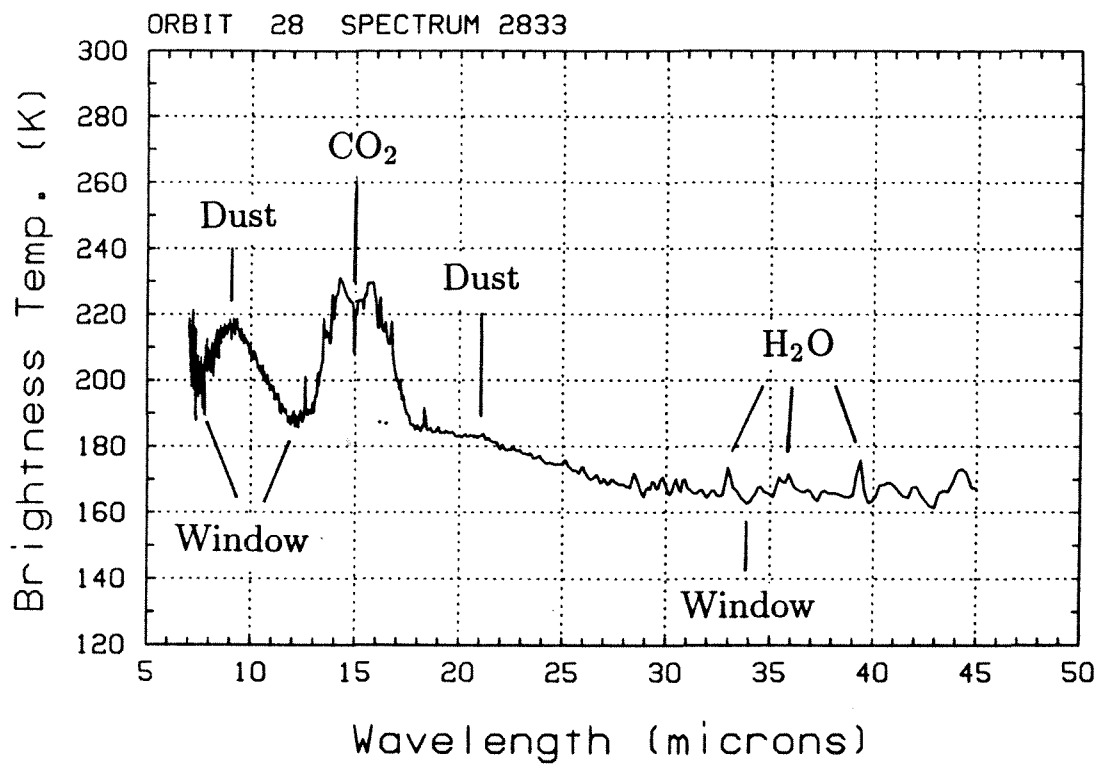


Figure 3.7: IRIS spectrum of south polar cap obtained on orbit 28. Emission features due to gaseous CO₂ and atmospheric dust, atmospheric window wavelengths indicated.

3.1.2 Television Observations

The Mariner 9 television subsystem consisted of two vidicon cameras: the wide-angle (A) camera, equipped with various filters, and the narrow-angle (B) camera (Cutts, 1974). The cameras were boresighted on the scan platform along with the IRIS, the ultraviolet spectrometer and the infrared radiometer. Wide angle camera images are used for comparison with the IRIS data because their fields of view are large enough to include entire IRIS footprints. The geometric information from the Supplementary Experimental Data Record (SEDR) used in processing the images in this study is essentially identical to that in Table 3.1.

The selected images were filtered to remove bit errors and reseaux, linearized, and then corrected for shading using calibration software now available from the U. S. Geological Survey in Flagstaff, Arizona. Residual image correction was also performed on the orbit 116 image (derived reflectances from images that were not corrected for residual image effects are approximately 5% too high). Geometric distortion, due mainly to beam bending in the vidicon, was also removed. After these procedures, the resulting images closely approximated the actual scenes observed. Although considerable effort has gone into the calibration of the Mariner 9 television data (Seidman *et al.*, 1973; Appendix A), significant radiometric errors remain. To minimize these errors whenever possible, images obtained through the orange filter (effective wavelength 0.61μ) were chosen, for which the most complete set of calibration data exists. The absolute accuracy of the derived reflectance for

each pixel in these images is about 20% (estimated from comparison with Viking Orbiter images of Phobos), while the relative accuracy is about 10% (Appendix A). The images used for the orbit 188 analysis were obtained through the 60° polarizing filter (effective wavelength 0.57μ), for which uncertainties in derived reflectance are slightly higher.

Lambert albedos were determined by dividing pixel values by the cosines of the local solar zenith angles, as calculated using the SEDR data. The assumption of Lambertian scattering is not valid in general for the surface of Mars, but the relative deviation from Lambertian behavior within a single IRIS footprint ($\sim 5^\circ$ incidence angle variation) is believed to be small. Because the spectral reflectance of Mars varies significantly in visible light, the Lambert albedos derived from images taken through the orange or 60° polarizing filter are not equal to the bolometric albedo. I therefore derived approximate bolometric albedos by comparing Mariner 9 and Earth-based spectral reflectance measurements of Arabia.

Spectral geometric albedo measurements of Arabia by McCord and Westphal (1971) were weighted by the solar spectral flux from 0.3 to 4.0 microns (Arvesen *et al.*, 1969) to yield a bolometric albedo of 0.30. By weighting McCord and Westphal's data by the orange filter response, the albedo of Arabia as seen through the orange filter is estimated to be 0.29. Similarly, Arabia's albedo through the polarizing filter would be 0.20. The actual spectral reflectance of the south polar frosts and surrounding terrain are not known, so I have assumed that the spectral reflectance

of the surrounding terrain is similar to that of Arabia and that the reflectances of the frosts do not vary with wavelength. As shown in the previous chapter, the color of Arabia is independent of phase angle. Therefore, the moderate phase angle of the south polar observations is assumed not to affect the color of the surface. With these assumptions, measured orange filter or polarizing filter reflectances were converted to bolometric reflectances by multiplying them by a scaling factor.

The location of points in the images that were observed by IRIS and the relative amount of time each point was observed is essential to this analysis. To determine the regions sampled, the locations of the spectra were interpolated at 9 points in time during the 21 second IRIS integration periods, as shown in Figures 3.1 and 3.3. Histograms of relative albedo values were generated for each of the nine overlapping polygons that define the IRIS field of view by considering only pixels that fall within each polygon. The nine histograms are added together to yield a histogram for each IRIS spectrum that takes into account the motion of the spacecraft during the integration period (Figure 3.8).

Scan platform pointing knowledge errors of up to 0.1 degree of arc are present in both the IRIS and imaging data sets. Since these data were generally not obtained at the same points in a given orbit, the locations of the IRIS footprints relative to the images could be in error by up to 0.2 degree of arc. This corresponds to offsets of approximately 15 pixels in the images used here. Arbitrary offsets of the footprints of this magnitude result in errors of about 5% in the histograms.

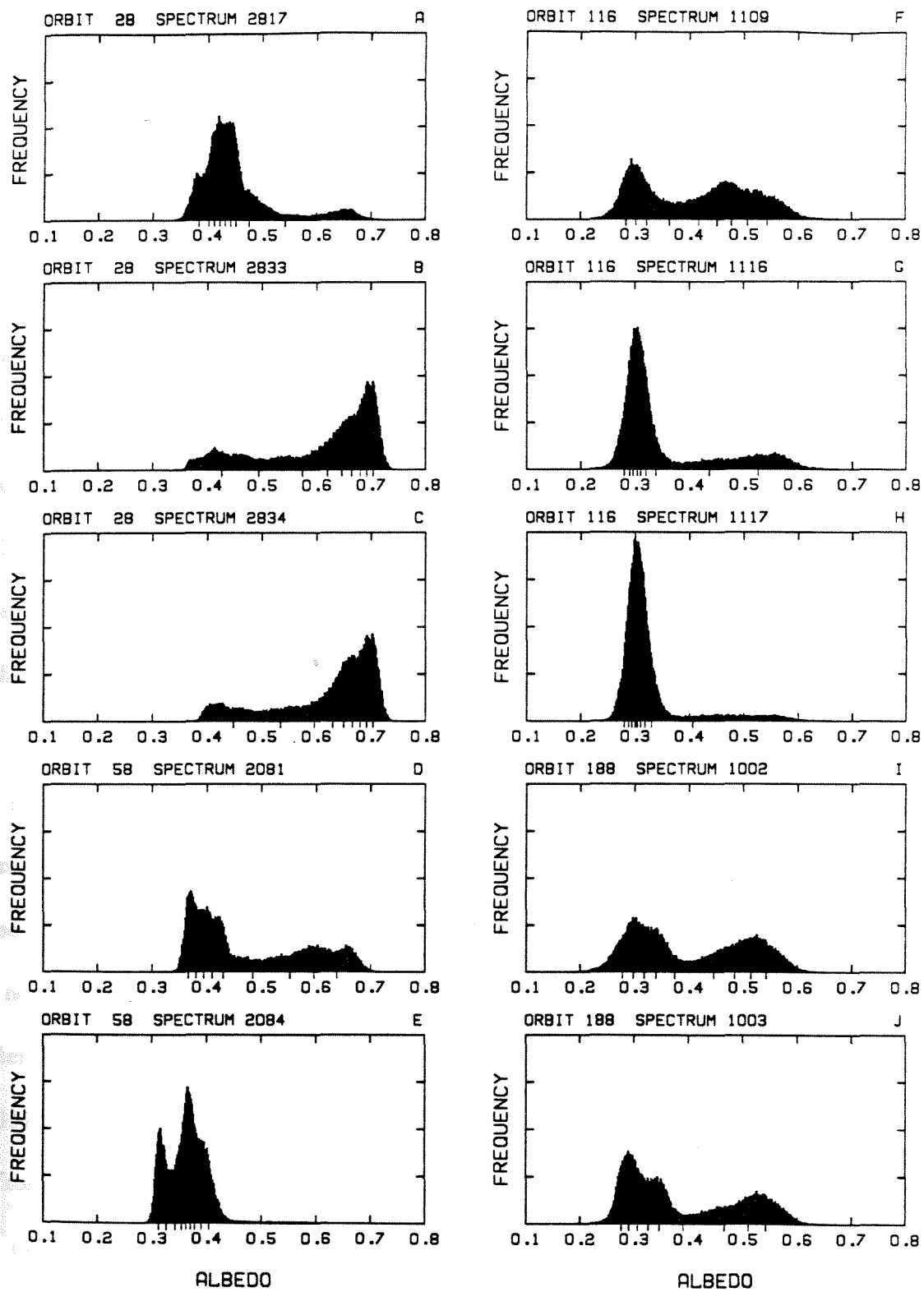


Figure 3.8: Histograms of Lambert albedo for areas sampled in each IRIS spectrum. Downward tick marks along bottom axes indicate cumulative percentages in 10% intervals.

The albedos presented in the histograms are also affected by dust in the Martian atmosphere. Mariner 9 arrived at Mars during the subsiding phase of the 1971 global dust storm. The dust opacity was near unity over the south polar cap (Pang and Hord, 1973), where the storm cleared earlier than over the rest of the planet. Although the atmosphere at the south pole appeared to be less dusty than at more equatorial latitudes, it still contained significant quantities of dust during the summer season. At orbit 28, Pang and Hord (1973) have estimated the dust opacity over the south polar cap to be 0.8 at $\lambda = 0.3\mu$, decreasing to 0.4 by orbit 116 and to 0.1 by orbit 188. If the dust optical properties given by Pollack (1982) are assumed, then dust opacities at the wavelength of the Mariner 9 orange camera filter would be approximately 10% greater than those at 0.3μ .

The histogram albedos are not estimates of actual surface albedo. In general, the surface scattering in this region is not isotropic, so the Lambert albedos reported here will not be necessarily valid over a wide range of illumination and observing geometries. Also, scattering models show that one of the major effects of atmospheric dust is to decrease apparent surface albedo contrasts. Atmospheric dust tends to make bright surfaces appear darker, and dark surfaces brighter (Thorpe, 1978; Davies, 1979; Paige and Ingersoll, 1985). Changes in the histogram albedos from one orbit to the next are therefore due to the combined effects of changes in atmospheric dust opacity, surface reflectance, and observational geometry. The albedos in the histograms from the later orbits (Figure 3.8f-j) are the best estimates

of the actual bolometric albedo of the surface.

Despite the effects of atmospheric dust, the boundaries of frosted and unfrosted regions within the IRIS fields of view are clearly visible in the images used in this study. This is also evident in the histograms, which generally show bi-modal (and sometimes tri-modal) distributions of measured reflectance. However, the histograms illustrate that there are areas of intermediate albedo within and near the residual cap. For example, spectrum 2834 is well centered on the cap but includes a significant area of intermediate albedo material (Figure 3.8c). Conversely, spectrum 2084 includes very little of the cap, and the corresponding histogram (Figure 3.8e) shows two distinct albedo units in the unfrosted ground. The histograms are used to infer the proportions of dark and light material within the IRIS fields of view. The fraction of bare ground within each IRIS footprint is essential to the analysis and discussion below.

3.1.3 Analysis

Paige *et al.* (1989) show in detail how the temperature of the south polar residual cap be used to constrain its composition. They presume that the two most likely constituents of the residual cap are dirty water ice and clean CO₂ frost. When solid carbon dioxide is present, the surface will be cooled to the equilibrium temperature of CO₂ at the ambient atmospheric pressure. CO₂ frost at 148K is in solid-vapor equilibrium with the atmosphere at the mean Martian surface pressure of 6.1

millibar (mb). Due to the high elevation of the south polar cap, the atmospheric pressure is probably only 4 mb, corresponding to a CO₂ frost temperature of 145K (Dobrovolskis and Ingersoll, 1975). The above temperatures assume unit emissivity; lower emissivities will result in lower brightness temperatures. The brightness temperature of the southern residual cap as measured by the Viking Infrared Thermal Mappers (IRTM) was 142K, indicating an emissivity slightly less than 1 (Paige and Ingersoll, 1985).

If only H₂O frost is present, however, the surface will heat up until it reaches radiative equilibrium, as the effect of latent heat on water ice surface temperatures is negligible (Briggs, 1974; Kieffer, 1979). The Viking IRTM observed water ice temperatures in excess of 205K on the north polar residual cap during summer (Kieffer *et al.*, 1976a). Equilibrium temperatures of water ice and bare ground are determined by the balance of insolation, thermal emission and conduction.

The IRIS spectra studied here include bare ground as well as residual frost within the fields of view, not only at the perimeter of the cap but in dark bands crossing the cap. In addition, high resolution images (Figure 3.4) show that the residual cap became more variegated as summer progressed, so that dark ground is exposed even within the cap. The cap is almost certainly variegated below the resolution of the television images as well. It is therefore essential that the imaging data be used to estimate the relative proportions of frost and bare ground within

each IRIS footprint. The histograms of albedos from the images (Figure 3.8) are used by Paige *et al.* (1989) to model the IRIS spectra (Figure 3.6), as is described below.

Two-Component Model

Hanel *et al.* (1972a) modeled an average of 6 IRIS spectra taken during orbits 29 and 30. Using only these IRIS data, they assumed that the surface was composed of two thermal components: cold condensates (H₂O or CO₂) and warm bare ground. On this basis, they derived a frost temperature of $140 \pm 10\text{K}$, a bare ground temperature of $235 \pm 10\text{K}$, and an average frost coverage of $65 \pm 5\%$. This type of model cannot distinguish more than two thermal components within the IRIS field of view. Furthermore, the amount of 140K component is very sensitive to the assumed bare ground properties.

Paige *et al.* (1989) applied this type of model to a single IRIS spectrum, as illustrated in Figure 3.9. The warm component was assumed to be at 235K and the cold component was set at 133K. A fractional cold component coverage of 75% fits the data well at the three window wavelengths, and agrees with the result reported by Hanel *et al.* (1972a). More importantly, this fractional coverage is consistent with the albedo histogram for this spectrum (Figure 3.8b). However, this type of combined television and IRIS analysis could not be applied to all of the polar cap spectra due to low signal/noise in the 7μ window. To less ambiguously treat all of

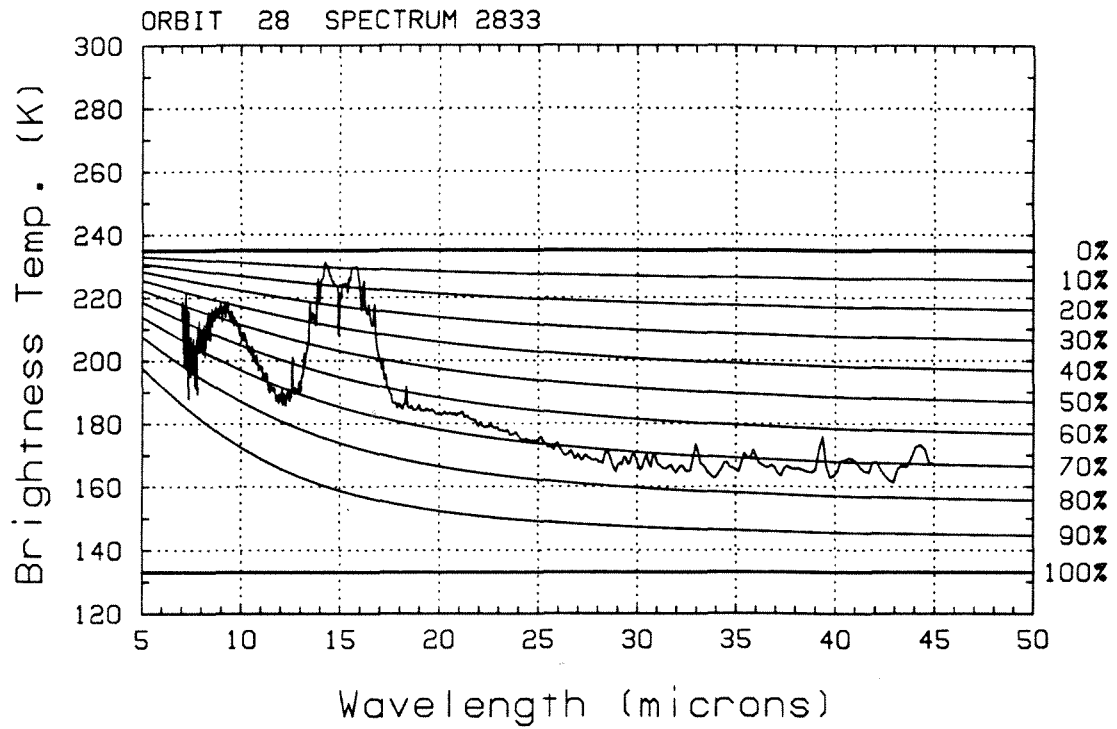


Figure 3.9: Comparison of brightness temperatures calculated using 2-component model with various CO₂ fractions and IRIS spectrum from orbit 28. Model assumes 235K warm component, 133K cold component.

the spectra, Paige *et al.* (1989) therefore constructed a three-component model to analyze the IRIS data without averaging spectra, using the histograms of surface albedos within each IRIS field of view.

Three-Component Model

In this approach the surface emission is assumed to be the weighted sum of three thermal components: bare ground, water ice, and carbon dioxide frost. The blackbody emission of each component is weighted by its fractional surface coverage. The observed emission at the 12 and 34 μ windows can then be modeled using the observed fractional bare ground coverage plus the constraint that the total of the three fractional coverages is unity (Paige *et al.*, 1989). The resulting three equations still have four unknowns, the temperatures of the three components and the fractional coverage of either the water ice or CO₂ frost. Hence, this set of equations cannot be solved explicitly until an additional constraint is provided.

To extract a conclusion, then, a wide range of water ice and CO₂ fractions were used to model the coldest spectra from each of the orbits studied (Figure 3.10), as described in detail by Paige *et al.* (1989). The maximum CO₂ fraction (horizontal axis in Figure 3.10) is conservatively estimated from the histograms in Figure 3.8, assuming the 5% uncertainty in the histograms determined above. The resulting models indicate that a wide variety of water ice temperatures are consistent with the data at 12 and 34 μ (within ± 1 K) when CO₂ frost is present, even though the bare

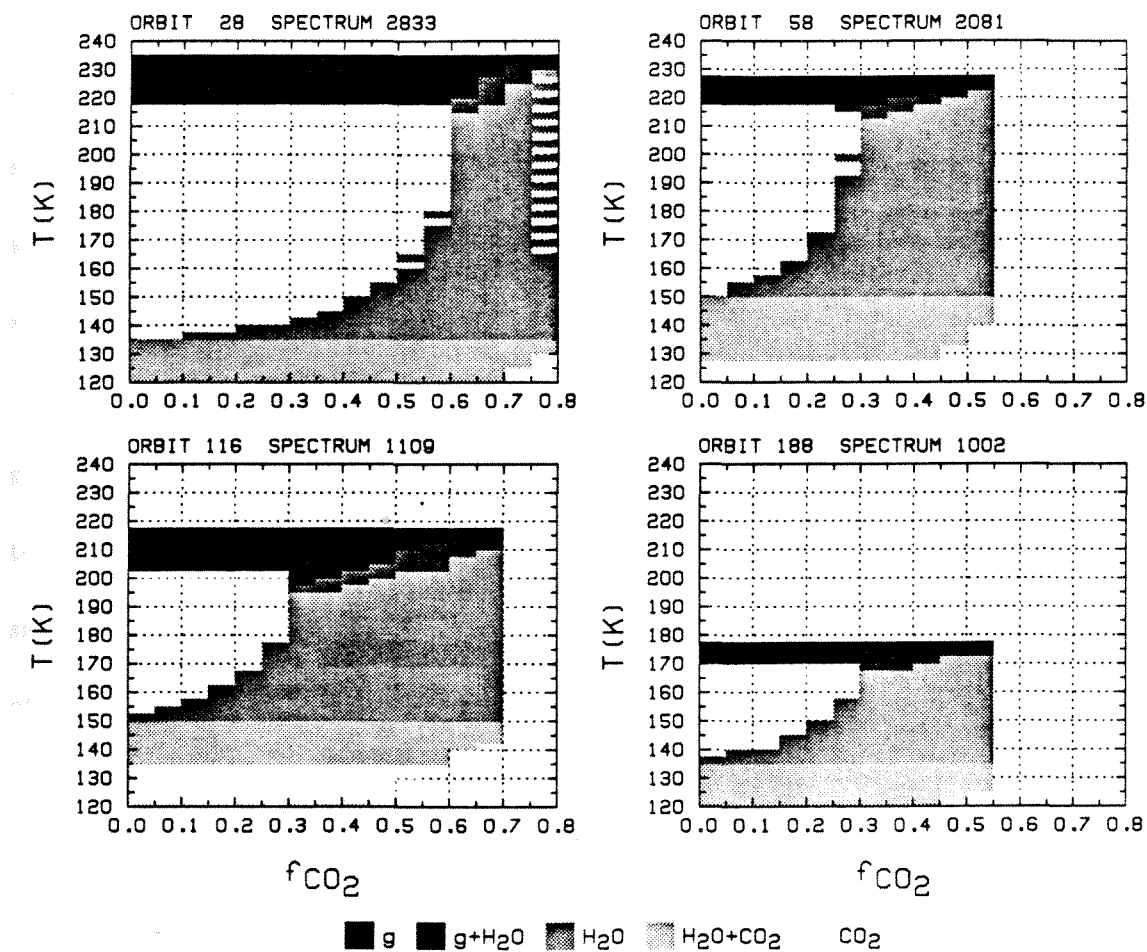


Figure 3.10: Three-component model results. Shaded regions show range of calculated bare ground, H₂O and CO₂ frost temperatures consistent with IRIS spectra. Overlapping regions denoted by intermediate shades.

ground temperatures are well constrained. However, and most importantly for the primary conclusion, models with no CO₂ present can account for the observations *only if the water ice temperature is 150K or less*. Any H₂O frost must therefore be cooled by sublimating CO₂. The physical notion that water ice would rise to its radiative equilibrium temperature in the absence of sublimating CO₂ effectively supplies the missing constraint. This result implies that CO₂ was present on the surface of the residual cap during all of the orbits studied, cooling the surface to its sublimation temperature.

Additional confidence in the three-component modeling arises from the good agreement between the bare ground temperatures derived by the model and the brightness temperatures actually measured slightly off the residual cap (at the same latitude as the cap). Spectrum 2084 (Figure 3.6e) on orbit 58 is over 90% off the cap (Figures 3.5b and 3.8e) and has a 12 μ brightness temperature of 223K, easily within the range of bare ground temperatures in the model (Figure 3.10). Spectra 2817 (Figure 3.6a) and 1117 (Figure 3.6h) include slightly more of the cap (Figures 3.5 and 3.8), and are therefore have 12 μ brightness temperatures that are slightly less than the modeled bare ground temperatures in Figure 3.10. Thus, Paige *et al.* (1989) actually derive bare ground temperatures subject to observational tests, unlike Hanel *et al.* (1972a).

The time evolution of the three-component model is now examined. The upper and lower limits of bare ground, water ice and carbon dioxide frost tempera-

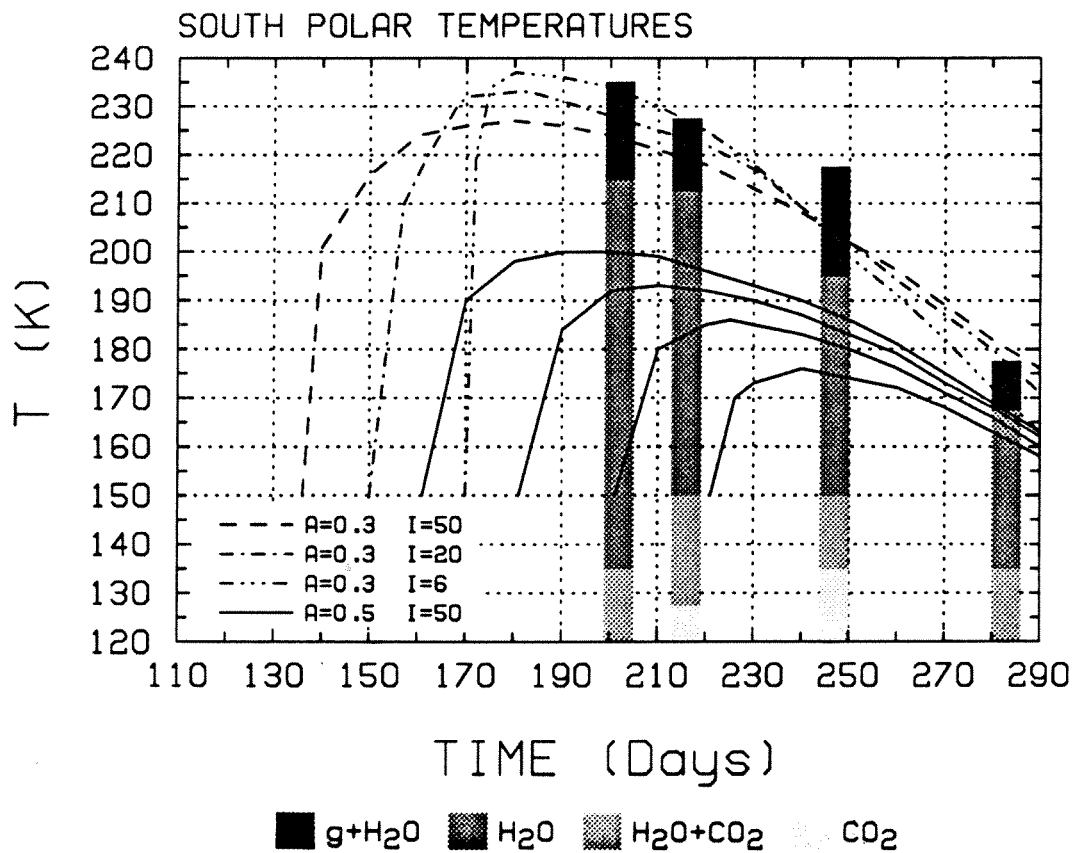


Figure 3.11: Three-component model time evolution. Dashed lines show bare ground thermal evolution for an albedo of 0.3 and a variety of thermal inertias. Solid lines show water ice cap thermal evolution for albedo and thermal inertia indicated (Kieffer, 1979).

tures are indicated for each orbit in Figure 3.11. Also shown are calculated surface temperatures at 88°S latitude of a water ice cap and of bare ground exposed at various times during the southern summer (Kieffer, 1979). A thermal inertia I of $50 \times 10^{-3} \text{ cal cm}^{-2} \text{ sec}^{-1/2}$ is assumed for the water ice, and various values of I are used to model the bare ground temperatures. The surface albedo of the ice cap is assumed to be 0.5, and the albedo of the bare ground is 0.3 in these calculations. Kieffer's models show that a water ice cap would be expected to warm up to at least 170K, even if exposed late in the summer.

The albedo of 0.3 in Kieffer's models fits the bare ground temperatures predicted by the three-component model rather well (Figure 3.11), and agrees with the dark ground albedos in the histograms (Figure 3.8). This agreement lends further credence to the derivation of bolometric albedos in section 3.1.2, although the histograms do show significant variations in bare ground albedos within individual footprints.

3.1.4 Discussion

Why are the derived CO₂ frost brightness temperatures so low for orbits 28 and 188? Spectra 2833 and 1002 (Figure 3.10) are consistent only with carbon dioxide frost temperatures below 135K. Kieffer *et al.* (1977) invoked local CO₂ depletion (5% of the average Martian atmosphere is other gases) to explain the low brightness temperatures observed by the Viking IRTM during the southern winter.

However, such a decrease in partial pressure is caused by local condensation of CO₂, and therefore cannot account for the low *summertime* temperatures indicated by the three-component model, since CO₂ could not condense then.

Another possibility might be the combination of low frost emissivity and high surface elevation used by Kieffer *et al.* (1977) to explain the ~140K brightness temperatures over most of the winter cap. However, an unreasonably low emissivity and/or very high elevation are required to reduce the brightness temperature to 135K (Kieffer *et al.*, 1976b).

How, then, can the 135K CO₂ brightness temperatures be explained? My preferred reconciliation of the dilemma is as follows. The histograms of albedo data from the nearly simultaneous images place limits on the amount of dark ground in the IRIS fields of view, and these results were used to constrain the fractional coverage of CO₂ in the models. Note, however, that if CO₂ frost is *hidden* in topographic depressions in the dark ground, it could cool the ground but still appear dark in the images. Such a situation would imply that the estimates of bare ground fraction in the thermal models above are too high, and thus could explain the low CO₂ temperatures indicated by the models. A larger fractional coverage of CO₂ frost allows higher CO₂ temperatures (Figure 3.10) and implies that all of the areas of intermediate albedo in Figure 3.8 are cooled to the sublimation temperature of CO₂.

Topographic roughness in the dark areas may allow CO₂ frost to remain

on the surface throughout the summer but hidden from view. In order to cool the exposed dark areas by thermal conduction, the length scale of the topography must probably be on the order of centimeters or less. Because the frost would only occur in shadows, the surface would appear dark to the orbiting cameras. Late in the summer, the maximum solar elevation in this area is only $\sim 10^\circ$, so that small-scale roughness of this magnitude could suffice to protect the CO_2 frost and make the surface appear dark. Earlier in the summer, such areas may appear darker than pure frost, but brighter than the surrounding dark ground due to partial frost cover. Color and albedo mapping in the south polar region also indicates that mixtures of frost and bare ground exist adjacent to the residual cap (Herkenhoff and Murray, 1989), as described in the next section.

3.2 Color and Albedo of the South Polar Layered Deposits

The composition of the layered deposits must be understood in order to determine the processes responsible for their formation and erosion, and hence the mechanisms by which climatic variations are recorded. A common presumption among Mars researchers is that the layering somehow reflects variations in the proportions of dust and ice deposited during many climate cycles (Toon *et al.*, 1980; Cutts *et al.*, 1979; Squyres, 1979; Cutts, 1973b). The purpose of the work

presented here is to use photometric measurements of the surface reflectance and color of the layered deposits to constrain their composition and texture, and hence their origin. The results described below imply that the non-volatile component of the layered deposits is mostly bright red dust with a small amount of dark material. Areas are identified within the layered terrain that may be the site of current layer formation.

Thomas and Weitz (1989) analyzed the color and albedo of the north polar layered deposits by using high resolution Viking Orbiter images. Comparable studies of the south polar region have been limited by the lower resolution of the Viking imaging data. The striking contrasts in size, setting, and appearance of the north and south polar layered deposits suggest significant differences in their formation and evolution. Further photometric and morphologic study of the south and comparison of the two regions may offer insights into Mars' climate history over the last 10^8 years or more.

Viking Orbiter 2 imaged the south polar region in three colors, typically at a resolution of a few hundred meters per pixel. The processing of the color data is described below, followed by a discussion of the effects of atmospheric scattering on the apparent surface brightnesses. The dust scattering in shadows was modeled and the results were used to estimate the atmospheric component of brightness in the images (details of the method are presented in Appendix B). The dust scattering properties found in this analysis are similar to those found in previous studies.

Removal of the atmospheric effects from the color images then allows estimation of surface reflectance and permits five color/albedo surface units to be quantified within the south polar layered terrain. The color and albedo of these mapped units are then interpreted in terms of composition and texture. Finally, several hypotheses of the composition of the layered deposits are considered.

3.2.1 Processing and Mapping Methods

T. Becker (U. S. Geological Survey, Flagstaff) used Viking Orbiter 2 images of the south polar region taken through three different filters (violet, green and red) to construct the digital color mosaic shown in Figure 3.12. The 18 images (6 in each of 3 colors) in the mosaic were taken nearly simultaneously during orbit 407 ($L_s = 341^\circ$), at phase angles around 85 degrees. The incidence (solar zenith) angle varies from about 60 degrees at the top of the mosaic to 85 degrees at the bottom. The south pole is at bottom center, near the lower edge of the residual cap.

The images were radiometrically calibrated in Flagstaff using the Planetary Image Cartography System (PICS), so that the data value in each pixel represents the actual reflectance (I/F) observed. The relative calibration error measured where the images overlap is as large as 10%, so that the absolute uncertainty in calibration is no less than 10%. This result is consistent with the 13% (1σ) absolute uncertainty near midscale in the Viking television calibration reported by Klaasen *et al.* (1977). No estimates of the radiometric accuracy of PICS have been

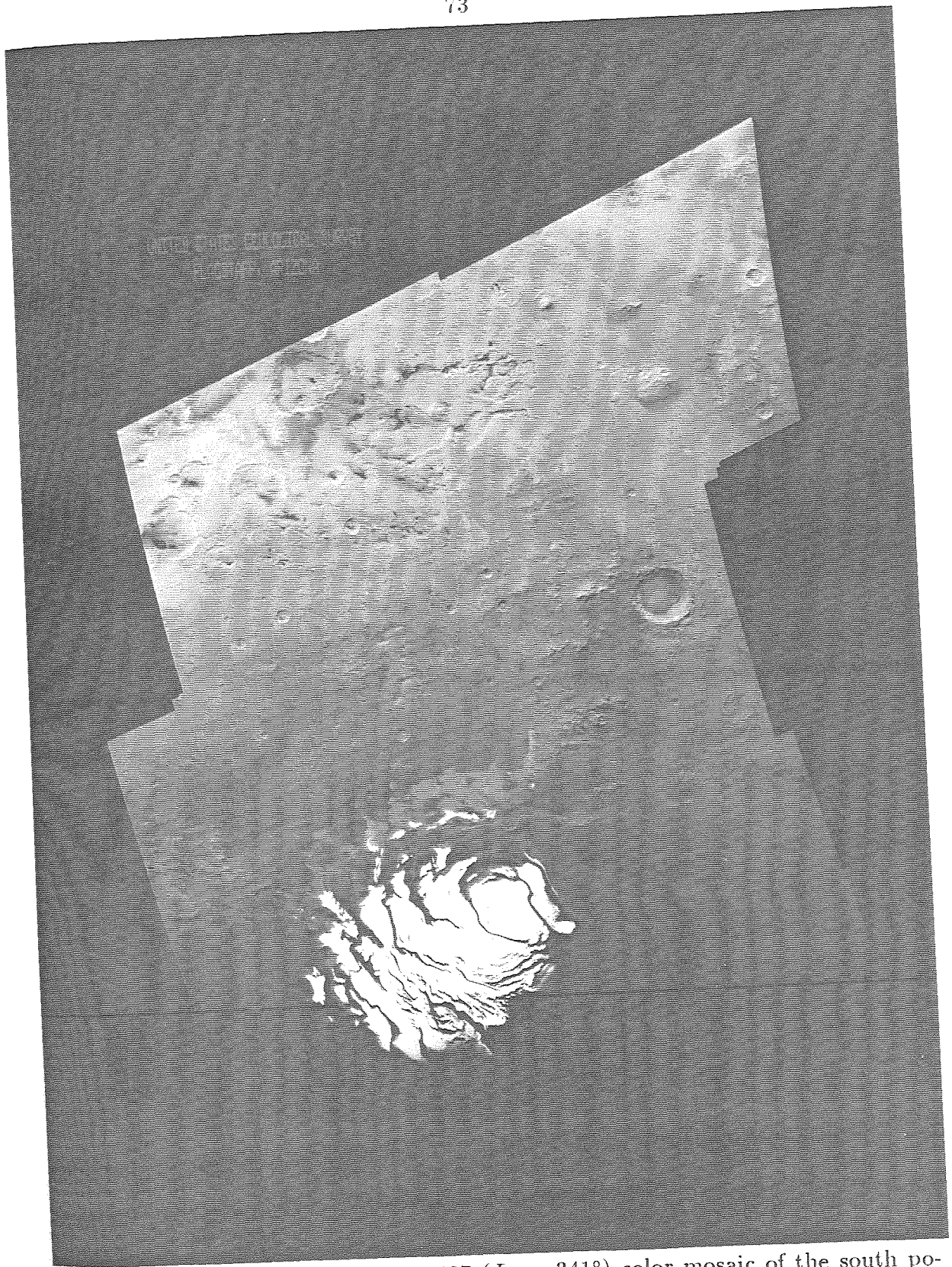


Figure 3.12: Viking Orbiter 2 rev 407 ($L_s = 341^\circ$) color mosaic of the south polar region, with 500 meters/pixel resolution. Orthographic projection with $0^\circ W$ longitude at 12 o'clock, sun toward 11 o'clock.

published, and the absolute uncertainty of the Viking Orbiter calibration may be greater than 13%. Preliminary analysis of Viking Orbiter 1 Phobos images shows differences of up to 18%, as discussed in the previous chapter. In the absence of precise knowledge of the absolute radiometric uncertainty in the Viking data used here, the 13% absolute uncertainty given by Klaasen *et al.* (1977) is used in the discussions that follow.

Because the green filter bandpass ($\lambda_{eff} = 0.54\mu$) overlaps both the red ($\lambda_{eff} = 0.59\mu$) and violet ($\lambda_{eff} = 0.45\mu$) filter bandpasses, the red mosaic was divided by the violet mosaic pixel by pixel to obtain maximum color information. The resulting red/violet (R/V) mosaic is shown in Figure 3.13. Errors in registration of the color mosaics (relative to each other) are not greater than 5 pixels, as indicated by the bright rims around the polar cap. Despite the presence of atmospheric scattering, distinct surface units can be recognized in the R/V mosaic. Near the top of the mosaic, neutral¹ and darker material appears in topographic depressions that can act as natural saltation traps. The polar cap and outliers of seasonal frost appear black ($R/V \leq 1.7$) in this rendition of the mosaic, but are actually slightly red in color, in part due to atmospheric scattering. Variations in the color of the surface of the layered deposits are also evident, and will be described in detail in the next section.

By measuring the brightness observed in shadows, the component of bright-

¹All of the surface units examined in this study are red in color, but the units that are less red shall be referred to as "neutral" in color.

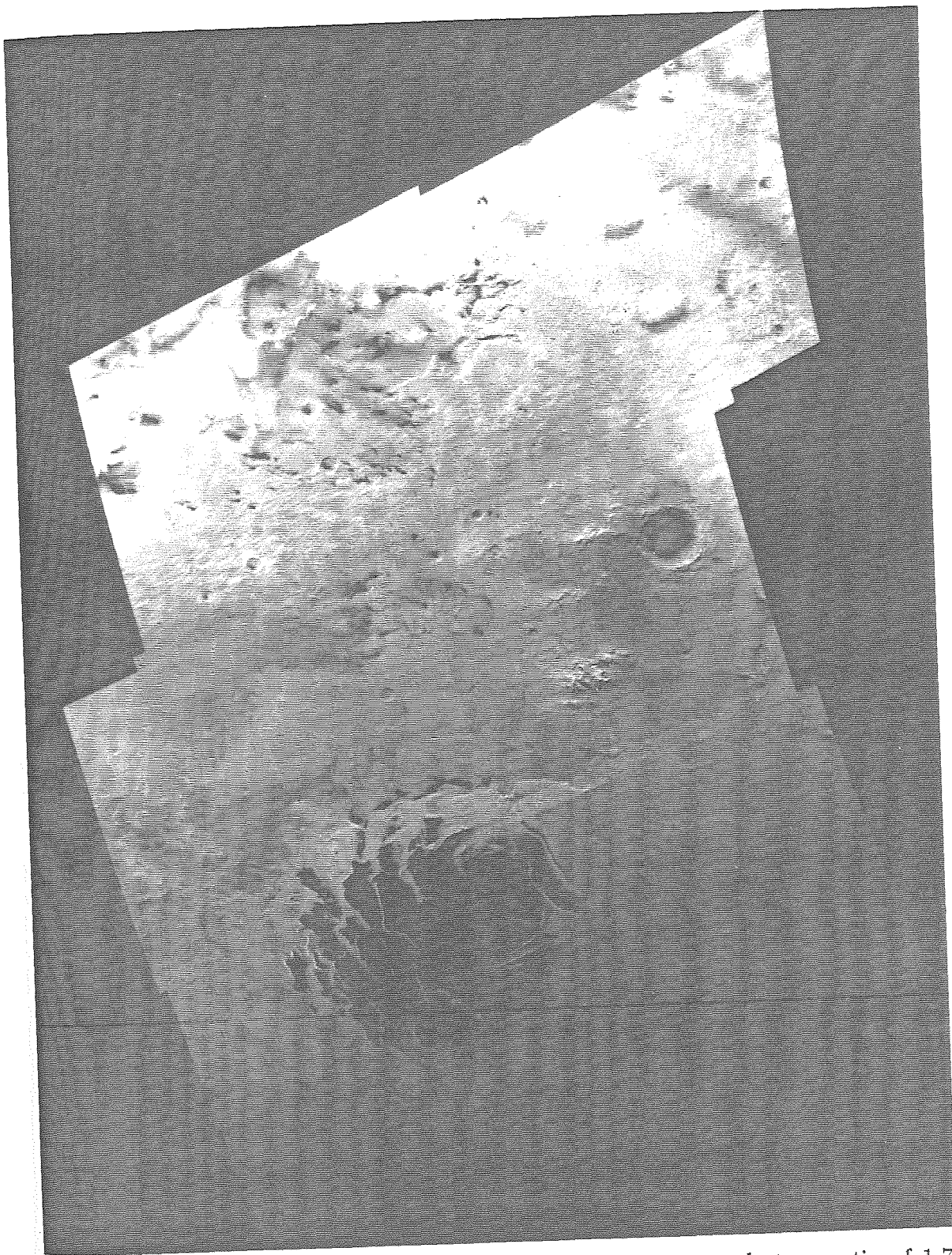


Figure 3.13: Rev 407 red/violet ratio image. Black corresponds to a ratio of 1.7, white is $R/V = 2.8$. The bright lines bordering the polar cap are due to slight misregistration of the two mosaics. Seams between individual images in mosaic are visible, due to offsets of up to 10%.

ness due to atmospheric dust scattering can be estimated at various points in the mosaic. Over 100 of the measured shadow brightnesses are shown in Figures B.1-B.3, along with model fits described in Appendix B. The uncertainty in the absolute calibration of the television data, due mainly to the uncertainty in dark current subtraction, can be significant in evaluating atmospheric brightness. The error in dark current subtraction is greater at low raw data values, so that shadow brightnesses near the bottom of the mosaic are the most uncertain. Thirteen percent error bars are plotted in Figures B.1-B.3, illustrating the absolute uncertainty in the shadow data except near the terminator, where the error is larger. While determination of the dust scattering parameters (as described in Appendix B) is sensitive to errors in absolute calibration, delineation of surface color/albedo units is limited only by noise in the data. The signal/noise is too low to identify surface units only in the bottom right corner of the mosaic.

The lower portion of the mosaic, where the layered deposits appear, was corrected for atmospheric scattering (Figure 3.14) and used to create the R/V mosaic shown in Figure 3.15. The atmospheric brightness and attenuation at selected points in the mosaic was predicted using 2.5μ radius particles with the scattering properties given in Table B.1. The best fit model (normal optical depth = 0.13) was run at 35 points in a 400×400 pixel grid, then bilinear interpolation was used to approximate the atmospheric brightness and attenuation at every other pixel in each color mosaic. The interpolated atmospheric brightness was subtracted from

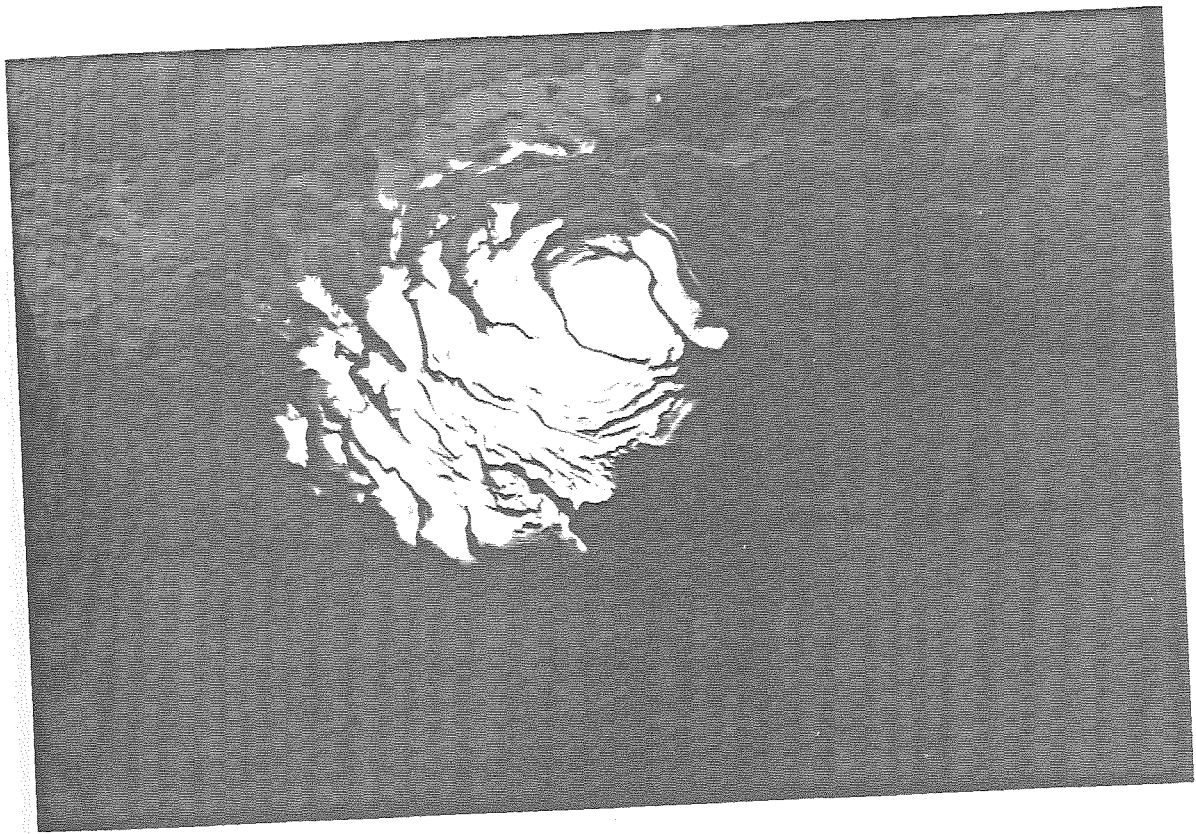


Figure 3.14: Part of rev 407 color mosaic, corrected for atmospheric scattering. Note albedo variations in layered deposits near the polar cap. The area shown is 1200 km across.

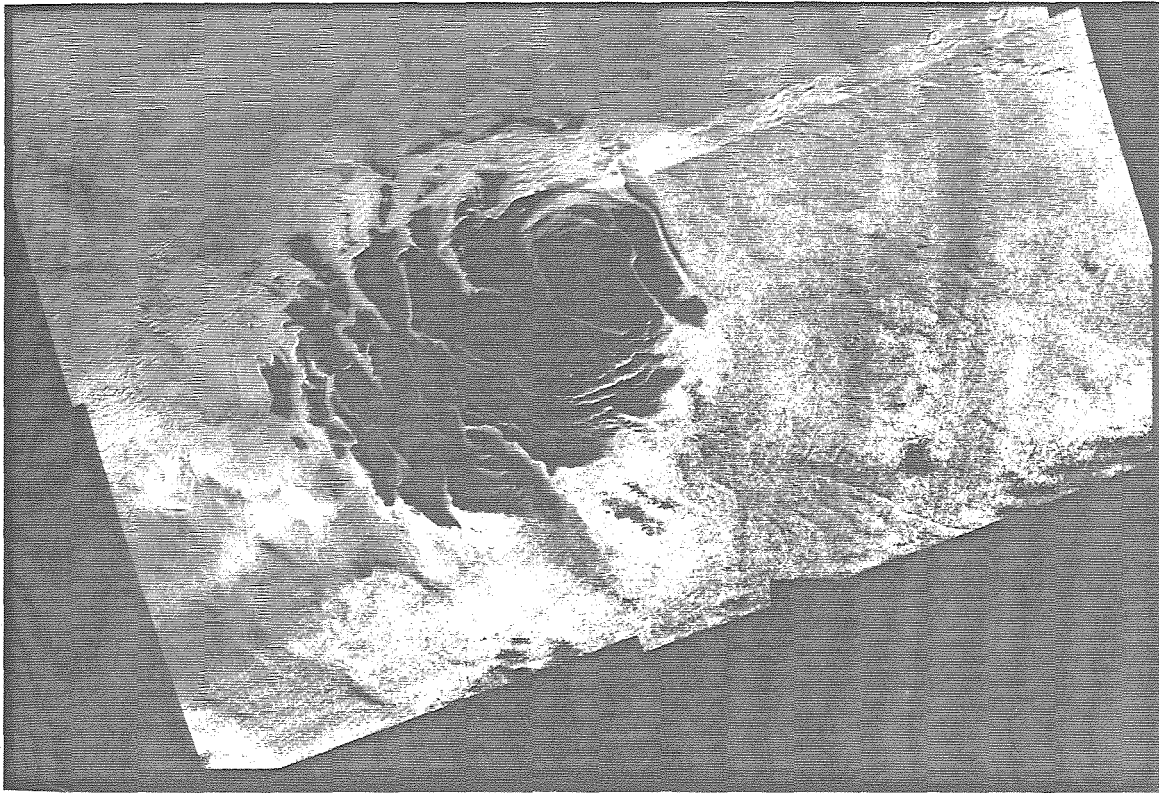


Figure 3.15: Red/violet ratio mosaic, corrected for atmospheric scattering. Signal/noise is rather low at the bottom and at the right side of the mosaic.

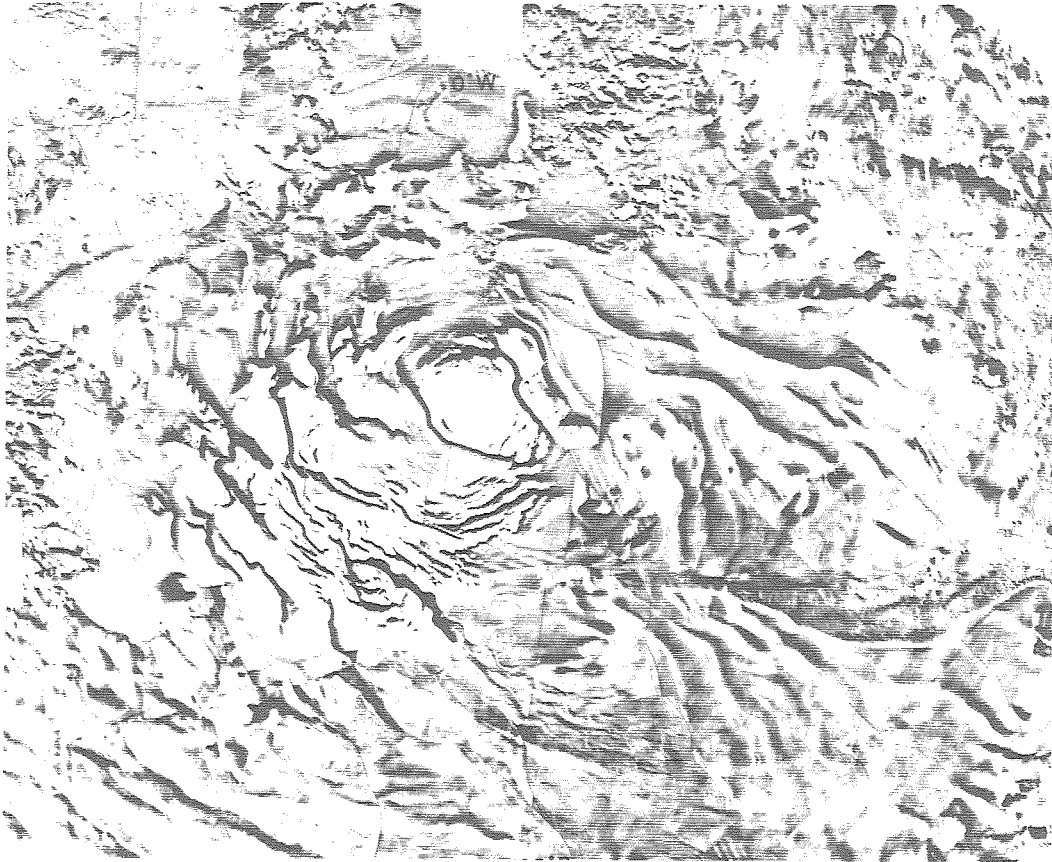


Figure 3.16: Section of U. S. Geological Survey controlled photomosaic MC-30A/B (I-1647), original scale = 1:2,000,000. Note off-cap colian grooves at bottom, deflected left by Coriolis force. The south pole is just below and left of center.

each pixel value, and the result divided by the total attenuation of the incoming and outgoing radiation to approximate the atmosphereless reflectance of the surface.

The R/V and color mosaics were used to identify five color/albedo units in the layered terrain. The units were mapped (Figure 3.17) where the noise level in the mosaics is sufficiently low using an overlay on the 1:2,000,000 photomosaic shown in Figure 3.16. Tanaka and Scott (1987) mapped the area at the top of

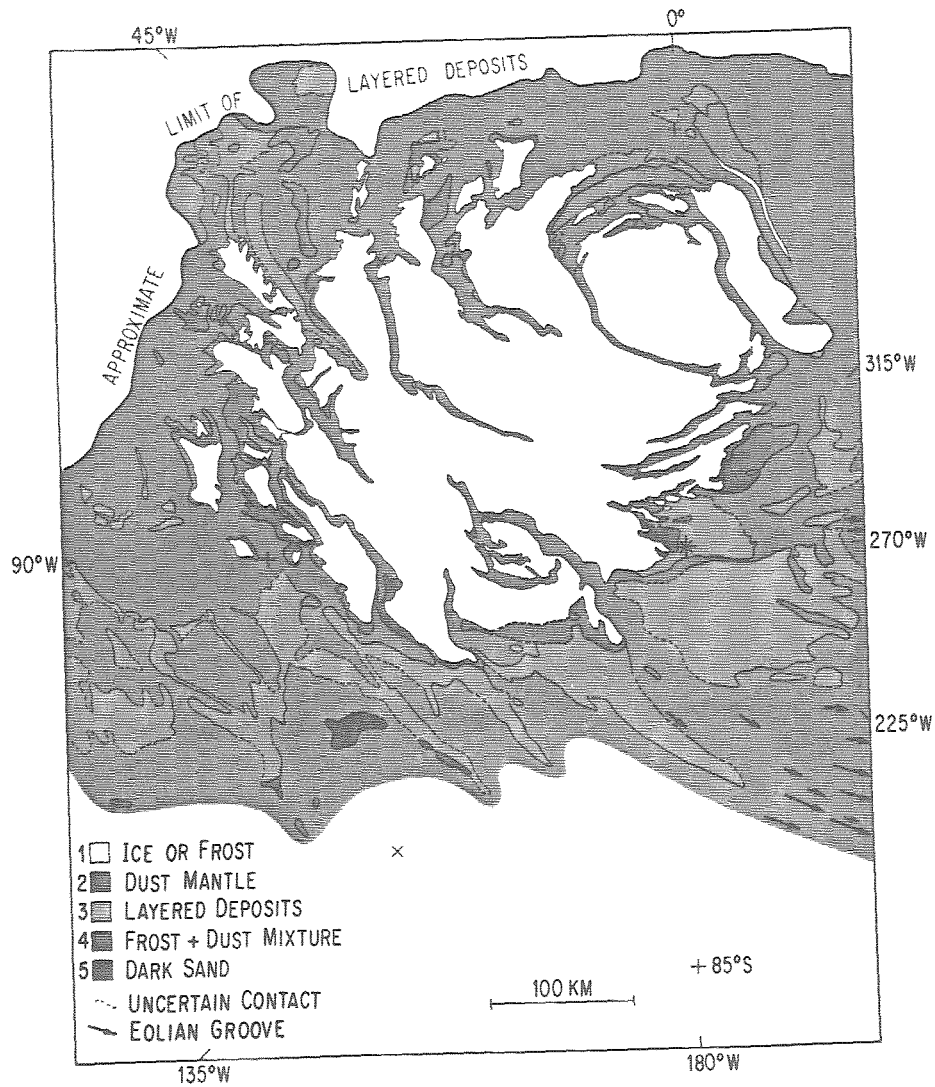


Figure 3.17: Map of color/albedo units in the south polar layered terrain, originally mapped at 1:2,000,000 scale. Drafted lines are located to accuracies of a few kilometers or better. Dashed lines represent uncertain or gradational contacts.

Figures 3.14, 3.15 and 3.17 as layered deposits, but I find no evidence of layering in that area, neither in the digital mosaics used here, in the 1:2,000,000 photomosaic, nor in high-resolution Mariner 9 images of the area. This area may be an exposure of the basal member(s) of the layered deposits, or a separate unlayered unit. For the purposes of this study, "layered deposits" are defined as those units in which distinct layering can be seen. My primary interest is in the layered deposits, so I have chosen to map only the area within the layered deposits and polar cap, as delineated in Figure 3.17. Some areas in the layered deposits have the same color and albedo as areas outside the layered terrain, but only the layered deposits have been subdivided.

Contacts between color/albedo units were located on both the R/V mosaic and the photomosaic, and have been drafted to an accuracy of a few kilometers or better (mosaic resolution is 0.5 km/pixel). The five surface color/albedo units (and corresponding interpretations) are: [1] bright neutral (polar frost), [2] bright red (dust), [3] dark red (layered deposits), [4] bright intermediate (mixture of units 1 and 2), and [5] dark neutral (sand). The R/V ratios of unit 4 are similar to those of unit 3, but the two units may be distinguished by their overall albedos: unit 4 is brighter than the other units (except unit 1), while unit 3 is slightly darker than unit 2 (Table 3.2). Because of the variation in illumination across the mosaic, the average reflectances of selected 5×5 pixel areas were divided by the cosine of the incidence angle to facilitate comparison. The resulting Lambert albedos (Table 3.2) are not

Unit	Interpretation	Violet	Red	R/V
1	Frost	0.18-0.43	0.27-0.53	1.2-1.6
2	Dust mantle	0.04-0.05	0.14-0.18	3.2-3.8
3	Layered deposits	0.03-0.05	0.10-0.13	2.5-3.2
4	Mixture of units 1+2	0.05-0.09	0.18-0.27	2.2-2.9
5	Dark material	0.02-0.05	0.04-0.10	1.8-2.1

Table 3.2: Lambert albedos and colors of surface units.

comparable to the albedos used in the atmospheric scattering model (Appendix B) because the assumption of a Lambert photometric function is incorrect in general. The unit map shows that many of the contacts between these units are gradational, as would be expected where sand or dust cover is incomplete, or where relative amounts of dust and frost vary. Location of contacts is uncertain where the signal to noise ratio is low (at the bottom of the mosaic). However, some of the contacts between the frost or frost mixtures (units 1 or 4) and surrounding darker units are quite sharp, probably due to topographic control of their boundaries.

Surface albedos higher than the values of 0.09 (violet) and 0.25 (red) used in the atmospheric model must be used to correct for atmospheric effects over areas of bright frost. Frost albedos of 0.5 (violet) and 0.6 (red) were used to model the atmospheric reflectance over several points in the polar cap. Similarly, surface albedos of 0.15 (violet) and 0.35 (red) were used to correct for atmospheric scattering over unit 4. The above surface albedos were estimated from the brightness contrast between the bright units and the surrounding areas, and adjusted iteratively to approach the color of the corrected data. The R/V ratios of these higher surface

albedos (frost = 1.2; unit 4 = 2.33) are consistent with the R/V ratios of the corrected surface data, as indicated in Table 3.2. The lower surface albedos yield slightly higher corrected R/V ratios because the redness of the surface reflection is overestimated.

3.2.2 Results and Interpretations

A multistream radiative transfer model was applied to a Viking Orbiter color mosaic of the south polar region. The parameters used in the model are similar to those found by other workers: normal optical depth = 0.13, single-scattering albedo = 0.57 to 0.85, asymmetry parameter = 0.31 to 0.49, extinction efficiency = 2.64 to 2.75 with 2.5 micron particles, and surface albedos of 0.09 (violet), 0.18 (green) and 0.25 (red). This model should also be valuable for future photometric measurements of the Martian surface and atmosphere.

In the absence of any wavelength-dependence in the photometric function and neglecting the difference in color between the surface and atmospheric scattering, topography should vanish in an R/V ratio image. However, some topographic features are still visible in the R/V image (Figure 2), and there is an overall decrease in the R/V ratio (from 2.6 to 1.8) with increasing incidence angle. Guinness (1981) found that the color of the soil at the Viking Lander 1 site depends on phase angle, but since phase variations in the mosaic used here are less than 5° , the overall R/V gradient cannot be explained by phase-dependent color variations. Dust scattering

in the atmosphere contributes to the overall R/V gradient (from top to bottom) in Figure 3.13, as indicated by the shadow data described in the Appendix. As demonstrated below, the appearance of topographic features in Figure 3.13 is also due to atmospheric scattering.

The mountains at right center and sun-facing scarps in Figure 3.13 are more red on their northern (sunward) slopes. This phenomenon is due to the contribution to illumination of the surface by diffuse, relatively "bluer" atmospheric scattering. As shown in Appendix B, the R/V ratio of atmospheric scattering in shadows is about 2.0, while the surface R/V ratio is close to 3.0. Increased direct solar reflection on sunward-facing slopes increases the R/V ratio of the total reflected radiation relative to adjacent level areas, where reflected diffuse atmospheric illumination is a larger fraction of the total. The variation in R/V with incidence angle is no longer evident when the effects of atmospheric scattering are removed. An area near the top of the mosaic (at about 68° incidence angle) was corrected for atmospheric effects using the model described in Appendix B. Dark material in topographic depressions in this area has $R/V = 1.7$ to 2.1, similar to dark material (unit 5) at higher incidence angles. The plains in the low incidence region have R/V ratios between 3.0 and 3.5, similar to the plains at the top of Figure 3.15 at about 77° incidence angle. Occasional bright areas at low incidence have $R/V = 3.6$, comparable to the dust in the layered terrain (unit 2).

Examination of the R/V mosaics (see Figure 3.15) shows no detectable

color change between the layered deposits and the surrounding unfrosted terrain. In particular, the boundary of the layered deposits cannot be seen at the left and right sides of Figure 3.15. This lack of contrast indicates that the surfaces of the layered deposits and the surrounding terrains are composed of the same material, or that there is a dust mantle covering the entire area. As discussed below, there is morphological evidence suggesting that a dust mantle has been stripped away in some places.

The R/V ratio of unit 2 varies from 3.3 to 3.8 where the noise level in the mosaic is low. Darker, more neutral ($R/V \approx 2.9$) areas of unit 3 occur throughout the layered deposits, and in many cases appear to be associated with eolian erosional features. Unit 3 cannot simply be an exhumed flat-lying dark layer, because significant relief can be seen within a large area of the unit near $89.5^{\circ}\text{S}, 200^{\circ}\text{W}$ (Figures 3.16 and 3.18). Although this unit may represent a mantling of darker, more neutral material, I consider it more likely that this area has been stripped of its dust mantle by winds blowing off the polar cap. In Figure 3.16, linear grooves can be seen cutting across complexly terraced landforms, suggesting extensive wind erosion (Cutts, 1973a). These grooves are parallel to the elongate areas of unit 3 below the polar cap (in Figure 3.17), but are mostly coated by the dust mantle (unit 2). Evidently the cutting of the grooves was followed by deposition of the dust mantle, which has been partially removed elsewhere by further eolian activity. A layer of dust only about 10μ thick should be sufficient to conceal the underlying

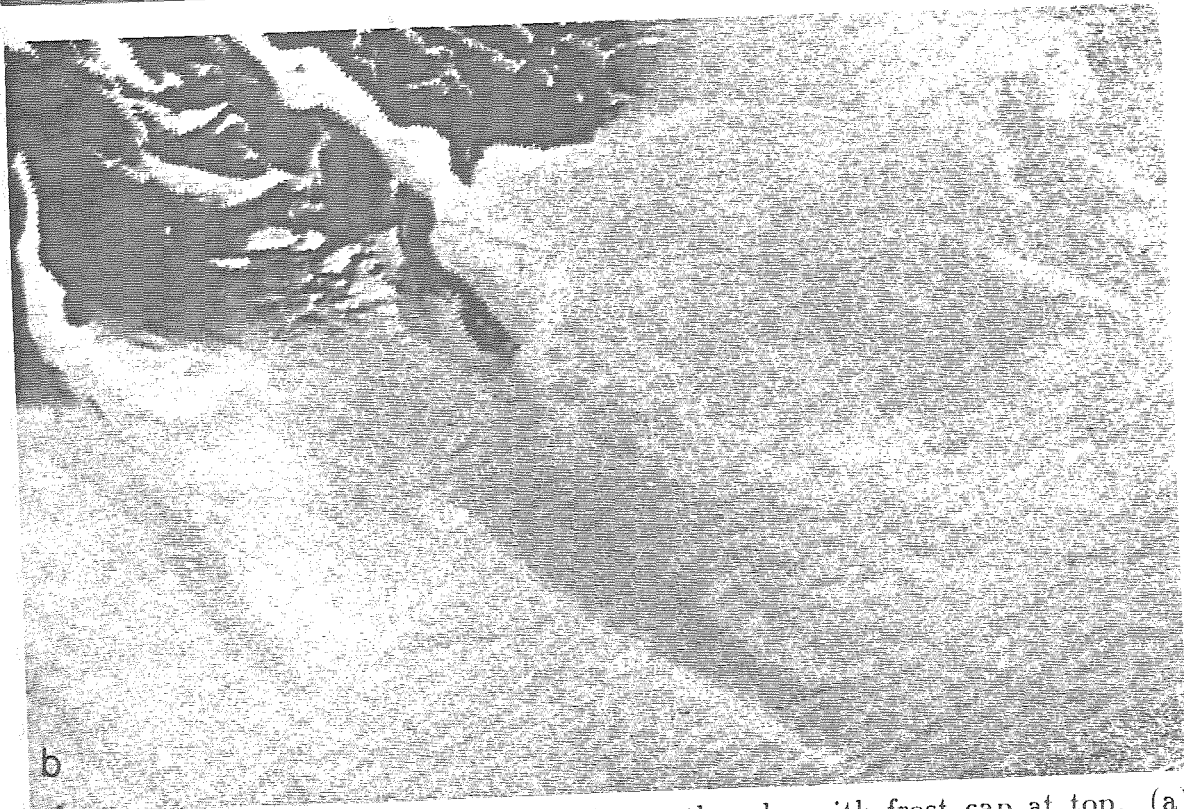
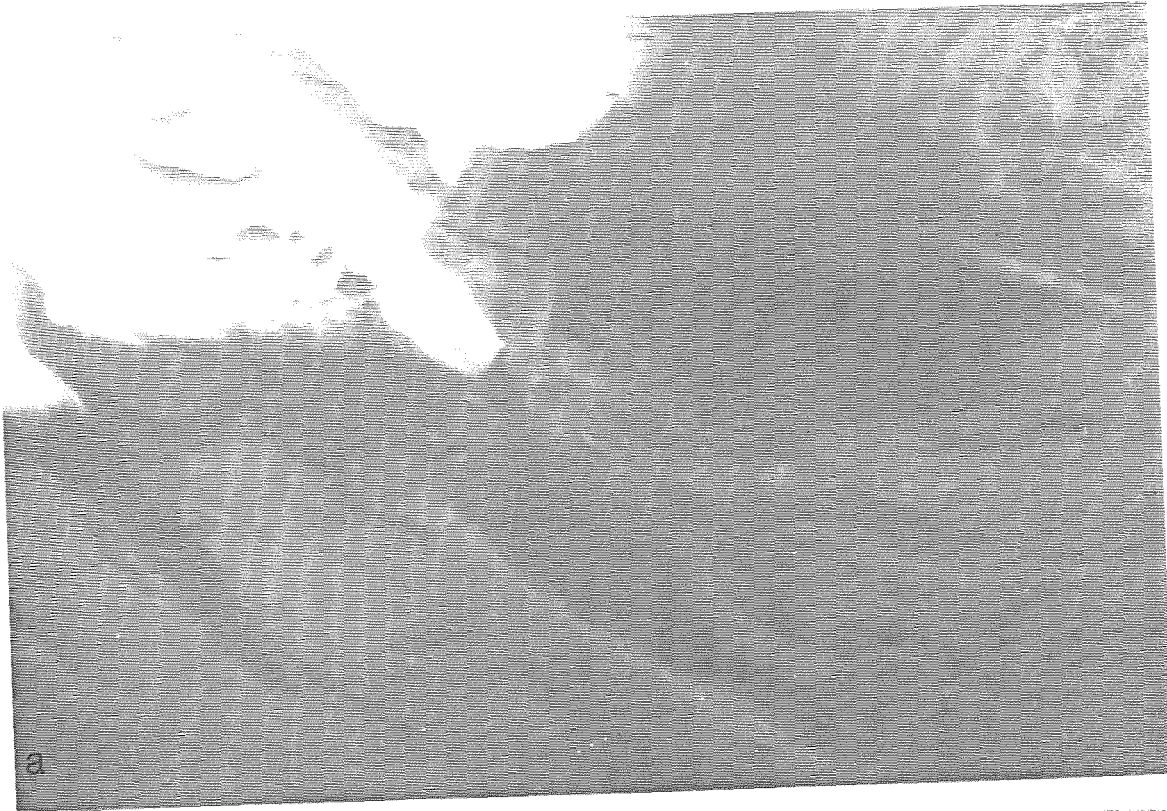


Figure 3.18: Detail of the vicinity of the south pole, with frost cap at top. (a) Portion of red mosaic showing elongate areas of lower albedo (unit 3). (b) Portion of red/violet ratio mosaic showing that darker areas (unit 3) are also less red.

bedrock. I conclude that unit 3 represents exposures of layered deposit "bedrock" that are darker and less red than the dust mantle that covers much of the area. The R/V of unit 3 is the same as that of the north polar layered deposits, as reported by Thomas and Weitz (1989).

The occurrence of bright, less red areas (unit 4) adjacent to the polar frost cap (unit 1) suggests that these areas are mixtures of frost and red dust (unit 2) below the resolution of the images. Mariner 9 returned the first high-resolution pictures of the south polar region, showing incomplete frost cover within the residual cap at a variety of spatial scales (Murray *et al.*, 1972). Although variegation in the frost cap is also evident in the mosaics used here, the details of the frost distribution are not indicated in Figure 3.17 for simplicity. Violet Lambert albedo is plotted against the R/V ratio in Figure 3.19, where atmospheric scattering has been removed. The data are fit well by a model that assumes linear mixing of two color components below the image resolution: $R/V = A_1 + A_2/V$, where A_1 and A_2 are constants dependent upon the color and albedo of pure frost (unit 1) and pure dust (unit 2), and R and V are the red and violet Lambert albedos, respectively. This model calculates the consequence of a macroscopic dust/frost "checkerboard" with possible length scales from millimeters to 100 meters (the resolution of the best images). A least squares fit of the data in Figure 3.19 gives $A_1 = 1.0$ and $A_2 = 0.11$, comparable to the values given by James *et al.* (1979) for mixtures of seasonal frost and bare ground: $A_1 = 1.257$; $A_2 = 0.105$. The residual cap has an

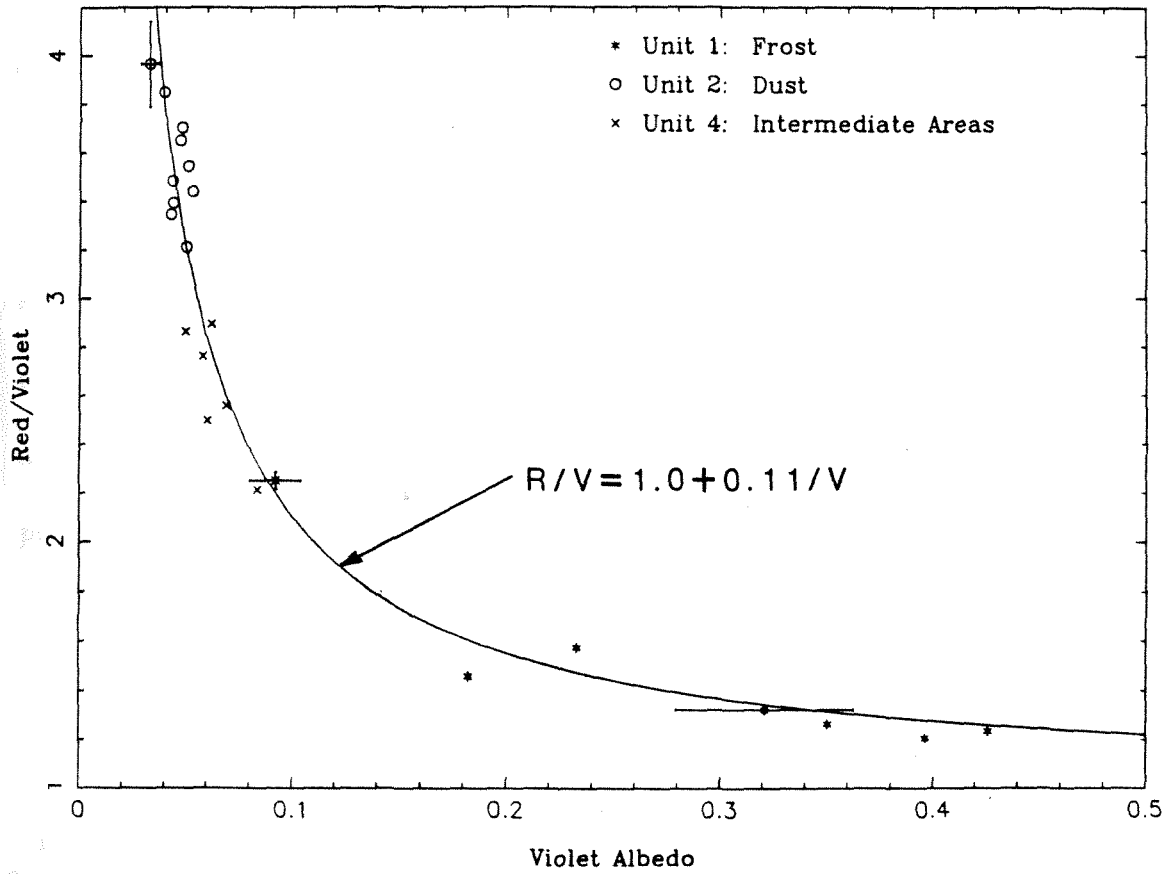


Figure 3.19: Red/violet ratio vs. violet Lambert albedo for representative points in 3 surface units near the south polar residual cap. Error bars represent 13% absolute uncertainty in albedos, sampling noise in 5×5 pixel areas in R/V mosaic.

R/V ratio of about 1.2, similar to the R/V of 1.25 found by James *et al.* (1979). Evidently the frost in unit 4 is less red than the seasonal frost observed during the spring, resulting in a decrease in A_1 with time. This is consistent with the temporal brightening of the south polar seasonal cap (Kieffer, 1979; Paige, 1985) due to dust removal or sinking of dust grains into the frost.

Unit 4 appears to be the surface expression of a deposit that is younger than the surrounding layered terrain: secondary craters from a 17 km impact crater at 84.5°S, 359°W (Plaut *et al.*, 1988) are present in the layered terrain, but “are either much rarer or more muted” (Howard *et al.*, 1982b) in the area of unit 4 at 84.8°S, 356°W. This unit has apparently been deposited since the impact that produced the secondary craters (Howard *et al.*, 1982b). Perhaps the persistence of seasonal frost in this area late into the summer (due to a regional poleward slope or to small topographic depressions) allows entrained dust to remain throughout the year, rather than being removed by winds. The net annual accumulation of small amounts of dust trapped in this manner might produce the observed young deposit if continued for many seasonal cycles. The thickness of dust and/or frost needed to produce the observed burial of the ≤ 2 km diameter secondary craters is at most a few hundred meters, assuming depth/diameter ≈ 0.2 (Pike, 1979).

A large area of similar brightness and R/V ratio (not mapped in Figure 3.17) appears around 83°S between roughly 0 and 30°W. This bright area is commonly occupied by an outlier of seasonal frost early in the southern summer,

and was interpreted by James *et al.* (1979) to be "due to dust entrained during the condensation process." Although dust deposits are probably stabilized by surface volatiles, the color and albedo of this unit indicates that the presence of frost below the limit of resolution is responsible for its high albedo. This area may also be a site of recent deposition.

Unit 5 is the darkest and most neutral in color of the units found in the south layered deposits. It is found only in what appear to be topographic lows, suggesting that it may be composed of sand-sized particles caught in saltation traps. Material of the same color ($R/V \approx 1.9$) is found in craters and other depressions in the upper part of Figure 3.12, indicating that it is widespread and has therefore probably been transported by winds. Thomas and Weitz (1989) found a similar R/V ratio for the north polar erg. The presence of dark material (unit 5) at the downwind ends of some exposures of unit 3 (Figure 3.17) suggests that saltation aids in the removal of the dust mantle.

The source of the dark material (unit 5) is not evident in the data used here. If the source of the dark material is not the layered deposits, it must have been transported into the layered terrain from more equatorial areas by saltation or suspension. The current Martian atmosphere cannot support grains larger than about 50μ in suspension (Arvidson, 1972), and extensive transport and deposition of dust from suspension is unlikely for particles larger than about 10μ . Alternatively, the dark material may be composed of fluffy particles (Saunders *et al.*, 1985;

1986), but such particles still must have saltated to become trapped in topographic depressions if they were deposited initially from suspension. Saltating grains would be expected to erode any dust mantle, so that transport of the dark material into the layered terrains could not have occurred since the deposition of the dust mantle. If the dark material was deposited before the dust mantle, it would not be apparent today unless the dust was able to trickle down into the open spaces between particles or was injected into suspension by local saltation of the larger particles. Mineral grains about 100μ in size are the most easily saltated under current Martian atmospheric conditions, while 10μ particles require about twice the wind velocity to initiate saltation (Greeley *et al.*, 1980). The dust particles are probably less than 10μ in diameter, so that if the dark material consists of $\sim 100\mu$ particles, they may have been cleaned of dust by local saltation. Therefore, unit 5 could have been transported from a source outside the layered terrain and deposited before the dust mantle.

Conversely, the source of unit 5 may be local but not obvious in the images used here. The genetic relationships between scarps and dune fields can be inferred from high resolution Viking north polar images (Thomas and Weitz, 1989), but are not resolved in the lower resolution south polar data used here. The hypothesis that the dark material is eroded from the layered deposits (Thomas and Weitz, 1989) is supported by the color and albedo of units 2, 3 and 5 (Figure 3.20). The color/albedo of the layered deposits (unit 3) is intermediate between that of

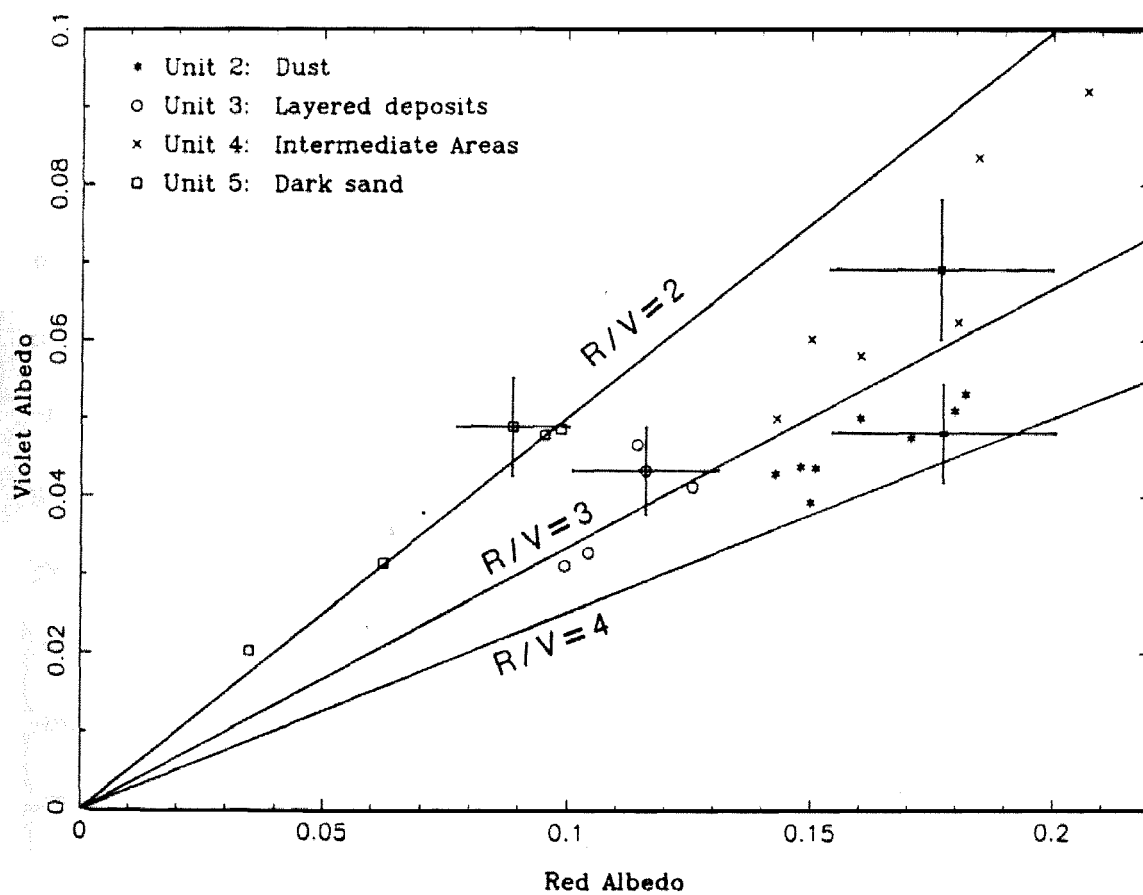


Figure 3.20: Violet vs. red Lambert albedo for 3 surface units in the vicinity of the south polar residual cap. Error bars represent 13% uncertainty in absolute albedos, sampling noise in 5×5 pixel areas in R/V mosaic.

dust (unit 2) and the dark material (unit 5), consistent with their being a mixture of dust and dark material. The dark material therefore may have originated locally within the layered deposits.

3.2.3 Discussion

Before discussing the implications of these results in conjunction with previous work, the inherent assumptions in this analysis must be stated. The lateral extent and constant thickness of individual layers suggests that the layered deposits were formed by eolian deposition; only such processes are considered. Despite the significant differences in the size, appearance and setting of the north and south layered deposits, I assume that their origin and evolution were similar. The current contrast may be due to the north/south asymmetries in Martian topography and climate (Mars' orbital eccentricity is higher than average now). The variable climate presumably controls the relative and overall effects of the depositional and erosional processes common to both hemispheres. I accept the "conventional wisdom" that water ice plays an important role in the formation of the layered deposits, and assume that solid H₂O cements the darker (presumably silicate) particles together. Finally, the possibility that periodic volcanic eruptions have caused most of the layering is excluded, although this mechanism cannot be ruled out completely (see next section).

If the south polar layered deposits are composed only of bright red dust

and ice, their color and albedo suggest that ice is not abundant at the surface, since the layered deposits are darker than the dust that mantles them. However, Clark and Lucey (1984) have shown that there is very little change in visual reflectance of soil and ice mixtures with increasing soil content for soil fractions above $\sim 1\%$ by weight. It is not clear from their data what effect (if any) adding small amounts of ice to the soil has on the visual reflectance of the mixture. A little ice could even make the soil appear darker, as it did in their experiments with bright kaolinite. Clearly, the albedo of the layered deposits is not a reliable measure of their ice content.

In any case, calculations of the stability of water ice in the polar regions of Mars (Toon *et al.*, 1980; Hofstadter and Murray, 1989) indicate that water ice should not currently be present at the surface of the layered deposits. This implies that the observed color/albedo of the layered deposits must be due to non-volatile components.

Four hypotheses for the composition of the layered deposits are now considered, all presuming that water ice is the cementing material but does not affect the observed reflectance. The widely held notion that the layered deposits are composed of only dust and ice is discussed, along with some alternatives for the source of the dark saltating material. I then discuss the possibility of only dark sand and ice in the layered deposits, and finally consider a mixture of dust and dark sand.

Dust Only

The first possibility considered here is that the dark, saltating material (unit 5) is a sublimation product of the layered deposits, which are composed only of bright dust and ice. This hypothesis was proposed by Saunders *et al.* (1985), who invoked dark carbonaceous meteoritic dust (which is probably unstable under oxidizing Martian surface conditions) to coat and darken the saltating filamentary sublimation residue (FSR) particles derived from erosion of the layered deposits. Their mechanism cannot explain the presence of dark material near its source, however, as saltation across an area with dark dust at the surface is required. The FSR particles have roughly the same albedo as the dust from which they are made, although neither the reflectance properties of the FSR nor the dust that was used to make them were measured quantitatively (A. Storrs, personal communication, 1989). Thomas and Weitz (1989) showed that dark material is present very near to its apparent source in the north polar layered deposits, implying that the dark material is already dark upon erosion. Although the FSR may be somewhat darker than the dust from which it forms, it is unlikely that this process can produce particles that are at least 3 times darker in red light than the dust mantle (Table 3.2).

Formation of the dark dunes from erosion of layered deposits composed only of dust and ice by this mechanism is therefore implausible unless there is a second, darker type of dust in the layered deposits as well. A (possibly minor) dark component of dust could preferentially form FSR and therefore dark saltating mate-

rial, leaving the bright dust to be injected into suspension and removed. Pollack *et al.* (1977; 1979) found that the Viking lander sky brightness measurements are consistent with the existence of $\sim 1\%$ magnetite ($\text{Fe}^{2+}\text{Fe}^{3+}\text{O}_4$) in the atmospheric dust. Hargraves *et al.* (1979) noted that the reference test chart magnet on Viking Lander 1 continued to attract magnetic particles from the atmosphere during the extended mission, and suggest that maghemite ($\gamma - \text{Fe}_2^{+3}\text{O}_3$) is the most likely candidate for the magnetic material. They conclude that "the results of Pollack *et al.* (1977) may not be inconsistent with the presence of a slightly ferroan maghemite" in the Martian atmosphere. About 1-7% of the soil at the Viking lander sites is magnetic (Hargraves *et al.*, 1979), suggesting that more dark (dense) magnetic material may be carried in suspension during epochs of greater atmospheric pressure. If magnetite notes are transported by suspension into the polar regions, incorporated into the layered deposits and eventually eroded, it may form FSR particles either alone or mixed with phyllosilicate dust, perhaps aided by its magnetic properties (A. Storrs, personal communication, 1989). Such dark particles may then saltate to form the dunes that probably represent 1-10% of the eroded volume of the layered deposits (Thomas, 1982). An attempt to form FSR from magnetite or maghemite dust has not been made (E. Laue, personal communication, 1989), but if FSR can be formed using these minerals, it would probably be dark. Hence, erosion of magnetite or maghemite particles in the layered deposits could conceivably account for the dark dunes described by Thomas and Weitz (1989), and the albedo of unit 3 (interme-

diate between dust and dark material; Figure 3.20) may be due to a concentration of dark material at the weathered surface of the deposits.

Storrs *et al.* (1988) argue that "the low thermal conductivity of the FSR seems inconsistent with the thermal inertia" of the polar dunes, which is no greater than $6.5 \times 10^{-3} \text{ cal cm}^{-1} \text{ sec}^{-1/2} \text{ K}^{-1}$ (Paige and Kieffer, 1987). Using the density and thermal conductivity of montmorillonite FSR given by Storrs *et al.* (1988) and the mean specific heat of various silicates ($0.14 \text{ cal gm}^{-1} \text{ K}^{-1}$ at 220 K) given by Winter and Saari (1969), a thermal inertia of 2×10^{-3} is indicated for the FSR. The presence of the Martian atmosphere and even small amounts of water ice will tend to increase the thermal conductivity of the FSR. Given that Paige and Kieffer (1987) regard their thermal inertia of the polar dunes as an upper limit, and that the thermal conductivity of the FSR in a good vacuum (A. Storrs, personal communication, 1989) is greater than the thermal conductivities at low ambient pressure of a wide range of rock powders and sands measured by Wechsler and Glaser (1965), I do not feel that the thermal conductivity of the FSR and the thermal inertia of the polar dunes are necessarily inconsistent. Therefore, the possibility of the polar dunes being composed of FSR particles cannot be excluded on the basis of thermal inertia data.

Sand from External Sources

The source of the dark material may not be the layered deposits, however. It is possible that dark sand partially or completely covers the layered deposits periodically, and is removed when the polar wind patterns change. The main problem with this hypothesis is that dark dunes appear to have sources in the north polar layered deposits (Thomas, 1982; Thomas and Weitz, 1989). In addition, this concept does not reconcile the difference between the albedos of the dust mantle (unit 2) and the layered deposits (unit 3). The Mars Observer camera may be able to obtain images that will allow detailed study of the scarps in the layered deposits and their relationships to the adjacent dune fields. Since the available images indicate that dark material is being eroded from the north polar deposits and forming dunes (Thomas, 1982), hypotheses that are consistent with the layered deposits being the source of the dark saltating material are preferred.

Sand Only

Could the layered deposits be composed of dark sand and ice only? As stated above, large amounts of ice are not expected to be present at the surface of the layered deposits, so that their albedo must be due to non-volatile material. Because the layered deposits appear brighter than the dark dunes in both polar regions, it is unlikely that the layered deposits are composed only of dark material and ice.

Dust and Sand Mixture

Perhaps the layered deposits are made up of a mixture of dust, dark sand, and ice. The question then is, how could sand become incorporated into the layered deposits? Thomas and Weitz (1989) conclude that only small amounts of sand in the north polar deposits are required to produce the observed dunes. I agree with their assertion that it is unlikely that sand could be carried in suspension, even by a much denser Martian atmosphere, and that sand must therefore be transported to the polar regions by saltation. The problem is how to deposit dust and sand simultaneously, as saltating sand will inject dust into suspension, carrying it away from the surface. Perhaps the dust is codeposited with water ice and effectively cemented to the surface by solid H_2O . Then sand could saltate over the polar cap, becoming trapped in topographic depressions. The entire layered deposits may have been covered periodically by a thin sand sheet, but laterally continuous saltating sheets of such constant thickness are not found on Earth, and are probably also unlikely on Mars. It is more likely that if sand is present within the layered deposits, it is in patches a few meters in size at most, and is therefore undetectable in even the best Viking images. Such a mixture can account for the color and albedo of the layered deposits (unit 3) with respect to the dust mantle (unit 2) and the dark material (unit 5).

3.2.4 Summary of Color and Albedo Results

Five albedo/color units have been identified and mapped in the south polar layered deposits, including polar frost. Much of the south polar region appears to be mantled by material (probably dust) with R/V ratios between 3.2 and 3.8. Eolian erosion of linear grooves near the south pole was followed by deposition of the dust mantle. This mantle has been removed (presumably by off-cap winds) from certain areas in the layered deposits, exposing slightly darker, less red "bedrock." Measured layered deposit colors and albedos lie between those of the dark material and the dust mantle, consistent with the layered deposits being a mixture of dark material and bright dust.

A bright, neutral unit, adjacent to the polar cap, is a mixture of frost and bare ground below the resolution of the images. Frost/ground patchiness on a horizontal scale of less than about 100 meters is indicated in these areas. Thomas and Weitz (1989) found a similar unit in the north polar deposits. Patches of bright frost are apparently stable late into the summer, perhaps because they are partially shaded from the sun in topographic depressions. In at least one area this unit appears to be younger than the surrounding layered terrain, perhaps due to trapping of dust by seasonal frost. A large area of similar color and albedo just outside of the layered terrain, the site of an outlier of seasonal frost, may also be undergoing deposition. The Mars Observer camera should be used to attempt to resolve patches of frost and bare ground in these areas.

Darker, more neutral material is occasionally present in topographic depressions in the layered deposits and elsewhere in the south polar region. The source of this dark material is not evident in the data considered in this paper, but may be local. If the source is not local, the lack of dust mantling these dark deposits is paradoxical. A possible resolution of this paradox may be that the dark deposits are composed of larger ($\sim 100\mu$) particles that are more easily moved by winds than the micron-sized dust that forms the mantle (Iversen and White, 1982). In this case, local saltation of the dark material since the deposition of the dust mantle could allow the dust to settle between dark grains and out of view, or eject dust into suspension. Again, the Mars Observer camera should be used to obtain high resolution images of areas of dark material in the southern layered deposits and study them in detail. Such data may indicate the source of the dark material.

While much of the south polar layered deposits appear to have been at least partially eroded, deposition has occurred recently in some areas near the residual cap. The geologic history of the south polar layered deposits is therefore rather complex, with deposition occurring in areas where frost lingers late into the summer, and eolian erosion of the dust mantle in other areas. The map units defined here should be used in future mapping of the south polar layered deposits.

Under the assumptions that the layered deposits are eolian in origin and that the evolution of the north and south deposits are similar, I conclude that the layered deposits are probably composed of dust and ice, with small amounts of dark

dust or sand. In the case of dark sand, climatic changes seem necessary to provide a net poleward wind regime, enabling sand to saltate into the layered deposits. The implications of these hypotheses will be discussed in the next chapter.

3.3 High Resolution Topography and Albedo of the South Polar Layered Deposits

The objective of this investigation is to derive improved knowledge of the topography and albedo of the southern layered deposits. Such results can constrain hypotheses for the formation and evolution of the deposits. The analysis presented below combines stereophotogrammetry with two-image photoclinometry (McEwen, 1985) to find the slopes and albedos of exposures of layered deposits in the south polar region of Mars. This technique makes use of two images of the same area taken with differing solar illumination, while previous photoclinometric profiling in the north polar layered deposits used only one image at a time and assumed a constant surface albedo and a Minnaert photometric function (Howard *et al.*, 1982a). Hapke's (1984) photometric function is used here, and is recognized as the most physically realistic representation of surface reflectance (Veeverka *et al.*, 1986). Hapke's function is not easily applied to photoclinometry (McEwen, 1989). The method used here does not involve ratios of the photometric function, so that the surface roughness correction derived by Hapke (1984) may be included in the

photoclinometric solution for the first time.

Details of the technique will be presented in the next section, after a description of the processing steps required to calibrate the images, remove the effects of atmospheric dust scattering, and produce smooth profiles. Photoclinometric solutions are very sensitive to the assumed values of atmospheric brightness (Howard *et al.*, 1982a), so I have employed a multistream radiative transfer model to remove the effects of atmospheric dust scattering. Surface scattering parameters are chosen that produce overall topographic relief that is consistent with the stereogrammetric results described below. The results (discussed in section 3.3.2) indicate that the majority of the albedo variations in exposures of the south polar layered deposits are due to the presence of frost, and that slopes of at least 10 and perhaps as high as 20 degrees occur. Such steep slopes have not been reported before and imply that the material comprising the layered deposits is rather competent.

3.3.1 Data Processing and Modeling

The highest-resolution images of the south polar region so far available were taken by the Mariner 9 orbiter in 1971-72. Hundreds of Mariner 9 B (narrow-angle) camera pictures were examined and the best images of the layered deposits were selected. This subset of images was then searched for stereo coverage, with the additional requirement that the two solar azimuths in the stereo pair be as different as possible (the opposite of the usual requirement for stereo images). A

large difference in solar illumination between two images of the same area permits two-image photoclinometry to be applied (McEwen, 1985). Profiles that are nearly perpendicular to the solar azimuth in one image and more parallel in the other image are most desirable: in the former case the variations in reflectance along the profile are due mainly to albedo differences, while topographic modulation is more significant in the latter case. Finally, images that were acquired close in time are desirable because of changes in frost coverage in the polar regions.

Altogether, the above constraints are met by only a few Mariner 9 frames. The best single pair of Mariner 9 images of the south polar layered deposits that fulfills the above requirements is shown in Figures 3.21 and 3.22. Throughout this paper they will be identified by their picture numbers, 173B1 and 188B2. The first three digits in each identifier represent the Mariner 9 orbit number (or "rev"), and the last digit is the frame number in the orbital sequence. The images were taken about a week apart (February 8th and 15th, 1972) by the narrow angle (B) camera during late southern summer ($L_s = 342$ and 346), when the polar cap had reached its minimum size. An earlier image, 124B7, was used to confirm the stereophotogrammetric results reported below.

Bright residual (and perhaps some seasonal) frost covers much of the area in the images, and is interrupted by defrosted bands which have been previously shown to face toward the equator (Murray *et al.*, 1972; Dzurisin and Blasius, 1975). Layering is evident in these dark bands, especially in 188B2 (Figure 3.22). The



Figure 3.21: Mariner 9 south polar residual cap frame 173B1, corrected for atmospheric scattering. Profile 1 indicated by solid line across dark (unfrosted) band, with directions toward sun and north pole indicated. Projected pixel size on the surface is ~ 112 m, so that features as small as ~ 250 m across can be resolved.

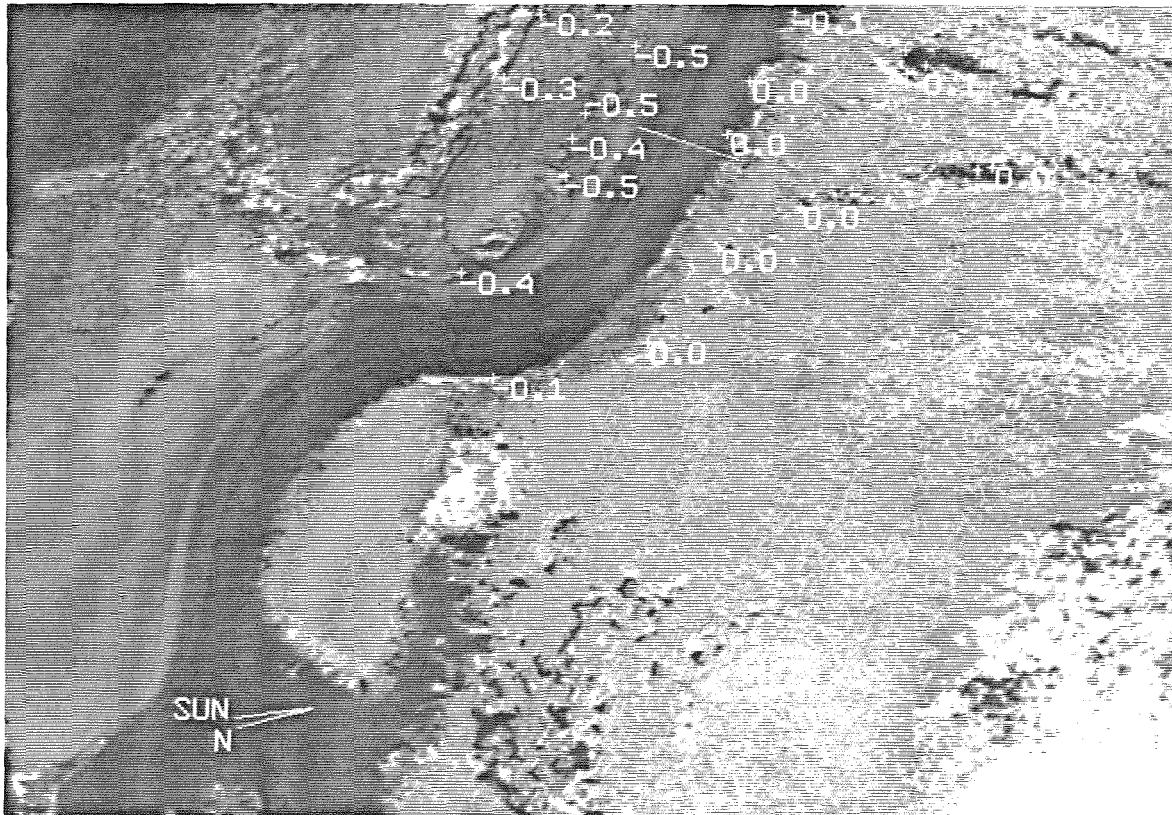


Figure 3.22: Mariner 9 south polar residual cap 188B2, corrected for atmospheric scattering. Profile 1 indicated by solid line across dark (unfrosted) band, with elevations of selected points relative to an arbitrary datum. Each + symbol marks location of stereophotogrammetric elevation measurement. Projected pixel size on the surface is ~ 96 m, so that features as small as ~ 200 m across can be resolved.

images were not geometrically transformed to remove camera distortions or projected in any way that would have involved resampling the data. Such resampling of the images could have resulted in the loss or distortion of detail near the limit of resolution.

The direction of solar illumination is different in the two images, as shown in Figures 3.21 and 3.22. The image in which the illumination is nearly parallel to the strike of the layers will be referred to as the "albedo" image, because the variations in reflectance between layers is mainly due to variations in surface albedo. Similarly, the image in which the illumination is nearly perpendicular to the strike of the layers will be referred to as the "topography" image, because in this case variations in slope have a dominant effect on the reflectance.

Radiometric Calibration

The Mariner 9 images were corrected for noise and artifacts, and each pixel was converted into light intensity values using the procedures described by Herkenhoff *et al.* (1988) and reproduced in Appendix A. Absolute calibration was achieved by comparing Mariner 9 and Viking Orbiter images of the same face of Phobos, assuming that the Viking calibration is correct. The absolute accuracy of the Mariner 9 calibration is therefore limited by the 13% (1σ) absolute accuracy of the Viking Orbiter cameras (Klaasen *et al.*, 1977). A full discussion of the absolute accuracy of spacecraft imaging is beyond the scope of this paper. A reasonable

estimate of the absolute accuracy of the Mariner 9 calibration by this method is about 20% RMS. Relative errors within each image and between images are about 8% (Herkenhoff *et al.*, 1988), and somewhat larger at low exposure levels. The effect of these uncertainties on the results will be discussed in section 3.3.2.

Stereophotogrammetry

The camera pointing information for each image was refined using PICS software (Edwards, 1987; Batson, 1987) and a controlled digital mosaic of the south polar region provided by the U. S. Geological Survey. The errors in correcting the camera angles were never greater than 4 pixels, corresponding to a latitude offset of less than 0.01 degree. The improved pointing information was then used in an interactive PICS stereophotogrammetry program to yield the elevations plotted in Figure 3.22. The vertical offset in the intersections of vectors calculated by the program is 120 m or less. This elevation uncertainty is comparable to the 122 m uncertainty estimated using equation 13 of Blasius (1973). The overall topography and relief across the defrosted band (Figure 3.22) are in good agreement with the results presented by Dzurisin and Blasius (1975), and indicate that the traces of layers in the dark band are essentially horizontal. The strike of the layers is therefore assumed to be parallel to the trace seen in the images, so that the surface dips perpendicular to the trace.

Stereogrammetry was also used to find the elevations at the endpoints of

two profiles. The total relief of each profile (500 ± 90 m for profile 1; 300 ± 160 m for profile 2) will be used to constrain photoclinometric solutions. Similar results are obtained from stereogrammetric analysis of another pair of images of the same area, 124B7 and 173B1.

Atmospheric Scattering Model

In order to deduce the true magnitude of surface reflectance modulations arising from surface albedo or slope variations, the intensity contribution from atmospheric scattering must be estimated and removed. Atmospheric opacity is most directly estimated using measurements of brightness in shadows (Herkenhoff and Murray, 1989; McEwen, 1985). No distinct shadows could be found in either of the images shown in Figures 3.21 or 3.22, so images taken on or near the same orbits were searched for shadows. Good shadows were found in high resolution images of the south polar region taken during revs 173 and 187, but not rev 188. The images were radiometrically calibrated, then 5×5 pixel areas were averaged within shadows and on nearby level areas at the same incidence (solar zenith) angle. The dust scattering model described by Herkenhoff and Murray (1989) was used to fit these data as shown in Figure 3.23. The single-scattering albedo of 0.81, Henyey-Greenstein asymmetry parameter of 0.48 and extinction efficiency of 2.72 used in the model were interpolated to the Mariner 9 B camera effective wavelength of 0.56μ from the results of models of Viking Orbiter color data (Herkenhoff and Murray, 1989).

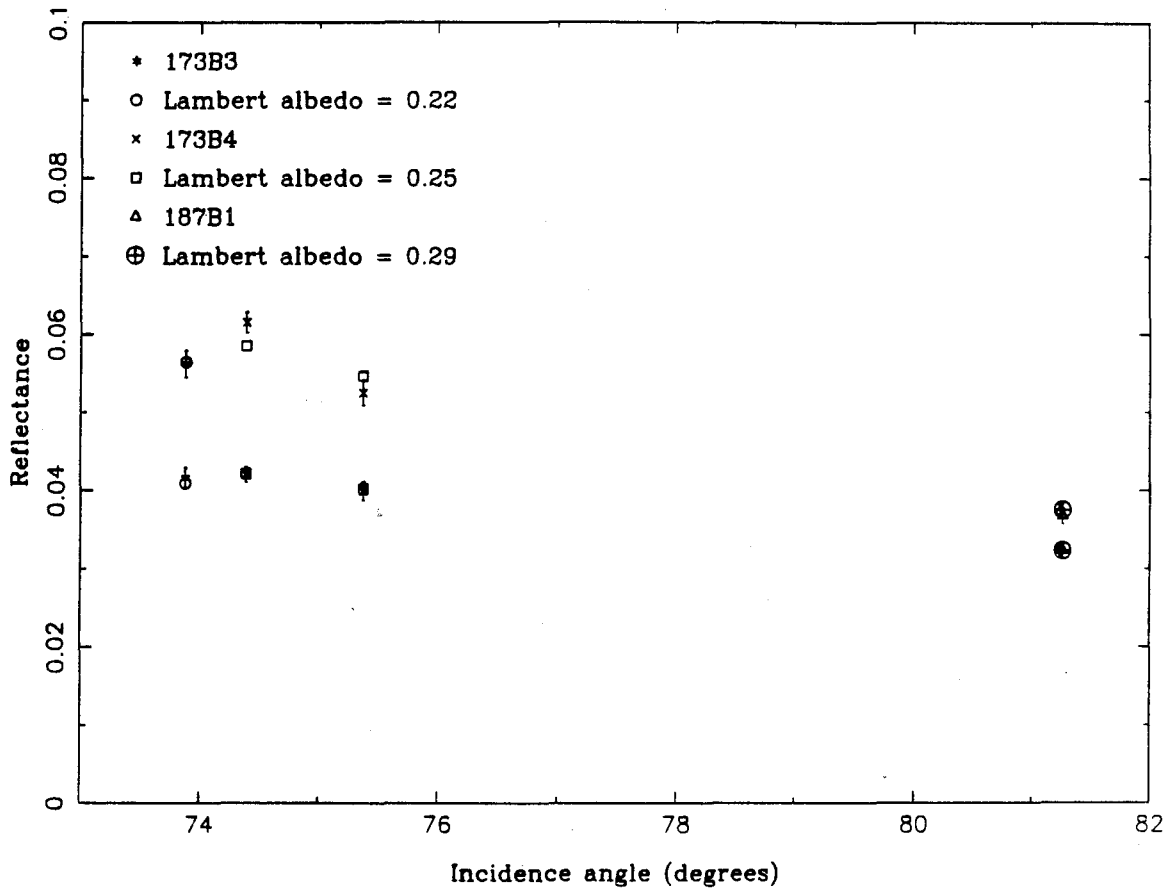


Figure 3.23: Shadow (lower points) and nearby level surface (upper points) reflectance data. Error bars represent standard deviation of values within 5×5 pixel areas. Model fits for optical depth = 0.30 indicated.

The assumption of Lambertian surface scattering in the atmospheric model is clearly not valid in general for the surface of Mars. However, this approximation is sufficient within a relatively confined region because the direct surface reflectance is generally a small fraction of the total observed flux at high incidence angles (Figure 3.23). Deviations from Lambertian behavior are most significant in the direct surface reflection, and are less important in the calculation of diffuse reflection. The total reflectance (upper points in Figure 3.23) is sensitive to changes in surface albedo, but insensitive to changes in optical depth. The Lambert albedos in Figure 3.23 were therefore found by fitting the total reflectance measurements, then the optical depth was varied to fit the shadow data. Although the dust opacity over the south polar region was gradually decreasing during the Mariner 9 primary mission (Pang and Hord, 1973), a constant opacity over this short time interval is plausible.

The dust concentration in the atmospheric model decays exponentially with a scale height of 10 km up to a maximum of 50 km, so that much of the total opacity is due to dust near the surface. Regional elevation differences will therefore affect the atmospheric opacity calculated by the model. The topography of south polar region is unknown except in the area of the residual cap (Dzurisin and Blasius, 1975). The areas modeled in Figure 3.23 are several hundred kilometers from the residual cap, near the edge of the layered deposits. The radio occultation and stereogrammetric data presented by Dzurisin and Blasius (1975) indicate that

the portion of the residual cap in Figure 3.22 is about 2 km higher than the areas modeled for atmospheric scattering. The vertical dust distribution was therefore modified to account for the greater surface elevation in images 173B1 and 188B2 by removing the bottom 2 km of dust from the model used to fit the shadow data. This effectively reduces the dust optical depth to 0.25.

In order to correct 173B1 and 188B2 for atmospheric effects, an average Lambert surface albedo must be chosen for use in the model. The width of the dark band of exposed layered terrain is less than an atmospheric scale height, so surface reflection from bright frost will be a significant component of the illumination of suspended dust particles. However, a surface albedo similar to those in Figure 3.23 is more appropriate for calculating the surface reflection of diffuse radiation from the atmosphere. It is therefore expected that a surface albedo greater than that of the dark ground and less than that of the bright frost will most accurately correct for atmospheric effects in the dark band. The Lambert albedo of the residual frost at the effective wavelength of the B camera is near 0.5 (Herkenhoff and Murray, 1989), so the proper surface albedo for atmospheric correction is estimated to be between 0.3 and 0.5 in this case. Surface albedos greater than 0.45 resulted in excessive subtraction of atmospheric scattering and surface reflectances of zero in some areas. Lambert albedos between 0.3 and 0.45 are therefore indicated for the atmospheric model. The method by which a surface albedo of 0.37 was chosen to correct for atmospheric effects will be described below. The atmospheric correction

Profile	Start		End	
1	-86.91	346.84	-87.00	348.38
2	-86.62	350.15	-86.58	352.18
3	-87.01	345.12	-87.06	346.23

Table 3.3: Latitudes and Longitudes of Profile Endpoints.

Image	Profile	Start			End		
		ι	ϵ	α	ι	ϵ	α
173B1	1	83.526	45.876	68.765	83.569	46.066	68.755
173B1	2	83.810	45.775	68.506	83.936	44.878	68.412
173B1	3	83.406	45.892	68.870	83.443	46.010	68.855
188B2	1	80.946	46.124	61.205	81.041	46.101	61.098
188B2	2	80.673	45.590	61.374	80.650	45.393	61.356
188B2	3	81.042	46.341	61.152	81.094	46.308	61.089

Table 3.4: Incidence, Emission and Phase Angles at Profile Endpoints.

using this value is only valid for the dark band, and frost cap reflectances are therefore overestimated.

Profiles

Profile endpoints were located using surface features that were visible in both images (173B1 and 188B2). The latitudes and longitudes of the endpoints in the two images (Table 3.3) were derived using the stereogrammetric software described above. Incidence, emission, and phase angles at each of the profile endpoints were then found using the corrected camera pointing information (Table 3.4). The errors in these angles are of the same order as the uncertainty in location of surface points, less than 0.01° .

It was necessary to include pixels adjacent to the line connecting profile

endpoints because of noise in the images because the layers are barely resolved. Pixel values within a given range of the profile center line were projected perpendicularly to the center line, under the assumption that layers are perpendicular to the profile. In some cases the profile was not exactly perpendicular to the strike of the layers, so that only pixels close to the profile could be projected. In Figure 3.21, profile 1 is perpendicular to the layers, but in Figure 3.22 the same profile appears inclined due to the oblique viewing geometry. The best estimates of surface reflectance, shown in Figure 3.24 were obtained with a 6 or 8 pixel range (3-4 pixels on either side of the center line). A few points in some of the profiles were clearly erroneous (usually bit errors) and were deleted. The edited data were then averaged in 2 pixel bins along the profile length, as plotted in Figure 3.24. Smaller bins were tested, but resulted in much rougher profiles and are not realistic given the modulation transfer function of the camera (Cutts, 1974). 2 pixel averages of data corrected for atmospheric effects were used in the photometric modeling described below.

Photometric Function

In order to derive slopes from the reflectance profiles, the scattering properties of the surface are modeled using Hapke's (1984) photometric function. Hapke's function is sufficiently complicated that it will not be reproduced here. Certain parameters in the function do not vary with position along the profiles and were set in advance of any modeling. The phase angles of the Mariner 9 observations

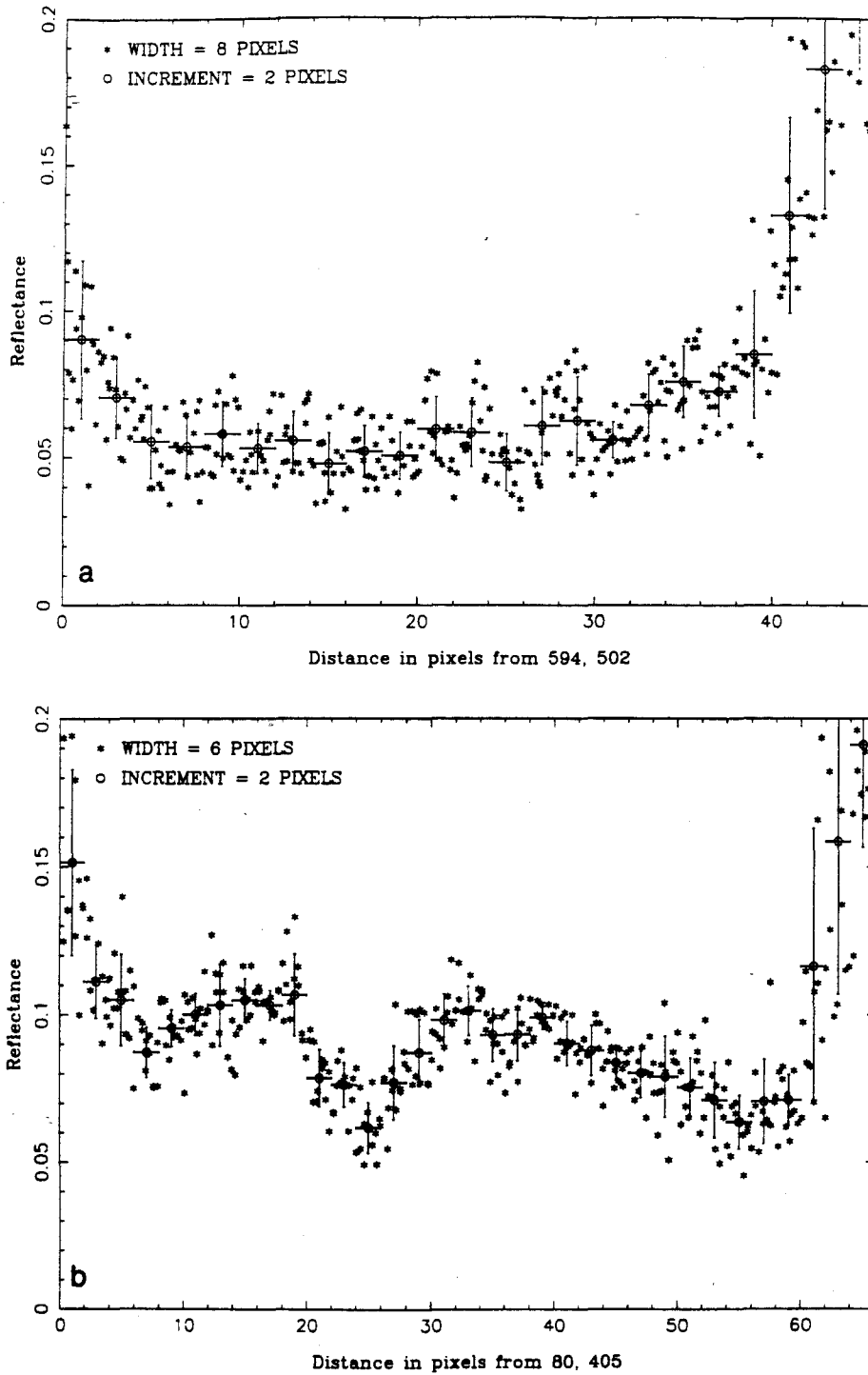


Figure 3.24: Profile 1 data with averages of 2-pixel increments. Vertical error bars indicate standard deviation of pixel values in each increment. Increased reflectance near profile endpoints is due to inclusion of residual frost. (a) 173B1 ("albedo" image) data from 8-pixel wide swath around profile. (b) 188B2 ("topography" image) data from 6-pixel wide swath around profile.

studied here are large enough that the backscatter function B can be neglected and the backscatter parameter h is set to zero.

Helfenstein (1988) noted that the Hapke function is inaccurate at high incidence angles for rough (mean macroscopic surface slope angle $\bar{\theta} > 10^\circ$) surfaces, so $\bar{\theta} = 5^\circ$ is used. The layered deposits appear smooth down to the limit of resolution in Viking and Mariner 9 images, so this choice of $\bar{\theta}$ is plausible. Using $\bar{\theta} = 0^\circ$ gives essentially the same numerical results as $\bar{\theta} = 5^\circ$. For comparison, Arvidson *et al.* (1989) found that $\bar{\theta} \approx 6^\circ$ in dust deposits at the Viking Lander 1 site. Multiple scattering between macroscopic facets on a rough surface is not considered in Hapke's function (Buratti and Veverka, 1985), but should not be significant in this case.

Thorpe (1982) fit Hapke's (1981; $\bar{\theta} = 0^\circ$) photometric function to Viking Orbiter observations of Mars at small phase angles through both red and violet filters. The parameters he reports provide reasonable limits for the single-scattering albedo w and phase coefficient b of particles on the surface of the layered deposits. Color and albedo mapping by Herkenhoff and Murray (1989) indicates that the surface of the layered deposits in 173B1 and 188B2 is mantled by bright, red dust. Assuming that this dust has roughly the same optical properties as the bright dust in Arabia or Chryse studied by Thorpe (1982) and Arvidson *et al.* (1989), it is expected that $0.5 \leq w \leq 0.8$ at the effective wavelength of the B camera. In any case, the single-scattering albedo of (non-volatile) surface particles probably does

not exceed 0.81, the albedo of the atmospheric dust particles.

The range of phase angles α in the images considered here is small enough (Table 3.4) that the simple phase function $P(\alpha) = 1 + b \cos \alpha$ is adequate. Thorpe (1982) fit low-phase observations using the same function, and gives values of b for various areas in both red and violet light. His results indicate that $0.2 \leq b \leq 0.5$ for bright areas at the effective wavelength of the B camera.

The minimum reflectances in all of the profiles within each image are roughly equal, suggesting that they represent level areas. Assuming this to be the case, the minimum values can be modeled using the parameters described above and the geometric information in Table 3.4. The values of w and b were varied within reasonable limits to fit the minimum reflectances in both images simultaneously, assuming in addition that the albedo of the surface did not change in the week between the two images. A good fit to the data could be made after correcting for atmospheric effects using surface Lambert albedos between 0.35 and 0.4. A surface albedo of 0.37 yields reflectances that are well fit by $b = 0.5$ and $w = 0.75$. Next, it will be shown how these values were chosen to produce topographic profiles that are in agreement with stereogrammetric data.

Photoclinometry

A FORTRAN program was developed that iteratively finds the slope of a surface element required to match (within 1% of the standard deviations shown in

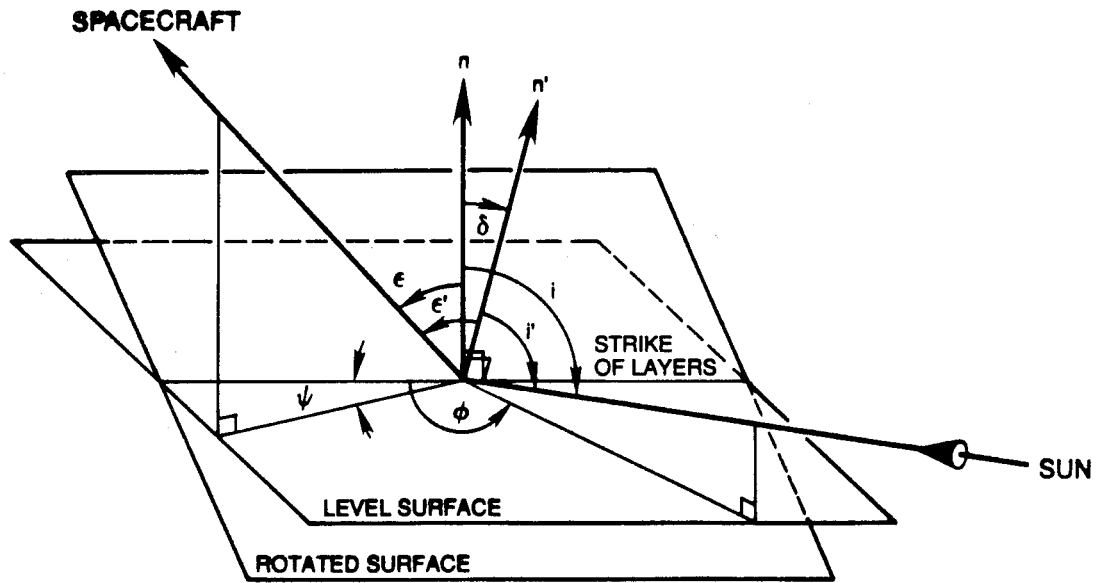


Figure 3.25: Diagram illustrating geometric relationships defined in the text. Level surface normal denoted n , rotated surface normal denoted n' .

Figure 3.24) each averaged reflectance datum using Hapke's photometric function. The incidence, emission and phase angles at each point in the profile are interpolated from the angles at the profile endpoints (Table 3.4). The surface element is rotated about the strike of the layers (see Figure 3.25) until the reflectance is fit to within the specified tolerance. The incidence ι' and emission ϵ' angles on the rotated element are related to the interpolated incidence ι and emission ϵ angles of a level surface at the same location by

$$\cos \iota' = \cos \iota \cos \delta + \sin \iota \sin \delta \sin \phi$$

$$\cos \epsilon' = \cos \epsilon \cos \delta + \sin \epsilon \sin \delta \sin \psi ,$$

where δ is the dip angle and ϕ and ψ are the angles between the strike of the layers and the azimuths of the sun and spacecraft, respectively:

$$\cos \phi = \frac{\cos \iota_1 - \cos \iota_2 \cos \gamma}{\sin \iota_2 \sin \gamma}$$

$$\cos \psi = \frac{\cos \epsilon_1 - \cos \epsilon_2 \cos \gamma}{\sin \epsilon_2 \sin \gamma} .$$

Here the subscripts refer to the starting and ending points of the profile, and γ is the planetocentric angular difference between the endpoints of the profile, defined by

$$\cos \gamma = \sin \lambda_1 \sin \lambda_2 + \cos \lambda_1 \cos \lambda_2 \cos(\beta_1 - \beta_2) ,$$

where λ is latitude and β is longitude of the endpoints, with the subscripts having the same meaning as above. The interpolated phase angle does not change as the surface element is rotated. The relationships between these angles are illustrated in Figure 3.25, and are similar to those presented by Howard *et al.* (1982a), with minor corrections. No correction is made for parallax offsets (Davis and Soderblom, 1984), as they should only be significant in profile 2 (discussed below).

It is first assumed that the single-scattering albedo of the surface particles is constant along the profiles, *i.e.*, the variations in reflectance along the profiles are due mainly to slopes. This is clearly not the case near the ends of the profiles where polar frost is included (see Figure 3.24a, where the solar illumination is nearly parallel to the strike), and erroneous results are expected in these areas. By ignoring the slopes derived near the ends of the profiles where frost is present, the

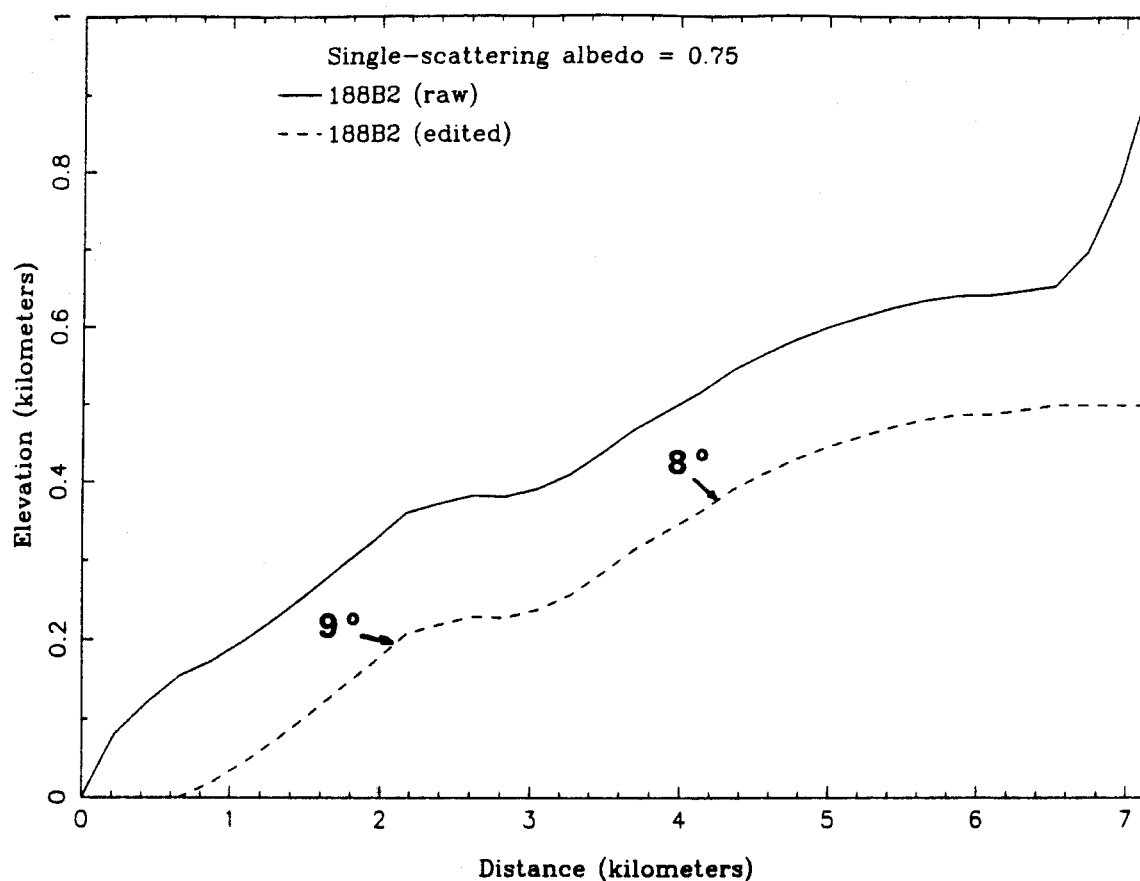


Figure 3.26: Constant- w model topography for profile 1 with $b = 0.5$. Dashed curve shows same profile with slopes set to zero in areas containing abundant frost. Vertical exaggeration $5.2\times$, maximum slopes indicated.

overall relief of the profiles found by photogrammetry can be compared with the relief found using stereogrammetry (Figure 3.26). Such a comparison for profile 1 in 188B2 indicates that $w = 0.75 \pm 0.02$ and $b = 0.5 \pm 0.1$, as other values yield either more or less than 500 ± 90 m of total relief. The single-scattering albedo w and phase coefficient b used in this model are consistent with the results of Thorpe (1982), and are applied to the other profiles in this study.

Figure 3.27 shows that the topographic profile derived from the reflectance

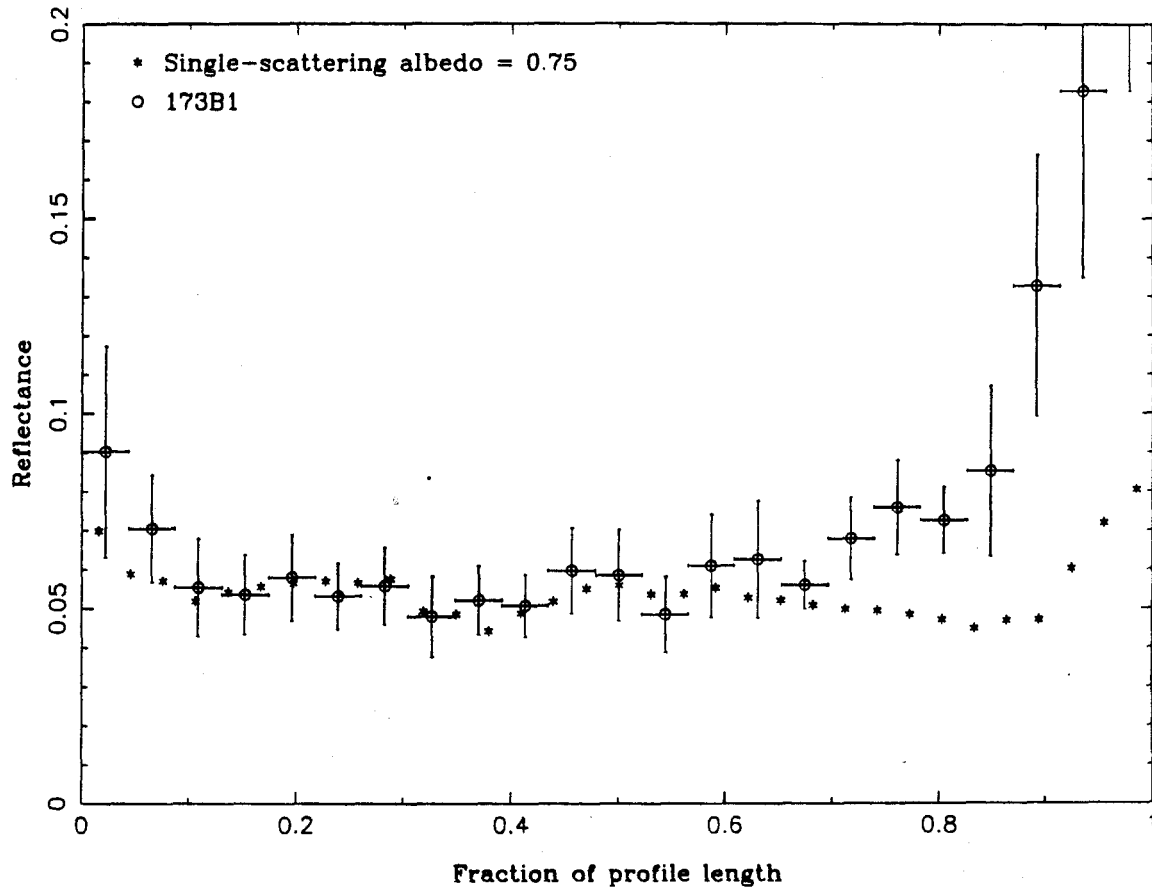


Figure 3.27: Comparison of reflectance predicted by model slopes with profile 1 data from "albedo" image.

variations in 188B2 is consistent with the 173B1 reflectance data within the standard deviations of the pixel values. The solar illumination in 173B1 is nearly parallel with the strike of the layers, so that surface albedo variations should dominate topographic modulation of the reflectance. The good agreement between the reflectance predicted by the model and the data (except near the endpoints) indicates that the assumption of constant single-scattering albedo is valid within the uncertainties in the data, and that temporal variations in frost cover are not significant along this profile. This result will be discussed further in the next section.

Alternatively, w may be allowed to vary with distance along the profile. In this case, an initial single scattering albedo is used to estimate the slope at each point in the topography image (188B2) as above except that the tolerance for model fitting is relaxed to 50% of the standard deviation of the reflectance data. The initial slopes are then interpolated to the points in the albedo image (173B1) and used to evaluate the model reflectance at each point. If the model reflectance does not agree with the actual reflectance within 50% of the standard deviation of the data, the single-scattering albedo is iteratively perturbed until the reflectances converge. These albedos are then used to revise the slopes at each point in the topography image as above by interpolating w at each point. The topographic profile found in this manner is then used to re-calculate w in the albedo image. The entire sequence is repeated until the solutions converge within the 0.5σ tolerance, typically within 3 iterations. In the discussion that follows, this model will be referred to as the

“general” model.

The resulting profile (Figure 3.28) has the same overall relief as the constant- w profile within the stereogrammetric uncertainty. Hence, slopes of up to 9° along this profile are consistent with the stereogrammetric data. Other combinations of Lambert surface albedo (in the atmospheric model), w and b can satisfy the stereogrammetric constraint only in the constant- w case, indicating that the parameters used here are most consistent with the data. These parameters were then used to model the slopes and albedo along two other profiles in this image pair (Figures 3.29-3.37).

3.3.2 Results and Discussion

A limited amount of regional topographic information is revealed by stereophotogrammetric analysis of the image pair shown in Figures 3.21 and 3.22. The elevation data in Figure 3.22 indicate that the areas covered by the residual frost cap are either level or slope gently toward the south pole. Such a poleward slope may be responsible for the offset of the residual cap from the geometric pole, as suggested by Dzurisin and Blasius (1975). The maximum slopes of $2.5^\circ \pm 1.5^\circ$ occur in the upper leftmost area of stereo coverage in Figure 3.22. Similar poleward-facing slopes were found in the north polar layered deposits by Blasius *et al.* (1982).

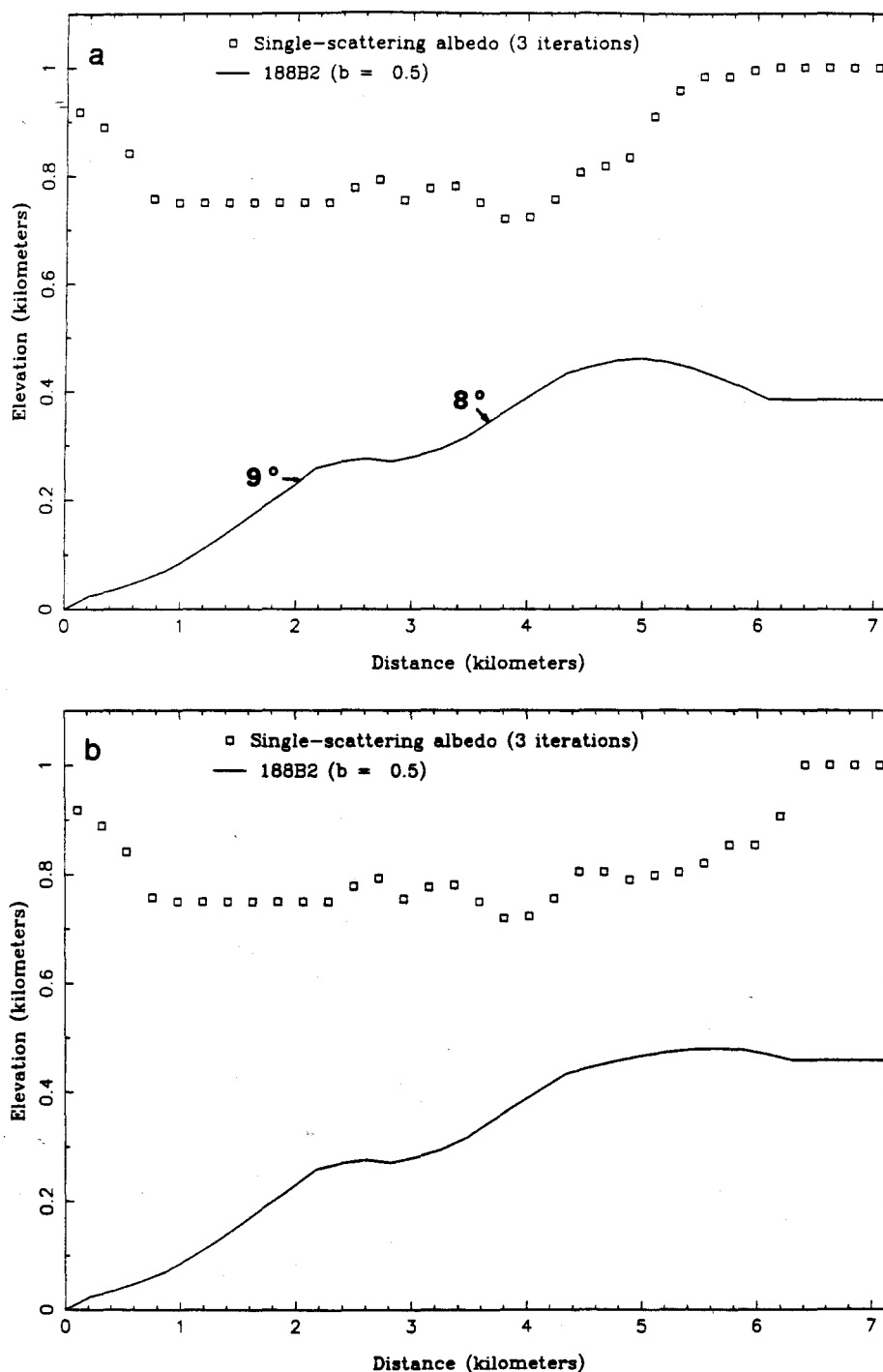


Figure 3.28: Profile 1 topography and albedo from iterative model. Albedos of 1.0 in bright areas due to use of atmospheric model appropriate only for dark surface, not included in solution. Vertical exaggeration $4.7\times$, maximum slopes indicated. (a) Negative slope 5-6 km from starting point due to change in albedo between images. (b) Results for modified "albedo" image data, as described in the text.

Profile 1

Comparison of the profiles in Figure 3.24 indicates that there is some correlation between features in the two images. The prominent dip in reflectance ~ 25 pixels from the start of the profile in 188B2 is much more subdued in 173B1, while the smaller dip ~ 36 pixels from the starting point in 188B2 is quite obvious 25 pixels from the starting point in 173B1. Because the layers in 173B1 are illuminated nearly parallel to their strike, topographic variations will have a small effect on the reflectance compared to albedo variations. This suggests that at least some of the reflectance differences in 173B1 are due to albedo variations.

However, the profile 1 data are consistent with a constant single-scattering albedo of 0.75, as shown in Figures 3.26 and 3.27. The discrepancy between the model and the data in the last (far right) 0.3 of the profile in Figure 3.27 is probably due to the presence of seasonal frost during rev 173 that sublimed away by rev 188. This hypothesis was tested by setting the 173B1 reflectance data in this area to the value at 0.67 of the profile length and re-calculating the slopes using the general model. As shown in Figure 3.28, the raw data predict a negative (poleward) slope in this area, while the edited data yield a more realistic (nearly zero) slope. This illustrates a danger in assuming temporally invariant surface albedos in two-image photogrammetry in the polar regions. The analysis of profile 2, discussed below, further clarifies this problem.

In any case, the results shown in Figure 3.28 suggest that albedo and

slope are inversely correlated. The reflectance dip described above is well modeled by a slightly lower albedo on a 8° slope 4 km from the starting point, while level areas tend to have higher albedos. Both models resolve 2 layers, each between 200 and 300 m thick. The total range of albedo variation in the central section of profile 1 (where not contaminated by the frost cap) is only 12%, less than the noise level in the albedo image. Another profile was therefore analyzed in the same area (Figure 3.29) to determine if albedo variations are significant, and will be discussed later. First, however, the results of analysis of a profile in a different area will be introduced.

Profile 2

Profile 2 is located in a unique, slightly poleward-facing exposure of layered deposits (Figure 3.29). The profile is nearly perpendicular to the solar azimuth in 188B2, so that I shall refer to 188B2 as the albedo image in this case. The topography image (173B1) profile (Figure 3.30a) has the same general shape as that in Figure 3.24b, except that the reflectances 19 pixels from the starting point are much greater than the minimum values around 43 pixels from the start. The albedo profile (Figure 3.30b) is not as constant as in Figure 3.24a, with a marked increase in reflectance near the middle of the profile. This suggests that the albedo variations in profile 2 are much greater than those in profile 1.

As expected, the constant- w model does not yield reasonable slopes, as

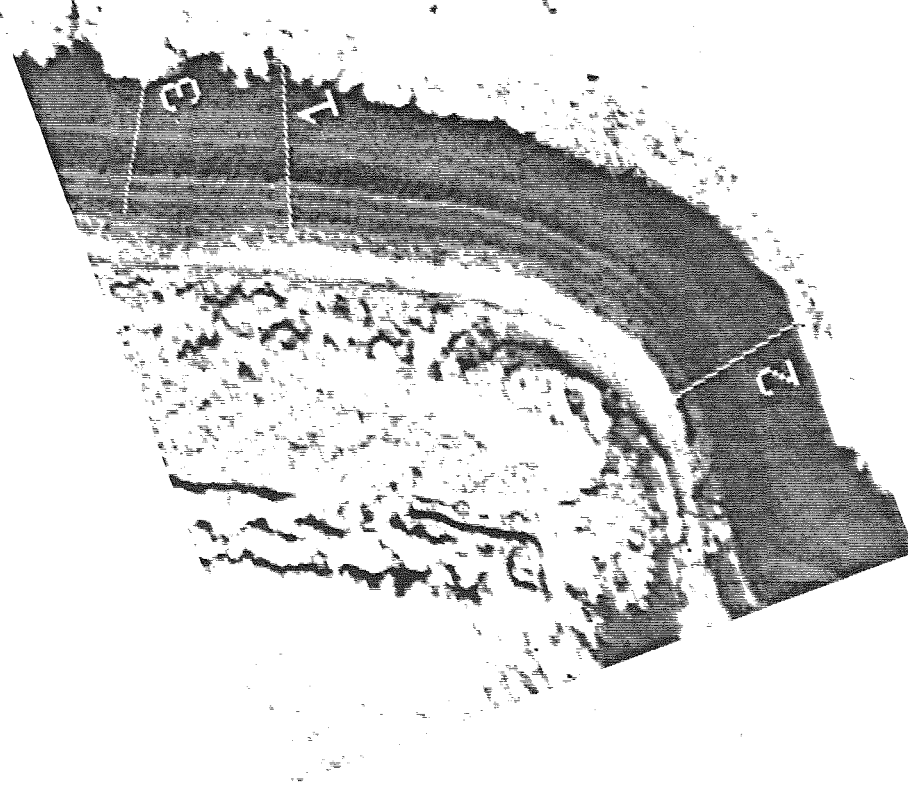
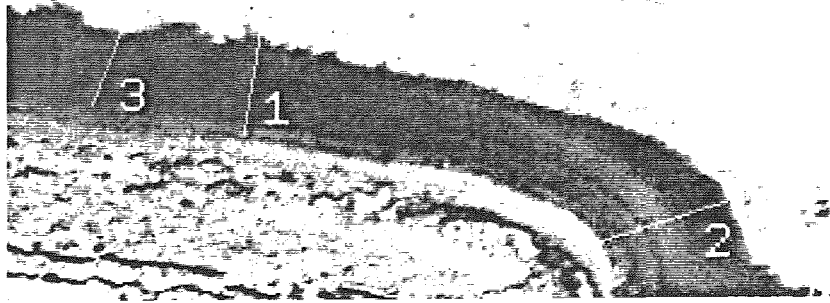


Figure 3.29: Portions of images corrected for atmospheric scattering effects, contrast enhanced to display reflectance variations in dark bands: black corresponds to 0.03, white to 0.16. Profiles appear to be inclined to layers by different amounts in each image due to oblique viewing. (a) 173B1. (b) 188B2.

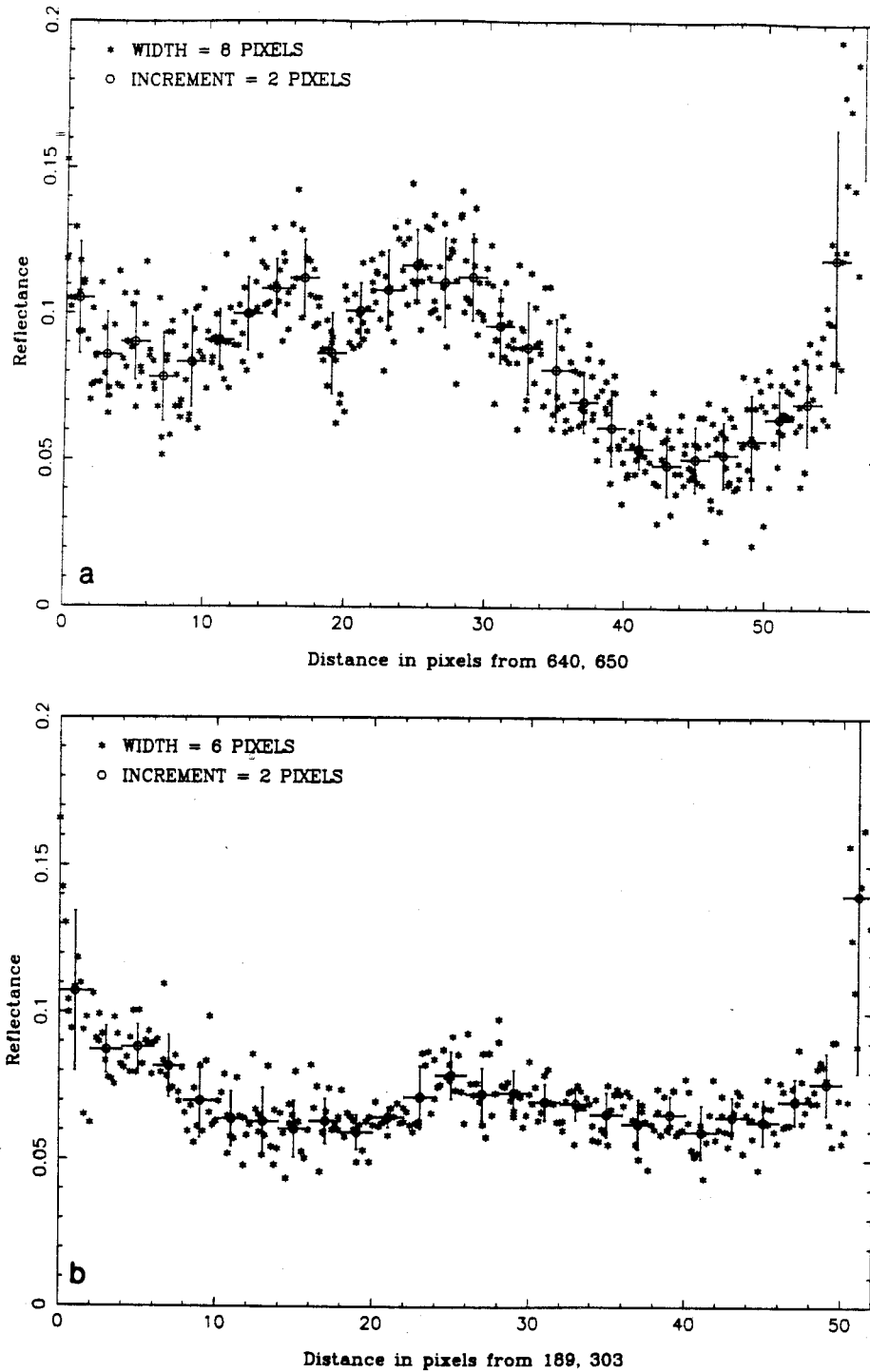


Figure 3.30: Profile 2 data with averages of 2-pixel increments. Vertical error bars indicate standard deviation of pixel values in each increment. Increased reflectance near profile endpoints is due to inclusion of residual frost. (a) 173B1 (“topography” image) data from 8-pixel wide swath around profile. (b) 188B2 (“albedo” image) data from 6-pixel wide swath around profile. Note increase in reflectance at center of profile.

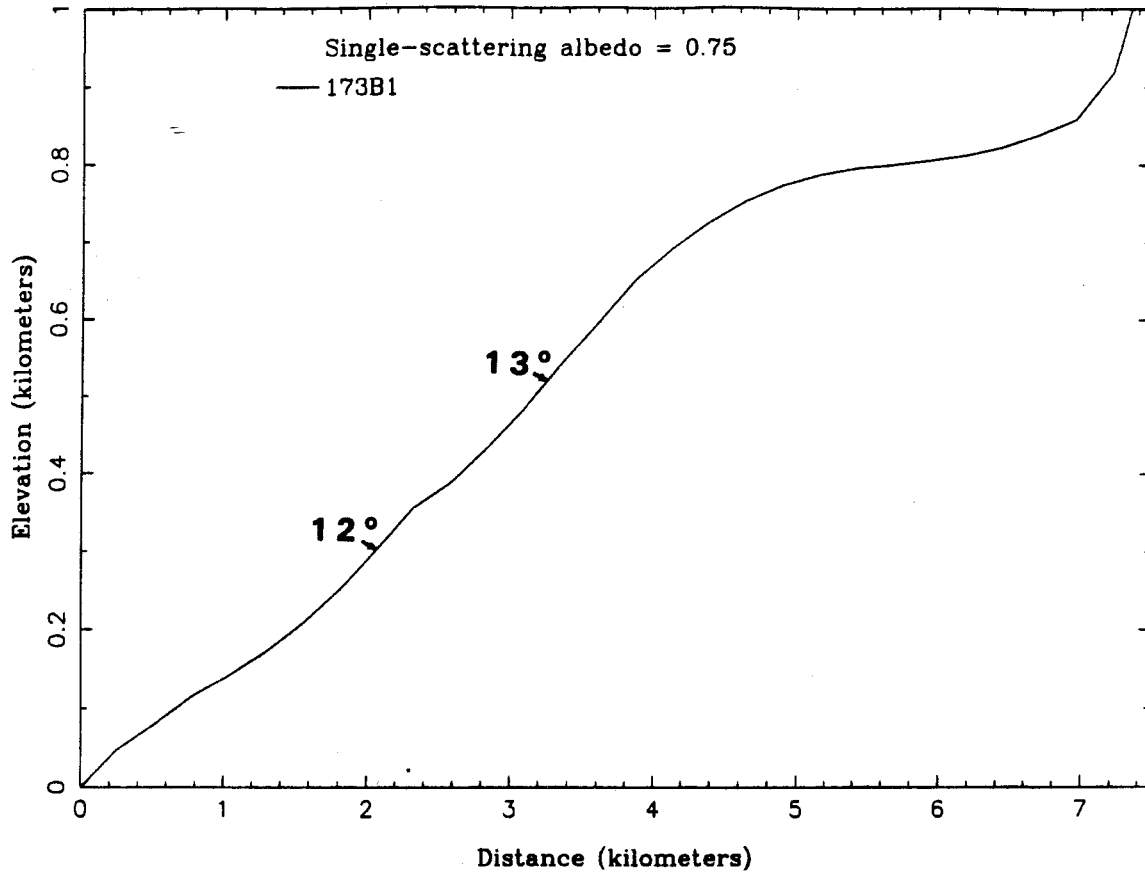


Figure 3.31: Constant- w model topography for profile 2 with $b = 0.5$. Vertical exaggeration $5.4\times$, maximum slopes indicated.

shown in Figure 3.31. Stereogrammetry indicates only 300 ± 160 m of total relief across profile 2, much less than the total relief in Figure 3.31 even if the erroneously large slopes (due to the inclusion of polar cap reflectances) near the endpoints are neglected. The reflectance data in the albedo image are not consistent with a constant surface albedo, as illustrated in Figure 3.32. Because this area does not face equatorward and therefore receives less solar radiation on average than other exposures of layered deposits, the most likely cause of the albedo variations along profile 2 is the presence of frost.

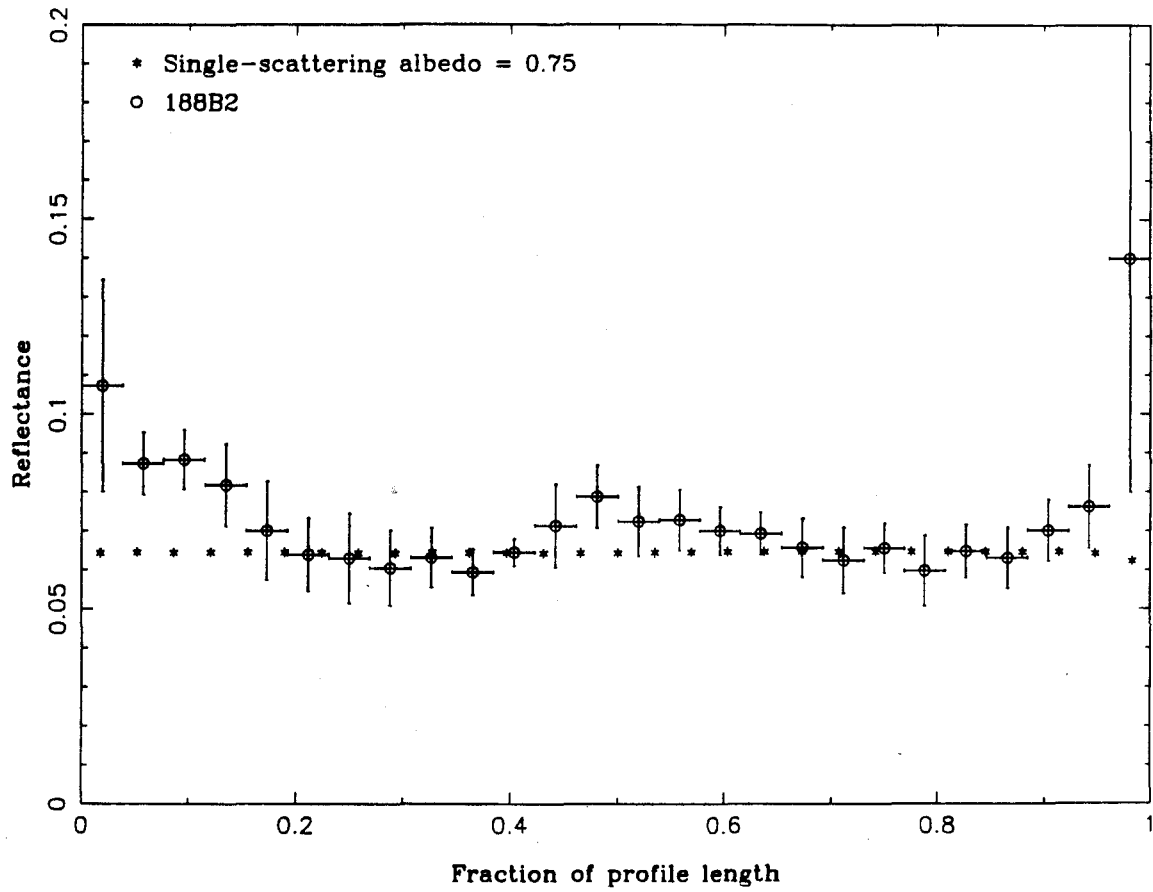


Figure 3.32: Comparison of reflectance predicted by model slopes and profile 2 data from "albedo" image. Note marked discrepancies between model and data.

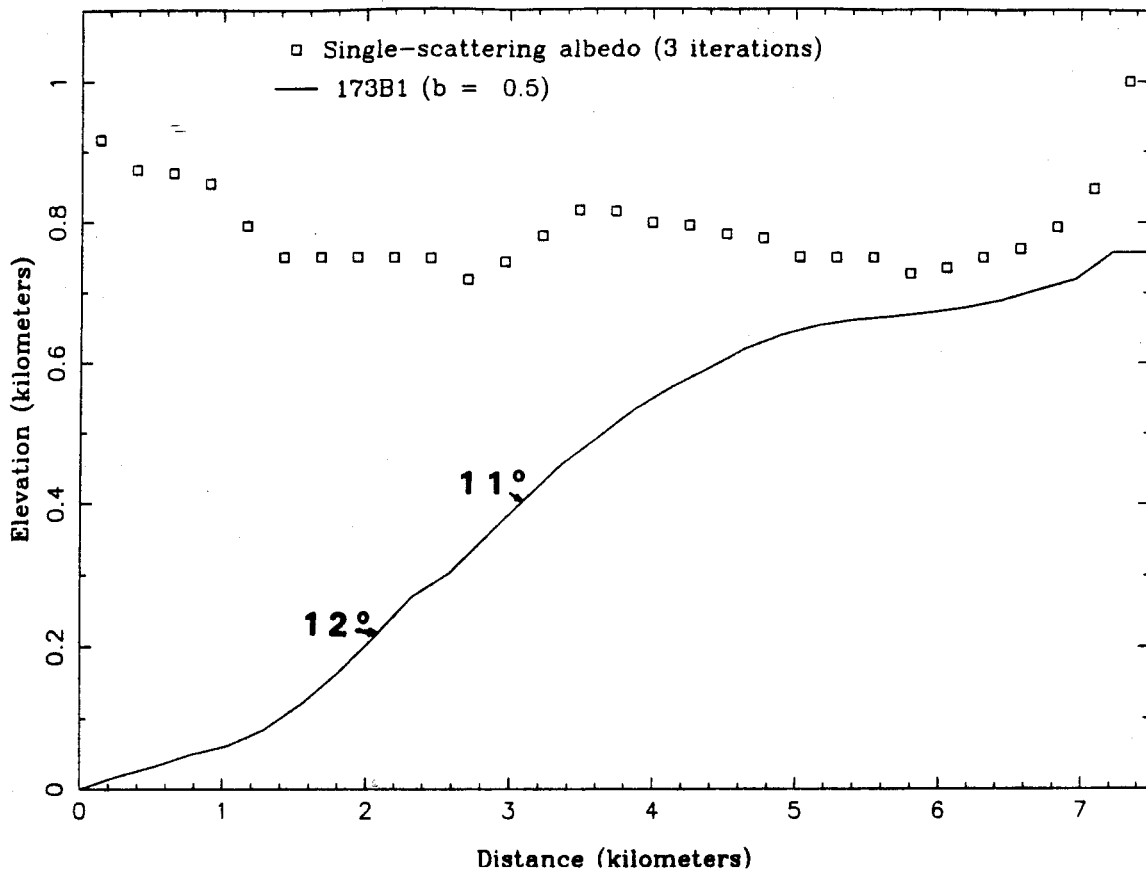


Figure 3.33: Profile 2 topography and albedo from iterative model. Albedos of 1.0 are not included in the solution. Vertical exaggeration $4.9\times$, maximum slopes indicated.

However, even when the surface albedo is allowed to vary along the profile, at least 700 m of relief is required to model the reflectance data (Figure 3.33). This amount of relief is definitely outside the limits of uncertainty in the stereogrammetric data, which allow a maximum of ~ 450 m of relief on profile 2. The most likely cause of this discrepancy is a temporal change in frost cover between the two images, but the effects of foreshortening must also be considered.

Foreshortening, caused by the oblique viewing geometry in these images

($\epsilon \approx 46^\circ$), has a significant effect on slopes along profile 2 in the albedo image. For example, a 20° slope will appear 59% as wide as a level area of the same actual width, if the profile is viewed parallel to its length. Similarly, a 1 km slope will appear only 805 m wide in 188B2 if its average slope is 10° . Because the resolution of the images used here is no better than 200 m and the longest continuous slopes are about 1 km long, foreshortening will have a significant effect only on slopes greater than about 10° along profile 2, and even less effect on the other profiles. Only "albedo" profiles are viewed nearly parallel to their length in this study, so that foreshortening has practically no effect on the results. I conclude that foreshortening cannot explain the large overall relief in Figure 3.33, and that a temporal change in frost coverage along profile 2 is therefore implied.

Profile 3

The location of profile 3 was chosen to facilitate comparison with the results from profile 1, as discussed above. In the absence of surface features that could be located in both images at the base of profile 3 for stereogrammetric measurements, starting points in both images were approximately located (Figure 3.29). The starting point in the topography image (188B2) was chosen so that the profile appears perpendicular to the trace of the layers. Because of the oblique viewing geometry, this profile is not actually perpendicular to the strike of the layers. The spacecraft azimuth is nearly perpendicular to the layer strike in the albedo image

(173B1), so that the angular relationship between the profile and the layers can be better seen. The endpoint of profile 3 is at the same elevation as the endpoint of profile 1 within 100 m, but the elevation of the start of profile 3 is not precisely known. However, given the stereogrammetric data near the starting points of both profiles (Figure 3.22), the total relief across profile 3 is expected to be roughly equal to that across profile 1 (500 m).

The endpoints of profile 3 do not extend as far into the polar cap as does profile 1, so that less bright material is included (Figure 3.34). Profile 3 should therefore be compared to the central section of profile 1. The two profiles are basically similar in both images, but there are some important differences. The changes in reflectance 20 to 32 pixels from the start of profile 1 in Figure 3.24a are not apparent in Figure 3.34a between 14 and 22 pixels from the start of profile 3. The reflectance near the end of profile 3 in the topography image (Figure 3.34b) is never as low as it is 20 pixels from the starting point. The latter difference is due to the irregular boundary of the residual cap: profile 1 extends farther into the cap in a dark embayment (Figure 3.29). In addition, two bright layers are resolved 7 and 12 pixels from the start of profile 3 (Figure 3.34b), but are not resolved in Figure 3.24b.

Examination of Figure 3.29 indicates that the differences between profiles 1 and 3 may be due to lateral variations in the layers, but the images are sufficiently noisy that such a conclusion is debatable in some cases. However, the reflectance dip

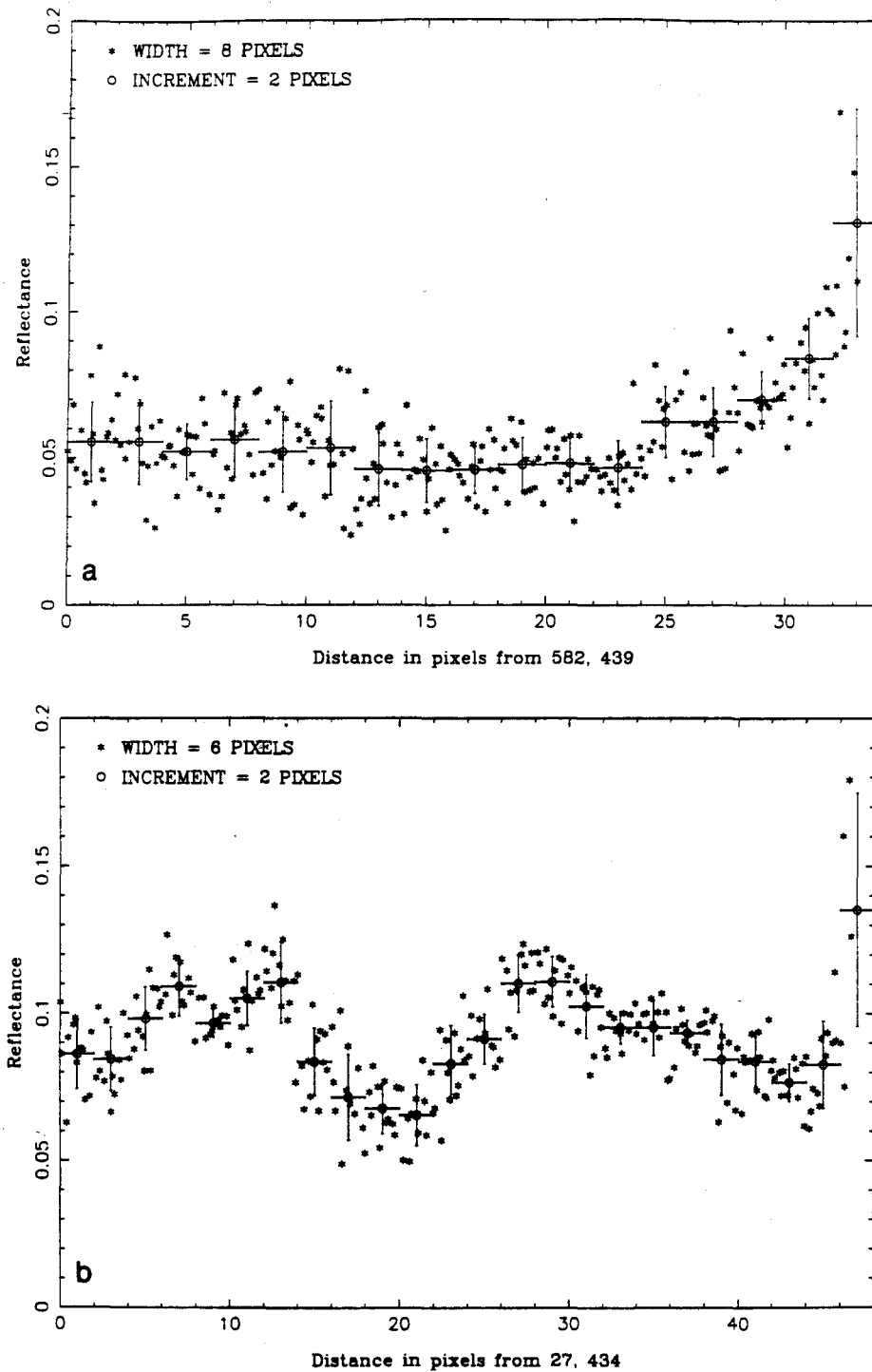


Figure 3.34: Profile 3 data with averages of 2-pixel increments. Vertical error bars indicate standard deviation of pixel values in each increment. Increased reflectance near profile endpoints is due to inclusion of residual frost. (a) 173B1 (“albedo” image) data from 8-pixel wide swath around profile. (b) 188B2 (“topography” image) data from 6-pixel wide swath around profile.

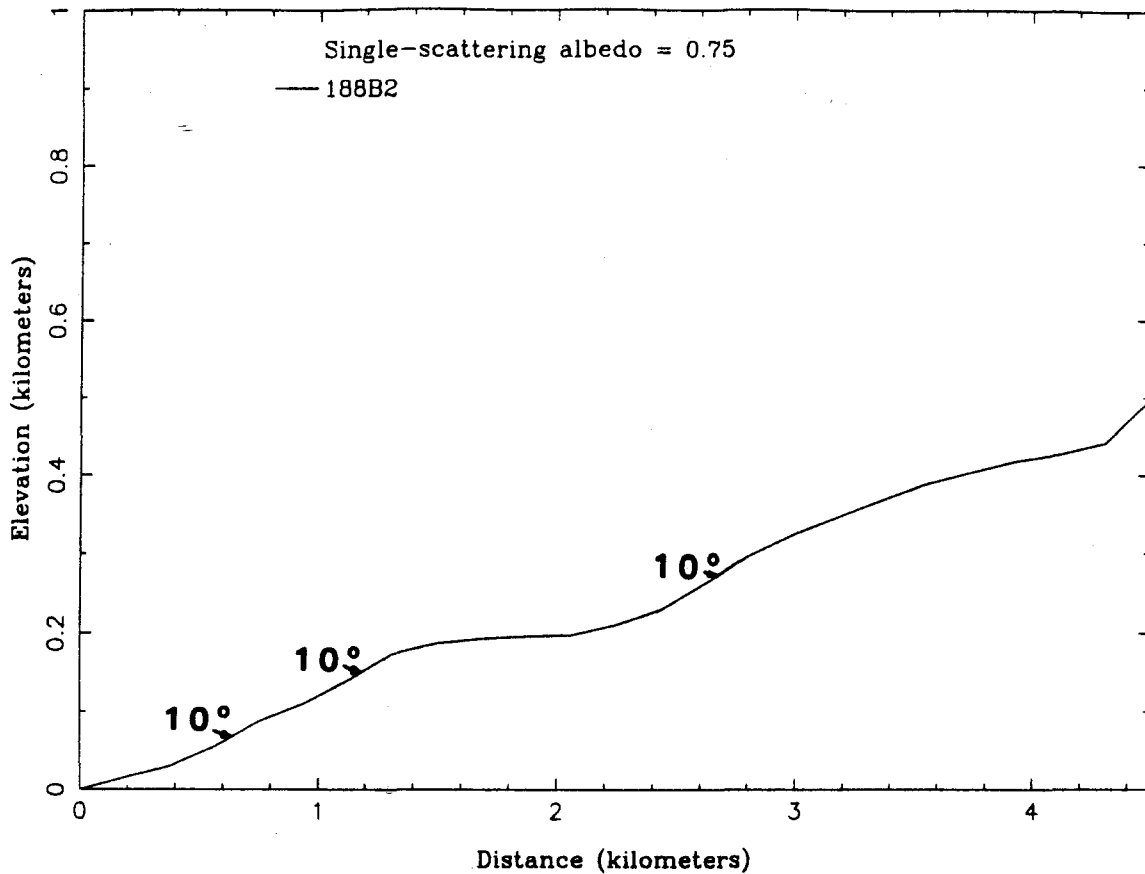


Figure 3.35: Constant- w model topography for profile 3 with $b = 0.5$. Vertical exaggeration $3.25\times$, maximum slopes indicated.

in the albedo image profile (Figure 3.34a) 0.4 to 0.7 from the starting point appears to be due to the presence of a darker layer (Figure 3.29a). This layer, whether due to topographic or albedo variations, appears to pinch out toward profile 1, where it is barely visible in the image.

The constant- w model was used to produce the topographic profile shown in Figure 3.35, where the excessive slope at the end of the profile is due to improperly modeled residual frost (as above). The total relief derived is slightly less than that

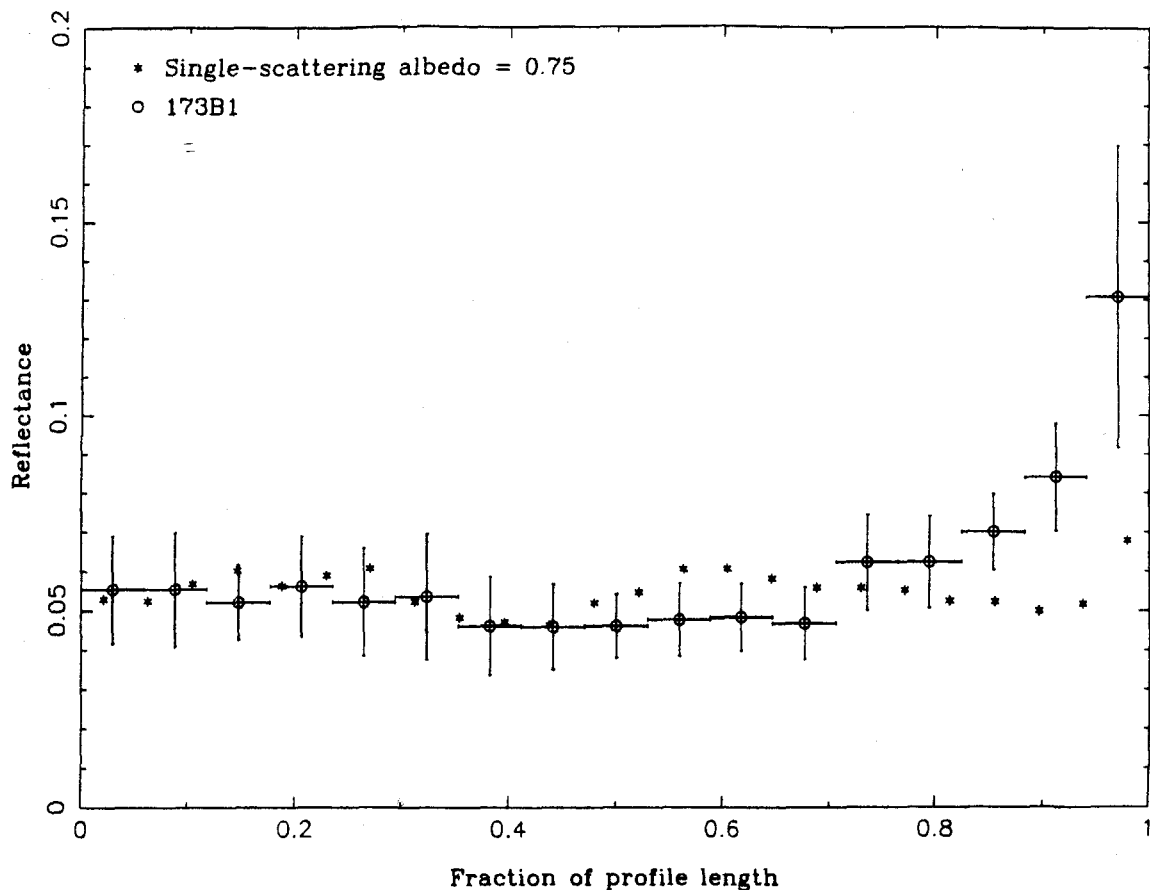


Figure 3.36: Comparison of reflectance predicted by model slopes with profile 3 data from "albedo" image. Note discrepancies between model and data around 0.6 of profile length.

for profile 1 (Figure 3.26). The reason for the low relief in this case is that the albedo is not constant within the uncertainties in the profile 3 reflectance data, as indicated in Figure 3.36. The $> 1\sigma$ deviation of all of the model points between 0.5 and 0.7 indicates that the constant- w model is not valid in this case.

The general model yields a topographic profile that has the same overall relief as profile 1 (Figure 3.37), with surface albedo variations of up to 25%. The lower layer in profile 1 is resolved into two 100 m thick layers, overlain by a single

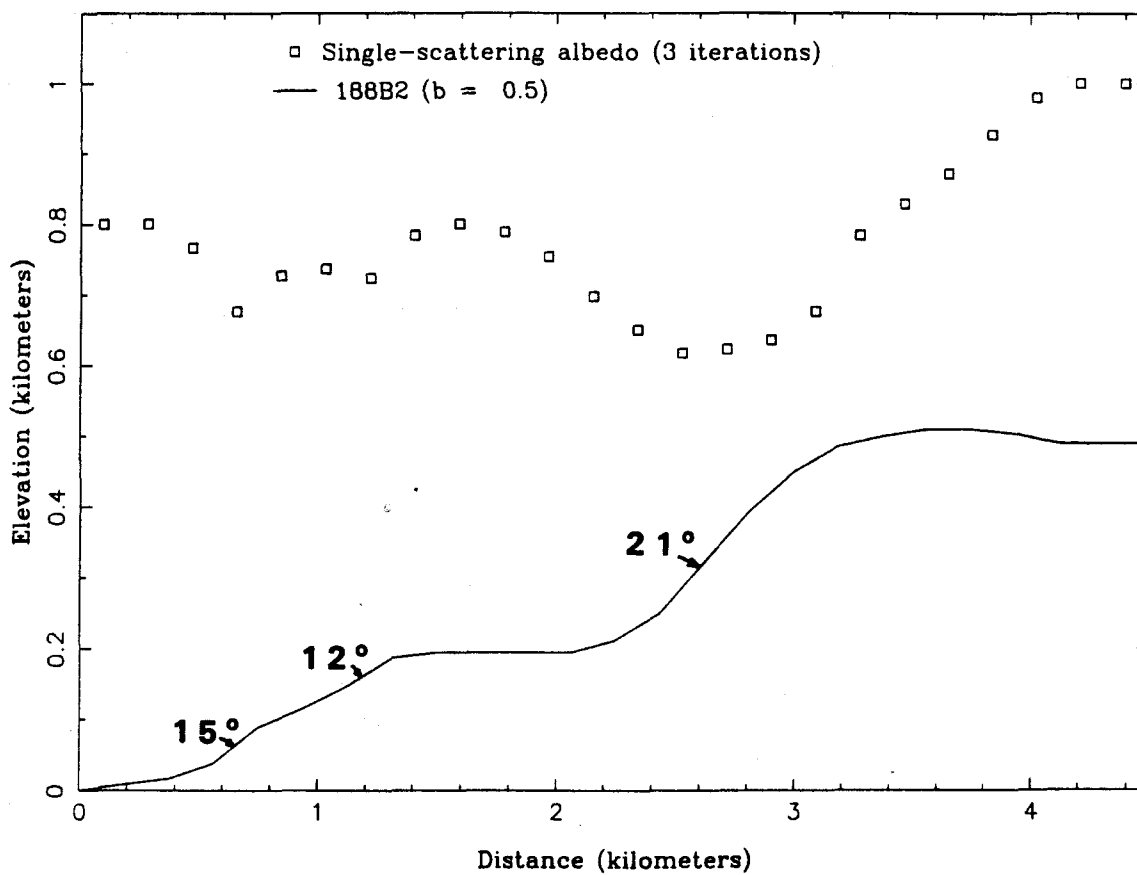


Figure 3.37: Profile 3 topography and albedo from iterative model. Albedos of 1.0 are not included in the solution. Note inverse correlation between slope and albedo. Vertical exaggeration 3 \times , maximum slopes indicated.

300 m thick layer. The inverse correlation of slope and albedo, suggested by profile 1 results, is much more pronounced in Figure 3.37. The lowest single-scattering albedo (0.62) occurs on the steepest slope (21°). In addition, two layers near the start of the profile are darkest on their steepest slopes. This relationship suggests that the albedo variations are caused by differential frost retention on exposures of layered deposits, although differences in composition between layers cannot be ruled out entirely.

The inverse correlation of slope and albedo was also noted by Blasius *et al.* (1982) in the north polar layered deposits. Steep equator-facing slopes defrost more quickly than level areas because of increased insolation. Howard *et al.* (1982b) found that the frost cover is laterally variable in the northern deposits, as also indicated here by the difference between profiles 1 and 3. Comparison of Figures 3.28 and 3.37 shows that more complete defrosting (hence lower albedo) in profile 3 is due to steeper slopes.

The maximum slopes derived here are larger than the $1-8^\circ$ slopes reported in the northern layered deposits (Blasius *et al.*, 1982). While the 21° slope in profile 3 provides the best fit to the data, a slightly smaller slope (and higher albedo) for this layer can also fit the reflectances within their uncertainties. However, as shown in Figure 3.36, the albedo in this area must be lower than for the rest of the profile. Therefore, the slope must be greater than 10° in order to fit the reflectance data in both images, and is probably at least 15° . The significance of maximum slopes of this

magnitude will be discussed after the uncertainties in these results are quantified.

Error Analysis

The estimated 20% error in absolute calibration does not directly affect the results reported here. Multiplicative errors of this magnitude will not change the ratio of atmospheric to total scattering, and therefore will not significantly change the optical depth fits described above. Because the Lambert albedo used in correcting for atmospheric scattering in 173B1 and 188B2 was not well constrained by the imaging data, it is not affected by the absolute calibration uncertainty. The single-scattering albedo w and phase function parameter b were also chosen to be consistent with stereogrammetric data, and are therefore not directly influenced by errors in absolute calibration. However, relative errors are of similar magnitude and have a significant effect on the results.

The noise level in Mariner 9 images is roughly independent of camera response, so that the reflectance uncertainty decreases from $\sim 25\%$ at 0.05 to $\sim 10\%$ at 0.10. These uncertainties are larger than the 8% relative error predicted by Herkenhoff *et al.* (1988) because of the low exposure levels in the images (exposed for bright polar cap, not for dark bands). The determination of w is mainly dependent upon the $\sim 25\%$ uncertainties in the albedo image, corresponding to a 15% uncertainty in w . Hence, the 12% variation in w along profile 1 (Figure 3.28) is consistent with no variation in w (Figure 3.26). The uncertainty in the maximum slopes, however,

is primarily due to the $\sim 10\%$ uncertainties in the largest reflectances in the topography image. Reflectance errors of this magnitude result in errors in slope of about 2° . Lower reflectance values in the topography image are more uncertain, so that the shallowest slopes are uncertain by as much as 3° . The slightly negative slopes in Figures 3.26 and 3.28b are therefore consistent with a level surface.

Errors in correction for atmospheric effects have a significant effect on the reflectance profiles. In particular, the Lambert surface albedo used in the atmospheric model is rather uncertain, as described above. Varying the Lambert albedo in the atmospheric model results in an additive offset of the reflectance profiles, causing a change in the derived slopes. However (as described above) the Lambert surface albedo was constrained by the stereogrammetric data for profile 1, and therefore does not contribute to the uncertainty in the slopes derived along the other profiles. Errors in the estimation of the dust optical depth in the atmospheric model cause multiplicative variations in the reflectances that influence the fit of parameters in the photometric function. Once again, however, the agreement between the photoclinometric and stereogrammetric results indicates that these parameters are correct. The uncertainty in correction for atmospheric effects is therefore determined by the uncertainty in the stereogrammetry, so that errors in the atmospheric scattering model do not significantly increase the uncertainty the derived slopes.

Clearly, the error in the overall slope of profile 1 (derived from stereogrammetry) has an effect on the derived slopes. The 90 m relief uncertainty for profile 1

corresponds to an overall slope uncertainty of $\pm 0.7^\circ$. This error is small compared to the errors in slope due to reflectance uncertainties, so that the combined error in slope is no more than 3° .

Topography and Albedo of the Layered Deposits

The photoclinometric profiling presented here confirms the observations, first presented by Murray *et al.* (1972), that most of the visible layering in the south polar deposits is caused by "staircase" topography. However, the present analysis indicates slopes of about $10 - 20^\circ$ in at least some exposures of layered deposits, implying either rather competent beds or sand-sized particles, because layers composed purely of uncemented dust would not be expected to form the "staircase" topography shown in Figures 3.28 and 3.37. I therefore consider two alternatives for the composition of the layers: uncemented sand-sized particles and cemented dust particles.

Uncemented sand-sized or larger particles can easily form slopes as steep as 20° , but such a composition is at odds with the widely held view that dust is the major non-volatile constituent of the layered deposits (Cutts, 1973b; Howard, 1978; Cutts *et al.*, 1979; Squyres, 1979; Toon *et al.*, 1980; Carr, 1982). It seems impossible to form laterally extensive layers of almost constant thickness without invoking eolian deposition, so that particles larger than fine sand are ruled out on the grounds that they cannot be plausibly transported by the present Martian atmosphere. The

possibility that the layered deposits are composed purely of sand-sized particles cannot be eliminated by the observations presented here, but is considered to be unlikely.

A more reasonable hypothesis is that the layered deposits contain a significant amount of dust, perhaps with smaller quantities of sand-sized particles (Thomas and Wietz, 1989; Herkenhoff and Murray, 1989). Some type of cement or adhesion is then needed to allow slopes of up to 20° to form in the presence of Martian winds. Water ice is probably not present at the surface of the dark exposures because of the high temperatures expected there during summer (Toon *et al.*, 1980; Hofstadter and Murray, 1989), and therefore is not likely to provide the required surface bonding strength. Other cementing materials, such as carbonates, cannot be excluded but generally require the presence of liquid water.

The constraints that the non-volatile component of the layered deposits is mainly dust and that they form 20 degree slopes are both satisfied by the formation of a tough weathering rind by erosion of the deposits. Storrs *et al.* (1988) have shown that sublimation of mixtures of dust and water ice yields a residue of lightweight yet rather sturdy material. As proposed above, sublimate residue particles may preferentially form from dark magnetic dust grains and subsequently saltate, forming the dark deposits observed in the south polar region. Such particles may be derived from the weathered surface of the layered deposits, which is evidently competent enough to maintain ~20° slopes.

The albedo variations in the layered deposits described above may be due to compositional differences between layers. In this case, variations in source materials and/or atmospheric transport capability may be implied. However, given the temporal changes in albedo between the two images studied here, I conclude that variations in frost cover are the cause of the albedo differences. This interpretation is supported by the increased albedo observed along profile 2, which slopes toward the south pole. The 25% variation in albedo along profile 3 exceeds the 15% uncertainty in albedo determination, indicating that the model results are robust. The minimum (unfrosted) surface single-scattering albedo of 0.62 ± 0.09 at 0.56μ is consistent with values of w found by Thorpe (1982) and Arvidson *et al.* (1989) in Arabia and Chryse.

If the albedo variations between layers are due mainly to differences in frost coverage, the intrinsic variations in albedo between resolved layers are constrained to be less than 15%. This suggests that compositional variations in the non-volatile component of the deposits are minor. However, thin layers with different compositions and albedos may be present and simply not resolved in the images used here.

The exposures of layered deposits studied using high resolution stereo images (Figure 3.29) are mapped in Figure 3.17 as unit 2 (dust mantle). As discussed above, only a small area (crossed by profile 3) has an albedo that is significantly lower than the rest of the exposure (Figure 3.29a). This dark layer is not resolved in the Viking Orbiter color mosaic. In fact, the resolution of the color mosaic does not

pernit accurate measurement of the color and albedo of the area investigated using photoclinometry, due to the narrowness of the dark exposure. The red/violet ratio is about 3.0, on the border between units 2 and 4 (Figure 3.19), and the violet albedo is in the range of unit 4. These observations suggest that some frost may have been present in this area, although the data are questionable. The Viking Orbiter images in the color mosaic (Figure 3.12) were acquired slightly earlier ($L_s = 341$) than the stereo pair of Mariner 9 images. James *et al.* (1979) found that the southern polar cap receded more slowly during the Viking summer than during the Mariner 9 summer, so a greater frost cover is to be expected in the Viking Orbiter data. In any case, the interpretation in Figure 3.17 of this area being mantled by dust is doubtful, and the presence of partial frost cover is equally possible. This area may therefore have the same color and albedo as the exposed layered deposits (unit 3) seen elsewhere in the region, but is partially covered by frost.

3.3.3 Summary of High Resolution Topography and Albedo Results

Photoclinometric analysis of exposures of the south polar layered deposits indicates that slopes of up to $21^\circ \pm 2^\circ$ occur locally. There is evidence that the slopes within layered deposit exposures vary laterally. Frost is preferentially retained on level areas late into the summer and sublimed from steep equator-facing slopes, causing surface albedo variations of up to $25 \pm 15\%$. Interlayer variations in albedo

and are constrained to less than 15%, implying that the differences in resistance to erosion are caused by variations in ice content unless unresolved layers of different (non-volatile) composition are present. The minimum single-scattering albedo is similar to that observed in dusty areas on Mars, suggesting that dust is a major component of the layered deposits. Layer thicknesses of 100 to 300 m are observed, but thinner (unresolved) layers are possible or even probable.

Chapter 4

Conclusions and Recommendations

The major conclusions of this work are summarized in this chapter, and recommendations are made for future studies. First, the implications of each of the quantitative applications described above are discussed. The results are then considered together to infer some of the properties of the south polar layered deposits. Finally, a method for future absolute calibration of Mars imaging data using Phobos observations is proposed.

4.1 Genetic and Climatic Implications

The implications of the three quantitative applications of Mars television images are now discussed. The composition of the south residual polar cap in 1972 inferred from Mariner 9 observations is compared to Earth-based and spacecraft measurements, and the questions that these findings raise regarding the climate of

Mars are discussed. The constraints on the composition and formation of the layered deposits imposed by their color and albedo are then described. The high resolution measurements of the slopes and albedos of an exposure of layered deposits are used to infer that their surface is weathered, and these results are compared with the regional color and albedo data. Finally, a theory for the weathering and erosion of the layered deposits is proposed that can account for the available observations. Specific recommendations are made in each of the three sections below for future observations and analysis.

4.1.1 South Polar Residual Cap

The conclusion that solid CO₂ remained on the surface of the south polar residual cap throughout the summer of 1971-72 is in agreement with Viking Orbiter observations of the southern cap three Mars years later (Kieffer, 1979). However, Jakosky and Barker (1984) have pointed out that Earth-based observations of Mars in 1969 suggest that copious amounts of water vapor were released from the south residual cap that summer. Barker *et al.* (1970) spectroscopically detected 45 ± 11 precipitable microns of (globally-averaged) water vapor at $L_s = 323$, more than in their previous northern summer observations. Although there is no evidence for the source of the water vapor, their data suggest that water ice was exposed at the southern residual cap in 1969. Hence, the residual cap may not always be covered by CO₂ frost, and the amount of CO₂ present during the southern summers of 1971-72

and 1977 may therefore have been rather small.

As discussed by Paige *et al.* (1989), an unknown process (or processes) may conspire to keep the solid carbon dioxide reservoir near zero. The polar cap/atmosphere system may be in equilibrium with a large reservoir of adsorbed CO₂ in the regolith (Fanale and Cannon, 1974, 1979). Fanale *et al.* (1982) show how exchange of CO₂ between the polar caps and the regolith is modulated by variations in Mars' orbit and obliquity. It is therefore possible that the polar cap reservoir is presently near zero because the obliquity of Mars is currently near its mean value. Clearly, more Earth-based observations of water vapor in Mars' atmosphere need to be made in the future.

Areas of intermediate albedo and color in the Viking Orbiter mosaic are interpreted to be unresolved macroscopic mixtures of bare ground and frost. The combined analysis of Mariner 9 IRIS and imaging data taken during the same season indicates that at least some of the frost in these areas is CO₂. This raises the question: how can carbon dioxide frost coexist with dark ground or dirty water ice that should heat up due to insolation? The ground must somehow be cooled by subliming CO₂ that is not exposed to the sun. Small topographic depressions could protect the frost from solar radiation but still allow thermal contact with the rest of the surface. The variegation of the southern residual cap may be an expression of this roughness at the largest spatial scales. The surface may also be rough on length scales less than the best resolution of imaging data, about 150 meters (75 m/pixel).

It is tempting to interpret recent 6 cm radar observations of Mars as indicating a very rough surface at the southern residual cap, but other interpretations of these data are equally valid (Muhleman and Butler, personal communication, 1989). If the residual cap is indeed rough at a scale of meters, current ideas regarding the nature of the cap and any relationship to the origin of the layered deposits must be re-evaluated.

The Mars Observer camera will hopefully be able to resolve 3-5 meter-sized features and thus better constrain hypotheses regarding the state of carbon dioxide frost and water ice at the southern residual cap. In addition, the infrared instruments scheduled to fly on Mars Observer should provide key data that will help address this problem.

4.1.2 Color and Albedo

The implications for the formation of the layered deposits of the compositional hypotheses proposed above in connection with the regional color and albedo results are now considered, along with the variations in climate or circulation that seem to be required. I prefer two alternative hypotheses that include dark material in the layered deposits that reconcile the available observations: (1) bright dust, dark dust and ice, or (2) bright dust, dark sand and ice. The first invokes preferential formation of filamentary sublimation residue (FSR) particles from dark dust, but does not require climatic conditions that are different from the present. The

second hypothesis, however, calls for occasional net poleward atmospheric flow to transport dark sand-sized particles by saltation onto the layered deposits.

The dust and ice scenario involves formation of sublimation residue particles that saltate to form the dark dunes adjacent to the layered deposits. Because dark dust seems required to form dark FSR particles, I propose that magnetite or maghemite dust is deposited from suspension onto the layered deposits. The dust in the atmosphere over the Viking landers contained about 1% opaque phase (Pollack *et al.*, 1979), while the soil contained 1-7% magnetic material (Hargraves *et al.*, 1979). It is therefore possible that the amount of opaque phase in the atmospheric dust, identified as magnetite by Pollack *et al.* (1977), is roughly equal to the amount of magnetic material in the surface fines, and therefore that the dark material is easily transported in suspension. For comparison, the volume of dark dune deposits in the polar regions is estimated to be 1-10% of the eroded volume of the layered deposits (Thomas, 1982). This comparison suggests that dark magnetic material may be incorporated into the layered deposits in the same proportion as in the surface fines at the Viking Lander sites, as the percentage of dark material in the layered deposits is essentially identical to the percentage of magnetic material in the surface fines (considering the uncertainties involved). Because dark material presently appears to be suspended in the atmosphere, it is conceivable that layered deposits may be forming in the current climatic conditions. In any case, dark magnetic dust should preferentially form FSR particles upon erosion of the layered

deposits and subsequently saltate to form the observed dark dunes.

If, on the other hand, dark sand is mixed into the layered deposits, a poleward atmospheric flow is necessary to transport the sand by saltation onto the polar deposits. Thomas (1982) found that winds tend to blow off of the north polar cap, but the overall circulation pattern is rather complex. Sand is not expected to saltate during the winter and early spring when the dunes are covered by seasonal CO₂ frost, so that the summer circulation is most important to the net transport of sand. Saltating particles will eject dust into suspension, so that codeposition of dust and sand seems impossible. Transportation of sand by saltation into the polar regions requires that the surface be rather solid (perhaps frozen), as loose surface materials will either be removed or trap the sand particles. Saltating sand may become trapped in topographic depressions, forming small (meter-sized) lenses of dark material that would not be detectable in the best television images. This scenario seems more likely than the formation of an extensive, thin sand sheet over much of the polar region. In any case, it appears that sand is not currently being transported onto the north polar cap, and that a change in circulation would be needed to bring sand into the layered deposits (Thomas, 1982).

Mars Observer data will hopefully test the hypotheses presented here. Mars Observer's polar orbit enables repeated coverage of the polar regions, and is ideally suited to detailed study of the polar layered terrains. Although data returned by the "deselected" visual and infrared mapping spectrometer would probably have

constrained the composition of the polar deposits better than any of the remaining instruments, the mission as currently planned should be able to address important questions regarding the layered terrain. The high resolution camera will be able to examine in detail the geological relationships among the units described above. In particular, high resolution imagery should reveal any small lenses or thin layers of dark material that may occur within the layered deposits, and will allow detailed study of the relationships between the layered deposits and the dark dunes that appear to be derived from them. The altimeter will yield essential topographic information, and the gamma ray spectrometer may permit an estimate of the amount of H₂O near the surface. Finally, the thermal emission spectrometer and/or the pressure-modulated infrared radiometer may be able to distinguish sand from FSR particles in the dark material. Such observations will provide crucial tests of the hypotheses proposed here.

4.1.3 High Resolution Topography and Albedo

The steepness of the slopes and consideration of the instability of water ice at the surface of the layered deposits suggests that slopes on layered deposit exposures may be maintained by the presence of a strong weathering rind. In the absence of such a competent surface layer, sublimation of water ice from the layered deposits would leave only loose dust (and perhaps some sand-sized particles) that would presumably slump down or blow away. In either case, the removal of dust

would expose more water ice to the sun, resulting in rapid erosion of the layered deposits. Calculations by Toon *et al.* (1980) show that about 15 cm yr^{-1} of water ice would be sublimed from the layered deposits at 80°S latitude if the H_2O were not protected from the sun. Even if the layered deposits are mostly ice, this indicates that a few vertical kilometers per million years of the deposits could be removed by this type of erosion. Sunward-facing scarps would be expected to retreat at a much higher rate. This result suggests that water ice in the layered deposits is protected by a surface layer of some kind that insulates the H_2O from solar heating (Hofstadter and Murray, 1989). I propose that this surface layer is a weathering rind composed of self-cementing sublimation residue particles, such as those created in the experiments described by Saunders *et al.* (1986).

The stepped topography on layered deposit outcrops is probably caused by variations in resistance to erosion between layers (Howard, 1978). Such variations in erosive resistance may be due to differences in susceptibility to sublimation of water ice. Differences in ice/dust content and in dust composition may cause such variations in erosion rate. However, variations in dust composition must not result in surface albedo changes greater than 15%. The magnitude of surface slopes provides constraints on possible mechanisms for layered deposit erosion.

Future studies of the topography and albedo of the layered deposits should include examination of areas far from the residual cap, where there is less surface frost. Current investigations of the south polar deposits using the technique de-

scribed here are limited by the availability and quality of Mariner 9 stereo coverage. The Mars Observer camera, as currently planned, should be able to obtain images of the layered deposits that are well suited to analysis by this technique. In particular, it may be possible to image key areas near the poles at different times of day during the summer, providing the different solar illuminations required. Such high resolution images will probably resolve thinner layers and further constrain hypotheses for the origin and evolution of the deposits. In addition, the laser altimeter on Mars Observer will hopefully provide regional topographic data in the polar regions and better height control than the stereogrammetry used in this study.

4.1.4 Evolution of the Polar Layered Deposits

Viking color and albedo data show that areas adjacent to the southern residual cap are covered by a mixture of frost and bare ground below the resolution of the images. Similar patchiness of CO₂ frost is inferred from the comparison of Mariner 9 IRIS and imaging data, which indicates that even dark areas are apparently cooled below their radiative equilibrium temperatures. Together, these results indicate that the surface of the layered deposits (at least in some areas) is rough on a scale of hundreds of meters or less, allowing seasonal frost to linger in shadowed depressions late into the summer.

The presence of frost in such areas appears to stabilize dust deposits and results in net accumulation of non-volatile material. I have shown that an area of

patchy frost in the south polar region is the site of recent dust deposition. Other workers have concluded that the north perennial ice cap is the site of net dust deposition (Cutts *et al.*, 1979; Squyres, 1979; Howard *et al.*, 1982b). Thus, it is possible that layers composed of dust and ice are deposited where frost exists on the surface year-round, and that layers are presently being formed at both poles.

The concept of a dust/ice composition for the layered deposits is not new, but the presence of ice in the deposits has still not been proven. As discussed above, ice cannot easily be detected in the layered deposits by observing reflected radiation, and is not expected at the surface in any case. However, the investigations presented here indicate significant slopes on layered deposit exposures and therefore the presence of some type of cementing material. If the cement is H₂O, it must be protected from radiative heating or the layered deposits would have been eroded away during the last 10⁶ years. Thus, some type of protective layer is expected at the surface of the layered deposits.

I propose that the surface of the southern layered deposits may have become weathered by sublimation of water ice. The weathered material may consist of self-cemented FSR particles such as those described by Storrs *et al.* (1988). The surface is probably rougher than unweathered dust/ice "bedrock" because the FSR particles are much larger ($\sim 100\mu$) than the micron-sized dust that forms them. Such a weathering rind might be expected to have a lower albedo than an unconsolidated mantle of the same dust that comprises it, due to its rougher surface texture.

Hence, the layered deposit (unit 3) exposures mapped above using color data may be weathered and therefore darker than the dust mantle (unit 2).

The presence of frost on the area of Mariner 9 stereo coverage complicates the interpretation of the composition of the underlying surface. Future analysis of Viking Orbiter color data obtained later in the southern summer may better constrain the reflectance properties of the area studied in detail using Mariner 9 data, but will probably also be limited by the resolution of the images.

In the meantime, it appears that weathered layered deposit surfaces are darker than the dust that currently mantles parts of the region, perhaps due in part to their roughness. The layered deposits may also become darker as they are weathered due to selective concentration of dark magnetic minerals in FSR particles, as postulated above. The end product of such weathering may be the dark dune material inferred by Thomas and Weitz (1989) to be eroded from the layered deposits. Saltation of these FSR particles may eventually break them down into their component dust grains, allowing recycling into the layered deposits via atmospheric suspension. The possibility that these dark particles are sand rather than FSR particles cannot be ruled out, but is less likely considering the difficulty in depositing small amounts of sand over the large area of the layered deposits.

4.2 Absolute Calibration Improvement

Using Phobos Observations

More accurate absolute calibration of existing spacecraft images of Mars will require collection of better Earth-based spectrophotometric measurements of Phobos and precise determination of Phobos' albedo variations using spacecraft observations. The shape of Phobos could also be more precisely measured, but current topographic models are much more accurate than the photometric observations. Since Phobos' photometric properties are believed not to be changing, Phobos can be used as a photometric standard for future Mars observations. Planning for imaging experiments on future missions (including Mars Observer) should include observations of Phobos at low phase angles for instrumental calibration and to assure compatibility with earlier spacecraft imaging data.

Better knowledge of the photometry of Phobos will allow more accurate calibration of the television cameras that have observed it if observations are carefully planned. The favorable apparition of Mars in 1990 provides an excellent opportunity to make the required Earth-based observations, which should include spectrophotometry at low phase angle. A few photometric observations of Phobos were made during the 1988 apparition, and are currently being reduced (S. Stephens, personal communication, 1989). The Soviet Phobos '88 mission returned a few low-phase images of Phobos before loss of communication, but are as yet uncalibrated.

Such data may enable more accurate comparison of ground-based photometry with Viking Orbiter television data.

Appendix A

Mariner 9 Television Relative Calibration

The Mariner 9 Television Reduced Data Record (RDR) was the product of extensive analysis and processing of over 7000 images returned during the 1971-72 mission. Unfortunately, the RDR "decalibration" was based only on preflight calibration data and was found to lack internal consistency (Young, 1974a). The RDR is not sufficiently accurate (radiometrically) to permit full exploitation of the Mariner 9 television data to derive photometric properties of the Martian surface and atmosphere.

In general, both Mariner 9 and Viking imaging data are the basis of Mars Observer planning and data analysis. Improved processing of the Mariner 9 television data thus will materially aid the above endeavors and the growing number of researchers using digital data on image processing systems. These efforts on refining Mariner 9 calibration have paralleled similar work at the U. S. Geological Survey in Flagstaff on Viking orbiter images and have made use of the knowledge

and experience gained from Mariner 10 and from Voyager.

A.1 Inherent Uncertainties in Mariner 9 Television Data

The reduction of Mariner 9 raw TV data to obtain radiometrically accurate images of Mars is complicated by several camera peculiarities which, fortunately, were anticipated and investigated both before launch and during flight (Snyder, 1971; Thorpe, 1972). Specific problems with the television system are described below.

A.1.1 Residual Image

Vidicon responses to luminous intensity are affected by previous intensity levels in ways that remain poorly understood. Although the immediately preceding image has the greatest effect, earlier images also contribute to residual image. The residual intensity is a non-linear function of camera temperature, wavelength of incident light, position on the vidicon surface, and intensity of both the present and previous images (Seidman *et al.*, 1973). The residual image effect is most noticeable when the previous frame included a limb or other high-contrast feature such as the polar caps, but is present to some degree in all Mariner 9 pictures. This effect was greatly reduced in the subsequent Mariner 10 and Voyager television images by

electronic and operational redesign, and in Viking by use of a different sensor.

These problems were recognized before launch and calibration measurements were made for both the wide-angle (A) and narrow-angle (B) cameras. It was not possible, however, to investigate the full range of imaging sequence combinations, due to the required volume of calibration data. In particular, the effects of changing color filters between images was not studied. Only the orange and violet filters were used during A-camera residual image calibration. Images of black bar targets were recorded at five different exposure levels, followed by flat fields recorded at five different exposures, resulting in a 5 by 5 matrix of residual amplitude as a function of previous and current image data number (DN) (Green *et al.*, 1975). An attempt was made to use the same five exposures for previous or current images, and only the first image in each row or column of the 5 by 5 matrix was used in residual image reduction (P. Jepsen, personal communication, 1987). The temperature of the cameras was held close to the expected operating value during the calibration sequences. Calibration files were constructed for the B-camera and all the color filters on the A-camera using less complete data for the green and blue filters. Data for the green filter were used to process the polarizing filter images. These files consist of a 5 by 5 matrix for every five lines by five samples in the RDR format (950 samples by 800 lines). Geometric distortions were removed because the data processing sequence used to create the RDR corrected for geometric distortions before residual image reduction.

A.1.2 Dark Current

Both the magnitude and form of the dark current vary with time through the Mariner 9 mission. As noted by Thorpe (1972), the average dark current level decreased gradually during the mission, the greatest decrease occurring when the television subsystem was first turned off on March 16, 1972. The variations in average dark current level are less than 1 8-bit DN over a period of 30 days (60 orbits).

Typical dark current frames are shown in Figures A.1 and A.2. Note that large-amplitude variations occur only in the corners of the frame. Most of the dark current variability is in these "hot" corners, with the fluctuations in the rest of the frame being similar to the average overall variations (a few DN; see Figure A.3). Fortunately, these "hot" corners are partially covered by the vidicon masks, which extend about 20 samples into A-frames and about 30 samples into B-frames.

A.1.3 Light Transfer Curve

The response of vidicon cameras is not a linear function of incident intensity. The shape of the light transfer curve depends upon temperature, wavelength of the incident radiation, and location on the vidicon face. These problems were recognized before the mission, and extensive calibration testing and evaluation was completed before launch (Snyder, 1971). Inflight data pertinent to the study of light transfer non-linearity are limited, so preflight calibration data have been used

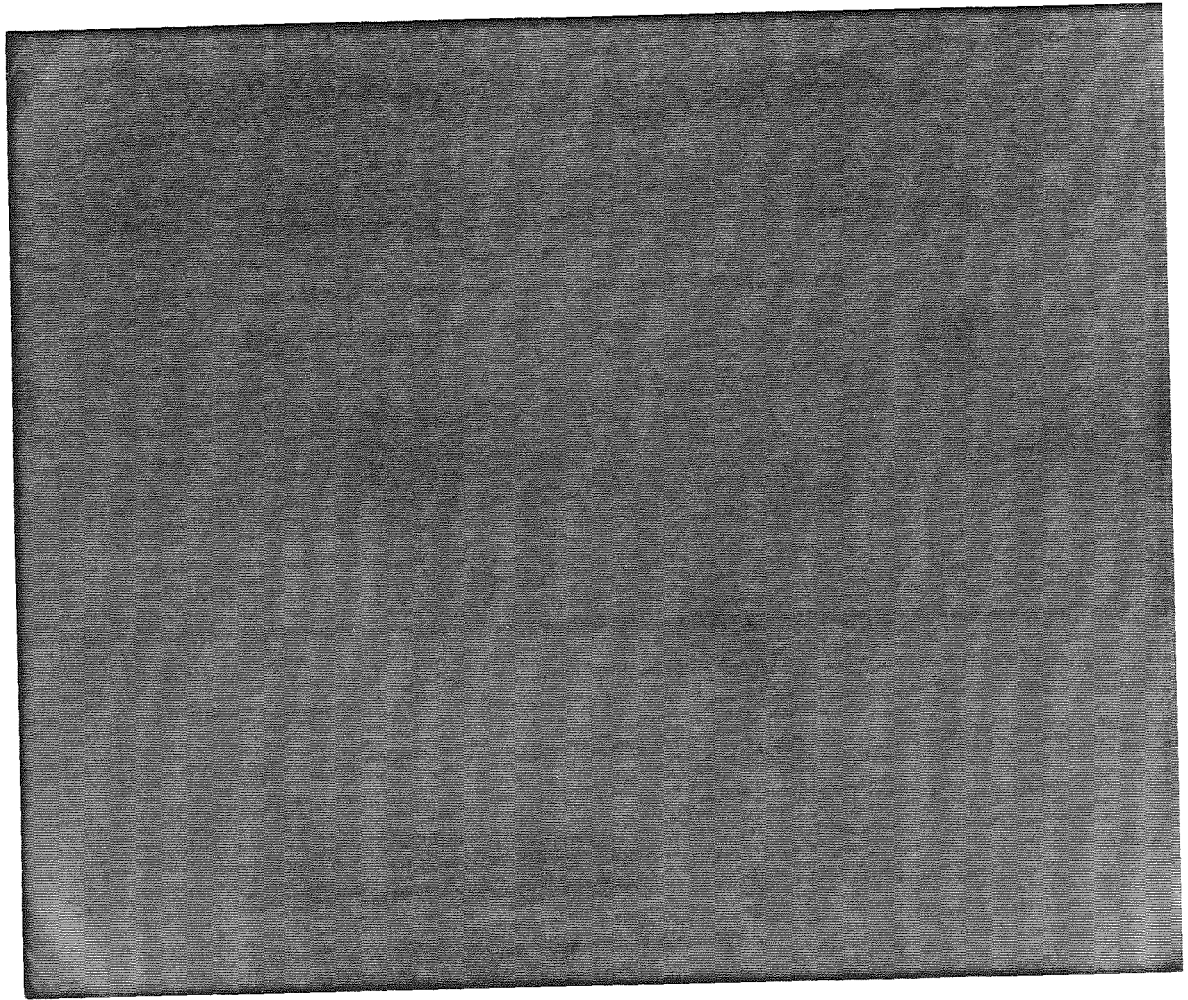


Figure A.1: A-camera dark current frame taken near time of orbital insertion. Note that the variation of noise level across the frame is smooth except at the corners.

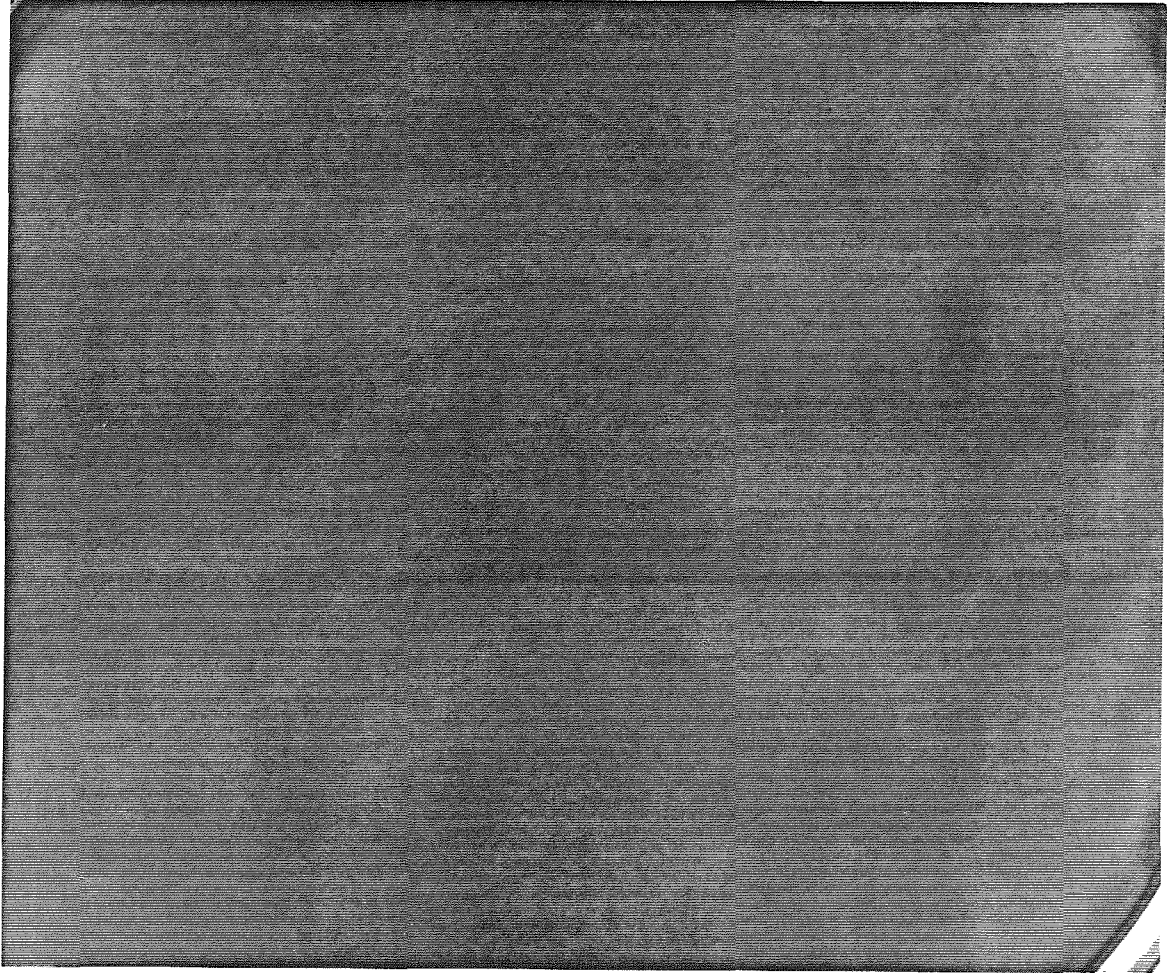


Figure A.2: Similar frame for B-camera, also taken near time of orbital insertion.

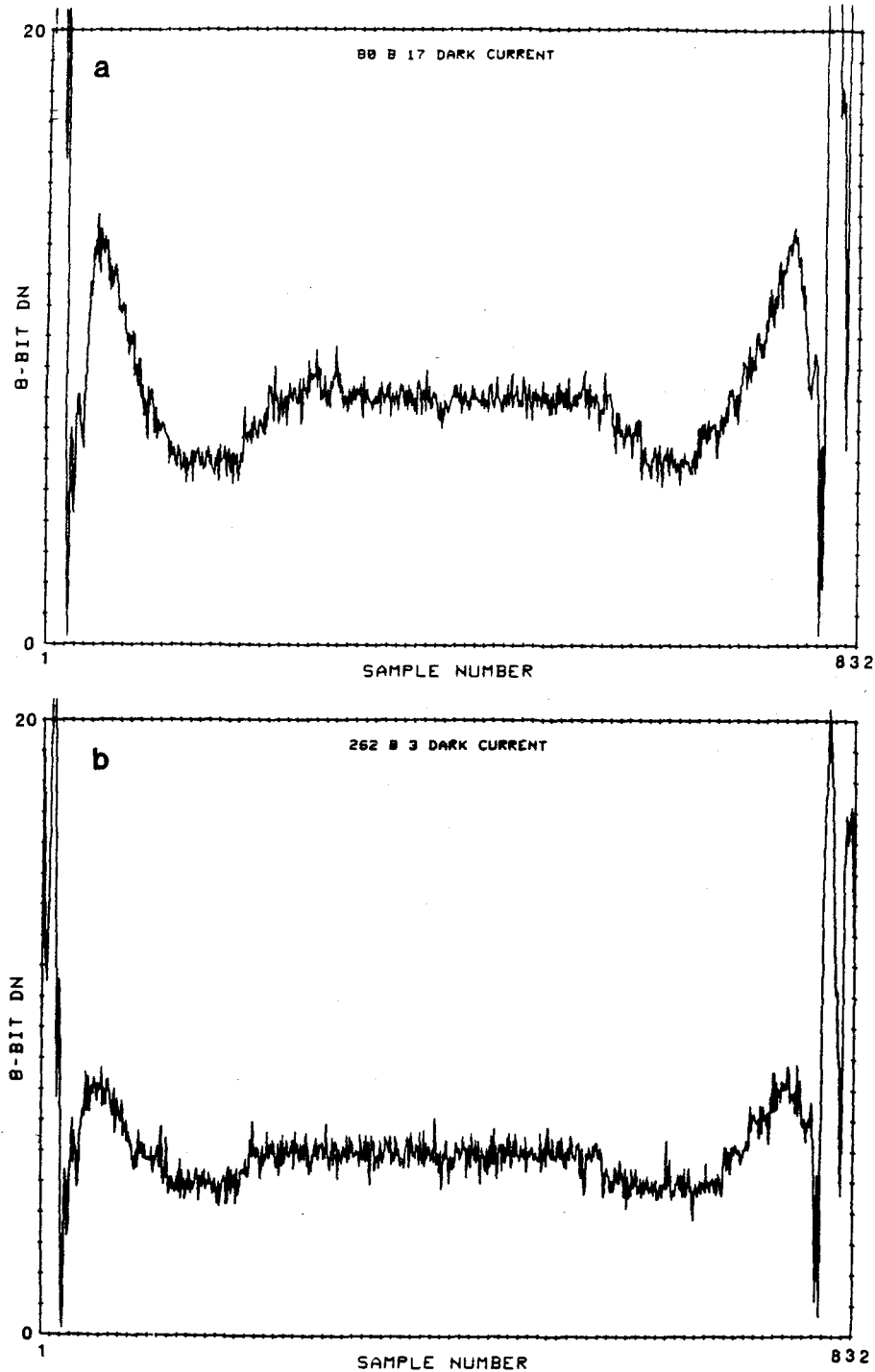


Figure A.3: Dark current profiles, diagonally across frame from corner to opposite corner. Vertical scale in 8-bit DN, up to 20 out of 255 DN. Data near the left and right edges of the profile are off scale, with maxima of ~ 40 DN. (a) Rev 80 dark current profile. (b) Similar dark current frame profile taken 91 days later on rev 262. Note decrease in amplitude and minor changes in shape of dark current.

here to quantify the light transfer curve. The shutter speed was held constant for each of the preflight calibration sequences. Inflight calibration sequences have been used to check for consistency, and will be described in the next section.

Examples of variations in the shape of the light transfer curve are shown in Figure A.4. The calibration data taken nearest to flight temperatures have been normalized to unity at half-scale (128 DN) to remove the effects of shading (discussed later). Normalization was performed using midscale values derived from second-order polynomial fits of the middle section of the light transfer curves. Abrupt changes in curvature at the upper right ends of the curves are due to vidicon saturation and should be avoided. The shape differences among the various areas of the vidicon are generally small, but not insignificant (usually up to 10 DN in the A-camera, less than 5 DN in the B-camera). Differences in shape from filter to filter are of somewhat lesser magnitude, as shown in Figure A.5. Here the data have been edited to remove the effects of saturation, and the dark current has been subtracted for each filter/vidicon area combination. Most of the scatter in this diagram is due to differences from one area to the next, as the average curves for each filter are fairly similar.

A.1.4 Shutter Exposure

Ground testing of the shutters for both cameras showed that the exposure time varies with temperature in a complex manner, the deviation being less than

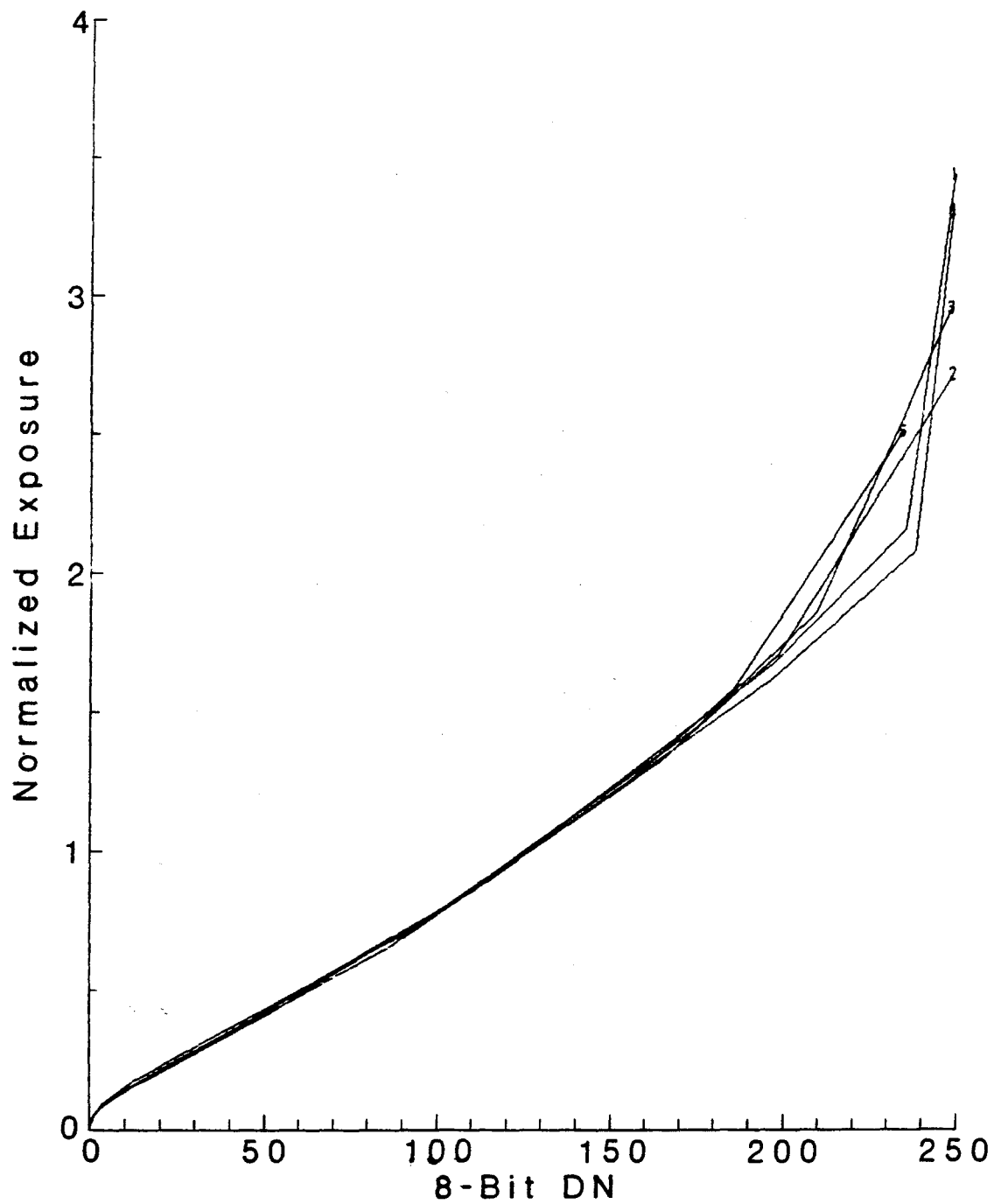


Figure A.4: Calibration data for A-camera, orange filter, environmental 8 (2.2°C), with exposure normalized to unity at 128 DN. Dark current values (at zero exposure) have been subtracted from the data values for each of the five vidicon areas.

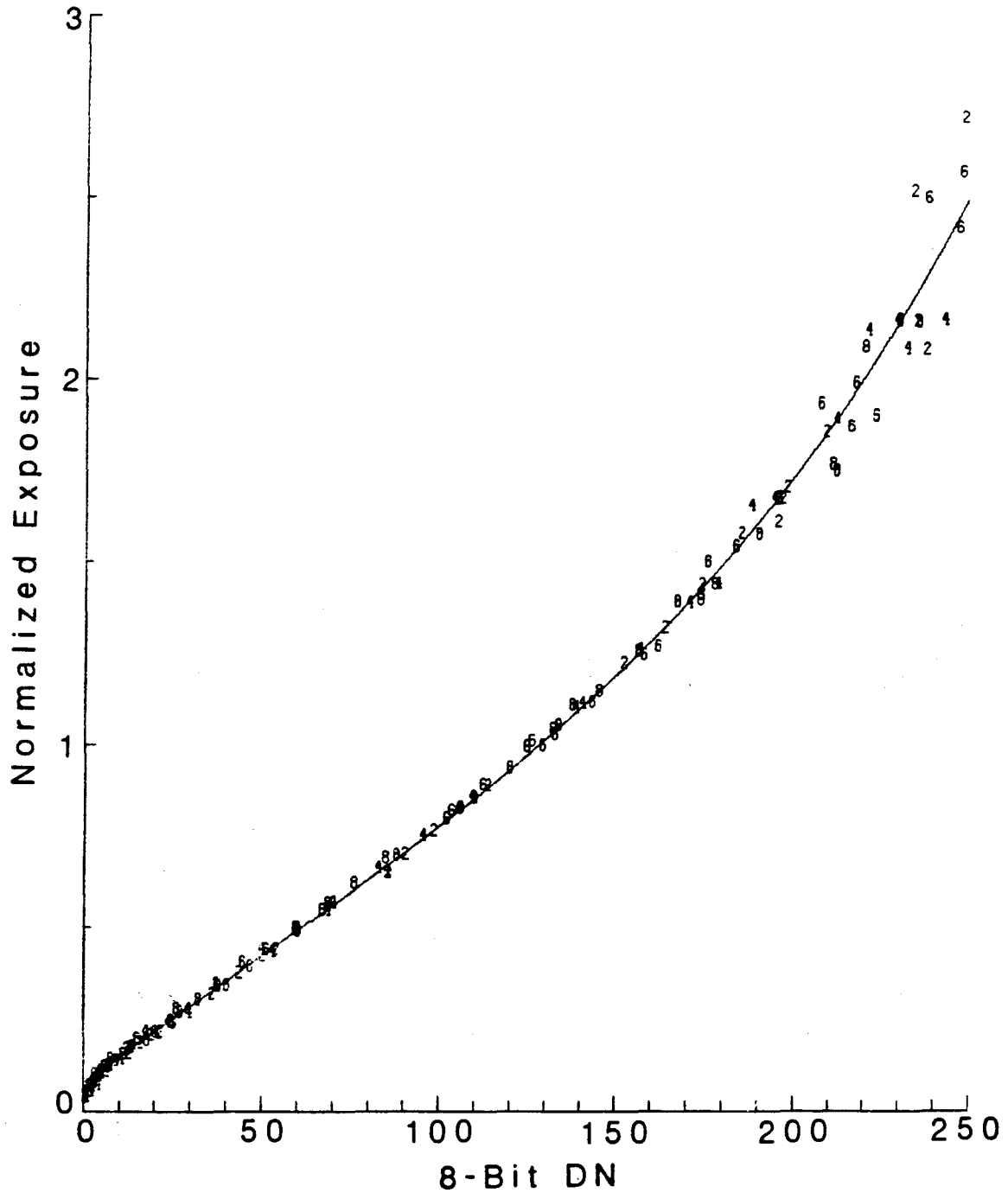


Figure A.5: Calibration data for A-camera, environmental 8, four color filters: 2 = orange, 4 = green, 6 = blue, 8 = violet. Data for all five vidicon areas have been corrected for dark current and plotted with exposure normalized to unity at 128 DN.

2% for the A-camera and less than 0.5% for the B-camera for the range of exposure times used and temperatures experienced during flight (Snyder, 1971). Changes in shutter exposure due to other effects during the mission are difficult to quantify. In addition, changes in vidicon sensitivity cannot be distinguished from changes in shutter speed (Thorpe, 1972).

A.1.5 Shading

Variability of camera response across the field of view (shading) is due to spatial variations in vidicon sensitivity, variations in transmittance across each filter aperture, and changes in exposure across the image plane caused by the camera shutters. Various types of blemishes appear in images from both cameras, most of which are due to dust specks on the vidicon faceplate (Thorpe, 1972; Young, 1974a). The worst blemish on the B-camera vidicon appears to vary in depth (contrast) with exposure level, and is apparently not a dust speck.

Examples of the magnitude of shading for both Mariner 9 cameras are given in Table A.1, expressed as the ratio of the data values in the four corner areas given by Snyder (1971) to that in the central area (3). Preflight calibration data values are averaged over the linear section of the light transfer curve, and are uncertain by about 2%. Revolution 3 values are averages of six images of a dust-shrouded Mars, corrected for photometric variations assuming Lambertian scattering. Note that the shading depends only weakly upon temperature. The

Camera A, orange filter				
Temperature	Area 1	Area 2	Area 4	Area 5
2.2°C	1.17	0.90	1.12	0.86
18.3°C	1.10	0.89	1.13	0.87
25.0°C	1.13	0.90	1.21	0.96
Rev 3 (6°C)	1.20 ± .01	.92 ± .02	1.257 ± .004	.940 ± .007
Camera B				
-12.2°C	1.19	1.02	1.09	0.97
1.7°C	1.22	1.03	1.15	1.02
17.3°C	1.22	1.03	1.15	1.01
25.0°C	1.24	0.99	1.20	1.00
Rev 3 (9°C)	1.26 ± .02	.98 ± .03	1.23 ± .04	1.03 ± .01

Table A.1: Mariner 9 vidicon shading.

A-camera showed a change in shading during the mission, the right side of the vidicon becoming less sensitive with time. This behavior may be due to repeated photography with the Martian terminator closer to the right side of the image (Cutts, 1974), or perhaps shutter aging.

A.1.6 Noise

Various types of noise are present in all Mariner 9 television data. Random noise, presumably originating in the preamplifier, was measured at 0.6 DN RMS in the B camera and 0.3 DN RMS in the A-camera. Coherent noise, with an amplitude of ~ 1 DN peak to peak (about 0.35 DN RMS) is probably due to beating of the carrier frequency with a harmonic of the spacecraft's power frequency. Complex noise has an amplitude of 2 to 15 DN, produced by mechanical vibrations of the UVS mirror that occurred at regular intervals in a repeatable position. The geometric

rectification performed on the RDR makes removal of noise that was parallel or perpendicular to the sampling direction more difficult.

Telemetry errors also affected picture quality in many cases: missing lines and bit errors are frequently present in Mariner 9 images. These errors are a function of the signal-to-noise ratio, which depends on the altitude of Mars above the Deep Space Network station's horizon, the range of the spacecraft from Earth, and the Earth-Sun-Mars geometry (Cutts, 1974).

A.2 Calibration Methods and Remaining Uncertainties

The calibration procedure described in this section differs significantly from previous methods (Seidman et al., 1973). In particular, images of Mars recorded during the mission have been used to evaluate changes in the dark current, create shading files, estimate uncertainties in residual image subtraction and light transfer characteristics, and quantify the absolute radiometric sensitivity of the cameras. Image processing is done in several independent steps, allowing greater flexibility and optimization for specific applications. The required computer software was developed and implemented on a dedicated Digital Equipment Corporation MicroVAX II for use under NASA's Technical Applications Executive. Readers having access to DEC systems running VMS may obtain the software and data files

needed to process raw Mariner 9 images by contacting Eric Eliason at the U. S. Geological Survey in Flagstaff. The U. S. G. S. Planetary Image Cartography System (PICS) applies radiometric calibration before any geometric transformation, and we have chosen to follow the same procedure with the Mariner 9 television data.

Solutions to the problems described in the previous section are detailed below, followed by estimates of the relative and absolute uncertainties in the Mariner 9 television data after application of the calibration data.

A.2.1 Residual Image

In order to remove residual image effects before any geometric transformation, the available preflight calibration data were transformed from the RDR (undistorted) format to the raw (distorted) format. This required creation of synthetic images from the calibration data to make use of existing image processing software. Undistorted frames (950 samples by 800 lines) were created using preflight data for each calibration sequence and camera/filter combination. Because the calibration data consist of values for every five lines and samples, the images were low-pass filtered to remove spatial discontinuities. The five similar previous or current images described in the preceding section were averaged to simplify application of the calibration data. Variations among similar frames were found to be less than 5% of their average. The resulting frames were then transformed to raw image space (832 samples by 700 lines) and sampled once for every 5 by 5 pixels to

form new calibration files.

Image pairs including the Martian limb have been used to quantify the effect of residual image in cases for which no preflight calibration data exist, and to evaluate the accuracy of the available calibration data. The few limb image pairs recorded at intensities above the highest levels of the preflight calibration data indicate that there is less change in residual amplitude at high previous image intensity levels than would be expected from a linear extrapolation of the calibration data. I have chosen to extrapolate residuals outside the range of the preflight data using half the slopes predicted by adjacent calibration data. A more precise formulation is not possible due to lack of pertinent data.

Residual image reduction accuracy was tested using limb images and, in the case of the B-camera, south polar frost images. The RMS deviations measured on brightness profiles were less than 4% of the current DN level, except at very low levels. Six limb images taken through the 60° polarizing filter were corrected to within 2% RMS using the green filter calibration data. Six B-camera limb images were also corrected to within 2% RMS, but were difficult to analyze in some cases due to the lack of limb sharpness at high resolution. Seventeen B frames of the south polar cap were corrected to 1% or less. The RMS deviation measured on 27 limb images taken through the orange filter was 3.7%.

I have also examined many image pairs in which the residual image occurs against dark space, so that the residual is superimposed on the dark current. The

results of this analysis were incorporated into the correction algorithm, but errors of 1 DN or so can occur. The effect of using different filters for previous and current frames was not investigated, as few high-quality image pairs of this type were recorded.

A.2.2 Dark Current

I have chosen several dark current frames of high quality to represent the variation in dark current throughout the Mariner 9 mission. These frames have been carefully filtered to remove bit errors and reduce other types of noise, but the spatial shape of the dark current has been preserved. Since the changes in the dark current are small (except in the corners), only a few frames are needed to characterize these changes to within 1 DN. Specifically, 10 B frames and 5 A frames have been selected for this purpose. A good dark current frame does not exist for the A-camera during the extended mission (after orbit 221).

A 1 DN error in dark current subtraction in a well-exposed image (mid-scale, 128 DN) corresponds to an error in observed brightness after processing of less than 1%. Errors in the frame corners will be larger, up to 40 DN, but are confined to within about 50 pixels of the corners.

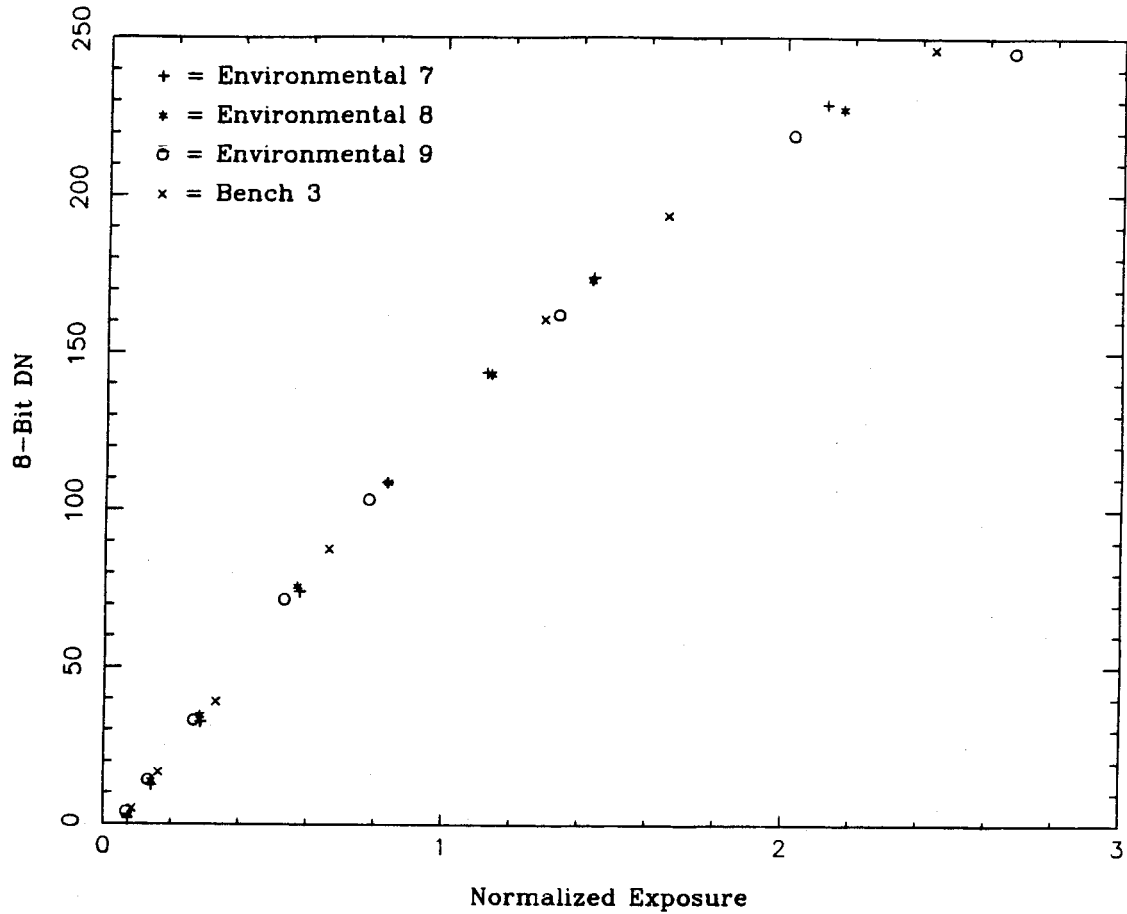


Figure A.6: Calibration data for B-camera, central area of vidicon, at four temperatures: environmental 9 = -12.2°C , environmental 8 = 1.7°C , environmental 7 = 17.3°C , bench 3 = 25°C . Dark current has been subtracted and exposures have been normalized to unity at 128 DN.

A.2.3 Light Transfer Curve

Because the light transfer curve shape variations between the five areas on the vidicon face are greater than the variations from one filter to the next, we have chosen to average the curves over all filters and retain the shape differences between areas. As shown in Figure A.6, the shape is fairly constant with temperature, so the calibration data taken both above and below flight temperatures have been used.

The subtle “negative residual image” effect in B-camera environmental 7 and 8 calibration data (Seidman *et al.*, 1973) does not appear to have caused a significant change in shape, so these data were used for the B-camera. Additionally, we have evaluated the shape of the curve at the lowest exposure levels by averaging over all filters and all areas. As shown in Figure A.5, the curvature is greatest at low exposure levels, but the differences in this region between the five areas are small. Functional fits to the calibration data are used to remove the non-linearity in the Mariner 9 vidicons, as described below.

The first step in the linearization algorithm is removal of the high-curvature “toe” at the low-exposure end of the light transfer curve. The entire curve was fit to a function of the form $E = ax^p + bx + cx/(x + d)$, where x is the calibration data value with dark current subtracted, E is the normalized exposure (unity at 128 DN), and p is a positive integer. The data value with the toe removed is therefore

$$x_t = x - \frac{cx}{x + d}.$$

The calibration data for each of the five areas were corrected as above and fit to a function of the form

$$E = A_1x_t + A_2(x_t^p - 128x_t^{p-1}) + A_3$$

so that the non-linear terms cancel at midscale. The best fit for both cameras had $p = 3$ and $A_3 \leq .01$, the latter indicating that the toe fit is good to 1% or better.

Linearized data values $L(x_t)$ are proportional to exposure:

$$L(x_t) = 128 \frac{E(x_t)}{E(128)}$$

and $E(128) = 128A_1$ (A_3 is small; neglected) so

$$L(x_t) = \frac{E(x_t)}{A_1} = x_t + \frac{A_2}{A_1}(x_t^3 - 128x_t^2).$$

The coefficient $A = A_2/A_1$ is found to vary slightly from area to area, and has therefore been interpolated and extrapolated to the entire vidicon face using a least-squares solution to

$$A(l, s) = c_1 l^2 + c_2 l + c_3 s + c_4 l s + c_5,$$

where l is line number and s is sample number. The entire linearization algorithm was tested on the preflight calibration data with a successful result to within a few DN below midscale and within 10% above midscale.

The applicability of the linearization procedure to inflight data was evaluated by processing the few calibration sequences recorded during the mission. Linearized values at several points in the A-camera images are plotted in Figure A.7. Surface features were used when possible to locate the same 10×10 pixel areas in each image. The average values of these areas had standard deviations of about 3% in most cases. A similar analysis could not be performed for the B-camera due to lack of appropriate inflight data and the loss of Mars Calibration I data. The Mars Calibration II data (taken before orbital insertion) are quite linear above

midscale, while the orbital image data define shallower light transfer curves. This apparent change in light transfer characteristics may also be caused by improper residual image correction, changes in exposure times, or changes in sensitivity with shutter exposure. Although residual image correction errors may contribute to the scatter of the data in Figure A.7, they cannot be entirely responsible for the largest deviations (10-15%). The scatter in the Mars Calibration II data is partially due to errors in location of identical points on Mars in the low-resolution images. Given the uncertainties as to the source of the deviations in orbital data, it is reasonable to conclude that the error in linearization of Mariner 9 data is roughly equal to the standard deviation of the preflight calibration data about the polynomial fits, about 4% (2% for the B-camera). Errors are somewhat larger at low light levels.

A.2.4 Shutter Exposure

Given the difficulties in distinguishing shutter exposure variations from changes in vidicon sensitivity, the exposure times measured before launch are used (Snyder, 1971). The values used have been interpolated to the observed flight temperatures.

A.2.5 Shading

The inflight shading characteristics of both cameras were evaluated using images recorded during revolution 3, when surface features were obscured by

the global dust storm. Seven "flat fields" taken by each camera were processed to remove residual image and dark current, and linearized as described above. Spacecraft position and camera pointing information from the Mariner 9 Supplementary Engineering Data Record (SEDR) as used to find the solar incidence angle at each pixel in these frames and create a "predicted brightness" image, assuming Lambertian scattering. The shading file is a normalized image derived from the ratio of a filtered, linearized image of Mars' atmosphere to the predicted brightness. The seven shading files for each camera were then averaged to reduce the contribution of variations in dust opacity and/or albedo. The shading correction is applied by multiplying the appropriate shading file by the linearized image to be corrected. Dust speck shadows are removed as well by this method, but the worst blemishes are not completely corrected, perhaps because of the contrast dependence on exposure.

Shading files for other filters can be obtained by this technique using similar data taken on later orbits, but their usefulness is limited because most of the Mariner 9 A-frames were taken through the orange (#2) or 60° polarizing (#5) filters. The A-camera filter wheel became stuck in position 5 during orbit 118, when the dust storm had cleared sufficiently that surface features were visible. A filter 5 shading file was created by multiplying the filter 2 shading file by the ratio of filter 5 shading to filter 2 shading. This ratio was found for every pixel by fitting a second-order polynomial in line and sample to the average shading ratio (derived from preflight calibration data) at the five vidicon areas.

Assessment of the accuracy of shading correction is complicated by the contribution of errors in each processing step leading to the creation of the shading files. In addition, the assumption of Lambertian scattering in the creation of the predicted brightness files must be examined. Phase variations need not be considered, since all images were taken within one degree of the same phase angle. Young (1974a) noted that the photometric behavior of the dust-shrouded planet, observed before orbital insertion, deviated from Lambertian near the limb. Figure A.8 shows that the data used to create the shading files lie within a nearly Lambertian region. Deviations from linearity at the higher brightness levels may be due to improper residual image subtraction or light transfer non-linearities, the latter being most likely. Spatial variations in the dust properties (albedo, opacity, etc.) may also contribute to the non-linearity, although the images used appeared remarkably smooth. The general shape of the ratio of the raw image data to the predicted brightness image was fairly constant except very near the terminator, and only similar results were used to create shading files.

The error in shading correction was estimated by calculating the standard deviation of the rev 3 data from the average (over temperature) of the preflight data in Table A.1. The rather large uncertainties, 9% for the A-camera and 8% for the B-camera, reflect the variation of shading with time. In addition, I have processed several overlapping A and B frames from later in the mission (revs 118, 119, and 227) to evaluate the accuracy of the shading correction. The average value of small

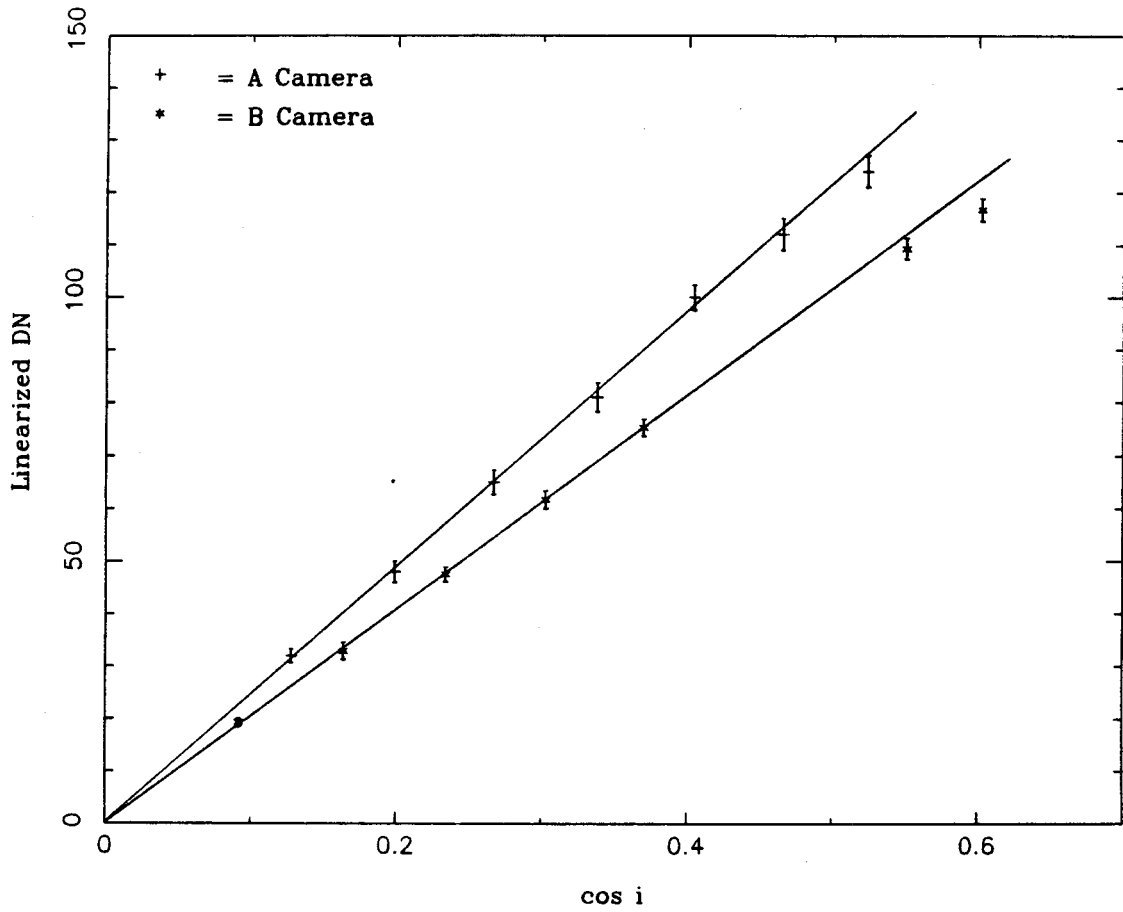


Figure A.8: Rev 3 linearized data values for central area of vidicon vs. cosine of incidence angle. Error bars denote the standard deviation of pixel values.

areas located using surface features was measured in the regions of the images that overlapped. The pairs of images used were taken nearly simultaneously through the same filter (orange or 60° polarizer on the A-camera). Measured differences did not exceed 8% in any of the pairs examined.

A.2.6 Noise

Telemetry errors are corrected in two steps: missing lines are replaced by the immediately preceding line, then bit errors are filtered out. If dropped lines occur repeatedly, the preceding line is used to correct all the missing lines. Bit errors are corrected when adjacent values on a line differ by more than a given tolerance, chosen to be greater than the maximum actual contrast in the scene. The "bad" pixel is replaced by the average of ten previously filtered pixel values and one unfiltered adjacent pixel unless the median of these values is significantly different from the average. No filtering occurs if the average of only the filtered values still differs from the median by more than a chosen tolerance, preserving high-contrast features such as the limb or the edge of the vidicon mask.

I have not attempted to remove low-amplitude random noise from Mariner 9 images due to the difficulty in preserving low contrast surface information. The vertical stripes (coherent noise) formed in these images can be removed, however. Since the typical spacing between stripes is six samples, they can be isolated by finding the difference between two low-pass filtered versions of the image: 25

Relative errors	A	B
Linearization	4%	2%
Shading	9%	8%
Random noise	0.2%	0.4%
Total	9.9%	8.3%
Absolute errors		
Relative errors	9.9%	8.3%
Residual subtraction	4%	2%
Dark current	1%	1%
Shutter exposure	2%	0.5%

Table A.2: Accuracy of Mariner 9 calibration.

lines $\times 1$ sample and 25×7 . The difference of these images is then subtracted from the original image to remove the noise pattern.

A.3 Conclusion

A summary of the most significant relative and absolute errors from various sources appears in Table A.2. Shutter exposure errors are upper limits; otherwise, standard deviations are given. The errors from random noise and from dark current variability are given with respect to a midscale (128 DN) response. Total expected errors are calculated by taking the square root of the sum of the squares of the errors, as they are essentially uncorrelated. Dark current variations will cause larger errors in the frame corners and at low exposure levels. Errors in linearization are somewhat greater at the highest exposures and, in general, uncertainties are greater at low exposure levels. These results are comparable to the Viking orbiter calibration

accuracy (Klaasen *et al.*, 1977): 2.3% relative, 9% absolute on average in the central
500 × 500 pixels.

Appendix B

Atmospheric Scattering Model

Analysis of the surface properties of Mars is complicated by the presence of dust in the Martian atmosphere. Determination of surface albedos and application of photoclinometric techniques, for instance, requires accurate removal of the atmospheric component of brightness. Evaluation of atmospheric dust scattering in shadows and at the terminator permits modeling and removal of the atmospheric component of brightness from the images when the opacity is less than unity. Such removal enables study of the spectrophotometric properties of the surface.

I have modeled dust scattering in the south polar region with a radiative transfer program described in detail by Michelangeli *et al.* (1988). The program uses the multistream Feautrier formulation for an inhomogeneous plane-parallel atmosphere with a single Henyey-Greenstein phase function. It assumes Lambertian scattering at the surface, and I have modified the code to account for the sphericity of the planet when calculating the incoming solar radiation. The plane-parallel assumption is unacceptable at high emission angles, but only moderate emission angles are modeled here. The program calculates the total radiation observed for

a given viewing geometry, as well as the attenuation of the downgoing solar and upgoing reflected radiation. The atmospheric component, including diffuse flux reflected from the surface, is calculated by subtracting the Lambert surface reflection from the total. Rayleigh scattering in the Martian atmosphere is insignificant compared to dust scattering (Kahn *et al.*, 1981), and was therefore not considered in this model.

In order to limit the number of variable parameters in the model, I have made use of published results regarding Martian dust scattering. The model has 9 altitude levels up to 50 km, the maximum dust height having been approximately determined using Viking Orbiter limb images (Jaquin *et al.*, 1986). The dust concentration decays exponentially with a scale height of 10 km, as inferred from Viking Lander observations by Pollack *et al.* (1977). The extinction efficiencies Q_{ext} given in Table 2 were taken from Pollack (1982). Since the 2.5 micron (cross-section weighted mean radius) dust particles are forward scattering (Pollack *et al.*, 1977), 12 azimuthal harmonics were used in the calculation. The error in approximation of the phase function is less than 7% for an asymmetry parameter of 0.55, and decreases as scattering becomes more isotropic. Use of a greater number of azimuthal harmonics does not significantly affect the results.

The remaining parameters to be determined are the optical depth τ , the single-scattering albedo ω_0 , the Henyey-Greenstein asymmetry parameter g , and the surface reflectance r_0 . Viking Lander observations show that τ is rarely less than

0.2 (Pollack *et al.*, 1977), while Viking Orbiter images have been used by Thorpe (1977a) to derive optical depths between 0.05 and 0.6, usually between 0.1 and 0.2. Opacities derived from Viking Orbiter limb observations by Jaquin *et al.* (1986) agree with those found by Pollack *et al.* (1977) over the Viking Lander sites, but are sometimes lower elsewhere on Mars. Images in which the "hard" planetary limb can be seen indicate that normal optical depths as low as 0.01 sometimes occur. The visibility of surface features places a rough upper limit on the opacity for the images under consideration. Images of interest should have normal optical depths between 0.01 and 1.

Pollack (1982) used Viking Lander sky brightness observations to find ω_0 , g and Q_{ext} as a function of wavelength in visible and near infrared light. His values of ω_0 are 0.74 and 0.88 at the effective wavelengths of the Viking Orbiter violet and red filters, respectively. Estimates of ω_0 using Viking Orbiter data have a larger difference between the red and violet filters. Thorpe (1978) modeled low-phase observations to find $\omega_0 = 0.5$ (violet) and 0.8-0.85 (red). Jaquin *et al.* (1986) analyzed limb observations to find the same single-scattering albedo (within 0.1) as Thorpe in violet light, but $\omega_0 = 0.94$ through the red filter. It is therefore expected that $0.5 \leq \omega_0 \leq 0.7$ for the violet filter and $0.8 \leq \omega_0 \leq 0.95$ for the red filter, and that the single-scattering albedo in green light will be intermediate between those in violet and red.

The asymmetry parameter g of Martian dust is known to be positive (for-

ward scattering), but its determination is highly model-dependent (Zurek, 1982). An asymmetry parameter for the red filter of 0.6 was used by Jaquin *et al.* (1986), while Kattawar and Young (1977) found that $g = 0.63$ fit their data well at similar wavelengths. The asymmetry factor given by Pollack *et al.* (1979) cannot be directly compared because they did not use a Henyey-Greenstein phase function. Lumme *et al.* (1981) modeled ground-based photometric data to find $g = 0.35 \pm 0.10$ in the V band. Jaquin *et al.* (1986) state that g is between 0.35 and 0.55 through the violet filter, but are less confident of their violet results. Thorpe (1979, 1981) found that g ranges from 0.0 to 0.6, and it is expected that the asymmetry parameter is in this range.

Ground-based spectrophotometric studies have shown that spatial variations in Mars' reflectivity are small at blue wavelengths (McCord and Westphal, 1971). Therefore, $r_0 = 0.09$ is used for the violet filter, which has a very similar bandpass to the B filter used by Lumme *et al.* (1981). Although the spectral reflectivity of the Martian surface in the south polar region has not been measured, telescopic maps of Mars indicate that it has an intermediate albedo. The green and red south polar surface reflectances should be greater than that of Syrtis Major ($r_0(\text{green}) = 0.11$; $r_0(\text{red}) = 0.14$), but less than Arabia's ($r_0(\text{green}) = 0.18$; $r_0(\text{red}) = 0.28$). These reflectances were derived by integration of the spectral geometric albedo data given by McCord and Westphal (1971; Figure 2.2) over the spectral bandpasses of the Viking Orbiter cameras (K. Klaasen, personal communication,

1987). They were then increased by 10% to agree with the blue band data of Lumme *et al.* (1981) and earlier studies (McCord and Adams, 1969). The surface albedo is assumed to be constant in the atmospheric model. Actual unfrosted ground albedos in the color mosaic vary by about a factor of 2, resulting in errors in atmospheric brightness on the same order as the absolute uncertainty in the calibration of the Viking cameras, 13%. Good shadow data near 75.5° incidence angle were used to subtract the atmospheric component from the observed violet and red brightnesses of nearby plains. The resulting surface reflectances have an R/V ratio of 2.8, so $r_0(\text{red}) = 0.25$ is used in the model.

A 3-color mosaic of Viking Orbiter 2 images of the south polar region was used to evaluate the brightness of the atmosphere in shadows during orbit 407 (Figure 3.12). Only the largest shadows gave consistent results due to the moderate resolution of the images, so minimum brightness levels that are represented by at least 2 pixels were chosen to avoid noisy data. The vertical scatter in the shadow data (Figures B.1-B.3) is partly caused by the inclusion of unshadowed terrain in some of the pixels, especially at lower incidence angles. Variations in surface albedo and roughness may also contribute to the scatter, but are not easily modeled. In addition, spatial variations in dust opacity will cause some scatter. Good shadows could not be found in the mosaic at incidence angles less than 70° . Near the terminator, shadows are longer and there is less scatter, indicating that the pixel values at high incidence angles are not contaminated by unshadowed ground. With this

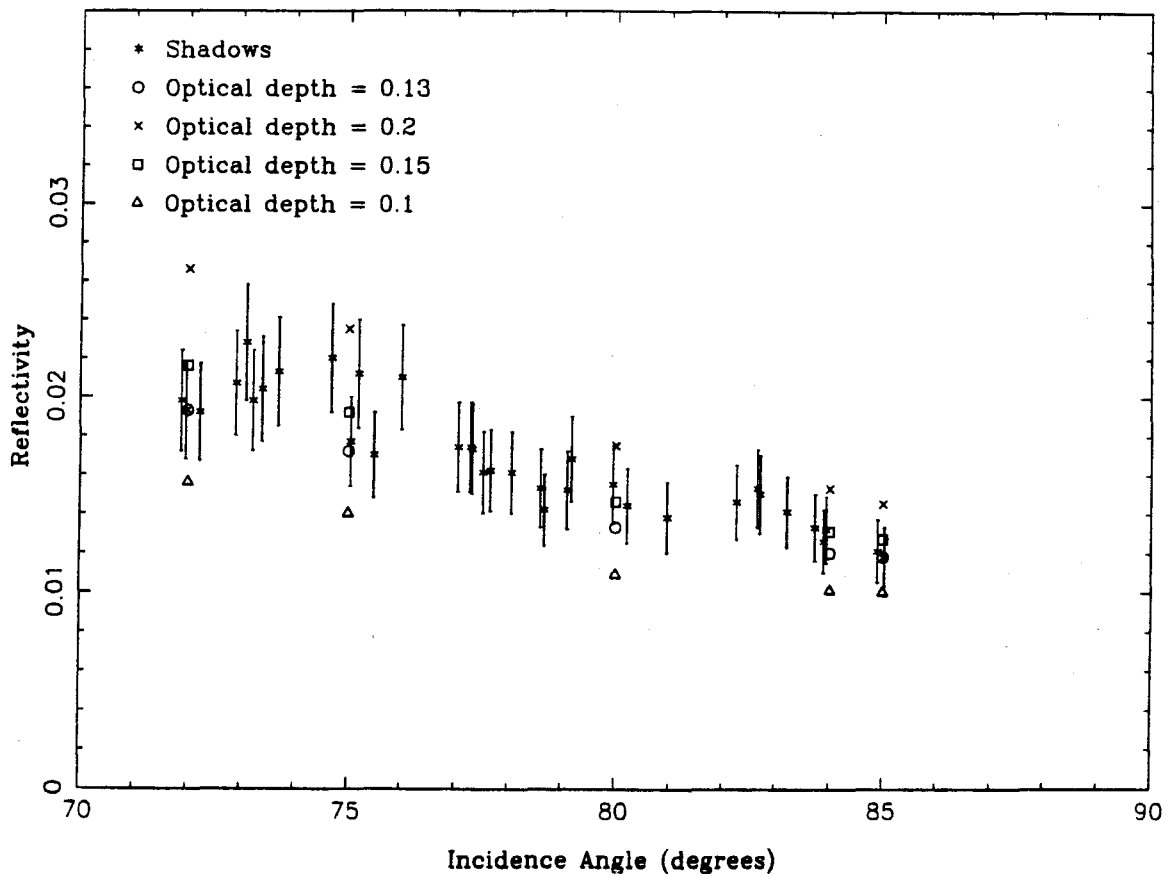


Figure B.1: Viking Orbiter 2 orbit 407 violet ($\lambda_{eff} = 0.45\mu$) shadow data with model fits, showing effect of varying optical depth. The vertical scatter in the data is due to the inclusion of unshadowed ground below the resolution of the images, especially at lower incidence angles, so the model was fit to the lower limit of the shadow data. Error bars represent the 13% absolute uncertainty in the Viking Orbiter television calibration (Klaasen *et al.*, 1977).

Filter	Violet	Green	Red
r_0	0.09	0.18	0.25
ω_0	0.57	0.79	0.85
g	0.31	0.47	0.49
Q_{ext}	2.64	2.71	2.75

Table B.1: Atmospheric dust scattering parameters.

in mind, I have endeavored to construct a model that defines a lower limit to the shadow data.

The best fit of the shadow data with the parameters described above has $\tau = 0.13$ and surface albedos and dust scattering parameters as shown in Table B.1. The spectral reflectances used are very similar to the spectral geometric albedo of “intermediate albedo” areas given by McCord and Westphal (1971), and to the reflectances of the soils at the Viking Lander 1 site (Guinness, 1981) when differences in spectral bandpass are taken into account. The effect of varying τ is shown in Figure B.1, ω_0 in Figure B.2, and g in Figure B.3. An image taken through the red filter during the same orbit (that was not included in the mosaic) was used to evaluate the atmospheric reflectance at the terminator. Several of the best shadow data points were chosen for modeling (based upon their low values in all three colors) near 72, 80, 84, and 85 degrees incidence angle, and at the terminator. The observational geometry of each of these points was determined using Supplementary Experiment Data Record (SEDR) data. The model fits the data within the 13% uncertainties except at 80°, where the shadows are evidently contaminated with illuminated ground below the resolution of the images or the dust opacity is greater.

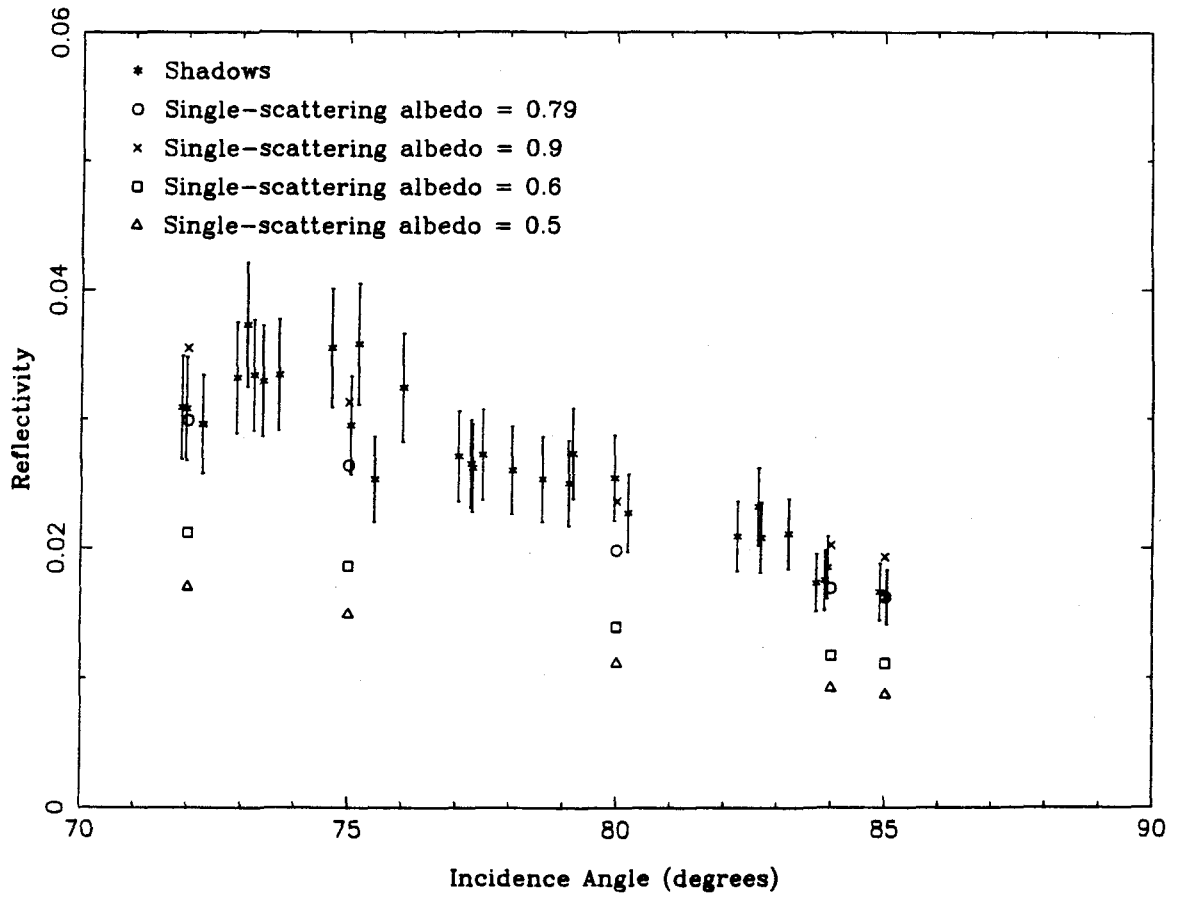


Figure B.2: Viking Orbiter 2 orbit 407 green ($\lambda_{eff} = 0.54\mu$) shadow data with model fits, showing effect of varying single-scattering albedo.

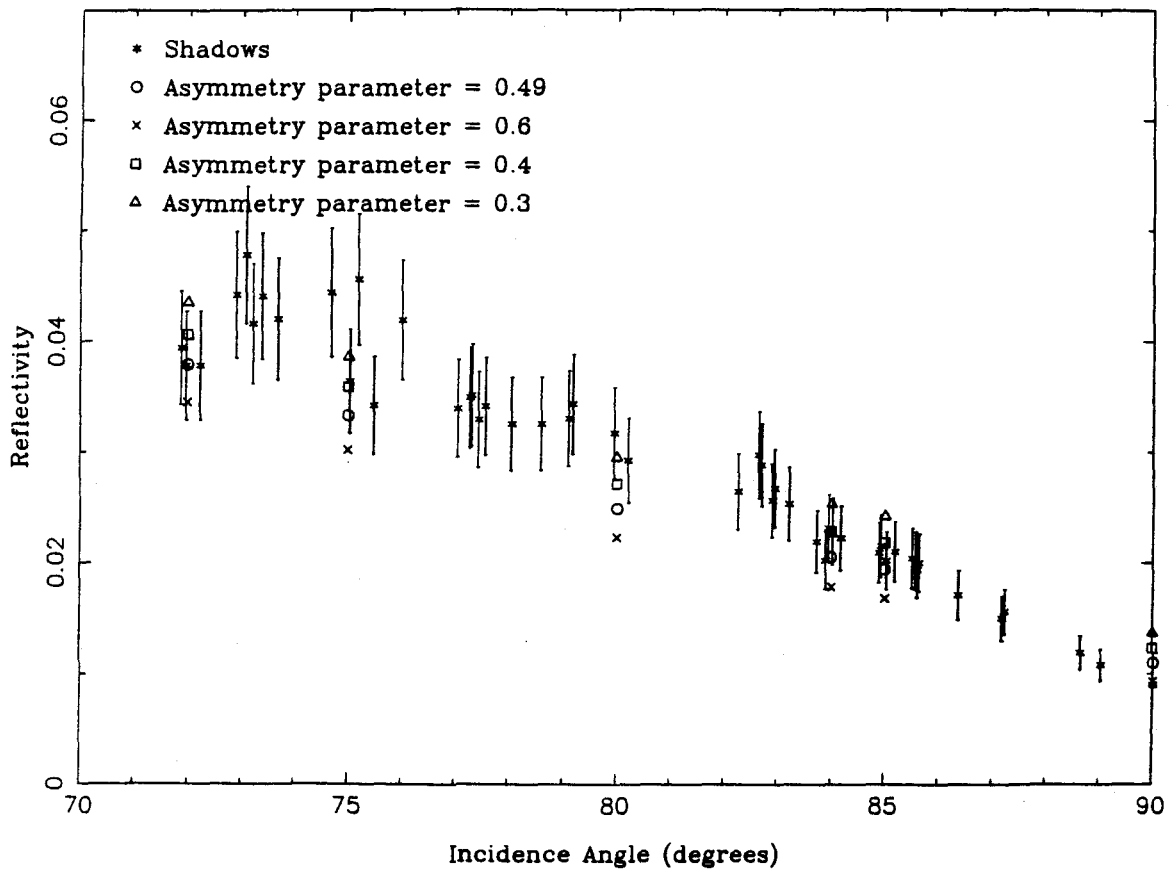


Figure B.3: Viking Orbiter 2 orbit 407 red ($\lambda_{eff} = 0.59\mu$) shadow data with model fits, showing effect of varying asymmetry parameter. Uncertainties in the shadow data are larger at high incidence angles due to the greater uncertainty in absolute calibration at low exposure levels.

Radiometric uncertainties in images exposed to low light levels are generally larger than for brighter scenes, so the discrepancy between the model and the data at the terminator is not considered serious. Variations in emission and azimuth angles across the mosaic have a significant effect on the atmospheric brightness, and have therefore been included in the model.

Once the optical depth and other model parameters have been determined in shadows, other points in the image can be modeled. Interpolation between modeled points in the image yields the approximate atmospheric brightness at any point, allowing removal of the atmospheric component of brightness across the entire image or any part of it. The interpolated atmospheric brightness is subtracted from the data value in each pixel, and the result is divided by the incoming and outgoing attenuation to find what the surface reflectivity would be if there were no atmosphere. This technique assumes that dust scattering properties and surface albedos are invariant across the image and that the shadowed regions are small compared to the dust scale height, so that their presence does not alter the atmospheric brightness. Variations in surface albedo are small in the area modeled, except in the polar frost. The effect of using low surface albedos to model atmospheric scattering over the polar cap was discussed in chapter 3. Although there is evidence in the color mosaic of spatial variations in dust opacity, it is not possible to account for such variability in this model. Errors due to interpolation are generally less than 3% (as indicated by model runs at points between those used), while variations in opacity

are seen to cause up to 20% variations in atmospheric brightness. Topographic variations in the south polar region are not precisely known, but a 1 km increase in altitude decreases the modeled atmospheric brightness by only 11%. The effect of topographic variations was not included in this model, but could be incorporated in the future.

Appendix C

FORTRAN code

The most important programs used in this study are reproduced below. All were implemented on a DEC MicroVAX II running the VMS operating system. Digital versions of these programs may be obtained by contacting the author via SPAN at MARS1::KEH.

C.1 Mariner 9 image processing software

The Mariner 9 calibration software in this section is now incorporated into PICS and are available through the U. S. Geological Survey in Flagstaff, Arizona. The program that extracts image data within IRIS footprints and creates histograms is also included in this section. The FORTRAN code is preceded by the corresponding PDF file that interfaces with the FORTRAN program, providing input and output parameters as designated by the user. These programs are intended for use under NASA's Transportable Applications Executive.

```

!*****
! BEF.PDF
!*****
PROCESS HELP=*
PARM FROM TYPE=(STRING,32)
PARM TO TYPE=(STRING,32)
PARM ITOL INTEGER,DEFAULT=(14)
PARM SL INTEGER,DEFAULT=(1)
PARM SS INTEGER,DEFAULT=(1)
PARM NL INTEGER,DEFAULT=(0)
PARM NS INTEGER,DEFAULT=(0)
PARM LINC REAL,DEFAULT=(1.)
PARM SINC REAL,DEFAULT=(1.)
END-PROC
.TITLE
BEF: Bit Error Filtering Program.
.HELP
PROGRAMMER: MARS1::KEH (Ken Herkenhoff; Caltech)
Filters 8-bit images with less than 1250 samples/line, removing bit
errors by replacing bad values with the average of 10 pixels above.
Only previously filtered data are used in calculating the average.
Pixels are filtered only if their value differs from the previous
pixel by more than the input tolerance ITOL. BEF is designed to
avoid improper filtering of real data such as limbs, but should be
used carefully in cases where large contrasts are expected. The
tolerance ITOL should be increased when filtering limb or satellite
images, for instance. BEF assumes that the first and last few pixels
of each line are in the vidicon mask and therefore do not need to be
filtered. The first two lines are filtered only minimally to assure
that the program is properly initialized.
.LEVEL1
.VAR FROM
INPUT IMAGE FILE NAME
.VAR TO
OUTPUT IMAGE FILE NAME
.VAR ITOL
FILTER TOLERANCE IN DN
.VAR SL
STARTING LINE
.VAR SS
STARTING SAMPLE
.VAR NL

```

NUMBER OF LINES

.VAR NS

NUMBER OF SAMPLES

.VAR LINC

LINE INCREMENT

.VAR SINC

SAMPLE INCREMENT

.LEVEL2

.VAR FROM

The input image must be 8-bit with less than 1250 samples per line. Reseaux should be found before BEF is run on an image, as it will remove reseau marks.

.VAR TO

The output image will be 8-bit with noise removed.

.VAR ITOL

The tolerance for the filter in DN. No filtering will occur if adjacent pixel values differ by less than ITOL. The default tolerance of 14 will preserve real data contrasts in most planetary images. Larger tolerances should be used for limb or satellite images.

.END

C PROGRAM: BEF

C

C BIT ERROR FILTERING PROGRAM

C ASSUMES VIDICON MASK AT LEFT AND RIGHT EDGES OF 8-BIT IMAGE

C

C KEN HERKENHOFF, 6/30/86; revised 8/12/87, 10/23/87

C

```

SUBROUTINE DOUSER(IBUF1,IBUF2)
LOGICAL*1 IBUF1(1),IBUF2(1),IBUF3(32767),IBUF4(32767)
INTEGER*2 WORK(1250),BOX(50),PREV(5),TOP(3),AVG,SUM
INCLUDE 'PIC$INC:TAEBAS.INC'
INCLUDE 'PIC$INC:DOIOCMN.INC'
INCLUDE 'PIC$INC:DOIOCMN2.INC'

```

```

DATA PRGNAM/' BEF'/,VERDAT/'4-NOV-87'/

```

```

IF (ISTEP.EQ.3) GO TO 100

```

```

IF (ISTEP.EQ.1) GO TO 10

```

```

IF (ISTEP.EQ.2) GO TO 20

```

```

      IF (ISTEP.EQ.4) GO TO 500
C*****
C ISTEP = 1 - Initialization (Prior to prompt of files)
C*****
  10 CONTINUE
     NBYTES = 32768
     NFI = 1          !let DOIO know there will be one input file
     NFO = 1          !let DOIO know there will be one output file
     IF (IEFLAG.EQ.1) STOP 'ERROR.'
     IEFLAG = 1
     RETURN
C*****
C ISTEP = 2 - Initialization (Post prompt of files)
C Write program name to the spooled file.
C set output bit the same the input bit.
C*****
  20 CONTINUE
     IF (IBITI(1).NE.8) STOP ' INPUT FILE MUST BE 8-BIT.'
     IBITO(1) = 8
     CALL XRINTG(BLOCK,'ITOL',1,ITOL,LEN,ICOUNT,ISTAT)
     RETURN
C*****
C ISTEP=3 - Line processing phase.
C*****
  100 CONTINUE
     CALL B2W(IBUF2(1),WORK(1),INS)
     IF (IL.GT.2) GOTO 200
     IF (IL.EQ.1) THEN
       WORK(1) = 0
       BOX(1) = 0
       DO 110 IS = 2,9
         IF (WORK(IS).GT.50) WORK(IS) = WORK(IS-1)
  110  CONTINUE
       DO 150 IS=6,INS-4
         IF ((IABS(WORK(IS)-WORK(IS-1)).LE.ITOL) GO TO 150
         SUM = 0
         DO 130 I = 1,9
           BOX(I) = WORK(IS+I-5)
           SUM = SUM + BOX(I)
  130  CONTINUE
         BOX(5) = WORK(IS-5)
         SUM = SUM - WORK(IS) + WORK(IS-5)

```

```

      N = 9
      NBP = 4
      DO 140 I = 7,9
        IF (IIABS(BOX(I) - BOX(I-1)).LE.ITOL) NBP = NBP - 1
140    CONTINUE
        CALL MEDFLT(WORK,BOX,SUM,IL,IS,ITOL,N,INS,NBP)
150    CONTINUE
        DO 160 IS=INS-3,INS
          IF (IIABS(WORK(IS)-WORK(IS-1)).GT.ITOL) WORK(IS)=WORK(IS-1)
160    CONTINUE
          CALL W2B(WORK(1),IBUF1(1),INS)
          CALL B2B(IBUF1(1),IBUF4(1),INS)
          RETURN
          END IF

      IF (WORK(1).GT.50) WORK(1) = 0          ! IL = 2
      IF (WORK(2).GT.50) WORK(2) = WORK(1)
      DO 190 IS = 3,INS-2
        IF(IIABS(WORK(IS)-WORK(IS-1)).LE.ITOL) GO TO 190
        IF(IIABS(WORK(IS)-WORK(IS+1)).LE.ITOL.AND.IIABS(WORK(IS+1)-
&          WORK(IS+2)).LE.ITOL) GO TO 190
        SUM = 0
        CALL B2W(IBUF4(IS-2),PREV(1),5)
        DO 170 I = 1,5
          SUM = SUM + PREV(I)
          BOX(I) = PREV(I)
170    CONTINUE
          BOX(6) = WORK(IS-2)
          BOX(7) = WORK(IS-1)
          BOX(8) = WORK(IS+1)
          BOX(9) = WORK(IS+2)
          SUM = SUM + BOX(6) + BOX(7) + BOX(8) + BOX(9)
          NBP = 2
          IF (IIABS(BOX(8) - BOX(9)).LE.ITOL) NBP = 1
          N = 9
          CALL MEDFLT(WORK,BOX,SUM,IL,IS,ITOL,N,INS,NBP)
190 CONTINUE
          IF (IIABS(WORK(INS-1)-WORK(INS-2)).GT.ITOL)
&          WORK(INS-1) = WORK(INS-2)
          IF (IIABS(WORK(INS)-WORK(INS-1)).GT.ITOL)
&          WORK(INS) = WORK(INS-1)
          CALL W2B(WORK(1),IBUF1(1),INS)

```

```

CALL B2B(IBUF1(1),IBUF3(1),INS)
RETURN

200 IF (WORK(1).GT.50) WORK(1) = 0          ! IL > 2
    IF (WORK(2).GT.50) WORK(2) = WORK(1)
    DO 300 IS = 3,INS-2
    IF (IIABS(WORK(IS)-WORK(IS-1)).LE.ITOL) GO TO 300
    IF (IIABS(WORK(IS)-WORK(IS+1)).LE.ITOL.AND.
    &      IIABS(WORK(IS+2)-WORK(IS+1)).LE.ITOL) GO TO 300
    SUM = 0
    CALL B2W(IBUF3(IS-2),PREV(1),5)
    CALL B2W(IBUF4(IS-1),TOP(1),3)
    DO 210 I = 1,3
        SUM = SUM + WORK(IS-I+1) + PREV(I) + TOP (I)
        BOX(I) = TOP(I)
        BOX(I+3) = PREV(I)
        BOX(I+6) = WORK(IS-I+1)
210    CONTINUE
    BOX(10) = PREV(4)
    BOX(11) = PREV(5)
    BOX(12) = WORK(IS+1)
    BOX(13) = WORK(IS+2)
    SUM = SUM + WORK(IS+2) + WORK(IS+1) + PREV(4) + PREV(5)
    N = 13
    CALL MEDFLT(WORK,BOX,SUM,IL,IS,ITOL,N,INS,3)
300 CONTINUE
    IF (IIABS(WORK(INS-1)-WORK(INS-2)).GT.ITOL)
    &      WORK(INS-1) = WORK(INS-2)
    IF (IIABS(WORK(INS)-WORK(INS-1)).GT.ITOL)
    &      WORK(INS) = WORK(INS-1)
    CALL W2B(WORK(1),IBUF1(1),INS)
    CALL B2B(IBUF3(1),IBUF4(1),INS)
    CALL B2B(IBUF1(1),IBUF3(1),INS)
    RETURN
C*****
C ISTEP=4 - Final line processing phase
C      add the processing history text and return to caller
C*****
500 CONTINUE
    ENCODE(80,510,IBUF1) ITOL
510 FORMAT('BEF: Bit Errors Filtered with ITOL =',I3)
    IBIT0(1) = 40

```

```

RETURN
END

SUBROUTINE MEDFLT(WORK,BOX,SUM,IL,IS,ITOL,N,INS,NEW)
C
C MEDIAN FILTER FOR BIT ERROR FILTERING PROGRAM
C
INTEGER*2 WORK(INS),BOX(N),SUM,AVG,IDIFF,TEMP

MNGP = N - NEW
MTOL = ITOL/(N/2)
NH = N
NL = 1

C
C SORT VALUES IN BOX
C
DO 200 I = N-1,1,-1
  NSTEP = N-I
  DO 100 J = 1,NSTEP
    IF (BOX(J).LE.BOX(J+I)) GO TO 100
    TEMP = BOX(J)
    BOX(J) = BOX(J+I)
    BOX(J+I) = TEMP
  100 CONTINUE
200 CONTINUE
  M = (N+1)/2
  AVG = (SUM + M)/N
  IDIFF = AVG - BOX(M)
  IF (IIABS(IDIFF).GT.MTOL) THEN
  IF (IDIFF.GT.0) THEN
    SUM = SUM - BOX(NH)
    NH = NH - 1
  ELSE
    SUM = SUM - BOX(NL)
    NL = NL + 1
  END IF
  N = N - 1
  IF (N.GE.MNGP) GO TO 200
C WRITE (6,210) MNGP,IS,IL,AVG
C 210 FORMAT(' Less than',I3,' good points around sample',
C & I4,' on line',I4,': AVG =',I4)

```

```
AVG = WORK(IS)
END IF
WORK(IS) = AVG
RETURN
END
```

```
! IRIST.PDF
PROCESS HELP=*
PARM FROM (STRING,32)
PARM TO (STRING,32)
PARM SPECN REAL
PARM XOFF REAL, DEFAULT=(0.0)
PARM YOFF REAL, DEFAULT=(0.0)
PARM NL INTEGER, DEFAULT=(800)
PARM NS INTEGER, DEFAULT=(950)
PARM SL INTEGER, DEFAULT=(1)
PARM SS INTEGER, DEFAULT=(1)
PARM LINC REAL, DEFAULT=(1.0)
PARM SINC REAL, DEFAULT=(1.0)
END-PROC
.TITLE
IRIST
.HELP
IRIST EXTRACTS IRIS FOOTPRINTS FROM MARINER 9 IMAGE DATA, USING 10
X,Y POINTS GIVEN IN DATA FILE. PRINTS HISTOGRAM INFORMATION TO FILE
####.HIS, WHERE #### IS THE SPECTRUM NUMBER. HISTOGRAMS FROM
SEVERAL INTERMEDIATE FOOTPRINTS BETWEEN THE STARTING AND ENDING
ONES ARE ADDED TOGETHER.
.LEVEL1
.VAR FROM
INPUT IMAGE FILE NAME
.VAR TO
OUTPUT IMAGE FILE NAME
.VAR SPECN
SPECTRUM NUMBER
.VAR XOFF
X (SAMPLE) OFFSET
.VAR YOFF
Y (LINE) OFFSET
.var nl
Number of lines
.var ns
Number of samples
.var sl
Starting line
.var ss
Starting sample
.END
```

```

C PROGRAM: IRIST
C
C   EXTRACTS IRIS FOOTPRINT STATISTICS FROM MARINER 9 IMAGE DATA
C   GIVEN 10 X,Y POINTS DEFINING FOOTPRINT
C   MODIFIED TO INCLUDE ARBITRARY X,Y OFFSET OF FOOTPRINTS, 6/25/86
C
C   KEN HERKENHOFF, 3/4/1986,7/7/87
C
      SUBROUTINE DOUSER(IBUF1,IBUF2)
      INTEGER*2 IBUF1(1),IBUF2(1)
      CHARACTER*5 CHSPEC
      CHARACTER*32 FILOUT,VFILE
      CHARACTER*1 CSTAR,CCUM
      CHARACTER*132 COUT,CBLANK
      CHARACTER*4 OLABEL
      BYTE IA(950,800),IN(512,512,9)
      DIMENSION IVXX(41),IVYY(41),VX(10,3),VY(10,3),
&   VVX(10,9),VVY(10,9),VVXX(10),VVYY(10),IHIST(400,9),ICOUNT(9),
&   TOT(400),HIST(400,9),AVX3(41),AVY3(41)
      DATA NX/950/,NY/800/,NV/10/,NSP/9/,PRGNAM/' IRIST '/,
&
&           VERDAT/'7-JUL-87'/
      INCLUDE 'DUAO:[TAE.IP]DOIOCMN.FOR'
      INCLUDE 'DUAO:[TAE.IP]DOIOCMN2.FOR'

C           Include TAE block
      INCLUDE 'DUAO:[TAE.INC]PGMINC.FIN'
      COMMON /TAEBLK/ BLOCK
      INTEGER BLOCK(xprdim) !array to receive the v-block
      INTEGER*4 NBYTES
      LOGICAL*1 LBUF(131072)
      COMMON /BUFFER/ NBYTES,LBUF
      DATA IEFLAG/0/

      GO TO(10,20,100,500),ISTEP
C*****
C ISTEP = 1 - Initialization (Prior to prompt of files)
C*****
      10 CONTINUE
      IF (IEFLAG.EQ.1) STOP
      IEFLAG =1

```

```

NBYTES = 131072
NFI = 1          !let DOIO know there will be ONE input file
NFO = 1          !let DOIO know there will be ONE output file
RETURN
C*****
C ISTEP = 2 - Initialization (Post prompt of files)
C Write program name to the spooled file.
C set output bit the same the input bit.
C*****
  20 CONTINUE
C
  IF (IBITI(1).NE.16) STOP 'Input image file not 16 bit.'
  IBITO(1) = 16
  CALL XRREAL(BLOCK,'SPECN',1,SPECN,ICOUNT,ISTAT)
  CALL XRREAL(BLOCK,'XOFF',1,XOFF,ICOUNT,ISTAT)
  CALL XRREAL(BLOCK,'YOFF',1,YOFF,ICOUNT,ISTAT)
C
  XMIN=950.
  YMIN=800.
  XMAX=1.
  YMAX=1.
  DO 40 J=1,3
  ENCODE(5,710,CHSPEC) SPECN-2.+FLOAT(J)
710 FORMAT(F5.0)
  IF (J.EQ.2) THEN
  FILOUT='WORK1:[KEH.M9.IRIS] '//CHSPEC//'HIS'
  OLABEL = CHSPEC(1:4)
  END IF
  VFILE='WORK1:[KEH.M9.IRIS] '//CHSPEC//'DAT'
  OPEN (UNIT=1,FILE=VFILE,STATUS='OLD',READONLY)
  DO 50 I=1,NV
    READ (1,*) VY(I,J),VX(I,J)
    VX(I,J) = VX(I,J) + XOFF
    VY(I,J) = VY(I,J) + YOFF
    IF (VX(I,J).LT.XMIN) XMIN=VX(I,J)
    IF (VY(I,J).LT.YMIN) YMIN=VY(I,J)
    IF (VX(I,J).GT.XMAX) XMAX=VX(I,J)
    IF (VY(I,J).GT.YMAX) YMAX=VY(I,J)
  50 CONTINUE
  CLOSE (1)
  40 CONTINUE
  IF (XMAX-XMIN.GT.500.0.OR.YMAX-YMIN.GT.500.) THEN

```

```

WRITE (IPR,51)
WRITE (ISP,51)
51 FORMAT (' FOOTPRINT MORE THAN 512 PIXELS ACROSS. ')
STOP
END IF
MINX=NINT(XMIN)-40
MINY=NINT(YMIN)-40
CALL STEP (NSP,NV,VX,VY,VVX,VVY)
DO 60 K=1,NSP
DO I=1,NY
DO J=1,NX
IA(J,I) = 0
END DO
END DO
DO I=1,NV
VVXX(I) = VVX(I,K)
VVYY(I) = VVY(I,K)
END DO
CALL SMOOTHLIPS (VVXX,VVYY,AVX3,AVY3)
DO I=1,41
IVXX(I) = NINT(AVX3(I))
IVYY(I) = NINT(AVY3(I))
IF(IVXX(I).LT.0.OR.IVXX(I).GT.NX) WRITE (IPR,57) K
IF(IVYY(I).LT.0.OR.IVYY(I).GT.NY) WRITE (IPR,58) K
57 FORMAT(' ELLIPSE',I2,' EXTENDS OUTSIDE LEFT OR RIGHT EDGE OF',
& ' IMAGE. ')
58 FORMAT(' ELLIPSE ',I1,
& ' EXTENDS OUTSIDE TOP OR BOTTOM OF IMAGE')
END DO
CALL IDGET1 (IVXX,IVYY,40,NX,NY,IA)
WRITE (*,59) K
59 FORMAT (' POINTS INSIDE ELLIPSE ',I1,' FOUND. ')
DO J=1,512
DO I=1,512
IF (I+MINX-1.LE.NX.AND.J+MINY-1.LE.NY)
& IN(I,J,K) = IA(I+MINX-1,J+MINY-1)
END DO
END DO
60 CONTINUE
C INITIALIZE HISTOGRAM
DO 80 K = 1,NSP
ICOUNT(J) = 0

```

```

      DO 80 I = 1,400
        IHIST(I,K) = 0
        HIST(I,K)=0.
80 CONTINUE
      DO 90 I=1,400
        TOT(I) = 0.
90 CONTINUE
      CSTAR='*'
      CCUM='%'
      DO 95 I=1,132
        CBLANK(I:I)=' '
95 CONTINUE
      IADD = 0
900 IF (JERR.GT.0) CALL ERRMES('GEOMLB','GEOMLB',JERR,'AB')
      RETURN
C*****
C ISTEP=3 - Line processing phase.
C       look at bit type and transfer input file to output file
C*****
100 CONTINUE
      CALL I2I(IBUF2,IBUF1,INS)
      IF (ILI.LT.MINY.OR.ILI.GT.MINY+511) RETURN
      IF (IADD.EQ.0) IADD = (IBUF2(MINX+30)+IBUF2(NINT(XMAX)-30))/20
      ILIS = ILI - MINY + 1
      DO 400 ISPN=1,NSP
        DO 200 IS = 1,INS
          IF (IS.LT.MINX.OR.IS.GT.MINX+511) GOTO 200
          IF (IN(IS-MINX+1,ILIS,ISPN).EQ.1) THEN
            IBUF1(IS) = IBUF1(IS) + IADD
C       ICOUNT IS THE NUMBER OF PIXELS IN EACH FOOTPRINT
            ICOUNT(ISPN) = ICOUNT(ISPN) + 1
            IH = NINT(FLOAT(IBUF2(IS))/20.)
            IF (IH.GT.400) IH = 400
C       IHIST IS THE NUMBER OF PIXELS AT LEVEL IH IN FOOTPRINT ISPN
            IHIST(IH,ISPN) = IHIST(IH,ISPN) + 1
          END IF
        200 CONTINUE
      400 CONTINUE
      RETURN
C*****
C ISTEP=4 - Final line processing phase
C       add the processing history text and return to caller

```

```

C*****
500 CONTINUE
   DO 600 I = 1,NSP
     DO 600 J = 1,400
C HIST IS THE PERCENTAGE OF FOOTPRINT I THAT IS AT LEVEL J
     HIST(J,I) = 100.*IHIST(J,I)/FLOAT(ICOUNT(I))
600 CONTINUE
   DO 700 I=1,NSP
     DO 700 J=1,400
C TOT IS THE TOTAL PERCENTAGE OF PIXELS AT LEVEL J IN ALL FOOTPRINTS
     TOT(J) = TOT(J) + HIST(J,I)/FLOAT(NSP)
700 CONTINUE
   OPEN (8,FILE=FILOUT,STATUS='NEW')
   WRITE (8,801) OLABEL
801  FORMAT (' HISTOGRAM FOR SPECTRUM ',A,':',/,
&          ' DN FREQUENCY TOTAL')
     CUMTOT=0.
     DO 840 J=1,400
       CUMTOT=CUMTOT+TOT(J)
       I=NINT(10.*TOT(J))
       IF (I.GT.105) I = 105
       II=NINT(CUMTOT)
       COUT=CBLANK
       DO 830 K=1,I
         COUT(K:K)=CSTAR
830      CONTINUE
       COUT(II:II)=CCUM
       WRITE (8,835) 20*J,TOT(J),CUMTOT,COUT(1:105)
835  FORMAT      (1X,I4,2F10.4, ' |',A)
840  CONTINUE
     WRITE (8,*) 'DONE'
     CLOSE (UNIT=8)
     RETURN
     END

```

```
!*****
!LINEARIZE.PDF
```

```
!*****
```

```
PROCESS HELP=*
```

```
PARM FROM TYPE=(STRING,32)
```

```
PARM TO TYPE=(STRING,32)
```

```
PARM SL INTEGER,DEFAULT=(1)
```

```
PARM SS INTEGER,DEFAULT=(1)
```

```
PARM NL INTEGER,DEFAULT=(0)
```

```
PARM NS INTEGER,DEFAULT=(0)
```

```
PARM LINC REAL,DEFAULT=(1.)
```

```
PARM SINC REAL,DEFAULT=(1.)
```

```
END-PROC
```

```
.TITLE
```

```
LINEARIZE - Linearize Mariner 9 images
```

```
.HELP
```

```
PROGRAMMER: MARS1::KEH (Ken Herkenhoff, Caltech)
```

Linearizes Mariner 9 images, using dark current frame from PIC\$MAR9 and calibration parameters described in Herkenhoff et al. (1988). Output image is 16-bit, input file must be 8-bit. DN values in output image are proportional to observed brightness, calculated as follows for each pixel:

OUTPUT = DNT + A*(DNT**3 - 128 DNT**2) where

DNT = SCALE*(INPUT - 128*B*INPUT/(INPUT + D)) and A depends upon the line L and sample S location in the frame:

A = C(1)*L*L + C(2)*L + C(3)*S + C(4)*L*S + C(5)

The constants A, B, D and SCALE are different for each camera, and the five C coefficients were found using preflight calibrations data. An estimate of the uncertainty in linearization is given in the reference.

Reference:

Herkenhoff et al., (1988). "Mariner 9 Television Calibration--Revisited." Icarus 75, 133-145.

```
.LEVEL1
```

```
.VAR FROM
```

```
INPUT IMAGE FILE NAME
```

```
.VAR TO
```

```
OUTPUT IMAGE FILE NAME
```

```
.VAR SL
```

```
STARTING LINE
```

```
.VAR SS
```

STARTING SAMPLE

.VAR NL

NUMBER OF LINES

.VAR NS

NUMBER OF SAMPLES

.VAR LINC

LINE INCREMENT

.VAR SINC

SAMPLE INCREMENT

.LEVEL2

.VAR FROM

The input Mariner 9 image must be 8-bit, and should have had noise and reseaux removed.

.VAR TO

The output image will be 16-bit, ranging from 0 to about 350 DN maximum. DN values in the output image are proportional to the observed brightness only at the center of the image,

.VAR SL

Starting line. The default is 1 which will start the processing with the first line or top of the image.

.VAR SS

Starting sample. The default is 1 which will start the processing with the first sample or left side of the image.

.VAR NL

Number of lines. The default is 0 which will process all lines of the image.

.VAR NS

Number of samples. The default is 0 which will process all samples of the image.

.VAR LINC

Line increment: The default is 1.0 which will process each line of the image. LINC=2.0 will process every other line and the output image will have half as many lines as the input. LINC=.5 will process each line twice and the output image will have twice as many lines as the input.

.VAR SINC

Sample increment. The default is 1.0 which will process each sample of the image. SINC=2.0 will process every other sample and the output image will have half as many samples as the input. SINC=.5 will process each sample twice and the output image will have twice as many samples as the input.

.END

```

SUBROUTINE DOUSER(IBUF1,IBUF2,IBUF3)
INTEGER*2 IBUF1(1),INLINE(832),DCLINE(832)
LOGICAL*1 IBUF2(1),IBUF3(1)
DIMENSION C(5),CA(5),CB(5)
CHARACTER CAM*1,LABEL*80
C*****
C
C PROGRAM: LINEARIZE
C
C     LINEARIZES MARINER 9 RAW IMAGE DATA:
C     SUBTRACTS DARK CURRENT, REMOVES NON-LINEARITIES IN TWO STEPS:
C     DNT = (DN - 128 * C * DN / (DN + D)) * SCALE
C     DNL(OUTPUT) = DNT + A * (DNT**3 - 128 * DNT**2)
C
C     WRITTEN BY KEN HERKENHOFF, CALTECH 170-25
C
C*****
      INCLUDE 'PIC$INC:TAEBAS.INC'
      INCLUDE 'PIC$INC:DOIOCMN.INC'
      INCLUDE 'PIC$INC:DOIOCMN2.INC'

      DATA IEFLAG/O/,CA/.6999002E-11,-.1260765E-07,.3610607E-08,
&      .168951E-10,.9157377E-05/,SCALEA/.90792416/,
&      BA/.1029981673/,DA/2./
      DATA CB/-.6654653E-11,.1243616E-07,.5302868E-09,-.1025861E-10,
&      .8699718E-05/,SCALEB/.9436151/,BB/.05998745874/,DB/.5/,
&      PRGNAM/'LINEARIZ'/,VERDAT/'25-AUG-87'/

      IF (ISTEP.EQ.3) GOTO 100 !For line processing phase
      IF (ISTEP.EQ.1) GOTO 10 !Initialization call
      IF (ISTEP.EQ.2) GOTO 20 !Initialization call
      IF (ISTEP.EQ.4) GOTO 500 !Final processing phase
C*****
C ISTEP = 1 - Initialization (Prior to prompt of files)
C*****
10 CONTINUE
      IF (IEFLAG.EQ.1) STOP
      IEFLAG = 1
      NFI = 2           !let DOIO know there will be two input files
      NFO = 1           !let DOIO know there will be one output file

```

```

        IFLAGI(2) = 1      !SECOND INPUT FILE IS NAMED IN ISTEP=2
        RETURN
C*****
C ISTEP = 2 - Initialization (Post prompt of files)
C Write program name to the spooled file.
C set output bit the same the input bit.
C*****
    20 CONTINUE
        IF (IBITI(1).NE.8) GOTO 9000
        IBITO(1) = 16

        CALL DISKEY ('RD',LUNI(1),ISBLKI(1),'FRAME_ID',LABEL,LEN,IERR)
        IF(IERR.LT.0) CALL ERRMES('GEOMLB','GEOMLB',6,'CO')
        CALL CHAR2I(LABEL,IFSC,1)
        IERR = 2
        CALL DISKEY ('RD',LUNI(1),ISBLKI(1),'CAMERA',CAM,LEN,IERR).
        IF (IERR.LT.0) WRITE (IPR,903)
903 FORMAT (' CAMERA NOT FOUND. ')

        IF (CAM.EQ.'A') THEN
            DO 30 I=1,5
                C(I) = CA(I)
    30     CONTINUE
            SCALE = SCALEA
            B = BA
            D = DA
            FILEI(2)='PIC$WORK:[MARINER9]1A0DC'
            IF(IFSC.GT.2927465) FILEI(2)='PIC$WORK:[MARINER9]72A6DC'
            IF(IFSC.GT.5436914) FILEI(2)='PIC$WORK:[MARINER9]139A2DC'
            IF(IFSC.GT.6768823) FILEI(2)='PIC$WORK:[MARINER9]150A31DC'
            IF(IFSC.GT.8243586) FILEI(2)='PIC$WORK:[MARINER9]221A4DC'
            IF(IFSC.GT.11000000) WRITE(ISP,905) IFSC
905     FORMAT(' DAS',I9,' in extended mission, no good',
&           ' A camera dark current. ')
        ELSE
            IF (CAM.EQ.'B') THEN
                DO 40 I = 1,5
                    C(I) = CB(I)
    40     CONTINUE
            SCALE = SCALEB
            B = BB
            D = DB

```

```

FILEI(2)='PIC$WORK:[MARINER9]1BODC'
IF(IFSC.GT.2031918) FILEI(2)='PIC$WORK:[MARINER9]22B31DC'
IF(IFSC.GT.3051127) FILEI(2)='PIC$WORK:[MARINER9]59B1DC'
IF(IFSC.GT.3874610) FILEI(2)='PIC$WORK:[MARINER9]68B2DC'
IF(IFSC.GT.4254325) FILEI(2)='PIC$WORK:[MARINER9]80B17DC'
IF(IFSC.GT.5340091) FILEI(2)='PIC$WORK:[MARINER9]129B9DC'
IF(IFSC.GT.6589168) FILEI(2)='PIC$WORK:[MARINER9]150B32DC'
IF(IFSC.GT.8243586) FILEI(2)='PIC$WORK:[MARINER9]221B3DC'
IF(IFSC.GT.10119506) FILEI(2)='PIC$WORK:[MARINER9]262B3DC'
IF(IFSC.GT.11000000) FILEI(2)='PIC$WORK:[MARINER9]479B1DC'
ELSE
  STOP ' ERROR:  INVALID CAMERA.'
END IF
END IF
WRITE(ISP,910) FILEI(1)
910 FORMAT(' Raw data file: ',A)
WRITE(ISP,915) FILEI(2)
915 FORMAT(' Dark Current file: ',A)

RETURN

C*****
C ISTEP=3 - Line processing phase.
C       look at bit type and transfer input file to output file
C*****
100 CONTINUE
  CALL B2W(IBUF2,INLINE,INS)
  CALL B2W(IBUF3,DCLINE,INS)

  DO 110 IS = 1,INS
    A = C(1)*IL*IL+C(2)*IL+C(3)*IS+C(4)*IL*IS+C(5)
    DN = INLINE(IS) - DCLINE(IS)
    DND = DN + D
    IF(DND.LE.0.) DND = 1.
    DNT = SCALE*(DN + B*DN/DND)
    IBUF1(IS) = ININT(DNT + A*(DNT**3 - 128.*DNT*DNT))
  110 CONTINUE

RETURN

C*****
C ISTEP=4 - Final line processing phase
C       add the processing history text and return to caller
C*****

```

```
500 CONTINUE
    DO LEN = 32,1,-1
        IF(ICHAR(FILEI(1)(LEN:LEN)).NE.32) GOTO 600
    END DO
600 DO LEN1 = 32,1,-1
    IF(ICHAR(FILEI(2)(LEN1:LEN1)).NE.32) GOTO 700
    END DO
700 ENCODE(32+LEN+LEN1,980,IBUF1) FILEI(1)(1:LEN),FILEI(2)(1:LEN1)
980 FORMAT('LINEARIZE: Raw file: ',A,' DC file: ',A)
    IBITO(1) = 32 + LEN + LEN1
    RETURN
C*****
C OOPS bit type not 8-bit
C*****
9000 CONTINUE
    WRITE(IPR,990)
990 FORMAT(' *** ERROR *** input file must be 8-bit data')
    IERROR = 1
    RETURN
    END
```

```

!M9MLRP.PDF
PROCESS HELP=*
  PARM FROM TYPE=(STRING,32),COUNT=1
  PARM TO TYPE=(STRING,32),COUNT=1
  PARM SL INTEGER,DEFAULT=(1)
  PARM SS INTEGER,DEFAULT=(1)
  PARM NL INTEGER,DEFAULT=(0)
  PARM NS INTEGER,DEFAULT=(0)
  PARM LINC REAL,DEFAULT=(1.)
  PARM SINC REAL,DEFAULT=(1.)
END-PROC

.TITLE
M9MLRP:  Mariner 9 Missing Line Repair Program
.HELP
PROGRAMMER:  MARS1::KEH (Ken Herkenhoff, Caltech)
M9MLRP repairs missing lines in Mariner 9 images by searching for
saturated pixels in the first two samples of each line.  The
previous line is simply copied onto the missing line.  In most
cases, missing lines in Mariner 9 images are flagged by two
saturated pixels followed by two zeros.  If this
marker is not found, the output line simply equals the input line.
.LEVEL1
.VAR FROM
INPUT IMAGE FILE NAME
.VAR TO
OUTPUT IMAGE FILE NAME
.VAR SL
STARTING LINE
.VAR SS
STARTING SAMPLE
.VAR NL
NO. OF LINES
.VAR NS
NO. OF SAMPLES
.VAR LINC
LINE INCREMENT
.VAR SINC
SAMPLE INCREMENT
.LEVEL2
.VAR FROM
The input image is a raw (8-bit) Mariner 9 image.
.VAR TO

```

The output image will be 8-bit with missing lines removed.
 .END

CP KEN HERKENHOFF

CL F

CD CORRECTS MISSING IMAGE DATA BY DUPLICATING PREVIOUS LINE

SUBROUTINE DOUSER(IBUF1,IBUF2)

IMPLICIT INTEGER*4 (I-N)

LOGICAL*1 IBUF1(1), IBUF2(1), IBUF3(32767)

C*****

C PROGRAM: M9MLRP

C

C This program will correct missing data by copying the
 C previous corresponding data.

C

C*****

INCLUDE 'PIC\$INC:TAEBAS.INC'

INCLUDE 'PIC\$INC:DOIOCMN.INC'

INCLUDE 'PIC\$INC:DOIOCMN2.INC'

C

DATA PRGNAM/' M9MLRP'/, VERDAT/'26-JUN-86'/

IF (ISTEP.EQ.3) GOTO 100 !The line processing phase.

IF (ISTEP.EQ.1) GOTO 10 !Initialization call

IF (ISTEP.EQ.2) GOTO 20 !Initialization call

IF (ISTEP.EQ.4) GOTO 500 !Final processing phase

C*****

C ISTEP = 1 - Initialization (prior to prompt of files)

C*****

10 CONTINUE

NBYTES = 32768

NFI = 1 !One input file to be returned to DOIO.

NFO = 1 !One output file to be returned to DOIO.

IF (IEFLAG.EQ.1) STOP

IEFLAG = 1

RETURN

C*****

C ISTEP = 2 - Initialization (post prompt of files)

C Write program name to the spooled file.

C Set output bit type the same as the input bit type.

C*****

```

20      CONTINUE
      IF (IBITI(1).NE.8) STOP ' INPUT FILE MUST BE 8-BIT.'
      IBITO(1) = IBITI(1)
      MNL = 0
      RETURN

C*****
C ISTEP = 3 - Line processing phase.
C*****
100     CONTINUE
      IF (IBUF2(1).NE.-1) THEN
      CALL B2B(IBUF2,IBUF3,INS)
      CALL B2B(IBUF2(1),IBUF1(1),INS)
      RETURN
      END IF
      IF (IBUF2(2).NE.-1.OR.IBUF2(3).NE.0.OR.IBUF2(4).NE.0) RETURN
      MNL = MNL + 1
      CALL B2B(IBUF3,IBUF1,INS)
      RETURN

C*****
C ISTEP = 4 - Final line processing phase.
C      Add the processing history text and return to caller.
C*****
500     CONTINUE
      ENCODE(36,970,IBUF1) MNL
970     FORMAT('M9MLRP:',I5,' missing lines repaired.')
      IBITO(1) = 36
      RETURN
      END

```

```

! M9PSR.PDF
PROCESS HELP=*
PARM FROM (STRING,32), COUNT=3
PARM TO (STRING,32)
PARM NL INTEGER, DEFAULT=(700)
PARM NS INTEGER, DEFAULT=(832)
PARM SL INTEGER, DEFAULT=(1)
PARM SS INTEGER, DEFAULT=(1)
PARM LINC REAL, DEFAULT=(1.0)
PARM SINC REAL, DEFAULT=(1.0)
END-PROC
.TITLE
M9PSR: Mariner 9 pinstripe removal
.HELP
M9PSR remove pinstripe noise by subtracting the difference between
1 X 25 and 7 X 25 low-pass filtered versions of the input image.
Only differences of 2 DN or less are subtracted. Pinstripe noise
is present in most Mariner 9 images, appearing as vertical lines
about one pixel wide and separated by about 6 samples. Their
amplitude is usually about 2 DN. All images must be 16-bit;
the output image will also be 16-bit. FLT16B may be used to
create the two filtered versions of the input image.
See PSFILT.PDF for automated filtering.
.LEVEL1
.VAR FROM
INPUT IMAGE FILE NAME
1 X 25 FILTERED VERSION
7 X 25 FILTERED VERSION
.VAR TO
OUTPUT IMAGE FILE NAME
.VAR NL
NUMBER OF LINES
.VAR NS
NUMBER OF SAMPLES
.VAR SL
STARTING LINE
.VAR SS
STARTING SAMPLE
.VAR LINC
LINE INCREMENT
.VAR SINC
SAMPLE INCREMENT

```

.LEVEL2

.VAR FROM

The input image must be 16-bit, and two low-pass filtered versions of the input image must be supplied. The procedure PSFILT will filter the image using FLT16B and run M9PSR. The input image must not have been geometrically transformed in any way, and is typically the result of level 1 processing (see M9LEVEL1).

.VAR TO

The output image will be 16-bit, with pinstripes removed.

.END

C PROGRAM: M9PSR

C

C REMOVES PINSTRIPES FROM MARINER 9 FRAMES

C

```

SUBROUTINE DOUSER(IBUF1,IBUF2,IBUF3,IBUF4)
INTEGER*2 IBUF1(1),IBUF2(1),IBUF3(1),IBUF4(1),IDIFF
INCLUDE 'PIC$INC:TAEBAS.INC'
INCLUDE 'PIC$INC:DOIOCMN.INC'
INCLUDE 'PIC$INC:DOIOCMN2.INC'
DATA PRGNAM/' M9PSR'/',VERDAT/'17-AUG-1987'/

```

GO TO(10,20,100,500),ISTEP

C*****

C ISTEP = 1 - Initialization (Prior to prompt of files)

C*****

10 CONTINUE

IF (IEFLAG.EQ.1) STOP

IEFLAG =1

NFI = 3 !let DOIO know there will be THREE input files

NFO = 1 !let DOIO know there will be ONE output file

RETURN

C*****

C ISTEP = 2 - Initialization (Post prompt of files)

C Write program name to the spooled file.

C set output bit the same the input bit.

C*****

20 CONTINUE

IF (IBITI(1).NE.16) THEN

WRITE (IPR,901)

```
901 FORMAT (' *** ERROR *** INPUT FILE MUST BE 16 BIT DATA')
      IERROR = 1
      RETURN
    END IF
      IBITO(1) = 16
      RETURN
C*****
C ISTEP=3 - Line processing phase.
C           look at bit type and transfer input file to output file
C*****
100 CONTINUE
      DO 200 IS = 1,INS
          IDIFF = IBUF3(IS) - IBUF4(IS)
          IBUF1(IS) = IBUF2(IS) - IDIFF
          IF (IABS(IDIFF).GT.2) IBUF1(IS) = IBUF2(IS)
          IF (IBUF1(IS).LT.0) IBUF1(IS) = 0
      200 CONTINUE
      RETURN
C*****
C ISTEP=4 - Final line processing phase
C           add the processing history text and return to caller
C*****
500 CONTINUE
      RETURN
      END
```

```

!*****
! M9RADIOM.PDF
!*****
PROCESS HELP=*
PARM FROM TYPE=(STRING,32)
PARM TO TYPE=(STRING,32)
PARM SL INTEGER,DEFAULT=(1)
PARM SS INTEGER,DEFAULT=(1)
PARM NL INTEGER,DEFAULT=(0)
PARM NS INTEGER,DEFAULT=(0)
PARM LINC REAL,DEFAULT=(1.)
PARM SINC REAL,DEFAULT=(1.)
END-PROC

.TITLE
M9RADIOM: Mariner 9 Radiometric Correction

.HELP
PROGRAMMER: MARS1::KEH (Ken Herkenhoff, Caltech)
M9RADIOM corrects Mariner 9 images for solar distance, exposure
time, and shading. SPICELAB must be run first to provide SEDR
data in the header of the input image. The input image should be
in raw distorted space. Both input and output images are 16-bit
data files. It is assumed that the input file has been linearized
(see LINEARIZE). The filter number in the formatted labels is
used to find the correct shading file, and the exposure time from
the labels is used to find the actual preflight exposure time.
The solar vector in the labels is used to calculate the distance
to the sun (R) in astronomical units. Each data value in the
image is then corrected as follows:
    OUTPUT = INPUT * FF * R*R * SHADING / EXPOSURE
where FF is a multiplicative factor that depends upon the filter
used and scales the output to units of I/F * 10000. I/F is the
ratio of the observed intensity to the solar flux, and is related
to albedo through the photometric function. For more details, see
Herkenhoff et al. (1988) Icarus 75, 133-145.

.LEVEL1
.VAR FROM
INPUT IMAGE FILE NAME
.VAR TO
OUTPUT IMAGE FILE NAME
.VAR SL
STARTING LINE
.VAR SS

```

```

STARTING SAMPLE
.VAR NL
NUMBER OF LINES
.VAR NS
NUMBER OF SAMPLES
.VAR LINC
LINE INCREMENT
.VAR SINC
SAMPLE INCREMENT
.LEVEL2
.VAR FROM

```

The input Mariner 9 image file must be linearized (16-bit), and not geometrically transformed.

```

.VAR TO
The 16-bit output file is radiometrically corrected, with
each pixel value equal to I/F * 10000.
.END

```

C PROGRAM: M9RADIOM

```

C   CORRECTS MARINER 9 IMAGES FOR SHADING, DISTANCE FROM SUN, AND
C   EXPOSURE TIME.  WRITTEN BY KEN HERKENHOFF 10/25/85.
C

```

```

SUBROUTINE DOUSER(IBUF1,IBUF2,IBUF3)
INTEGER*2 IBUF1(1),IBUF2(1),IBUF3(1)
CHARACTER CAMERA*4,MISSION*8,LABEL*80,FILTER*12
REAL AEXPT(10),BEXPT(10),FF(9)
REAL*8 SUN(3)
INCLUDE 'PIC$INC:TAEBAS.INC'
INCLUDE 'PIC$INC:DOIOCMN.INC'
INCLUDE 'PIC$INC:DOIOCMN2.INC'

```

```

DATA MISSION/'MARINER'/,AU/1.496E+08/,PRGNAM/'M9RADIOM'/,
&VERDAT/'30-DEC-87'/,
&AEXPT/3.93,6.75,12.66,24.51,48.26,95.67,190.42,379.98,759.,
& 1517.2/,
&BEXPT/3.98,6.95,12.86,24.62,48.42,95.80,186.5,380.1,759.,
& 1517./,
& FF/1000.,431.,263.,356.,263.,180.,263.,1000.,47.5/

```

```

GO TO(10,20,100,500),ISTEP

```

C*****

```

C ISTEP = 1 - Initialization (Prior to prompt of files)
C*****
10 CONTINUE
   NFI = 2           !let DOIIO know there will be two input files
   IFLAGI(2) = 1    !Second input file is named in ISTEP=2
   NFO = 1           !let DOIIO know there will be one output file
   RETURN
C*****
C ISTEP = 2 - Initialization (Post prompt of files)
C Write program name to the spooled file.
C set output bit the same the input bit.
C*****
20 CONTINUE
   IBITO(1) = 16
   CALL DISKEY('RD',LUNI(1),ISBLKI(1),'CAMERA',CAMERA,LEN,IERR)
   IF (IERR.LT.0) CALL ERRMES('GEOMLB','GEOMLB',4,'CO')
   IF (IERR.LT.0) JERR=1
   IF (CAMERA.NE.'A'.AND.CAMERA.NE.'B') STOP ' Invalid camera.'
   IERR=2
   CALL DISKEY('RD',LUNI(1),ISBLKI(1),'EXPOSURE_TIME',LABEL,LEN,
& IERR)
   IF (IERR.LT.0) STOP 'ERROR READING EXPOSURE TIME FROM LABELS.'
   CALL CHAR2R(LABEL,EXPTL,1)
   IERR=2
   CALL DISKEY ('RD',LUNI(1),ISBLKI(1),'SUN_VECTOR',LABEL,LEN,
& IERR)
   IF (IERR.LT.0) CALL ERRMES('GEOMLB','GEOMLB',16,'CO')
   IF (IERR.LT.0) JERR=1
   DECODE(LEN,22,LABEL) SUN(1),SUN(2),SUN(3)
22 FORMAT(3F15.0)
   IERR=2
   IF (CAMERA.EQ.'A') THEN
   CALL DISKEY('RD',LUNI(1),ISBLKI(1),'WAVE_LENGTH',FILTER,LEN,
& IERR)
   IF (IERR.LT.0) STOP 'ERROR READING FILTER FROM LABELS.'
   IERR=2
   FILEI(2)='PIC$WORK:[MARINER9] '//FILTER(1:1)//'SHADING.PIC'
   DECODE(40,21,FILTER(1:1)) IF
21 FORMAT (I1)
   ELSE
   IF = 9
   FILTER(1:1) = 'B'

```

```

        FILEI(2)='PIC$WORK:[MARINER9]BSHADING.PIC'
        END IF
        WRITE (IPR,26) EXPTL
26  FORMAT (' EXPOSURE TIME FROM LABELS IS ',F5.3,' SEC.')
        IF (CAMERA.EQ.'A') EXPT=AEXPT(ININT(ALOG(EXPTL/.003)/
& 0.6931471806)+1)
        IF (CAMERA.EQ.'B') EXPT=BEXPT(ININT(ALOG(EXPTL/.003)/
& 0.6931471806)+1)
        SUNDS = (SUN(1)*SUN(1)+SUN(2)*SUN(2)+SUN(3)*SUN(3))/(AU*AU)
        IF (SUNDS.LE.0.) THEN
            TYPE *,
& 'Solar vector not found: Enter distance to sun in A.U.'
            ACCEPT *, SUNAU
            SUNDS = SUNAU * SUNAU
        END IF
        WRITE(IPR,27) SQRT(SUNDS)
27  FORMAT(' SUN DISTANCE IS',F6.3,' AU.')
C
C  FF IS FILTER FACTOR FOR A CAMERA FILTERS 1-8, FF(9) FOR B CAMERA
C
        SF=FF(IF)*SUNDS/EXPT/10000.
        WRITE (ISP,31) FILEI(1)
31  FORMAT (' Linearized input file: ',A)
        WRITE (ISP,32) FILEI(2)
32  FORMAT (' Shading file: ',A)
        RETURN
C*****
C ISTEP=3 - Line processing phase.
C         look at bit type and transfer input file to output file
C*****
100 CONTINUE
        DO 200 IS = 1,INS
            OUT = FLOAT(IBUF2(IS))*SF*FLOAT(IBUF3(IS))
            IBUF1(IS) = ININT(OUT)
200 CONTINUE
        RETURN
C*****
C ISTEP=4 - Final line processing phase
C         add the processing history text and return to caller
C*****
500 CONTINUE
        ENCODE (80,900,IBUF1) FILTER(1:1),EXPT,SF

```

```
900 FORMAT ('M9RADIOM: FILTER ',A,', EXPOSURE =',F7.2,  
& ' msec., SF =',G10.3)  
  IBITO(1) = 80  
  RETURN  
  END
```

```

!*****
! M9RES.PDF
!*****
PROCESS HELP=*
PARM FROM TYPE=(STRING,32),COUNT=2
PARM TO TYPE=(STRING,32)
PARM SL INTEGER,DEFAULT=(1)
PARM SS INTEGER,DEFAULT=(1)
PARM NL INTEGER,DEFAULT=(0)
PARM NS INTEGER,DEFAULT=(0)
PARM LINC REAL,DEFAULT=(1.)
PARM SINC REAL,DEFAULT=(1.)
END-PROC
.TITLE
M9RES:  Subtracts residual image from Mariner 9 images
.HELP
PROGRAMMER:  MARS1::KEH (Ken Herkenhoff, Caltech)
Subtracts residual component from Mariner 9 images using preflight
calibration data as well as inflight data.  The previous image must
immediately precede the input file (DAS count is 70 less), and
should have had noise and reseaux removed.  Both input and output
files are 8-bit.
The Mariner 9 cameras were known to produce residual images (due to
incomplete erasure of previous image) before flight and extensive
calibration data was gathered.  These data were compressed into
several calibration files, one for each filter/camera combination.
Data files for camera A, orange, green and 60 degree polarizing
filters and for camera B have been created to date.  The input and
previous DN values are used to interpolate between (or extrapolate
from) calibration data values at each pixel to find the residual,
which is then subtracted from the input image.  For more
information see Herkenhoff et al., (1988).  Icarus 75, 133-145.
.LEVEL1
.VAR FROM
INPUT IMAGE FILE NAME
PREVIOUS IMAGE FILE NAME
.VAR TO
OUTPUT FILE NAME
.VAR SL
STARTING LINE
.VAR SS
STARTING SAMPLE

```

```
.VAR NL
NUMBER OF LINES
.VAR NS
NUMBER OF SAMPLES
.VAR LINC
LINE INCREMENT
.VAR SINC
SAMPLE INCREMENT
.LEVEL2
.VAR FROM
```

The input Mariner 9 image must be 8-bit, and should have had reseaux and noise removed. The previous frame (if it exists) must have a DAS count (spacecraft time) that is exactly 70 less than that of the input image. If no image that meets this criterion exists, specify "NONE" for previous image. The previous image must also be 8-bit and should have had reseaux and noise removed.

```
.VAR TO
The output image file will be 8-bit, with residual image
removed.
.END
```

```
C PROGRAM TO SUBTRACT RESIDUAL IMAGE FROM MARINER 9 FRAMES
```

```
C
```

```
C BY KEN HERKENHOFF, CALTECH 170-25
```

```
C
```

```
    SUBROUTINE DOUSER(IBUF1,IBUF2,IBUF3)
    LOGICAL*1 IBUF3(1),IBUF2(1),IBUF1(1)
    CHARACTER*1 CAM,FIL
    CHARACTER*40 FILTER1,FILTER2
    CHARACTER MISSION*8,SC*4,FILEIN*32
```

```
C*****
```

```
C
```

```
C PROGRAM: M9RES
```

```
C
```

```
C This program reads Mariner 9 frames and subtracts a residual
C using the calibration data for each camera. This program uses
C the DOI0 subroutine to perform all the I/O operations.
```

```
C*****
```

```
    INCLUDE 'PIC$INC:TAEBAS.INC'
    INCLUDE 'PIC$INC:DOI0CMN.INC'
```

```

INCLUDE 'PIC$INC:DOIOCMN2.INC'
LOGICAL*1 LBUF(131072),I1(166,5),I2(166,5),RESID(166,5,5)
INTEGER*2 IRES(166,6,6),CUR(832),PRE(832),OUT(832),IRES1,
&          IRES3,IRES4,IN1,IN2,N1(166,6),N2(166,6),EXTRAP
DATA IEFLAG/0/,PRGNAM/' M9RES '/,VERDAT/'22-JUN-87'/

IF (ISTEP.EQ.3) GOTO 100 !For line processing phase
IF (ISTEP.EQ.1) GOTO 10 !Initialization call
IF (ISTEP.EQ.2) GOTO 20 !Initialization call
IF (ISTEP.EQ.4) GOTO 500 !Final processing phase
C*****
C ISTEP = 1 - Initialization (Prior to prompt of files)
C*****
10 CONTINUE
IF (IEFLAG.EQ.1) STOP
IEFLAG = 1
NFI = 2          !let DOIO know there will be 2 input files
NFO = 1          !let DOIO know there will be one output file
RETURN
C*****
C ISTEP = 2 - Initialization (Post prompt of files)
C Write program name to the spooled file.
C
C*****
20 CONTINUE
IBITO(1) = 8

CALL DISKEY ('RD',LUNI(1),ISBLKI(1),'CAMERA',CAM,LEN,IERR)
IF (IERR.LT.0) STOP ' INVALID CAMERA.'
CALL DISKEY('RD',LUNI(1),ISBLKI(1),'MISSION',MISSION,LEN,IERR)
IF (IERR.LT.0) STOP ' MISSION NOT FOUND.'
IF (MISSION.NE.'MARINER') STOP ' MISSION NOT MARINER.'
CALL DISKEY('RD',LUNI(2),ISBLKI(2),'MISSION',MISSION,LEN,IERR)
IF (IERR.LT.0) STOP ' MISSION NOT FOUND.'
IF (MISSION.NE.'MARINER') STOP ' MISSION NOT MARINER.'
CALL DISKEY ('RD',LUNI(1),ISBLKI(1),'SPACECRAFT_NO',SC,LEN,
&          IERR)
IF (IERR.LT.0) STOP ' SPACECRAFT NUMBER NOT FOUND.'
IF (SC(LEN:LEN).NE.'9') STOP
& ' IMAGE 1 NOT MARINER 9 SPACECRAFT.'
CALL DISKEY ('RD',LUNI(2),ISBLKI(2),'SPACECRAFT_NO',SC,LEN,
&          IERR)

```

```

IF (IERR.LT.0) STOP ' SPACECRAFT NUMBER NOT FOUND.'
IF (SC(LEN:LEN).NE.'9') STOP
& ' IMAGE 2 NOT MARINER 9 SPACECRAFT.'
FIL = 'B'
IF(CAM.EQ.'B') GO TO 30
CALL DISKEY ('RD',LUNI(1),ISBLKI(1),'WAVE_LENGTH',FILTER1,LEN,
& IERR)
IF (IERR.LT.0) STOP ' FILTER NOT FOUND.'
CALL DISKEY ('RD',LUNI(2),ISBLKI(2),'WAVE_LENGTH',FILTER2,LEN,
& IERR)
IF (IERR.LT.0) STOP ' FILTER NOT FOUND.'
FIL = '4'
IF (FILTER1(1:1).EQ.'2'.OR.FILTER2(1:1).EQ.'2') FIL='2'
IF(FILTER2(1:1).EQ.'6'.OR.FILTER2(1:1).EQ.'8') THEN
  IF(FILTER1(1:1).EQ.'6'.OR.FILTER1(1:1).EQ.'8') FIL='6'
  IF(FILTER1(1:1).EQ.'8'.AND.FILTER2(1:1).EQ.'8') FIL='8'
END IF
30 FILEIN = 'PIC$WORK:[MARINER9] '//FIL//'RI.CAL'
OPEN(1,FILE=FILEIN,STATUS='OLD',FORM='UNFORMATTED',READONLY)
WRITE(7,40) FILEIN
40 FORMAT(' CALIBRATION FILE: ',A32)

IF(IBITI(1).NE.8) STOP 'Input picture file not 8-bit'
IF(IBITI(2).EQ.0) STOP 'Not enough input files'
IF(IBITI(2).NE.8) STOP 'Residual frame not 8-bit'
DO 50 I = 1,166
  N1(I,6) = 255
  N2(I,6) = 255
50 CONTINUE
RETURN
C*****
C ISTEP=3 - Line processing phase.
C*****
100 CONTINUE
CALL B2W(IBUF2,CUR,832)
CALL B2W(IBUF3,PRE,832)
IF(MOD(ILI,5).EQ.1) THEN
DO 200 I = 1,5
  READ(1) (I1(ISD,I),ISD=1,166)
  READ(1) (I2(ISD,I),ISD=1,166)
  CALL B2W(I1(1,I),N1(1,I),166)
  CALL B2W(I2(1,I),N2(1,I),166)

```

```

DO 200 J = 1,5
  READ(1) (RESID(ISD,J,I),ISD=1,166)
  CALL B2W(RESID(1,J,I),IRES(1,J,I),166)
200 CONTINUE
  END IF
  OUT(831) = CUR(831)
  OUT(832) = CUR(832)
  NSD1 = 0
  DO 400 IS = 1,830
    ISD = IS/5 + 1
    IDX1 = 1
    IDX2 = 1
    DO 300 I = 1,5
      IF(CUR(IS).GT.N2(ISD,I)) IDX2 = I + 1
      IF(PRE(IS).GT.N1(ISD,I)) IDX1 = I + 1
300   CONTINUE
    IF(IDX1.GT.5) THEN
      IN1 = N1(ISD,5)
      IF(IDX2.GT.5) THEN          ! IDX1>5,IDX2>5
        IN2 = N2(ISD,5)
        IF (NSD1.EQ.ISD) GO TO 330
        NSD1 = ISD
        DO 320 I = 1,2
          IRES(ISD,6,6-I) = EXTRAP(N1(ISD,4),IN1,
&           IRES(ISD,4,6-I),IRES(ISD,5,6-I))
          IRES(ISD,6-I,6) = EXTRAP(N2(ISD,4),IN2,
&           IRES(ISD,6-I,4),IRES(ISD,6-I,5))
320   CONTINUE
          IRES(ISD,6,6) = (EXTRAP(N2(ISD,4),IN2,IRES(ISD,6,4),
&           IRES(ISD,6,5)) + EXTRAP(N1(ISD,4),IN1,
&           IRES(ISD,4,6),IRES(ISD,5,6)) + 1)/2
330   IRES1 = IRES(ISD,5,6)
          IRES3 = IRES(ISD,6,5)
          IRES4 = IRES(ISD,5,5)
        ELSE          ! IDX1>5, IDX2<6
          IRES1 = IRES(ISD,5,IDX2)
          IRES(ISD,6,IDX2) = EXTRAP(N1(ISD,4),N1(ISD,5),
&           IRES(ISD,4,IDX2),IRES(ISD,5,IDX2))
&
          IF(IDX2.GT.1) THEN
            IN2 = N2(ISD,IDX2-1)
            IRES3 = EXTRAP(N1(ISD,4),N1(ISD,5),
&           IRES(ISD,4,IDX2-1),IRES(ISD,5,IDX2-1))

```

```

      IRES4 = IRES(ISD,5,IDX2-1)
ELSE                                     ! IDX1=6, IDX2=1
      IRES3 = 5
      IRES4 = 4
      IN2 = 0
      END IF
END IF
ELSE                                     ! IDX1<6
      IF (IDX2.GT.5) THEN                 ! IDX1<6, IDX2=6
          IN2 = N2(ISD,IDX2-1)
          IF (IDX1.EQ.1) THEN
              IRES1 = 0
              IRES3 = IRES(ISD,1,5)
              IRES4 = 0
              IN1 = 0
          ELSE                             ! 1<IDX1<6, IDX2=6
              IRES1 = EXTRAP(N2(ISD,4),IN2,
&                                     IRES(ISD,IDX1-1,4),IRES(ISD,IDX1-1,5))
              IRES(ISD,IDX1,6) = EXTRAP(N2(ISD,4),N2(ISD,5),
&                                     IRES(ISD,IDX1,4),IRES(ISD,IDX1,5))
              IRES3 = IRES(ISD,IDX1,5)
              IRES4 = IRES(ISD,IDX1-1,5)
              IN1 = N1(ISD,IDX1-1)
          END IF
      ELSE                                 ! IDX1<6, IDX2<6
          IF (IDX2.LE.1) THEN
              IN2 = 0
              IF (IDX1.LE.1) THEN         ! IDX1=1, IDX2=1
                  IRES1 = 0
                  IRES3 = N1(ISD,IDX1)/50
                  IRES4 = 0
                  IN1 = 0
              ELSE                         ! IDX1>1, IDX2=1
                  IRES1 = IRES(ISD,IDX1-1,1)
                  IRES3 = N1(ISD,IDX1-1)/50
                  IRES4 = N1(ISD,IDX1)/50
                  IN1 = N1(ISD,IDX1-1)
              END IF
          ELSE                             ! IDX1<6, 1<IDX2<6
              IN2 = N2(ISD,IDX2-1)
              IF (IDX1.EQ.1) THEN        ! IDX1=1, 1<IDX2<6
                  IRES1 = 0

```

```

      IRES3 = IRES(ISD,1,IDX2)
      IRES4 = 0
      IN1 = 0
      ELSE                                     ! 1<IDX1<6, 1<IDX2<6
      IRES1 = IRES(ISD,IDX1-1,IDX2)
      IRES3 = IRES(ISD,IDX1,IDX2-1)
      IRES4 = IRES(ISD,IDX1-1,IDX2-1)
      IN1 = N1(ISD,IDX1-1)
      END IF
    END IF
  END IF
END IF
      T = FLOATI(PRE(IS)-IN1)/FLOATI(N1(ISD,IDX1)-IN1)
      U = FLOATI(CUR(IS)-IN2)/FLOATI(N2(ISD,IDX2)-IN2)
      RES = (1.-T)*(1.-U)*FLOATI(IRES4) + T*(1.-U)*FLOATI(IRES3)
&      + T*U*FLOATI(IRES(ISD,IDX1,IDX2)) + (1.-T)*U*FLOATI(IRES1)
      OUT(IS) = CUR(IS) - ININT(RES/16.)
400 CONTINUE
      CALL W2B(OUT,IBUF1,832)
      RETURN
C*****
C ISTEP=4 - Final line processing phase
C       add the processing history text and return to caller
C*****
500 CONTINUE
      CLOSE (1)
      DO LEN = 32,1,-1
      IF(ICHAR(FILEI(1)(LEN:LEN)).NE.32) GOTO 600
      END DO
600 DO LEN1 = 32,1,-1
      IF(ICHAR(FILEI(2)(LEN1:LEN1)).NE.32) GOTO 700
      END DO
700 ENCODE(21+LEN+LEN1,980,IBUF1) FILEI(1)(1:LEN),FILEI(2)(1:LEN1)
980 FORMAT('PIC file: ',A,' RES file: ',A)
      IBITO(1) = 21 + LEN + LEN1
      RETURN
      END

      INTEGER*2 FUNCTION EXTRAP(IX1,IX2,IY1,IY2)
C
C       SIMPLE LINEAR EXTRAPOLATION FOR M9RES
C

```

```
INTEGER*2 IX1,IX2,IY1,IY2
EXTRAP = IY2 + (255-IX2)*(IY2-IY1)/(IX2-IX1)/2
IF(EXTRAP.LT.0) EXTRAP = 0
RETURN
END
```

```

! PSFILT.PDF
PROCEDURE HELP=*
  PARM FROM TYPE=(STRING,32)
  PARM TO TYPE=(STRING,32)
  LOCAL FILT1 TYPE=(STRING,32)
  LOCAL FILT7 TYPE=(STRING,32)
  LOCAL FILT1D TYPE=(STRING,32)
  LOCAL FILT7D TYPE=(STRING,32)
  BODY
  LET FILT1="&FROM"//"F1"
  LET FILT7="&FROM"//"F7"
  FLT16B &FROM,&FILT1,LPFV,25,1,FRACTION=.5
  FLT16B &FROM,&FILT7,LPFV,25,7,FRACTION=.5
  M9PSR FROM=(&FROM,&FILT1,&FILT7) TO=&TO
  LET FILT1D="&FILT1"//".PIC;*"
  LET FILT7D="&FILT7"//".PIC;*"
  DCL DEL &FILT1D
  DCL DEL &FILT7D
  END-PROC
  .TITLE
  PSFILT:  Mariner 9 Pinstripe Filter
  .HELP
  PROGRAMMER:  MARS1::KEH (Ken Herkenhoff, Caltech)
  This procedure finds and removes pinstripes in Mariner 9 images, as
  documented in M9PSR.  The input image must be 16-bit; the output
  image will also be 16-bit.  FLT16B is used to create two low-pass
  filtered versions of the input image:  1 x 25 pixels and 7 x 25
  pixels.  M9PSR is used to find the difference between the two
  filtered versions and subtract the difference from the input image.
  See M9PSR.PDF.
  .LEVEL1
  .VAR FROM
  MARINER 9 INPUT IMAGE FILE
  .VAR TO
  OUTPUT IMAGE FILE NAME
  .LEVEL2
  .VAR FROM
  The Mariner 9 input image file must be 16-bit, and is usually
  the result of level 1 processing.  The image must NOT have
  been geometrically transformed in any way.
  .VAR TO
  The output image will also be 16-bit, with pinstripe noise

```

removed.
.end

C.2 Photoclinometric software

The software in this section will run in any VMS environment, with the exception of PROFIL and FINDLS. PROFIL and FINDLS must be run under TAE, like the programs in the previous section.

```

C           AZIMUTH
C
C FIND ANGLES BETWEEN STRIKE DIRECTION AND AZIMUTHS TOWARD SUN,
C SPACECRAFT GIVEN INCIDENCE AND EMISSION ANGLES AT TWO OR MORE
C POINTS
C
      DOUBLE PRECISION DADPE,CADPE,SADPE,IO,I1,EO,E1,
&          LATO,LAT1,LONO,LON1
      CHARACTER*32 FILEIN
      TYPE *, 'ENTER INPUT FILENAME:'
      READ (5,10) FILEIN
10  FORMAT (A)
      OPEN (7,FILE='AZIMUTH.OUT',STATUS='NEW')
      OPEN (1,FILE=FILEIN,STATUS='OLD',READONLY)
      READ (1,*) LATO,LONO,Y,X,EO,IO
30  READ (1,*,END=90) LAT1,LON1,Y,X,E1,I1
      DADPE = DACOSD(DSIND(LATO)*DSIND(LAT1) +
&          DCOSD(LATO)*DCOSD(LAT1)*DCOSD(LONO-LON1))
      CADPE = DCOSD(DADPE)
      SADPE = DSIND(DADPE)
      COSAZI = (DCOSD(IO) - DCOSD(I1)*CADPE)/(DSIND(I1)*SADPE)
      COSAZE = (DCOSD(EO) - DCOSD(E1)*CADPE)/(DSIND(E1)*SADPE)
      IF (COSAZI.GT.1.) COSAZI = 1.
      IF (COSAZI.LT.-1.) COSAZI = -1.
      IF (COSAZE.GT.1.) COSAZE = 1.
      IF (COSAZE.LT.-1.) COSAZE = -1.
      WRITE (7,*) ACOSD(COSAZI),ACOSD(COSAZE)
      LATO = LAT1
      LONO = LON1
      EO = E1
      IO = I1
      GO TO 30
90  CLOSE(1)
      CLOSE(7)
      STOP
      END

```

```

! FINDLS.PDF
PROCESS HELP=*
PARM FROM (STRING,32)
PARM IN (STRING,32)
PARM DISTORTD (STRING,1)
PARM NL INTEGER, DEFAULT=(0)
PARM NS INTEGER, DEFAULT=(0)
PARM SL INTEGER, DEFAULT=(1)
PARM SS INTEGER, DEFAULT=(1)
PARM LINC REAL, DEFAULT=(1.0)
PARM SINC REAL, DEFAULT=(1.0)
END-PROC
.TITLE
FINDLS
.HELP
FINDLS FINDS LINE, SAMPLE LOCATION OF LAT, LONG IN GIVEN IMAGE
.LEVEL1
.var IN
INPUT DATA FILE
.var FROM
IMAGE FILE
.VAR DISTORTD
IMAGE IS DISTORTED? (Y OR N)
.var nl
Number of lines
.var ns
Number of samples
.var sl
Starting line
.var ss
Starting sample
.END

```

```

C   FINDLS
C   FINDS LINE AND SAMPLE IN IMAGE FOR GIVEN LATITUDE AND LONGITUDE
C   POINTS IN INPUT FILE (UP TO 100 POINTS).
C
C       BY KEN HERKENHOFF, 6/25/87; REVISED 7/2/88
C
C       INCLUDE 'PIC$INC:TAEBAS.INC'
C       CHARACTER FILE*32, ADATE*9, ATIME*8, DATFIL*32

```

```

CHARACTER MISSION*8,CAMERA*4,PLANET*10,DISTORT*1
REAL LAT(100),LON(100),NORAZ,INC
REAL*8 C(3),S(3),TCM(9),TC(3),P(3),CM(9),SUN(3),MW(9),TSUN(3),
&      JD
DATA IPR/6/,ISP/7/,IFLAG/0/
C
CALL XZINIT(BLOCK,xprdim,6,xabort,ISTAT)
CALL XRSTR(BLOCK,'FROM',1,FILE,LEN,ICOUNT,ISTAT)
CALL XRSTR(BLOCK,'IN',1,DATFIL,LEN,ICOUNT,ISTAT)
CALL XRSTR(BLOCK,'DISTORTD',1,DISTORT,LEN,ICOUNT,ISTAT)
OPEN(UNIT=ISP,NAME='PRINT.PRT',ACCESS='APPEND',TYPE='UNKNOWN')
CALL DATE(ADATE)
CALL TIME(ETIME)
WRITE(ISP,5) ADATE,ETIME
5 FORMAT(' *** FINDLS *** ',A9,2X,A8)
C
CALL DISKIO('IN',1,ISBLK,FILE,NBLK,IERR)
JFLAG = 1
IF (DISTORT.EQ.'N') JFLAG = 0
OPEN(2,FILE=DATFIL,STATUS='OLD',READONLY)
N = 0
100 N = N + 1
READ(2,*,END=200) LAT(N), LON(N)
IF(N.LE.100) GO TO 100
STOP ' MORE THAN 100 INPUT PAIRS.'
200 CLOSE(2)
DO 500 I = 1,N-1
CALL PHOSUN(Y,X,1,ISBLK,2,IFLAG,JFLAG,1,LAT(I),LON(I),EMA,
&      INC,PHASE,SCAZ,SUNAZ,NORAZ,RES,IER)
IF(IER.EQ.-1) WRITE(ISP,210) LAT(I),LON(I)
210 FORMAT(F10.3,',',F10.3,' IS OFF PLANET.')
C
CALL LBSPICE(ISBLK,1,PLANET,MISSION,ISC,CAMERA,IFSC,JD,C,S,
&      SUN,P,JERR)
CALL MISSPR(MISSION,ISC,CAMERA,FL,CX,CY)
CALL CMAT(C,CM,0)
CALL PMW(P,MW,0)
CALL EMEPLAN(MW,CM,S,SUN,TCM,TC,TSUN,0)
C FIND DISTANCES TO SUN AND TO SPACECRAFT FROM CENTER OF PLANET
DSUN = DSQRT(TSUN(1)*TSUN(1)+TSUN(2)*TSUN(2)+TSUN(3)*TSUN(3))
DSUNAU = DSUN/1.496E+08
DSC = DSQRT(TC(1)*TC(1) + TC(2)*TC(2) + TC(3)*TC(3))

```

```

      IRESM = JNINT(1000. * RES)
      OBSAZ = ACOSD((COSD(PHASE)-COSD(EMA)*COSD(INC))/(SIND(EMA)*
&      - SIND(INC)))
C
      WRITE (ISP,9) FILE
      9 FORMAT(' Image: ',A32)
      WRITE (ISP,10) Y,X,LAT(I),LON(I)
      10 FORMAT(' Line ',F5.0,', sample ',F5.0,' is at latitude ',F9.5,
&      ', longitude ',F9.4)
      WRITE (ISP,20) EMA,INC,PHASE
      20 FORMAT(' Emission angle =',F9.5,', Incidence angle =',F9.5,
&      ', Phase angle =',F9.4,' (degrees).')
      WRITE (ISP,30) SCAZ,SUNAZ,NORAZ
      30 FORMAT(' Clockwise angle from 3:00 on image:',/,
&      ' to spacecraft = ',F6.2,' to sun = ',F6.2,
&      ', to north pole = ',F6.2,' (degrees).')
      WRITE (ISP,40) IRESM,OBSAZ
      40 FORMAT(' Resolution =',I4,' meters per pixel, '
&      'Observer/solar azimuth =',F9.4)
      WRITE (ISP,50) DSUN,DSUNAU
      50 FORMAT(' Distance to sun =',E10.3,' kilometers (',F5.3,
&      ' A.U.)')
      WRITE (ISP,60) DSC
      60 FORMAT(' Distance of spacecraft from center of planet =',F7.0,
&      ' kilometers.')
      500 CONTINUE
      STOP
      END

```

```

C           HAPKE
C
C           EVALUATES BIDIRECTIONAL REFLECTANCE USING FORMULAE GIVEN BY
C           HAPKE (1984) Icarus 59, 41-59.
C
SUBROUTINE HAPKE(I,E,G,THETA,W,P,H,R)
IMPLICIT REAL*8 (A-M,O-Z)
REAL*4 R
CH(X) = (1.DO + 2.DO*X)/(1.DO + 2.DO*X*DSQRT(1.DO - W))
PI = 3.1415926535897932384626
AG = DABS(G)
BO = DEXP(-W*W/2.DO)
IF (W.GT.1.DO) W = 1.DO
C EVALUATE BACKSCATTER FUNCTION B DEPENDING ON H AND PHASE ANGLE AG
B = 0.DO
IF (AG.GT.90.DO.OR.H.EQ.0.DO) GO TO 10
IF (AG.LE.1.DO) THEN
  B = BO*(1.DO - 3.DO*AG/(2.DO*H))
ELSE
  HCOTG = H*DCOSD(AG)/DSIND(AG)
  B = BO*(1.DO-DTAN(AG)*(3.DO-DEXP(-HCOTG))*
&      (1.DO-DEXP(-HCOTG))/(2.DO*H))
END IF
10 COSI = DCOSD(I)
SINI = DSIND(I)
COSE = DCOSD(E)
SINE = DSIND(E)
IF(THETA.EQ.0.DO) THEN
  R = W/(4.DO*PI)*COSI/(COSI+COSE)*
&      ((1.DO+B)*P-1.DO+CH(COSI)*CH(COSE))
RETURN
END IF
COSPSI = (DCOSD(G) - COSI*COSE)/(SINI*SINE)
IF(COSPSI.GT.1.DO) COSPSI = 1.DO
IF(COSPSI.LT.-1.DO) COSPSI = -1.DO
PSI = DACOSD(COSPSI)
SIN2P2 = DSIND(PSI/2.DO)*DSIND(PSI/2.DO)
F = 0.DO
IF (PSI.NE.1.8D2) F = DEXP(-2.DO*DTAND(PSI/2.DO))
TANTHE = DTAND(THETA)
COTTHE = DCOSD(THETA)/DSIND(THETA)
COT2TH = COTTHE*COTTHE

```

```

COTI = COSI/SINI
COTE = COSE/SINE
COT2I = COTI*COTI
COT2E = COTE*COTE
AFACT = 1.DO/DSQRT(1.DO+PI*TANTHE*TANTHE)
EXPI = DEXP(-COT2TH*COT2I/PI)
EXPE = DEXP(-COT2TH*COT2E/PI)
EXP2I = DEXP(-2.DO*COTTHE*COTI/PI)
EXP2E = DEXP(-2.DO*COTTHE*COTE/PI)
MUO10 = AFACT*(COSI + SINI*TANTHE*EXPI/(2.DO-EXP2I))
MU10 = AFACT*(COSE + SINE*TANTHE*EXPE/(2.DO-EXP2E))
IF (I.LE.E) THEN
  DENOM = (2.DO - EXP2E - PSI*EXP2I/PI)
  MUO1 = AFACT*(COSI + SINI*TANTHE*(COSPSI*EXPE + SIN2P2*EXPI)
&      /DENOM)
  MU1 = AFACT*(COSE + SINE*TANTHE*(EXPE - SIN2P2*EXPI)/DENOM)
  R = W/(4.DO*PI)*MUO1/(MUO1+MU1)*((1.DO+B)*P-1.DO+CH(MUO1)*
&      CH(MU1))*MU1*COSI*AFACT/(MU10*MUO10*(1.DO-F+F*COSI*AFACT
&      /MUO10))
ELSE
  DENOM = (2.DO - EXP2I - PSI*EXP2E/PI)
  MUO1 = AFACT*(COSI + SINI*TANTHE*(EXPI - SIN2P2*EXPE)/DENOM)
  MU1 = AFACT*(COSE + SINE*TANTHE*(COSPSI*EXPI + SIN2P2*EXPE)/
&      DENOM)
  R = W/(4.DO*PI)*MUO1/(MUO1+MU1)*((1.DO+B)*P-1.DO+CH(MUO1)*
&      CH(MU1))*MU1*COSI*AFACT/(MU10*MUO10*(1.DO-F+F*COSE*AFACT
&      /MU10))
END IF
RETURN
END

```

```

C PROGRAM: PROFAV
C
Calculates averages along profile length using output data from
C PROFIL.
C Writes output file with standard deviation of Y values in X
C increment XINC.
C
      DIMENSION X(1000),Y(1000)
      CHARACTER*32 FILEIN,FILOUT,TITLE
      CHARACTER*2 INC
      TYPE *, ' Enter input filename:'
      READ (5,10) FILEIN
100 FORMAT(A)
      TYPE *, ' Enter X increment:'
      READ (5,*) XINC
      TYPE *, ' Enter output filename:'
      READ(5,10) FILOUT
      N = 1
      COUNT = 0.
      SUM = 0.
      OPEN(7,FILE=FILOUT,STATUS='NEW',FORM='FORMATTED')
      OPEN(1,FILE=FILEIN,STATUS='OLD',READONLY)
      READ (1,*) NFILES
      READ (1,10) TITLE
      READ (1,*) NP
      IF (NP.GT.1000) STOP ' MORE THAN 1000 INPUT POINTS.'
      DO 100 I = 1,NP
      READ(1,*) X(I),Y(I)
100 CONTINUE
      CLOSE (1)
      ENCODE (2,110,INC) JNINT(XINC)
110 FORMAT (I2)
      TITLE = 'INCREMENT '//INC//' PIXELS'
      WRITE (7,10) TITLE
      CALL SORT2(X,Y,NP)
      DO 300 I = 1,NP
      XMAX = XINC*FLOAT(N)
      IF(XMAX.GT.X(NP)) XMAX = X(NP)
      IF (X(I).LT.XMAX) THEN
          SUM = SUM + Y(I)
          COUNT = COUNT + 1.
      ELSE

```

```
XAVG = XINC*(FLOAT(N)-0.5)
YAVG = SUM/COUNT
DEVSUM = 0.
DO J = I-INT(COUNT),I-1
    DEVSUM = DEVSUM + (Y(J)-YAVG)**2
END DO
XERR = XINC/2.
YERR = SQRT(DEVSUM/COUNT)
WRITE(7,*) XAVG,YAVG,XERR,YERR
N = N + 1
IF(N.GT.100) STOP ' MORE THAN 100 OUTPUT POINTS.'
COUNT = 0.
SUM = 0.
END IF
300 CONTINUE
WRITE (7,*) N-1
CLOSE (7)
STOP
END
```

```

!*****
! PROFIL.PDF
!*****

PROCESS HELP=*
PARM FROM TYPE=(STRING,32)
PARM TO TYPE=(STRING,32)
PARM LINE REAL,COUNT=2
PARM SAMPLE REAL,COUNT=2
PARM WIDTH REAL
PARM SL INTEGER,DEFAULT=(1)
PARM SS INTEGER,DEFAULT=(1)
PARM NL INTEGER,DEFAULT=(0)
PARM NS INTEGER,DEFAULT=(0)
PARM LINC REAL,DEFAULT=(1.)
PARM SINC REAL,DEFAULT=(1.)
END-PROC

.TITLE
PROFIL: Finds profile in image given endpoints
.HELP
PROGRAMMER: MARS1::KEH (Ken Herkenhoff, Caltech)
Given starting line and sample, ending line and sample in an image,
PROFIL projects all pixel values within a given width of the line
connecting the input endpoints to the profile. The data is written
to a data file on disk. The input file must be 16-bit.
.LEVEL1
.VAR FROM
Input image file name
.VAR TO
Output file name
.VAR LINE
Line of starting point
Line of endpoint
.VAR SAMPLE
Sample of starting point
Sample of endpoint
.VAR WIDTH
Width in pixels of profile
.VAR SL
Starting line
.VAR SS
Starting sample
.VAR NL

```

```

Number of lines
.VAR NS
Number of samples
.VAR LINC
Line increment
.VAR SINC
Sample increment
.END

```

```

C PROGRAM: PROFIL

```

```

C

```

```

Calculates profile between two points in a level 1 image by

```

```

C including all points within given width.

```

```

C Output is written to a disk file.

```

```

C WRITTEN BY KEN HERKENHOFF 4/26/88

```

```

C

```

```

SUBROUTINE DOUSER(IBUF)
INTEGER*2 IBUF(1)
REAL M,MINV,M2,X(2);Y(2)
CHARACTER FILE*32,CWID*2
INCLUDE 'PIC$INC:DOIOCMN.INC'
INCLUDE 'PIC$INC:DOIOCMN2.INC'

```

```

C

```

```

Include TAE block

```

```

INCLUDE 'PIC$INC:TAEBAS.INC'

```

```

DATA PRGNAM/'PROFIL'/,VERDAT/'11-FEB-89'/,ZERO/0./

```

```

GO TO(10,20,100,500),ISTEP

```

```

C*****

```

```

C ISTEP = 1 - Initialization (Prior to prompt of files)

```

```

C*****

```

```

10 CONTINUE

```

```

NFI = 1 !let DOIO know there will be ONE input file

```

```

NFO = 0 !let DOIO know there will be NO output file

```

```

RETURN

```

```

C*****

```

```

C ISTEP = 2 - Initialization (Post prompt of files)

```

```

C Write program name to the spooled file.

```

```

C set output bit the same the input bit.

```

```

C*****

```

```

20 CONTINUE

```

```

IF(IBITI(1).NE.16) STOP ' INPUT FILE MUST BE 16-BIT.'
CALL XRREAL(BLOCK,'LINE',2,Y,ICOUNT,ISTAT)
CALL XRREAL(BLOCK,'SAMPLE',2,X,ICOUNT,ISTAT)
CALL XRREAL(BLOCK,'WIDTH',1,W,ICOUNT,ISTAT)
CALL XRSTR(BLOCK,'TO',1,FILE,LEN,ICOUNT,ISTAT)
OPEN(8,FILE=FILE,STATUS='NEW',FORM='FORMATTED')
WRITE(8,30) JNINT(2.*W)
30 FORMAT('WIDTH =',I2,' PIXELS')
XMIN=X(1)
XMAX=X(2)
IF(X(1).GT.X(2)) THEN
XMIN=X(2)
XMAX=X(1)
END IF
YMIN=Y(1)
YMAX=Y(2)
IF(Y(1).GT.Y(2)) THEN
YMIN=Y(2)
YMAX=Y(1)
END IF
M = (Y(2)-Y(1))/(X(2)-X(1))
M2 = M*M + 1.0
XL = SQRT(W*W/M2)
XS = SQRT(W*W/(1.+1./(M*M)))
ISSI = INT(XMIN - XS)
INSI = INT(XMAX-XMIN + 2*XS) + 1
ISLI = INT(YMIN - XL)
INLI = INT(YMAX-YMIN + 2*XL) + 1
ILNXTI = ISLI
BPROF = Y(1) - M*X(1)
MINV = 1./M
DENOM = M + MINV
NOUT = 0
RETURN
C*****
C ISTEP=3 - Line processing phase.
C      look at bit type and transfer input file to output file
C*****
100 CONTINUE
YY = FLOAT(ILI)
DO 200 IS = 1,INSI
XX = FLOAT(IS+ISSI-1)

```

```
XINT = ((YY + MINV*XX) - BPROF)/DENOM
DXX = XX - XINT
DXX2 = DXX * DXX
DYY = YY - M*XINT - BPROF
DYY2 = DYY * DYY
IF(SQRT(DXX2 + DYY2).GT.W) GO TO 200
IF(XINT.LT.XMIN.OR.XINT.GT.XMAX) GO TO 200
DX = XINT - X(1)
D = SQRT(DX*DX*M2)
WRITE(8,*) D,FLOATI(IBUF(IS))/10000.,ZERO,ZERO
NOUT = NOUT + 1
200 CONTINUE
RETURN
C*****
C ISTEP=4 - Final line processing phase
C           add the processing history text and return to caller
C*****
500 CONTINUE
WRITE(8,*) NOUT
CLOSE(8)
RETURN
END
```

```

C           SLOPE1
C
C           PROGRAM TO FIT REFLECTANCE PROFILE (GIVEN ALBEDO)
C           USING HAPKE'S (1984) BI-SCOPIC REFLECTANCE FUNCTION.
C           INPUT READ FROM DATA FILE WITH ARBITRARY DISTANCE COORDINATE,
C           OUTPUT WRITTEN TO DATA FILE NORMALIZED TO TOTAL DISTANCE.
C           ASSUMES SLOPE VARIES ONLY ALONG PROFILE (ROTATION ABOUT AXIS
C           PERPENDICULAR TO BOTH PROFILE AND PLANETARY RADIUS VECTOR).
C
C           WRITTEN BY KEN HERKENHOFF, 3/23/89
C
C           DIMENSION R(1000),RERR(1000),X(1000),SLOPE(1000)
C           DOUBLE PRECISION A,B,C,D,E,EPS,P,Q,S,T,TOL1,XM,IPRIME,EPRIME,
C           &           DELTA
C           REAL I,IO,I1,I2,I3
C           CHARACTER*32 GEOM1,GEOM2,PROF1,PROF2,FILOUT,STRING,PICNO1
C           CHARACTER*1 NPROF
C           DATA ZERO/0./,IONE/1/,ITWO/2/,EPS/2.8E-17/,PI/3.14159265/
C           DATA FACTOR/0.01/
C           IPRIME(DELTA) = DACOSD(DCOSD(DELTA)*COSI +
C           &           DSIND(DELTA)*SINI*SINAZI)
C           EPRIME(DELTA) = DACOSD(DCOSD(DELTA)*COSE +
C           &           DSIND(DELTA)*SINE*SINAZE)
C           TYPE *, ' Enter picture number of first image (topo):'
C           READ (5,10) PICNO1
10  FORMAT (A)
C           TYPE *, ' Enter picture number of second image (albedo):'
C           READ (5,10) PICNO2
C           TYPE *, ' Enter profile number:'
C           READ (5,10) NPROF
C           LEN1 = INDEX(PICNO1,' ') - 1
C           LEN2 = INDEX(PICNO2,' ') - 1
C           PROF1 = PICNO1(1:LEN1)//'.AV'//NPROF
C           PROF2 = PICNO2(1:LEN2)//'.AV'//NPROF
C           GEOM1 = PICNO1(1:LEN1)//'.IEG'//NPROF
C           GEOM2 = PICNO2(1:LEN2)//'.IEG'//NPROF
C           FILOUT = PICNO1(1:LEN1)//'.S'//NPROF
C           TYPE *, ' Enter single-scattering albedo:'
C           READ (5,*) WO
C           OPEN (2,FILE=GEOM1,STATUS='OLD',READONLY)
C           READ (2,*) IO,EO,GO
C           READ (2,*) I1,E1,G1

```

```

READ (2,*) THETA,H,BP
READ (2,*) ADPE
READ (2,*) AZI1,AZE1
CLOSE (2)
PROLEN = ADPE*58.9921
OPEN (2,FILE=GEOM2,STATUS='OLD',READONLY)
READ (2,*) I2,E2,G2
READ (2,*) I3,E3,G3
READ (2,*) THETA,H,BP
READ (2,*) ADPE2
READ (2,*) AZI2,AZE2
CLOSE (2)
IF(ADPE2.NE.ADPE) PAUSE 'DIFFERENCE IN GEOMETRY DATA FILES.'
OPEN (1,FILE=PROF1,STATUS='OLD',READONLY)
READ (1,10) STRING
DO 50 J = 1,1000
    READ (1,*,END=60) X(J),R(J),XINC,RERR(J)
50 CONTINUE
STOP 'MORE THAN 1000 POINTS IN PROFILE.'
60 NP = J - 1
IF(NINT(X(J)).NE.NP) STOP 'ERROR IN FIRST PROFILE DATA FILE.'
TOTAL = X(NP) + XINC
CLOSE(1)
DO J = 1,NP
    X(J) = X(J)/TOTAL
END DO
OPEN(7,FILE=FILOUT,STATUS='NEW')
WRITE(7,*) IONE,PROLEN
WRITE(7,10) PICNO1
WRITE(7,80) WO
80 FORMAT('=',F5.2)
WRITE(7,*) NP
SINAZI = SIND(AZI1)
SINAZE = SIND(AZE1)
DO 200 J = 1,NP
    TOL = RERR(J)*FACTOR
    I = X(J)*(I1-IO) + IO
    EM = X(J)*(E1-EO) + EO
    G = X(J)*(G1-GO) + GO
    PP = 1. + BP*COSED(G)
    COSI = COSD(I)
    SINI = SIND(I)

```

```

COSE = COSD(EM)
SINE = SIND(EM)
C
C
C
      FIND VALUES OF DELTA THAT BOUND DESIRED VALUE
C
B = 0.DO
      CALL HAPKE(IPRIME(B),EPRIME(B),G,THETA,WO,PP,H,RFO)
RDIFF = PI*RFO - R(J)
110      B = B - RDIFF
      CALL HAPKE(IPRIME(B),EPRIME(B),G,THETA,WO,PP,H,RF1)
      IF((PI*RF1-R(J))*RDIFF.GT.0.) GO TO 110.
C
C
C
      FOLLOWING SECTION OF CODE FINDS ROOT OF HAPKE'S FUNCTION
      USING BRENT'S METHOD, FROM Numerical Recipes, p. 253.
C
A = 0.DO
FA = PI*RFO - R(J)
FB = PI*RF1 - R(J)
FC = FB
DO 150 ITER = 1,100
      IF(FB*FC.GT.0.) THEN
          C = A
          FC = FA
          D = B - A
          E = D
      END IF
      IF(ABS(FC).LT.ABS(FB)) THEN
          A = B
          B = C
          C = A
          FA = FB
          FB = FC
          FC = FA
      END IF
      TOL1 = 2.DO*EPS*DABS(B)
      XM = 5.D-1*(C-B)
      IF (DABS(2.DO*XM).LE.TOL1 .OR. FB.EQ.0.) GO TO 190
      IF (DABS(E).GE.TOL1 .AND. ABS(FA).GT.ABS(FB)) THEN
          S = FB/FA
          IF (A.EQ.C) THEN
              P = 2.DO*XM*S
              Q = 1.DO - S

```

```

ELSE
  Q = FA/FC
  T = FB/FC
  P = S*(2.DO*XM*Q*(Q-T) - (B-A)*(T-1.DO))
  Q = (Q-1.DO)*(T-1.DO)*(S-1.DO)
END IF
IF (P.GT.O.DO) Q = -Q
P = DABS(P)
IF (2.DO*P.LT.DMIN1(3.DO*XM*Q-DABS(TOL1*Q),DABS(E*Q)))
&   THEN
  E = D
  D = P/Q
ELSE
  D = XM
  E = D
END IF
ELSE
  D = XM
  E = D
END IF
A = B
FA = FB
IF (DABS(D).GT.TOL1) THEN
  B = B + D
ELSE
  B = B + DSIGN(TOL1, XM)
END IF
CALL HAPKE(IPRIME(B), EPRIME(B), G, THETA, WO, PP, H, RF)
FB = PI*RF - R(J)
IF (D.NE.O.DO) XM = 5.D-1*DMIN1(DABS(D), DABS(XM))
IF (XM.EQ.O.DO) XM = D
IF (ABS(FB).LT.TOL) GO TO 190
150   CONTINUE
TYPE *, XM, FB, TOL
PAUSE ' TOO MANY ITERATIONS REQUIRED TO FIND SLOPE.'
C
C   END OF ROOT-FINDING SECTION FROM NUMERICAL RECIPES
C
190   SLOPE(J) = B
WRITE (7, *) X(J), SLOPE(J), TOL, XM
200  CONTINUE
CLOSE (7)

```

```

        FILEOUT = PICNO2(1:LEN2)//'.R'//NPROF
        OPEN(8,FILE=FILEOUT,STATUS='NEW')
        WRITE(8,*) ITWO
        WRITE(8,210) WO
210  FORMAT ('Single-scattering albedo =',F5.2)
        WRITE(8,*) NP
        SINAZI = SIND(AZI2)
        SINAZE = SIND(AZE2)
        DO 400 J = 1, NP
            I = X(J)*(I3-I2) + I2
            EM = X(J)*(E3-E2) + E2
            G = X(J)*(G3-G2) + G2
            PP = 1. + BP*COSD(G)
            COSI = COSD(I)
            SINI = SIND(I)
            COSE = COSD(EM)
            SINE = SIND(EM)
            B = SLOPE(J)
            CALL HAPKE(IPRIME(B),EPRIME(B),G,THETA,WO,PP,H,RF)
            WRITE (8,*) X(J),PI*RF,ZERO,ZERO
400  CONTINUE
        OPEN (4,FILE=PROF2,STATUS='OLD',READONLY)
        READ (4,10) STRING
        DO 450 J = 1,1000
            READ (4,*,END=460) X(J),R(J),XINC,RERR(J)
450  CONTINUE
        STOP 'MORE THAN 1000 POINTS IN SECOND PROFILE.'
460  N = X(J)
        CLOSE(4)
        IF (N.NE.J-1) STOP 'ERROR IN SECOND PROFILE DATA FILE.'
        TOTAL = X(N) + XINC
        XINC = XINC/TOTAL
        WRITE(8,10) PICNO2
        WRITE(8,*) N
        DO 500 J = 1,N
            X(J) = X(J)/TOTAL
            WRITE (8,*) X(J),R(J),XINC,RERR(J)
500  CONTINUE
        CLOSE (8)
        STOP
        END

```

```

C           TNA (TOPOGRAPHY AND ALBEDO)
C
C           PROGRAM TO FIT REFLECTANCE PROFILE (GIVEN INITIAL ALBEDO)
C           USING HAPKE'S (1984) BI-SCOPIC REFLECTANCE FUNCTION.
C           INPUT READ FROM DATA FILE WITH ARBITRARY DISTANCE COORDINATE,
C           OUTPUT WRITTEN TO DATA FILE NORMALIZED TO TOTAL DISTANCE.
C           ASSUMES SLOPE VARIES ONLY ALONG PROFILE (ROTATION ABOUT AXIS
C           PERPENDICULAR TO BOTH PROFILE AND PLANETARY RADIUS VECTOR).
C           ALBEDOS OF 1 NOT INCLUDED IN SOLUTION.
C           OPTION TO RE-EVALUATE ALBEDO USING DERIVED TOPOGRAPHY, THEN
C           RE-CALCULATE TOPOGRAPHY USING NEW ALBEDOS (ITERATE).
C
C           WRITTEN BY KEN HERKENHOFF, 4/7/89
C
C           DIMENSION R(1000),RERR(1000),X(1000),W(1000),XW(1000)
C           DIMENSION SLOPE(1000),R2(1000),RERR2(1000)
C           DOUBLE PRECISION A,B,C,D,E,EPS,P,Q,S,T,TOL1,XM,IPRIME,EPRIME,
C           DOUBLE PRECISION SLOPEO,WI,WE,DELTA
C           REAL I,IO,I1,I2,I3
C           CHARACTER*32 GEOM1,GEOM2,PROF1,PROF2,FILOUT,STRING,PICNO1
C           CHARACTER*1 NPROF
C           DATA ZERO/O./,IONE/1/,EPS/2.8E-17/,PI/3.14159265/,FACTOR/O.5/
C
C           STATEMENT FUNCTIONS EVALUATE INCIDENCE AND EMISSION ANGLES ON
C           ROTATED SURFACE ELEMENT
C
C           IPRIME(DELTA) = DACOSD(DCOSD(DELTA)*COSI +
C           &                      DSIND(DELTA)*SINI*SINAZI)
C           EPRIME(DELTA) = DACOSD(DCOSD(DELTA)*COSE +
C           &                      DSIND(DELTA)*SINE*SINAZE)
C           TYPE *, ' Enter picture number of first image (topo):'
C           READ (5,10) PICNO1
10  FORMAT (A)
C           TYPE *, ' Enter picture number of second image (albedo):'
C           READ (5,10) PICNO2
C           TYPE *, ' Enter profile number:'
C           READ (5,10) NPROF
C           TYPE *, ' Enter initial single-scattering albedo:'
C           READ (5,*) WO
C           LEN1 = INDEX(PICNO1,' ') - 1
C           LEN2 = INDEX(PICNO2,' ') - 1
C           PROF1 = PICNO1(1:LEN1)//'.AV'//NPROF

```

```

PROF2 = PICNO2(1:LEN2)//'.AV'//NPROF
GEOM1 = PICNO1(1:LEN1)//'.IEG'//NPROF
GEOM2 = PICNO2(1:LEN2)//'.IEG'//NPROF
FILOUT = PICNO1(1:LEN1)//'.S'//NPROF
TYPE *, ' Enter desired number of iterations:'
READ (5,*) MAXI
OPEN (2,FILE=GEOM1,STATUS='OLD',READONLY)

C
C READ GEOMETRIC AND PHOTOMETRIC FUNCTION PARAMETERS FOR TOPO IMAGE
C
    READ (2,*) IO,EO,GO
    READ (2,*) I1,E1,G1
    READ (2,*) THETA,H,BP

C
C READ ANGULAR DIFFERENCE BETWEEN PROFILE ENDPOINTS
C
    READ (2,*) ADPE
    READ (2,*) AZI1,AZE1
    CLOSE (2)
    OPEN (2,FILE=GEOM2,STATUS='OLD',READONLY)

C
C READ GEOMETRIC AND PHOTOMETRIC PARAMETERS FOR ALBEDO IMAGE
C
    READ (2,*) I2,E2,G2
    READ (2,*) I3,E3,G3
    READ (2,*) THETA,H,BP
    READ (2,*) ADPE
    READ (2,*) AZI2,AZE2
    CLOSE (2)
    OPEN (1,FILE=PROF1,STATUS='OLD',READONLY)

C
C READ AVERAGED PROFILE DATA FROM TOPO IMAGE
C
    READ (1,10) STRING
    DO 50 J = 1,1000
        READ (1,*,END=60) X(J),R(J),XINC,RERR(J)
50 CONTINUE
    STOP 'MORE THAN 1000 POINTS IN PROFILE.'

C
C NP IS THE TOTAL NUMBER OF DATA POINTS IN THE TOPO PROFILE
C
60 NP = J - 1

```

```

IF(NINT(X(J)).NE.NP) STOP 'ERROR IN FIRST PROFILE DATA FILE.'
TOTAL = X(NP) + XINC
CLOSE(1)
DO J = 1, NP
  X(J) = X(J)/TOTAL
  SLOPE(J) = 0.
END DO
OPEN (4, FILE=PROF2, STATUS='OLD', READONLY)
READ (4, 10) STRING
C
C READ PROFILE DATA FROM ALBEDO IMAGE
C
DO 80 J = 1, 1000
  READ (4, *, END=85) XW(J), R2(J), XINC, RERR2(J)
80 CONTINUE
  STOP 'MORE THAN 1000 POINTS IN PROFILE.'
C
C N IS THE TOTAL NUMBER OF DATA POINTS IN THE ALBEDO PROFILE
C
85 N = J - 1
CLOSE(4)
IF(NINT(XW(J)).NE.N) STOP 'ERROR IN SECOND PROFILE DATA FILE.'
TOTAL = XW(N) + XINC
DO J = 1, N
  W(J) = W0
  XW(J) = XW(J)/TOTAL
END DO
C
C OPEN OUTPUT FILE
C
OPEN(7, FILE=FILOUT, STATUS='NEW')
WRITE(7, *) IONE, ADPE*58.99
WRITE(7, 89) PICNO1(1:LEN1), BP
89 FORMAT (A6, ' (b =', F5.1, ')')
WRITE(7, 90) MAXI
90 FORMAT ('(', I1, ' iterations)')
WRITE(7, *) NP
IT = 0
100 SINAZI = SIND(AZI1)
SINAZE = SIND(AZE1)
XW(N+1) = 1.
C

```

```

C  EXTRAPOLATE SINGLE SCATTERING ALBEDO TO END OF PROFILE
C
      W(N+1) = W(N) + (1.-XW(N))*(W(N)-W(N-1))/(XW(N)-XW(N-1))
      DO 200 J = 1,NP
        IF(IT.EQ.0) GO TO 107
C
C      INTERPOLATE TO FIND ALBEDO AT TOPO PROFILE POINTS
C
      K = 0
105      K = K + 1
      IF(XW(K).LT.X(J).AND.K.LE.N) GO TO 105
      IF (K.EQ.1) THEN
        WO = (X(J)-XW(1))/(XW(2)-XW(1))*(W(2)-W(1)) + W(1)
      ELSE
        WO = (X(J)-XW(K-1))/(XW(K)-XW(K-1))*(W(K)-W(K-1)) + W(K-1)
      END IF
      IF (WO.GT.1.) WO = 1.
      IF (WO.EQ.1.) THEN
        B = 0.DO
        XM = 0.DO
        FB = 999.
        GO TO 190
      END IF
C
C  SET TOLERANCE DEPENDENT UPON STANDARD DEVIATION OF PROFILE DATA
C
107      TOL = RERR(J)*FACTOR
C
C  INTERPOLATE TO FIND INCIDENCE, EMISSION, PHASE AT EACH POINT
C
      I = X(J)*(I1-IO) + IO
      EM = X(J)*(E1-EO) + EO
      G = X(J)*(G1-GO) + GO
C
C  EVALUATE PHASE FUNCTION
C
      PP = 1. + BP*COSD(G)
      COSI = COSD(I)
      SINI = SIND(I)
      COSE = COSD(EM)
      SINE = SIND(EM)
C

```

```

C      FIND VALUES OF DELTA THAT BOUND DESIRED VALUE
C
      B = SLOPE(J)
      CALL HAPKE(IPRIME(B),EPRIME(B),G,THETA,WO,PP,H,RFO)
      RDIFF = PI*RFO - R(J)
      ADIFF = ABS(RDIFF)
      XM = RDIFF
      IF (ADIFF.LT.TOL .OR. ADIFF.LT.EPS) GO TO 195
110      B = B - RDIFF
      CALL HAPKE(IPRIME(B),EPRIME(B),G,THETA,WO,PP,H,RF1)
      IF((PI*RF1-R(J))*RDIFF.GE.O.) GO TO 110

C
C      FOLLOWING SECTION OF CODE FINDS ROOT OF HAPKE'S FUNCTION
C      USING BRENT'S METHOD, FROM Numerical Recipes, p. 253.
C
      A = 0.DO
      FA = RDIFF
      FB = PI*RF1 - R(J)
      FC = FB
      DO 150 ITER = 1,100
        IF(FB*FC.GT.O.) THEN
          C = A
          FC = FA
          D = B - A
          E = D
        END IF
        IF(ABS(FC).LT.ABS(FB)) THEN
          A = B
          B = C
          C = A
          FA = FB
          FB = FC
          FC = FA
        END IF
        TOL1 = 2.DO*EPS
        XM = 5.D-1*(C-B)
        IF (DABS(2.DO*XM).LT.TOL1 .OR. FB.EQ.O.) GO TO 190
        IF (DABS(E).GE.TOL1 .AND. ABS(FA).GT.ABS(FB)) THEN
          S = FB/FA
          IF (A.EQ.C) THEN
            P = 2.DO*XM*S
            Q = 1.DO - S

```

```

ELSE
  Q = FA/FC
  T = FB/FC
  P = S*(2.DO*XM*Q*(Q-T) - (B-A)*(T-1.DO))
  Q = (Q-1.DO)*(T-1.DO)*(S-1.DO)
END IF
IF (P.GT.O.DO) Q = -Q
P = DABS(P)
IF (2.DO*P.LT.DMIN1(3.DO*XM*Q-DABS(TOL1*Q),DABS(E*Q)))
&   THEN
  E = D
  D = P/Q
ELSE
  D = XM
  E = D
END IF
ELSE
  D = XM
  E = D
END IF
A = B
FA = FB
IF (DABS(D).GT.TOL1) THEN
  B = B + D
ELSE
  B = B + DSIGN(TOL1, XM)
END IF
CALL HAPKE(IPRIME(B), EPRIME(B), G, THETA, WO, PP, H, RF)
FB = PI*RF - R(J)
IF (D.NE.O.DO) XM = 5.D-1*DMIN1(DABS(D), DABS(XM))
IF (XM.EQ.O.DO) XM = D
IF (ABS(FB).LT.TOL) GO TO 190
150   CONTINUE
TYPE *, XM, FB, TOL
STOP ' TOO MANY ITERATIONS REQUIRED TO FIND SLOPE.'
C
C   END OF ROOT-FINDING SECTION FROM NUMERICAL RECIPES
C
190   SLOPE(J) = B
195   IF(IT.EQ.MAXI) WRITE(7,*) X(J), SLOPE(J), WO, XM
200  CONTINUE
C

```

```

C NEXT ITERATION
C
      IT = IT + 1
      IF (IT.GT.MAXI) THEN
          CLOSE (7)
          STOP
      END IF
      SINAZI = SIND(AZI2)
      SINAZE = SIND(AZE2)
      X(NP+1) = 1.
      SLOPE(NP+1) = SLOPE(NP)
      WRITE (6,202) IT
202 FORMAT(' Correcting albedo profile for slope effects:',
&         ' pass number',I2)
      DO 400 J = 1,N
          IF(W(J).EQ.1.) THEN
              B = W(J)
              GO TO 390
          END IF
C
C     INTERPOLATE TO FIND SLOPE AT EACH POINT IN ALBEDO PROFILE
C
      K = 0
205      K = K + 1
          IF(X(K).LT.XW(J).AND.K.LE.NP) GO TO 205
          IF (K.EQ.1) THEN
              SLOPEO = SLOPE(K)
          ELSE
              SLOPEO = (XW(J)-X(K-1))/(X(K)-X(K-1))*
&                     (SLOPE(K)-SLOPE(K-1)) + SLOPE(K-1)
          END IF
C
C SET TOLERANCE DEPENDENT UPON STANDARD DEVIATION OF PROFILE DATA
C
      TOL = RERR2(J)*FACTOR
C
C INTERPOLATE TO FIND INCIDENCE, EMISSION, PHASE AT EACH POINT
C
      I = XW(J)*(I3-I2) + I2
      EM = XW(J)*(E3-E2) + E2
      G = XW(J)*(G3-G2) + G2
C

```

C EVALUATE PHASE FUNCTION

C

```

PP = 1. + BP*COSD(G)
COSI = COSD(I)
SINI = SIND(I)
COSE = COSD(EM)
SINE = SIND(EM)
WI = IPRIME(SLOPEO)
WE = EPRIME(SLOPEO)

```

C

C FIND BOUNDS FOR SINGLE SCATTERING ALBEDO SEARCH

C

```

CALL HAPKE(WI,WE,G,THETA,W(J),PP,H,RFO)
RDIFF = PI*RFO - R2(J)
ADIFF = ABS(RDIFF)
IF (ADIFF.LT.TOL .OR. ADIFF.LT.1.2E-7) GO TO 400
WO = W(J)
220 W(J) = W(J) - RDIFF
IF (W(J).GT.1.) W(J) = 1.
CALL HAPKE(WI,WE,G,THETA,W(J),PP,H,RF1)
IF(RDIFF*(PI*RF1-R2(J)).GT.0.0.AND.W(J).LT.1.) GO TO 220
B = W(J)
XM = (W(J) - WO)/2.DO
IF (W(J).EQ.1.) GO TO 390

```

C

C FOLLOWING SECTION OF CODE FINDS ROOT OF HAPKE'S FUNCTION
C USING BRENT'S METHOD, FROM Numerical Recipes, p. 253.

C

```

A = WO
FA = RDIFF
FB = PI*RF1 - R2(J)
FC = FB
DO 300 ITER = 1,100
  IF(FB*FC.GT.0.) THEN
    C = A
    FC = FA
    D = B - A
    E = D
  END IF
  IF(ABS(FC).LT.ABS(FB)) THEN
    A = B
    B = C
  
```

```

      C = A
      FA = FB
      FB = FC
      FC = FA
    END IF
    TOL1 = 2.DO*EPS*DABS(B)
    XM = 5.D-1*(C-B)
    IF (DABS(2.DO*XM).LE.TOL1 .OR. FB.EQ.O.) GO TO 390
    IF (DABS(E).GE.TOL1 .AND. ABS(FA).GT.ABS(FB)) THEN
      S = FB/FA
      IF (A.EQ.C) THEN
        P = 2.DO*XM*S
        Q = 1.DO - S
      ELSE
        Q = FA/FC
        T = FB/FC
        P = S*(2.DO*XM*Q*(Q-T) - (B-A)*(T-1.DO))
        Q = (Q-1.DO)*(T-1.DO)*(S-1.DO)
      END IF
      IF (P.GT.O.DO) Q = -Q
      P = DABS(P)
      IF (2.DO*P.LT.DMIN1(3.DO*XM*Q-DABS(TOL1*Q),DABS(E*Q)))
&      THEN
        E = D
        D = P/Q
      ELSE
        D = XM
        E = D
      END IF
    ELSE
      D = XM
      E = D
    END IF
    A = B
    FA = FB
    IF (DABS(D).GT.TOL1) THEN
      B = B + D
    ELSE
      B = B + DSIGN(TOL1, XM)
    END IF
    CALL HAPKE(WI,WE,G,THETA,B,PP,H,RF)
    FB = PI*RF - R2(J)

```

```
                IF (ABS(FB).LT.TOL) GO TO 390
300             CONTINUE
                TYPE *, XM,FB,TOL
                PAUSE ' TOO MANY ITERATIONS REQUIRED TO FIND ALBEDO.'
C
C             END OF ROOT-FINDING SECTION FROM NUMERICAL RECIPES
C
C FOUND SINGLE SCATTERING ALBEDO
390             W(J) = B
400             CONTINUE
C
C USE NEW SINGLE SCATTERING ALBEDOS TO FIND SLOPES
C
                GO TO 100
                END
```

References

- Arvesen, J. C., R. N. Griffin, Jr., B. D. Pearson, Jr. (1969). Determination of Extraterrestrial Solar Spectral Irradiance From a Research Aircraft. *Applied Optics* 8, 2215-2232.
- Arvidson, R. E. (1972). Aeolian Processes on Mars: Erosive Velocities, Settling Velocities, and Yellow Clouds. *Geol. Soc. America Bull.* 83, 1503-1508.
- Arvidson, R. E., E. A. Guinness, M. A. Dale-Bannister, J. Adams, M. Smith, P. R. Christensen, and R. B. Singer (1989). Nature and Distribution of Surficial Deposits in Chryse Planitia and Vicinity, Mars. *J. Geophys. Res.* 94, 1573-1587.
- Barker, E. S., R. A. Schorn, A. Woszczyk, R. G. Tull, and S. J. Little (1970). Mars: Detection of Atmospheric Water Vapor during the Southern Hemisphere Spring and Summer Season. *Science* 170, 1308-1310.
- Batson, R. M. (1987). Digital Cartography of the Planets: New Methods, its Status, and its Future. *Photogramm. Eng. and Remote Sensing* 53, 1211-1218.
- Benesh, M. and T. Thorpe (1976). Viking Orbiter 1975 Visual Imaging Subsystem Calibration Report. Jet Propulsion Laboratory Document 611-125.
- Blasius, K. R. (1973). A Study of Martian Topography by Analytic Photogrammetry. *J. Geophys. Res.* 78, 4411-4423.

- Blasius, K. R., J. A. Cutts, and A. D. Howard (1982). Topography and Stratigraphy of Martian Polar Layered Deposits. *Icarus* 50, 140-160.
- Briggs, G. A. (1974). The Nature of the Residual Martian Polar Caps. *Icarus* 23, 167-191.
- Buratti, B. J. and J. Veverka (1985). Photometry of Rough Planetary Surfaces: The Role of Multiple Scattering. *Icarus* 64, 320-328.
- Carr, M. H. (1982). Periodic Climate Change on Mars: Review of Evidence and Effects on Distribution of Volatiles. *Icarus* 50, 129-139.
- Clark, R. N. and P. G. Lucey (1984). Spectral Properties of Ice-Particulate Mixtures and Implications for Remote Sensing. I. Intimate Mixtures. *J. Geophys. Res.* 89, 6341-6348.
- Clifford, S. M. (1987). Polar Basal Melting on Mars. *J. Geophys. Res.* 92, 9135-9152.
- Cutts, J. A. (1973a). Wind Erosion in the Martian Polar Regions. *J. Geophys. Res.* 78, 4211-4221.
- Cutts, J. A. (1973b). Nature and Origin of Layered Deposits of the Martian Polar Regions. *J. Geophys. Res.* 78, 4231-4249.
- Cutts, J. A. (1974). Mariner Mars 1971 Television Picture Catalog: Experiment Design and Picture Data. Jet Propulsion Laboratory Technical Memorandum

33-585, volume 1.

Cutts, J. A., K. R. Blasius, G. A. Briggs, M. H. Carr, R. Greeley, and H. Masursky (1976). North Polar Region of Mars: Imaging Results from Viking 2. *Science* 194, 1329-1337.

Cutts, J. A., K. R. Blasius, and W. J. Roberts (1979). Evolution of Martian Polar Landscapes: Interplay of Long-Term Variations in Perennial Ice Cover and Dust Storm Intensity. *J. Geophys. Res.* 84, 2975-2994.

Cutts, J. A. and B. H. Lewis (1982). Models of Climatic Cycles Record in Martian Polar Layered Deposits. *Icarus* 50, 216-244.

Davies, D. W. (1979). Effects of Dust Heating of Mars' Surface and Atmosphere. *J. Geophys. Res.* 84, 8289-8294.

Davis, P. A. and L. A. Soderblom (1984). Modeling Crater Topography and Albedo From the Monoscopic Viking Orbiter Images. 1. Methodology. *J. Geophys. Res.* 89, 9449-9457.

de Vaucouleurs, G. (1964). Geometric and Photometric Parameters of the Terrestrial Planets. *Icarus* 3, 187-235.

Dobrovolskis, A. and A. P. Ingersoll (1975). Carbon Dioxide-Water Clathrate as a Reservoir or CO₂ on Mars. *Icarus* 26, 353- 357.

- Dzurisin, D. and K. R. Blasius (1975). Topography of the Polar Layered Deposits of Mars. *J. Geophys. Res.* 80, 3286-3306.
- Edwards, K. (1987). Geometric Processing of Digital Images of the Planets. *Photogramm. Eng. and Remote Sensing* 53, 1219-1222.
- Fanale, F. P. and W. A. Cannon (1974). Exchange of Adsorbed H₂O and CO₂ Between the Regolith and Atmosphere of Mars Caused by Changes in Surface Insolation. *J. Geophys. Res.* 79, 3397-3402.
- Fanale, F. P. and W. A. Cannon (1979). Mars CO₂ Adsorption and Capillary Condensation on Clays. Significance for Volatile Storage and Atmospheric History. *J. Geophys. Res.* 84, 8404-8414.
- Fanale, F. P., J. R. Salvail, W. B. Banerdt, and R. S. Saunders (1982). Mars: The Regolith-Atmosphere-Cap System and Climate Change. *Icarus* 50, 381-407.
- Farmer, C. B., D. W. Davies and D. D. La Porte (1976). Mars: Northern Summer Ice Cap-Water Vapor Observations From Viking 2. *Science* 194, 1339-1341.
- Greeley, R., R. Leach, B. R. White, J. D. Iversen, and J. B. Pollack (1980). Threshold Wind Speeds for Sand on Mars: Wind Tunnel Simulations. *Geophys. Res. Lett.* 7, 121-124.
- Green, W. B., P. L. Jepsen, J. E. Kresnar, R. M. Ruiz, A. A. Schwartz, J. B. Seidman, (1975). Removal of Instrument Signature From Mariner 9 Television

Images of Mars. *Applied Optics* 14, 105-114.

Guinness, E. A. (1981). Spectral Properties (0.40 to 0.75 Microns) of Soils Exposed at the Viking 1 Landing Site. *J. Geophys. Res.* 86, 7983-7992.

Hanel, R. A., B. J. Conrath, W. A. Hovis, V. G. Kunde, P. D. Lowman, J. C. Pearl, C. Prabhakara, B. Schlachman, and G. V. Levin (1972a). Infrared Spectroscopy Experiment on the Mariner 9 Mission: Preliminary Results. *Science* 175, 305-308.

Hanel, R. A., B. Schlachman, E. Breihan, R. Bywaters, F. Chapman, M. Rhodes, D. Rodgers, and D. Vanous (1972b). Mariner 9 Michelson Interferometer. *Appl. Optics* 11, 2625-2634.

Hapke, B. (1981). Bidirectional Reflectance Spectroscopy. 1. Theory. *J. Geophys. Res.* 86, 3039-3054.

Hapke, B. (1984). Bidirectional Reflectance Spectroscopy. 3. Correction for Macroscopic Roughness. *Icarus* 59, 41-59.

Hargraves, R. B., D. W. Collinson, R. E. Arvidson, and P. M. Cates (1979). Viking Magnetic Properties Experiment: Extended Mission Results. *J. Geophys. Res.* 84, 8379-8384.

Helfenstein, P. (1988). The Geological Interpretation of Photometric Surface Roughness. *Icarus* 73, 462-481.

- Herkenhoff, K. E. and B. C. Murray (1989). Color and Albedo of the South Polar Layered Deposits on Mars. *J. Geophys. Res.* in press.
- Herkenhoff, K. E., L. A. Soderblom, B. C. Murray, and G. E. Danielson (1988). Mariner 9 Television Calibration—Revisited. *Icarus* 75, 133-145.
- Herr, K. C. and G. C. Pimentel (1969). Infrared Observations Near Three Microns Recorded Over the Polar Cap of Mars. *Science* 166, 496-499.
- Hofstadter, M. D. and B. C. Murray (1989). Ice Sublimation and Rheology: Implications for the Martian Polar Layered Deposits. Submitted to *Icarus*.
- Howard, A. D. (1978). Origin of the Stepped Topography of the Martian Poles. *Icarus* 34, 581-599.
- Howard, A. D., K. R. Blasius, and J. A. Cutts (1982a). Photoclinometric Determination of the Topography of the Martian North Polar Cap. *Icarus* 50, 245-258.
- Howard, A. D., J. A. Cutts, and K. R. Blasius (1982b). Stratigraphic Relationships within Martian Polar Cap Deposits. *Icarus* 50, 161-215.
- Ingersoll, A. P. (1974). Mars: The Case Against Permanent CO₂ Frost Caps. *J. Geophys. Res.* 79, 3403-3410.
- Iversen, J. D. and B. R. White (1982). Saltation thresholds on Earth, Mars, and Venus. *Sedimentology* 29, 111-119.

- Jakosky, B. M. and T. Z. Martin (1987). Mars: North Polar Atmospheric Warming During Dust Storms. *Icarus* 72, 528-534.
- Jakosky, B. M. and E. S. Barker (1984). Comparison of Ground-Based and Viking Orbiter Measurements of Martian Water Vapor: Variability of the Seasonal Cycle. *Icarus* 57, 322-334.
- James, P. B., G. Briggs, J. Barnes, and A. Spruck (1979). Seasonal Recession of Mars' South Polar Cap As Seen by Viking. *J. Geophys. Res.* 84, 2889-2922.
- Jaquin, F., P. Gierasch, and R. Kahn (1986). The Vertical Structure of Limb Hazes in the Martian Atmosphere. *Icarus* 68, 422-461.
- Kahn, R., R. Goody, and J. Pollack (1981). The Martian Twilight. *J. Geophys. Res.* 86, 5833-5838.
- Kattawar, G. W. and A. T. Young (1977). Planetary Isophotes as a Clue to Aerosol Characteristics. *Icarus* 30, 367-376.
- Kieffer, H. H. (1979). Mars South Polar Spring and Summer Temperatures: A Residual CO₂ Frost. *J. Geophys. Res.* 84, 8263-8288.
- Kieffer, H. H. (1979). Mars South Polar Spring and Summer Temperatures: A Residual CO₂ Frost. *J. Geophys. Res.* 84, 8263-8288.
- Kieffer, H. H. (1989). How Dirty is Mars's North Polar Cap, and Why Isn't it Black? Submitted to *J. Geophys. Res.*

- Kieffer, H. H., S. C. Chase, T. Z. Martin, E. D. Miner, and F. D. Palluconi (1976a).
Martian North Pole Summer Temperatures: Dirty Water Ice. *Science* 194,
1341-1344.
- Kieffer, H. H., S. C. Chase, E. D. Miner, F. D. Palluconi, G. Munch, G. Neugebauer,
and T. Z. Martin (1976b). Infrared Thermal Mapping of the Martian Surface
and Atmosphere: First Results. *Science* 193, 780-786.
- Kieffer, H. H., T. Z. Martin, A. R. Peterfreund, B. M. Jakosky, E. D. Miner, and
F. D. Palluconi (1977). Thermal and Albedo Mapping of Mars During the
Viking Primary Mission. *J. Geophys. Res.* 82, 4249- 4291.
- Klaasen, K. P., T. C. Duxbury, and J. Veverka (1979). Photometry of Phobos and
Deimos From Viking Orbiter Images. *J. Geophys. Res.* 84, 8478-8486.
- Klaasen, K. P., T. E. Thorpe, and L. A. Morabito (1977). Inflight Performance of
the Viking Visual Imaging Subsystem. *Applied Optics* 16, 3158-3170.
- Kliore, A. J., G. Fjeldbo, B. L. Seidel, M. J. Sykes, and P. M. Woiceshyn (1973). S-
Band Radio Occultation Measurements of the Atmosphere and Topography of
Mars with Mariner 9: Extended Mission Coverage of Polar and Intermediate
Latitudes. *J. Geophys. Res.* 78, 4331-4351.
- Leighton, R. B. and B. C. Murray (1966). Behavior of CO₂ and Other Volatiles on
Mars. *Science* 153, 136-144.

- Lumme, K., L. J. Martin, and W. A. Baum (1981). Theoretical Interpretation of Photometric Properties of the Martian Surface and Atmosphere. *Icarus* 45, 379-397.
- Malin, M. C. (1986). Density of Martian North Polar Layered Deposits: Implications for Composition. *Geophys. Res. Lett.* 13, 444-447.
- McCartney, E. J. (1976). *Optics of the Atmosphere*, John Wiley and Sons, New York.
- McCord, T. B. (1989). Responses to questioning at the 4th International Mars Conference, Tucson, Arizona, January, 1989.
- McCord, T. B. and J. B. Adams (1969). Spectral Reflectivity of Mars. *Science* 163, 1058-1060.
- McCord, T. B., R. L. Huguenin, D. Mink, and C. Pieters (1977). Spectral Reflectance of Martian Areas During the 1973 Opposition: Photoelectric Filter Photometry 0.33-1.10 μ . *Icarus* 31, 25-39.
- McCord, T. B., R. B. Singer, B. R. Hawke, J. B. Adams, D. L. Evans, J. W. Head, P. J. Mouginis-Mark, C. M. Pieters, R. L. Huguenin, R. and S. H. Zisk (1982). Mars: Definition and Characterization of Global Surface Units With Emphasis on Composition. *J. Geophys. Res.* 87, 10,129-10,148.

- McCord, T. B. and J. A. Westphal (1971). Mars: Narrow-Band Photometry, from 0.3 to 2.5 microns, of Surface Regions During the 1969 Apparition. *Astrophys. J.* 168, 141-153.
- McEwen, A. S. (1985). Topography and Albedo of Ius Chasma, Mars. *Lunar and Planet. Sci.* XVI, 528-529.
- McEwen, A. S. (1989). Photometric Functions for Photoclinometry and Other Applications. Submitted to *Icarus*.
- Michelangeli, D. V., M. A. Allen, Y. L. Yung, R. L. Shia, and D. Crisp (1989). Enhancement of the Actinic Flux by an Aerosol Layer. Submitted to *J. Geophys. Res.*
- Murray, B. C. and M. C. Malin (1973). Polar Volatiles on Mars—Theory Versus Observations. *Science* 183, 437-443.
- Murray, B. C., L. A. Soderblom, J. A. Cutts, R. P. Sharp, D. J. Milton, and R. B. Leighton (1972). Geological Framework of the South Polar Region of Mars. *Icarus* 17, 328-345.
- Neckel, H. and D. Labs (1984). The Solar Radiation Between 3300 and 12500Å. *Solar Physics* 90, 205-258.
- Neugebauer, G., G. Munch, H. H. Kieffer, S. C. Chase, Jr., and E. Miner (1971). Mariner 1969 Infrared Radiometer Results: Temperatures and Thermal Prop-

- erties of the Martian Surface. *Astron. J.* 76, 719-728.
- O'Leary, B. T. and L. Jackel (1970). The 1969 opposition effect of Mars: Full disk, Syrtis Major and Arabia. *Icarus* 13, 437-448.
- O'Leary, B. T. and D. G. Rea (1968). The Opposition Effect of Mars and Its Implications. *Icarus* 9, 405-428.
- Paige, D. A. (1985). The Annual Heat Balance of Martian Polar Caps. Ph.D. thesis, California Institute of Technology, Pasadena.
- Paige, D. A., K. E. Herkenhoff, and B. C. Murray, (1989). Mariner 9 Observations of the South Residual Polar Cap of Mars: Evidence for Residual CO₂ Frost. Submitted to *J. Geophys. Res.*
- Paige, D. A. and A. P. Ingersoll (1985). Annual Heat Balance of Martian Polar Caps: Viking Observations. *Science* 228, 1160-1168.
- Paige, D. A. and H. H. Kieffer (1987). The Thermal Properties of Martian Surface Materials at High Latitudes: Possible Evidence for Permafrost. *Lunar Planet. Inst. Tech. Rept.* 87-01, 93-95.
- Pang, K. D. and C. W. Hord (1973). Mariner 9 Ultraviolet Spectrometer Experiment: 1971 Mars Dust Storm. *Icarus* 18, 481-488.
- Pang, K. D., J. W. Rhoads, G. A. Hanover, K. Lumme, and E. Bowell (1983). Interpretation of Whole-Disk Photometry of Phobos and Deimos. *J. Geophys.*

Res. 88, 2475-2484.

Pike, F. J. (1979). Simple to Complex Craters: The Transition on Mars. *NASA Tech. Memo.* 80339, 132-134.

Plaut, J. J., R. Kahn, E. A. Guinness, and R. E. Arvidson (1988). Accumulation of Sedimentary Debris in the South Polar Region of Mars and Implications for Climate History. *Icarus* 75, 357-377.

Pollack, J. B. (1982). Properties of Dust in the Martian Atmosphere and Its Effect on Temperature Structure. *Adv. Space Res.* 2, 45-56.

Pollack, J. B., D. Colburn, F. M. Flasar, R. Kahn, C. Carlston, and D. Pidek (1979). Properties and Effects of Dust Particles Suspended in the Martian Atmosphere. *J. Geophys. Res.* 84, 4479-4496.

Pollack, J. B., D. Colburn, R. Kahn, J. Hunter, W. Van Camp, C. E. Carlston, and M. R. Wolf (1977). Properties of Aerosols in the Martian Atmosphere, as Inferred from Viking Lander Imaging Data. *J. Geophys. Res.* 82, 4479-4496.

Pollack, J. B. and O. B. Toon (1982). Quasi-Periodic Climate Changes on Mars: A Review. *Icarus* 50, 259-287.

Saunders, R. S., F. P. Fanale, T. J. Parker, J. B. Stephens, and S. Sutton (1986). Properties of Filamentary Sublimation Residues from Dispersions of Clay in Ice. *Icarus* 66, 94-104.

- Saunders, R. S., T. J. Parker, J. B. Stephens, E. G. Laue, and F. P. Fanale (1985). Transformation of polar ice sublimate residue into Martian circumpolar sand. *NASA Tech. Mem.* 87563, 300-302.
- Schultz, P. H. and A. Lutz (1988). Polar Wandering of Mars. *Icarus* 73, 91-141.
- Sears, F. W. (1949). *Optics*, Addison-Wesley, Reading, 3rd. ed.
- Seidman, J. B., W. B. Green, P. L. Jepsen, R. M. Ruiz, and T. E. Thorpe (1973). A User's Guide to the Mariner 9 Television Reduced Data Record. Jet Propulsion Laboratory Technical Memorandum 33-628.
- Snyder, L. M. (1971). Mariner 9 TV Subsystem Calibration Report. Jet Propulsion Laboratory Internal Report 610-202, volume 1.
- Soderblom, L. A., M. C. Malin, J. A. Cutts, and B. C. Murray (1973). Mariner 9 Observations of the Surface of Mars in the North Polar Region. *J. Geophys. Res.* 78, 4197-4210.
- Squyres, S. W. (1979). The Evolution of Dust Deposits in the Martian North Polar Region. *Icarus* 40, 244-261.
- Storrs, A. D., F. P. Fanale, R. S. Saunders, and J. B. Stephens (1988). The Formation of Filamentary Sublimate Residues (FSR) from Mineral Grains. *Icarus* 76, 493-512.

- Tanaka, K. L. and D. H. Scott (1987). Geologic Map of the Polar Regions of Mars. U. S. Geological Survey Miscellaneous Investigations Series Map I-1802-C.
- Thomas, P. (1982). Present Wind Activity on Mars: Relation to Large Latitudinally Zoned Sediment Deposits. *J. Geophys. Res.* **87**, 9999-10008.
- Thomas, P, K. Herkenhoff, A. Howard, B. Murray, and S. Squyres (1989) Polar Deposits of Mars. Submitted to *Mars*. University of Arizona Press, Tucson.
- Thomas, P. C. and C. Weitz (1989). Dune Sand Materials and Polar Layered Deposits on Mars. *Icarus*, in press.
- Thorpe, T. E. (1972). Mariner 9 Television Imaging Performance Evaluation. Jet Propulsion Laboratory Internal Report 610-237, volume 2.
- Thorpe, T. E. (1973a). Verification of Performance of the Mariner 9 Television Cameras. *Applied Optics* **12**, 1775-1784.
- Thorpe, T. E. (1973b). Mariner 9 Photometric Observations of Mars from November 1971 through March 1972. *Icarus* **20**, 482-489.
- Thorpe, T. E. (1977a). Viking Orbiter Observations of Atmospheric Opacity During July-November 1976. *J. Geophys. Res.* **82**, 4151-4159.
- Thorpe, T. E. (1977b). Viking Orbiter Photometric Observations of the Mars Phase Function July Through November 1976. *J. Geophys. Res.* **82**, 4161-4165.

- Thorpe, T. E. (1978). Viking Orbiter Observations of the Mars Opposition Effect. *Icarus* **36**, 204-215.
- Thorpe, T. E. (1979). A History of Mars Atmospheric Opacity in the Southern Hemisphere During the Viking Extended Mission. *J. Geophys. Res.* **84**, 6663-6683.
- Thorpe, T. E. (1981). Mars Atmospheric Opacity Effects Observed in the Northern Hemisphere by Viking Orbiter Imaging. *J. Geophys. Res.* **86**, 11419-11429.
- Thorpe, T. E. (1982). Martian Surface Properties Indicated by the Opposition Effect. *Icarus* **49**, 398-415.
- Toon, O. B., J. B. Pollack, W. Ward, J. A. Burns, and K. Bilski (1980). The Astronomical Theory of Climatic Change on Mars. *Icarus* **44**, 552-607.
- Veverka, J. and J. A. Burns (1980). The Moons of Mars. *Ann. Rev. Earth Planet. Sci.* **8**, 527-558.
- Veverka, J., P. Thomas, T. V. Johnson, D. L. Matson, and K. Housen (1986). The Physical Characteristics of Satellite Surfaces. In *Satellites* (J. Burns and M. S. Matthews, Eds.), pp. 342-402. University of Arizona Press, Tucson.
- Ward, W. R. (1974). Climatic Variations on Mars. 1. Astronomical Theory of Insolation. *J. Geophys. Res.* **79**, 3375-3386.

- Ward, W. R. (1979). Present Obliquity Oscillations of Mars: Fourth-Order Accuracy in Orbital e and I . *J. Geophys. Res.* **84**, 237-241.
- Ward, W. R., B. C. Murray, and M. C. Malin (1974). Climatic Variations on Mars. 2. Evolution of Carbon Dioxide Atmosphere and Polar Caps. *J. Geophys. Res.* **79**, 3387-3395.
- Wechsler, A. E. and P. E. Glaser (1965). Pressure Effects on Postulated Lunar Materials. *Icarus* **4**, 335-352.
- Winter, D. F. and J. M. Saari (1969). A Particulate Thermophysical Model of the Lunar Soil. *Astrophys. J.* **156**, 1135-1151.
- Young, A. T. (1974a). Television Photometry: The Mariner 9 Experience. *Icarus* **21**, 262-282.
- Young, A. T. (1974b). UVB Photometry of Mars. In *Exploration of the Planetary System*, pp. 253-285. Reidel, Dordrecht.
- Zellner, B. H. and R. C. Capen (1974). Photometric Properties of the Martian Satellites. *Icarus* **23**, 437-444.
- Zurek, R. W. (1982). Martian Great Dust Storms: An Update. *Icarus* **50**, 288-310.

This floppy diskette contains digital versions of the FORTRAN code in Appendix C of Ken Herkenhoff's doctoral dissertation. The files on this floppy were written using a MicroVAX II running VMS version 5.1. Mariner 9 image processing software is in the directory [M9], and photoclinometric software is in the directory [PC]. The programs in [M9] must be compiled using the files ending in .CMP and linked using files ending in .LNK on a system with TAE and PICS installed. Executable modules are included in the [PC] directory.

PLEASE NOTE:

The diskette is not included in this material. It is available for consultation at this author's graduate school library.

UNIVERSITY MICROFILMS INTERNATIONAL